Development of a Data Fusion-Based Multi-Sensor System for Hybrid Sheet Molding Compound

Zur Erlangung des akademischen Grades einer
DOKTORIN DER INGENIEURWISSENSCHAFTEN (Dr.-Ing.)

von der KIT-Fakultät für Maschinenbau des
Karlsruher Instituts für Technologie (KIT)
angenommene

DISSERTATION

von

M. Sc. Marielouise Schäferling, geborene Zaiß

Tag der mündlichen Prüfung: 29.03.2019
Hauptreferent: Prof. Dr.-Ing. Gisela Lanza
Korreferent: Prof. Dr. Michael Thompson
Korreferent: Prof. Dr.-Ing. Robert Schmitt

Preface by editor

The fast and efficient implementation of innovative technologies is supported by the following factors. The globalization of the economy is the decisive economic factor for manufacturing companies. As "value-added partners", universities can make a significant contribution to the competitiveness of industry by developing scientific foundations, new methods and technologies as well as actively supporting the implementation process in practical applications. Against this background, this series of publications will report the current research results of the Institute of Production Engineering (wbk) at the Karlsruhe Institute of Technology (KIT). Our research work is concerned with increasing the performance of manufacturing processes, associated machine tool and handling technologies as well as with the holistic consideration and optimization of the entire production system. On the same time technological and organizational aspects are considered here.

Prof. Dr.-Ing. Jürgen Fleischer

Prof. Dr.-Ing. Gisela Lanza

Prof. Dr.-Ing. habil. Volker Schulze

Vorwort des Verfassers

Kurzbeschreibung

In den letzten Jahren ist die Produktion von faserverstärkten Kunststoffen stetig gestiegen. Ein Teil davon ist das glasfaser-verstärkte Sheet Molding Compound (SMC), welches sich durch seine günstigen Herstellkosten und einfache Verarbeitung auszeichnet. Allerdings weist dieses Material schlechte mechanische Eigenschaften auf, welche eine Anwendung für Strukturbauteile verhindert. Um diesem Nachteil entgegen zu wirken, wird das diskontinuierliche Glasfaser-SMC lokal mit kontinuierlichem Carbonfaser-SMC verstärkt. Dadurch können die Vorteile des günstigen und leicht zu verarbeitenden Glasfaser-SMC mit den sehr guten mechanischen Eigenschaften von Carbonfaser-SMC in Faserrichtung kombiniert werden.

Die Kombination dieser beiden Werkstoffe kann bereits in einem frühen Produktionsschritt zu einer Vielzahl an möglichen Defekten wie beispielsweise Delamination, Falten oder Winkelabweichungen führen. Um keine weiteren wertschöpfenden Maßnahmen an defekten Bauteilen durchzuführen, muss die Qualitätssicherung bereits in einem frühen Prozessstadium durchgeführt werden.

Die zu entdeckenden Fehler werden in außen- und innenliegende Defekte unterteilt. Da kein System verfügbar ist, um alle relevanten Defekte zu detektieren, wird pro Defektklasse ein Messsystem benötigt. Zudem erstreckt sich der Anwendungsbereich neben dem Halbzeug auch auf das ausgehärtete Bauteil. Das Laserlichtschnittsystem und die aktive Thermografie, in Form der Puls-Phasen-Thermografie, haben sich als geeignet erwiesen.

Beide Systeme werden zunächst einzeln untersucht und für den vorliegenden Anwendungsfall angepasst. Dabei ist es möglich die Puls-Phasen-Thermografie methodisch zu einer Tiefenauswertung weiterzuentwickeln. Des Weiteren werden Fehler nicht nur detektiert, sondern auch definiert.

Anschließen werden die beiden Systeme in einem Multisensorik-System zusammengeführt. Mit Hilfe der Datenfusion sind eine Auswertung von außen- und innenliegenden Defekten, sowie die Ermittlung von geometrischen Zusammenhängen zwischen einzelnen Defekten möglich. Durch den Aufbau eines Schichtmodells wird zusätzlich eine benutzerfreundliche Auswertung ermöglicht, welche dem Anwender schnell einzelne Schichten aufzeigen kann. Mit der Ermittlung der Messunsicherheit des Multisensorik-Systems wird die Güte aufgezeigt.

Table of Contents

List of Abbreviations

Symbol	Item	Unit
$A(f)$	amplitude	[°C]
b	bias	[mm]; [°]
C	specific heat capacity	[J/(kg·K)]
c	coordinate	[°]
f	frequency	[Hz]
f_b	blind frequency	[Hz]
f_{ch}	characteristic frequency	[Hz]
f_l	focal length	[mm]
i	imaginary number	[-]
I_0	original intensity	[W/m^2]
Im	imaginary part of transform	[-]
k_{th}	thermal conductivity	[W/(m·K)]
k	coverage factor	[-]
k_{Cam}	f-number for Camera	[-]
l	length	[mm]
m	thermogram number	[-]
$\boldsymbol{M}_f$	matrix of a pinhole camera interior	[-]
$\boldsymbol{M}_i$	intrinsic parameters of camera	[-]
$\boldsymbol{M}_p$	projection matrix	[-]
n	frequency increment	[-]
N	number of measuring points	[-]
Q_{MS}	capability ratio (system)	[%]
Re	real part of transform	[-]
$\boldsymbol{Rt}$	extrinsic parameters of camera	[-]
s_θ	axial misalignment	[-]
s_x, s_y	sensor scaling in x and y direction	[-]
T	temperature	[K]
t	time	[s]

Symbol	Item	Unit
Δt	time resolution	[s]
TOL_{min}	minimum tolerance	[mm]; [°]
U	expanded measurement uncertainty	[mm]; [°]
u, v	pixel coordinates of digital image	[-]
u_c, v_c	main image points	[-]
u_α	uncertainty of the expansion coefficient	[K^{-1}]
u_b	standard uncertainty from systematic deviation	[mm]; [°]
u_{cal}	calibration standard uncertainty on a standard	[mm]; [°]
u_i	standard uncertainties	[mm]; [°]
u_{K_CMM}	uncertainty of the diameter of the ball standard	[mm]
u_{MPE}	length measurement uncertainty	[µm]
u_{MPE_angle}	length measurement uncertainty for angle	[°]
u_{MPE_plane}	length measurement uncertainty for plane	[µm]
u_{MT_CMM}	uncertainty due to probe deviation	[mm]
u_p	standard uncertainty from the measurement method	[mm]; [°]
u_w	uncertainty from material and production variation	[mm]; [°]
u_{wt_CMM}	uncertainty of workpiece expansion	[mm]
x_t	thickness	[m]
x	coordinate	[mm]
x, y	coordinates on optical image plane	[-]
X, Y, Z	coordinates of the world coordinate system	[-]
X_C, Y_C, Z_C	coordinates of the camera coordinate system	[-]
x_{cal}	value of the measured variable of the calibrated workpiece or measurement standard	[mm]; [°]
y	coordinate	[mm]
$\bar{y}$	arithmetic mean of the measured values	[mm]; [°]
y_i	is the measured values	[mm]; [°]
z_d	depth	[mm]

Symbol	Item	Unit
z_d	depth	[mm]
z	coordinate	[mm]
α	camera angle	[°]
β	laser angle	[°]
γ	lateral tilting (side panel angle 0°, 5°, 10°, 15°)	[°]
ε	relative uncertainty factor	[-]
ϑ	thermal diffusivity	[m^2/s]
λ	thermal wavelength	[µm]
μ	thermal diffusion length	[m]
μ_{CT}	material-specific attenuation coefficient	[-]
ρ	density	[kg·m^{-3}]
$\Phi(f)$	phase	[°]
φ	triangulation angle	[°]
ω	angular frequency	[s^{-1}]

Acronym	Notation
2D	two-dimensional
3D	three-dimensional
approx.	approximately
AVK	Industrievereinigung Verstärkte Kunststoffe e.V.
Blob	Binary Large Object
BMWi	Federal Ministry for Economic Affairs and Energy
cf.	confer
CFRP	carbon fiber reinforced plastics
CCD	Charge-Coupled Device
CMM	Coordinate Measuring Machine

Acronym	Notation
CMM	Coordinate Measuring Machine (used as an index)
CMOS	Complementary Metal Oxide Semiconductor
CO_2	Carbon Dioxide
CoDiCo-SMC	Continuous-discontinuous-Sheet Molding Compound
CoFRP	Continuous-fiber reinforced plastic
COG	Center of Gravity Mode
CoP	Cloud of Points
COS	Coordinate System
Co-SMC	Continuous-Sheet Molding Compound
CT	computer tomography
CT	computer tomography (used as an index)
cu	cured (used as an index and test name)
dB	decibel
DF	Data Fusion (used as an index)
DFG	German Research Foundation
DiCoFRP	Discontinuous-fiber reinforced plastic
DiCo-SMC	Discontinuous-Sheet Molding Compound
DTA	Decay Time Analysis
EoD	Effect of Defect
ESPI	Electronic Speckle Pattern Interferometry
FFT	Fast Fourier Transform
FRP	Fiber reinforced plastics
g	Gram
GFRP	Glass fiber reinforced plastic
GHz	Gigahertz
GigE	Gigabit Ethernet
GUM	Guide to the Expression of Uncertainty in Measurement

Acronym	Notation
HM	high modulus
HT	high tenacity
ICP	Iterative Closest Point
ICT	Fraunhofer Institute for Chemical Technology
IM	intermediate modulus
IRTG	International Research Training Group
JCGM	Joint Committee for Guides in Metrology
JDL	Joint Directors of Laboratories
K	kelvin
kg	kilogram
kHz	kilohertz
kJ	kilojoules
km	kilometer
kt	kiloton
LLSS	Laser Light Section System
LLSS	Laser Light Section System (used as an index)
MHz	megahertz
min	minute
mm	millimeter
MPE	Maximum Permissible Error
MSA	Measurement systems analysis
MSS	Multi-sensor System
MVS	Machine-Vision-System
mW	milliwatt
µm	micrometer
NaN	Not-a-Number
NC	Numerical Control

Acronym	Notation
NDT	Non-destructive Testing
nm	nanometer
NUC	Non-Uniformity-Correction
OPC	Open Platform Communications
PAN	Polyacrylonitrile
PLC	Programmable Logic Controller
PPT	Pulse-Phase Thermography
PPT	Pulse-Phase Thermography (used as an index)
ROI	Region of Interest
RTM	Resin Transfer Molding
sf	semi-finished (used as an index and test name)
SMC	Sheet Molding Compound
ST	super tenacity
TCP	Tool Center Point
UPPH	Unsaturated polyester polyurethane hybrid
vol.-%	volume percent
wbk	Institute of Production Science
wt.-%	weight percent

1 Introduction

1.1 Motivation and Problem Definition

Lightweight construction is considered a key topic of the future. In addition to already known materials such as aluminum, magnesium and high-strength steels, fiber-reinforced plastics (FRP) are used increasingly (Heuss et al. 2012). Even today, lightweight construction materials are playing an important role in various industrial, resulting in the enactment of laws by politicians. The reduction in CO_2 emissions set by regulation No 443/2009 of the European parliament and of the Council forces car manufacturers to act (Europaparlament und Europarat 2009). The approaches chosen focus on electric mobility and fuel-efficient drives, but weight reduction of the vehicle can also help. FRP can, therefore, be expected to establish themselves in the automotive industry instead of aluminum and steel components (Neitzel, Mitschang & Breuer 2014). In addition, lightweight design strategies can improve the dynamics and stiffness of components. Thus in addition to weight reduction, new applications and system features can be realized leading to possible cost reductions. (Fraunhofer-Institut für System- und Innovationsforschung ISI et al. 2014)

One FRP widely used today is the Sheet Molding Compound (SMC). The market overview of Industrievereinigung Verstärkte Kunststoffe e.V. (AVK) shows that the production volume in 2017 amounted to 202 kt and has risen steadily since 2014 with a further increase to be expected in the coming years. Therefore, SMC is the largest segment of FRP. (Witten, Sauer & Kühnel 2017; Lässig et al. 2012). SMC is characterized by short cycle times and high productivity (Teschner 2013) and hence is particularly suitable for FRP components with high numbers of pieces (Eickenbusch & Krauss 2014). Due to its high impact strength and corrosion resistance, SMC is used in the field of commercial vehicles for cabins and body panels (Stachel 2012; Bruderick et al. 2002). By reinforcing SMC components with unidirectional carbon fibers, the mechanical properties can be improved, thus opening up potential areas of application and fallows, such as in aircraft construction. (Wulfsberg et al. 2014)

The combination of discontinuous glass fiber SMC and continuous carbon fiber SMC is examined in the International Research Training Group (IRTG) 2078 "Integrated engineering of continuous-discontinuous long fiber reinforced polymer structures". The IRTG 2078 makes it clear that discontinuous glass fiber SMC, also known as DiCoFRP, has short cycle times and good formability, but low mechanical properties. In contrast,

continuous carbon fiber SMC, called CoFRP, has good mechanical properties, but is expensive and has longer cycle times. Further advantages and disadvantages of the individual materials are shown in Figure 1-1. For this reason, the IRTG 2078 combines the two materials in order to exploit the advantages of the individual materials and counteract their disadvantages (Kärger et al. 2016).
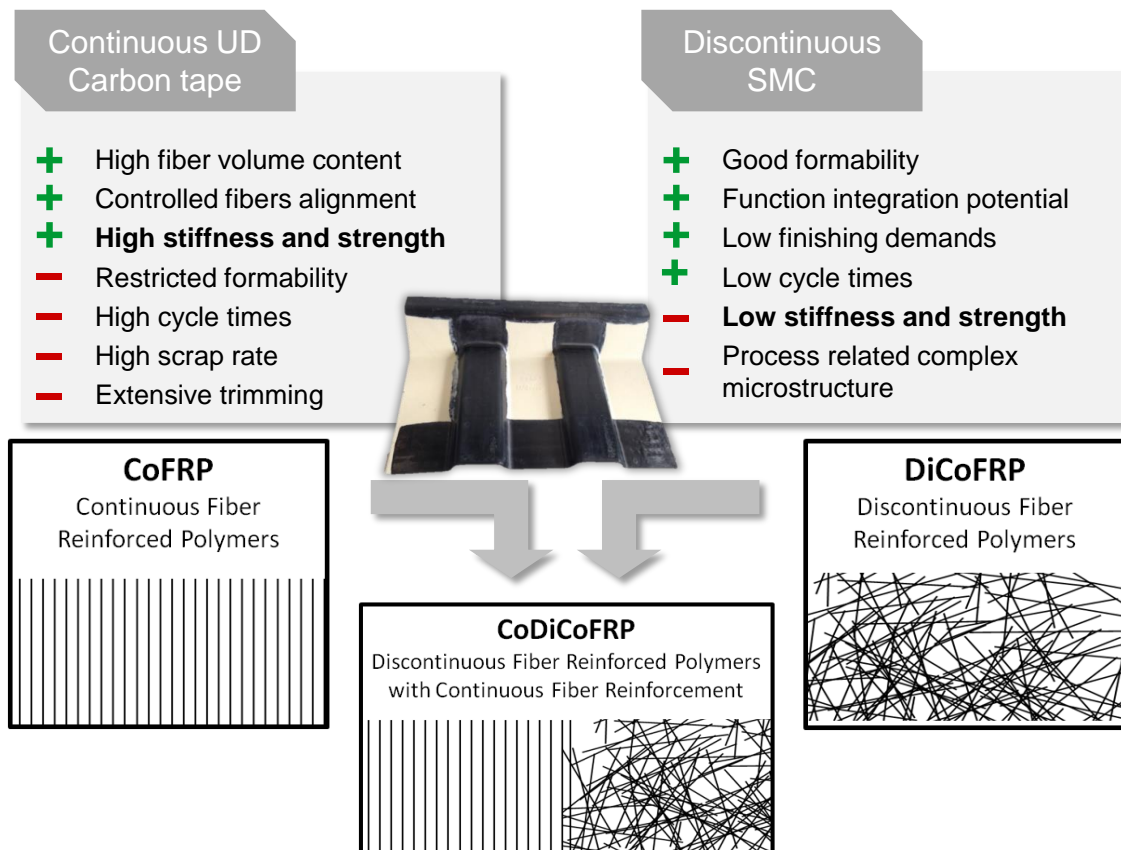
Figure 1-1: Advantages and disadvantages of continuous and discontinuous SMC, according to (Kärger et al. 2016)

The combination of these materials can lead to a multitude of defects that need to be avoided. An end-of-line inspection alone is not sufficient, since value-adding production steps may have already been carried out on defective components at this late point in time (Schmitt & Damm 2008). However, process-integrated testing and measuring procedures are also necessary for other reasons. For example, products with high safety relevance have to be examined or the zero-defect quality philosophy fulfilled. (Thiemann 2015)

In this way, customer satisfaction and the external image of a company can be improved by avoiding product defects and minimizing potential risks. Non-destructive processes can help to monitor and control production processes and thereby reduce manufacturing costs. (Imkamp & Berthold 2009)

1.2 Objective Target

By using this new hybrid material, made of discontinuous glass fiber SMC and continuous carbon fiber SMC, components with locally good mechanical properties can be produced cost-effective in a short production cycle. For this purpose, the quality of semi-finished products and final components has to be ensured. To achieve this goal, the integration of testing and measuring techniques into the production process is necessary (Cherif 2011).

Therefore, the aim of this work is to develop a measurement system for the used continuous-discontinuous material, possibly containing a multitude of possible defects. The examination has to be possible for both semi-finished and cured material. Thus, the focus of this work is on non-contact methods. Due to the difference of possible defects, one measuring method alone is not sufficient. To cover a wider spectrum of defects, a method for data fusion from different methods needs to be developed.

The present work is divided in three parts. Possible defects and their effect on the material's mechanical properties are addressed by the first two research questions:

1. Which critical defects in CoDiCo materials need to be examined?
2. What effects do the critical defects have on the mechanical properties?

The second part examines suitable test and measurement methods by answering the following research questions:

3. Which testing and measuring methods are suitable for the critical defects and what is the measurement uncertainty of the individual systems?
4. Do defects have different characteristics allowing them to be characterized by a single system?

In the third part, data evaluation and analysis is examined in more detail, addressed by the following research questions:

5. How to implement a quality-assuring measurement system and what is the impact of its measurement uncertainty?
6. How to perform a complete investigation by using data fusion approaches including depiction of a practicable evaluation for the user?

The listed research questions are to be answered in the present work and thus offer the possibility to create a system providing the user with a fast as well as clear analysis of defects and enables quality assurance of CoDiCo materials.

1.3 Structure of the work

The present thesis is segmented to 10 chapters, its structure is illustrated in Figure 1-2.

1 | Introduction

| 1.1 Motivation and Problem Definition | 1.2 Objective Target | 1.3 Structure of the work |

2 | Theoretical Background

| 2.1 Composites and fiber-reinforced plastics | 2.2 Quality Assurance of Fiber-Reinforced Plastics | 2.3 Data Fusion | 2.4 Uncertainty of Measurement |

3 | State of the Art

| 3.1 International Research Training Group | 3.2 Testing and measuring techniques for defects in sheet molding compounds | 3.3 Multi-sensor System and Data Fusion | 3.4 Deficit in Research |

4 | Solution Approach

5 | Defects and their Effects

| 5.1 Used Material | 5.2 Layer Structure of used Material | 5.3 Used Test Objects |

| 5.4 Defect Identification and Selection | 5.5 Mechanical Properties of defective Components |

6 | Laser Light Section System

| 6.1 Parameter for Laser Light Section System | 6.2 Measurement Uncertainty of Laser Light Section System |

7 | Active Thermography

| 7.1 Portal Interfaces | 7.2 Selection of suitable Active Thermography | 7.3 Parameter for Pulse-Phase Thermography | 7.4 In-depth Analysis of Pulse-Phase Thermography |

| 7.5 Characterization of Defects | 7.6 Measurement Uncertainty of Pulse-Phase Thermography |

8 | Multi-sensor System

| 8.1 Design of the Multi-Sensor System | 8.2 Data Fusion | 8.3 Added Value of Data Fusion | 8.4 Data Fusion Layer Model | 8.5 Data Fusion Measurement Uncertainty |

9 | Discussion and Outlook

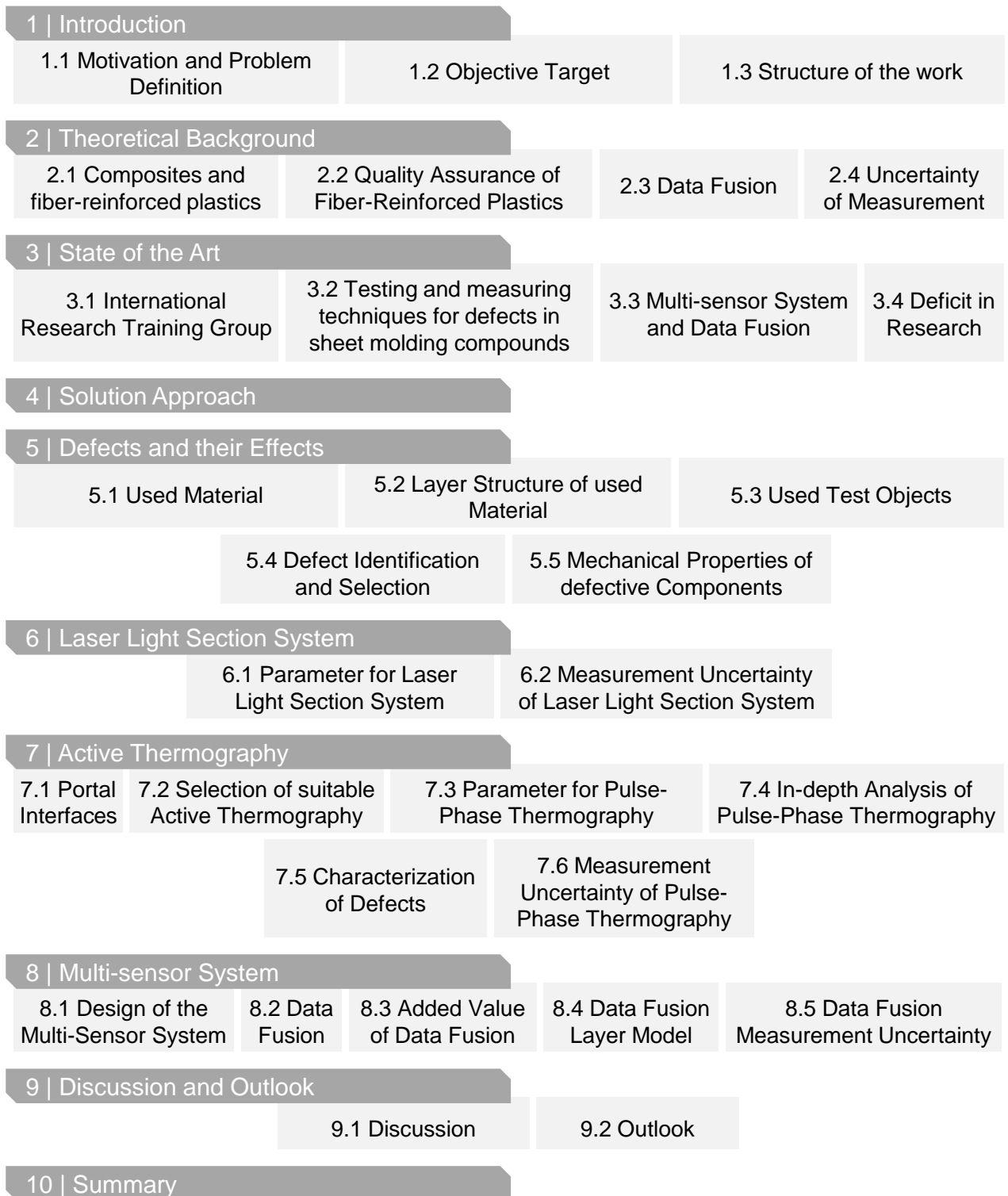| 9.1 Discussion | 9.2 Outlook |

10 | Summary

Figure 1-2: Structure of the thesis

2 Theoretical Background

The basic principles described in this chapter intend to form a basis for the work presented and thus facilitate understanding of the work. Foremost, the material of fiber-reinforced plastics (FRP) is introduced, afterwards the quality assurance of FRP is examined in more detail. This is followed by a closer examination of the data fusion and an explanation of the measurement uncertainty.

2.1 Composites and Fiber-Reinforced Plastics

In case of composites, both lightweight construction principle and combination of different materials compensating disadvantages of individual materials are in focus (Schürmann 2007). Composite materials are materials that consist of at least two different materials that are not soluble in one another, which are used in order to set specific properties. On a macroscopic level, these materials are quasihomogeneous (Dominghaus et al. 2012). Furthermore, the property to be optimized has to differ by a factor >3 for both materials and the proportion of one material has to be at least 10 % by weight. In composites, the load is carried by the reinforcing component while the embedding component is used for load transmission, shaping and protection of the reinforcing components. (Henning & Moeller 2011)

Fibers and reinforcing particles are used to tighten the composite material. A distinction is made between particle, short fiber, long fiber and continuous fiber reinforced composite materials. The embedding component can consist of polymeric, metallic or ceramic materials. (Henning & Moeller 2011)

The boundary layer between the two materials is of particular importance for composites. The necessary adhesion results from the mechanical, chemical and physical adhesion of the two individual materials, which is why a complete wetting of both is crucial for good adhesion. (Henning & Moeller 2011)

Fillers, which can be powdery, spherical or granular, are also used. They are applied in order to change density, but also to improve processability and change electrical as well as thermal properties. In addition, it is possible to replace some of the embedding material with fillers and thus reduce the costs of composites. (Roos & Maile 2015)

Fiber reinforced plastic (FRP) are a subgroup of fiber composites. As the name suggests, FRP consists of plastic and fibers. Composites with fibers can withstand considerably higher stresses than the individual components of the composite (Ehrenstein

2006). FRP is divided into high-performance fiber composites with continuous fiber re-inforcement and quasi-homogeneous composites, which again can be divided into short or long fiber-reinforced plastics by the length of the fiber (Henning & Moeller 2011). Therefore, the fibers can be subdivided according to their fiber length. A distinction is made between short, long and continuous fibers (Schürmann 2007). However, it is also possible that the fibers are in the form of semi-finished textile products. An overview of possible semi-finished products is given in the Figure 2-1. (Fürtjes 2016)
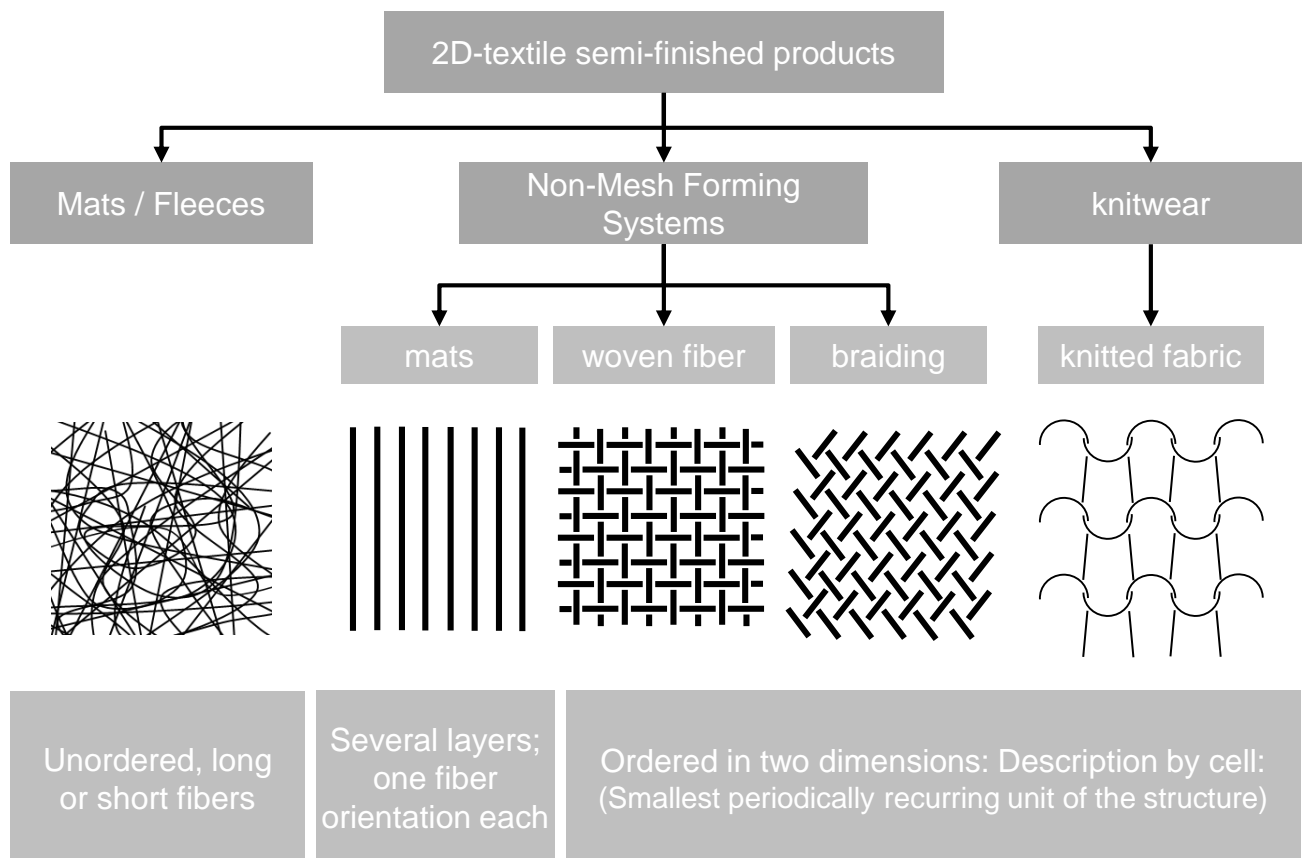
Figure 2-1: Overview of the classification of semi-finished textile fibers according to (Fürtjes 2016)

FRP have a number of advantages. These include the high strength and stiffness with simultaneous low density, the corrosion resistance of the individual components, the adjustable electrical conductivity, the low thermal conductivity, but also the possibility of using FRP as a crash element due to its high energy absorption capacity. The current main disadvantage are the cost, which are very high compared to metals. (Schürmann 2007)

As early as 1936, the first fiber-plastic composite was used for highly stressed struc-tures in the wings of a glider. The composite consisted of paper, which was reinforced

with phenolic resin sheets. Thus a weight saving of up to 15 % could be achieved compared to a wooden construction. The first series production process for fiber-plastic composites was the fiber winding technology and dates from 1945. (Schürmann 2007)

The main reinforcing fiber used today is glass fiber, accounting for approx. 90 % of plastic composites. Carbon fibers, aramid fibers and natural fibers are also used. These have a low density and increase the strength and rigidity of the composite. Based on their low weight, the reinforced plastics thus have a high performance level, depending on the fiber length. (Mathes & Witten 2014; Henning & Moeller 2011)

In Appendix A 1 and A 2, the two main components of FRP, matrix and fiber, are explained in more detail and their most important properties are presented.

2.1.1 Sheet Molding Compound

SMC is the name of the composite as well as of the manufacturing process. It is one of the oldest and most advanced processes for the production of FRP and was already realized in Germany in the 1960s (Schürmann 2007). SMC belongs to the class of flowable prepregs and consists of fibrous fleeces or mats embedded in duromer reaction resins. The fibers are mainly glass or carbon. The length of the fibers varies from 25 to 50 mm with discontinuous orientation in the material. However, it is also possible to insert oriented fibers up to 200 mm length or continuous fibers (Neitzel, Mitschang & Breuer 2014). The percentage of fibers is around 30 %, but materials with up to 60 % glass fiber content have already been realized (Mathes & Witten 2014). Unsaturated polyester or vinyl resins are often used as reaction resins. Mineral fillers are used to prevent shrinkage and as an inexpensive filler. Furthermore, thermoplastic additives are used to compensate for shrinkage (Mathes & Witten 2014).

The manufacturing process of SMC is explained in more detail below.

2.1.1.1 Manufacturing process Sheet Molding Compound

In the first step of the production process, the resin filler mixture has to be produced. All necessary raw materials, such as resin, hardener and additives are mixed. The resin filler mixture is produced in batches. Subsequently, the production of the semi-finished product begins on a continuous impregnation line. The resin filler mixture is applied to an upper and lower carrier foil with a defined thickness via two doctor blade boxes. Fibers are inserted discontinuously between these two layers with a roving chopping

cutting unit. Afterwards, the foils are brought together and tumbled. This process compresses the composite, prevents air inclusions and ensures complete impregnation of the fibers. The composite is then rolled up to a width of 1500 mm. In the next step, the so-called semi-finished product has to mature (chemical thickening) before it can be further processed. This maturing process takes between two and four weeks and requires certainly storage conditions, strongly depending on the respective formulation of the SMC. (Mathes & Witten 2014)

Figure 2-2 schematically shows the manufacturing process of the semi-finished product.
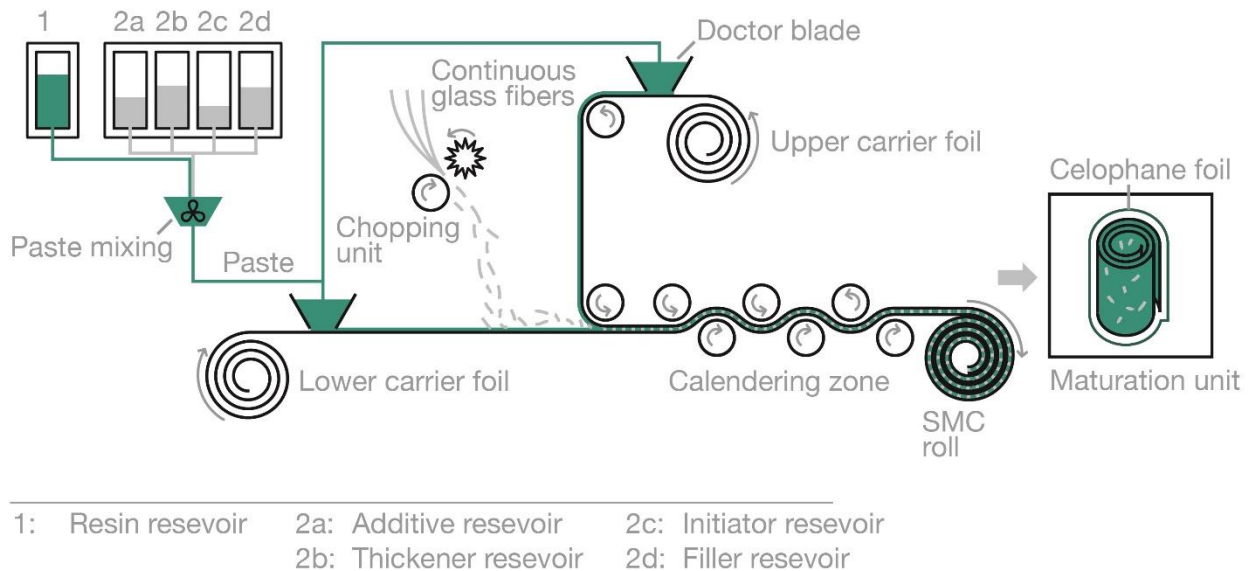
Figure 2-2: Production process of sheet molding compound (Zaiß et al. 2017b)

After maturing, the semi-finished SMC is hot-pressed into a cured part. This is an extrusion process allowing even complex 3D geometries to be produced. During the pressing process, pressures of 25 to 250 bar are effective and the mold temperature is between 140 and 160 C. Mold closing movement, as well as temperature and pressure, have great influence on the component quality allowing the semi-finished product to flow into the cavity as well as the matrix to harden under pressure through chemical interlinking. Subsequently, the component has to cool down and finishing operations such as deburring, drilling, milling or painting are necessary. Through automation processes, cycle times of a few minutes can be achieved. (Cherif 2011)

2.1.1.2 Manufacturing process unidirectional Sheet Molding Compound prepregs

In addition to the discontinuous SMC material, there are also unidirectional SMC pre-pregs with an also duromer matrix but endless and directed fibers. This allows high fiber volume proportions of up to 60 vol.-% to be achieved.

Edge Trim

Protective Paper

Fibers

Prepreg Winding   Cooling   Impregnation   Carrier Paper with Resin Film

Comb
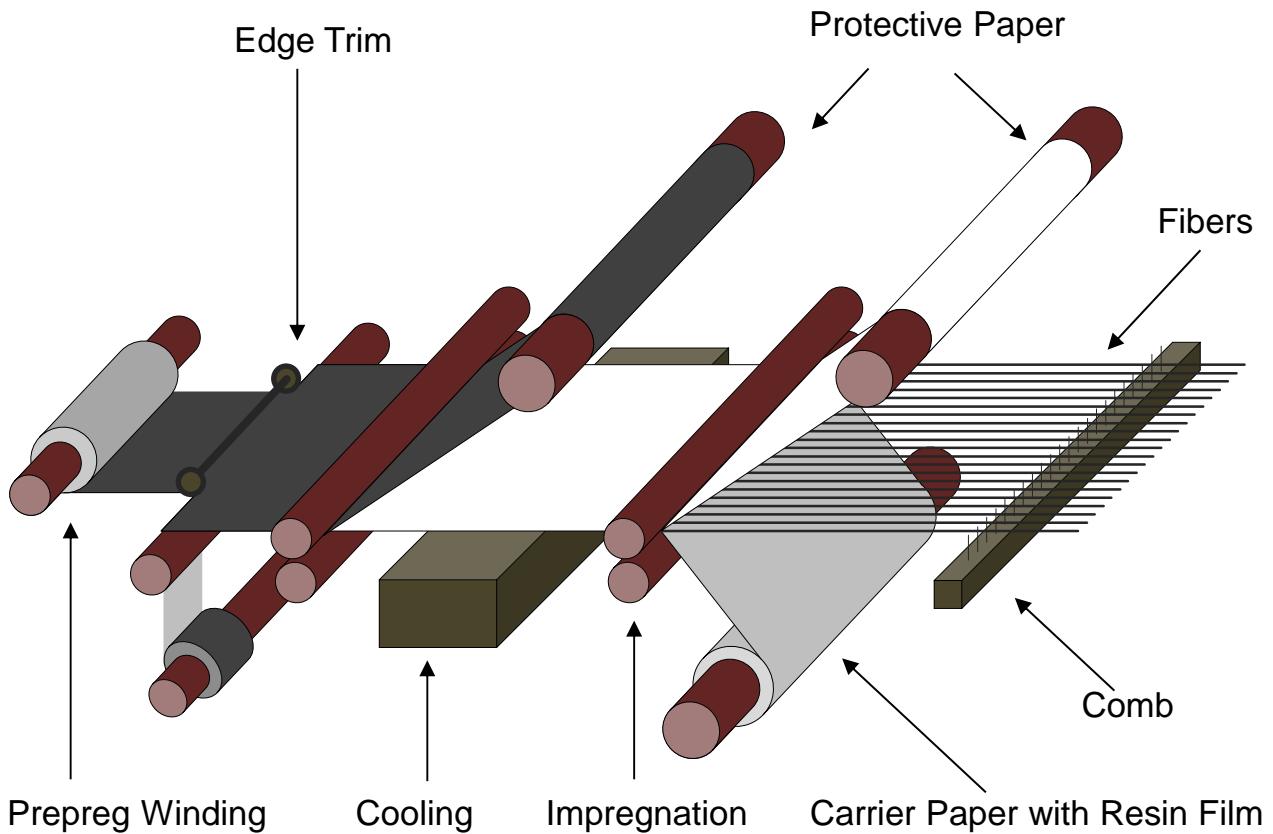
Figure 2-3: Continuous production of unidirectional thermoset prepregs according to (Mathes & Witten 2014)

For the production of this material variant there are two processes, the application by the solvent process and the application by means of carrier paper in the process of melt impregnation. Due to its high reproducibility, the process of melt impregnation has es-tablished itself in industry. In a preceding step, the carrier film is coated with the matrix resin at an elevated temperature of 60 to 90°C with the fibers impregnated in a separate device. The carbon fiber rovings are guided parallel through a comb in one plane. For the correct viscosity, the resin film is tempered by heated impregnation rollers and the fibers are introduced and wetted by the roller pressure. The prepreg has then to be cooled so that the interlacing does not progress any further. The production is shown schematically in Figure 2-3. (Neitzel, Mitschang & Breuer 2014; Mathes & Witten 2014; Cherif 2011)

2.1.1.3 Economic significance of Sheet Molding Compound

A big advantage of SMC is the low cycle time and the associated high productivity. (Teschner 2013). Therefore, this process is particularly well suited for the production of FRP components in large quantities and has already entered series production (Eickenbusch & Krauss 2014). According to the current 'Composites-Marktbericht 2017', the SMC process was the most important FRP process in 2014 at 190 kt. A positive trend can be noted in recent years, so that in 2017 a production volume of 202 kt is reached and a total production of glass fiber reinforced plastic (GFRP) of 1118 kt in Europe (see following Figure 2-4). (Witten, Sauer & Kühnel 2017)
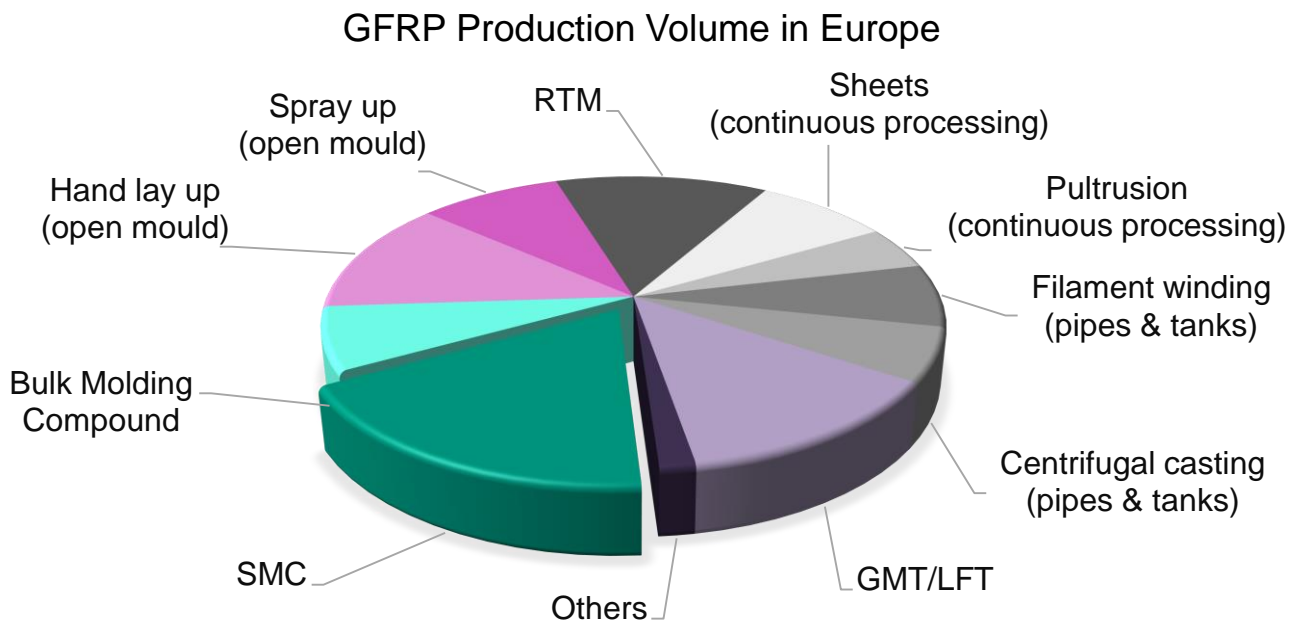
Figure 2-4: GFRP production volumes in europe by process according to (Witten, Sauer & Kühnel 2017)

SMC is used in various areas. In the electronics industry, for example, it is used as a ceramic substitute. It is also often used in railway technology because SMC can meet high flame-retardant requirements. Furthermore, cabins, trim parts and aero packages for the commercial vehicle sector are made of SMC, due to its high impact strength and corrosion resistance. (Stachel 2012) Besides commercial vehicles, SMC is relevant for the whole automotive sector, as the components are used for lightweight construction, for instance as tailgates or trunk lids. The transparency for electromagnetic waves is also a great advantage and the reason for its use in cars. Furthermore it is possible to realize very high quality (Class A) surfaces with SMC. Its use in the automotive sector is also promoted by its suitability for mixed construction, as the coefficient of thermal

expansion is similar to metals. In addition, the composite has a better corrosion resistance than metals. (Neitzel, Mitschang & Breuer 2014)

A disadvantage is the large number of individual components (fillers, additives) necessary for production. In order to achieve constant quality, continuous process monitoring has to be carried out, since even minor deviations and production fluctuations lead to a high reject rate up to 7 %. This scrap is often only detected after the pressing or painting process. (Neitzel, Mitschang & Breuer 2014)

Another disadvantage is the limited shelf life, as the semi-finished product has to be processed within a certain period of time due to the autocatalytic behavior (Stewart 2009).

2.1.2 Defects in Fiber-Reinforced Plastics

In FRP a large number of possible defects can cause undesirable effects. These could be only optical defects, but also reduce the mechanical properties. The most important defects are briefly described below. In literature, errors in FRP are well documented but not specifically for SMC. However, these defects can also be applied to SMC. The following Table 2-1 gives an overview of possible defects in FRPs.

Table 2-1: Overview about defects in FRP

Defects	Reference
Pores and Air Inclusions	(Kochan 2012; Oster 2012; Mayr et al. 2011; Krämer et al. 2014; Plank et al. 2013; Zaiß et al. 2017b; Busse & Solodov 2013),
Fiber Orientation	(Brabandt, Hettich & Lanza 2015; Zaiß et al. 2017b; Schmitt 2008; Schmidt & Dutta 2013)
Fold	(Schmitt 2008; Brabandt & Lanza 2015; Lizaranzu et al. 2015)
Fiber Gaps	(Schmidt & Dutta 2013)
Dry Areas	(Zaiß et al. 2017b; Neitzel, Mitschang & Breuer 2014)
Resin Nests	(Zaiß et al. 2017b; Neitzel, Mitschang & Breuer 2014; Kia 1993)

Form and Contour Accuracy	(Schmitt 2008; Brabandt, Hettich & Lanza 2015; Brabandt 2018)
Inclusions of Foreign Body	(Wandelt 2008; Vaara & Leinonen 2012; Gleiter, Spießberger & Busse 2010; Kochan 2012; Plank et al. 2013; Zaiß et al. 2017b; Mersmann 2012; Miene 2009)
Delamination	(Wandelt 2008; Kochan 2012; Oster 2012; Schmidt & Dutta 2013; Lasagni et al. 2015; Zaiß et al. 2017b; Busse & Solodov 2013; Krüger & Mook 2006; Muntzinger 2013; Schürmann 2007; Harich 2008)
Impact Damage	(Ibarra-Castanedo et al. 2008; Perterer et al. 2011; Maier et al. 2014; Geiss & Hornfeck 2015; Lasagni et al. 2015; Busse & Solodov 2013; Kochan 2012)
Surface Waviness	(Kia 1993; Keckl, Kuppinger & Henning 2014; Michaeli & Kremer 2010; Neitzel, Mitschang & Breuer 2014; Mathes & Witten 2014)
Incomplete Curing	(Eyerer & Wintergerst 1971; Eyerer & Busse 1983; Busse & Eyerer 1983)

The table shows a large number of possible defects without claiming to be complete. The most important defects in discontinuous and continuous SMC are marked and described in more detail in Appendix A 3. Some insights are based on own experiences.

2.2 Quality Assurance of Fiber-Reinforced Plastics

The errors described above have to be detected at an early stage. Therefore, test and measurement procedures for FRP are described in more detail below.

The terms measuring and testing are defined in (DIN 1319-1). According to this, testing is the determination whether the test object fulfils the requirements. In a measurement, the measured variable is compared quantitatively with the unit.

In principle, testing and measuring procedures can be divided into non-destructive and destructive procedures (Kochan 2012). Disadvantageous for destructive processes is the no longer useable component, thus they do not represent an alternative for process integration (Hochrein 2013). Therefore, these procedures are not considered further.

Non-destructive testing (NDT) is the examination of components and designs for defects in a way leaving component or construction unaffected (Erhard 2007). The aim is to determine the presence or absence of conditions or discontinuities having an effect on usefulness and operability of the test object (Hellier 2013). Furthermore, the focus is damage prevention (Erhard 2007). Figure 2-5 shows different processes, arranged

according to their physical principles. There is no claim to completeness. The presented methods are to be regarded as the most common non-destructive testing and measuring methods for FRP. (Kochan 2012)
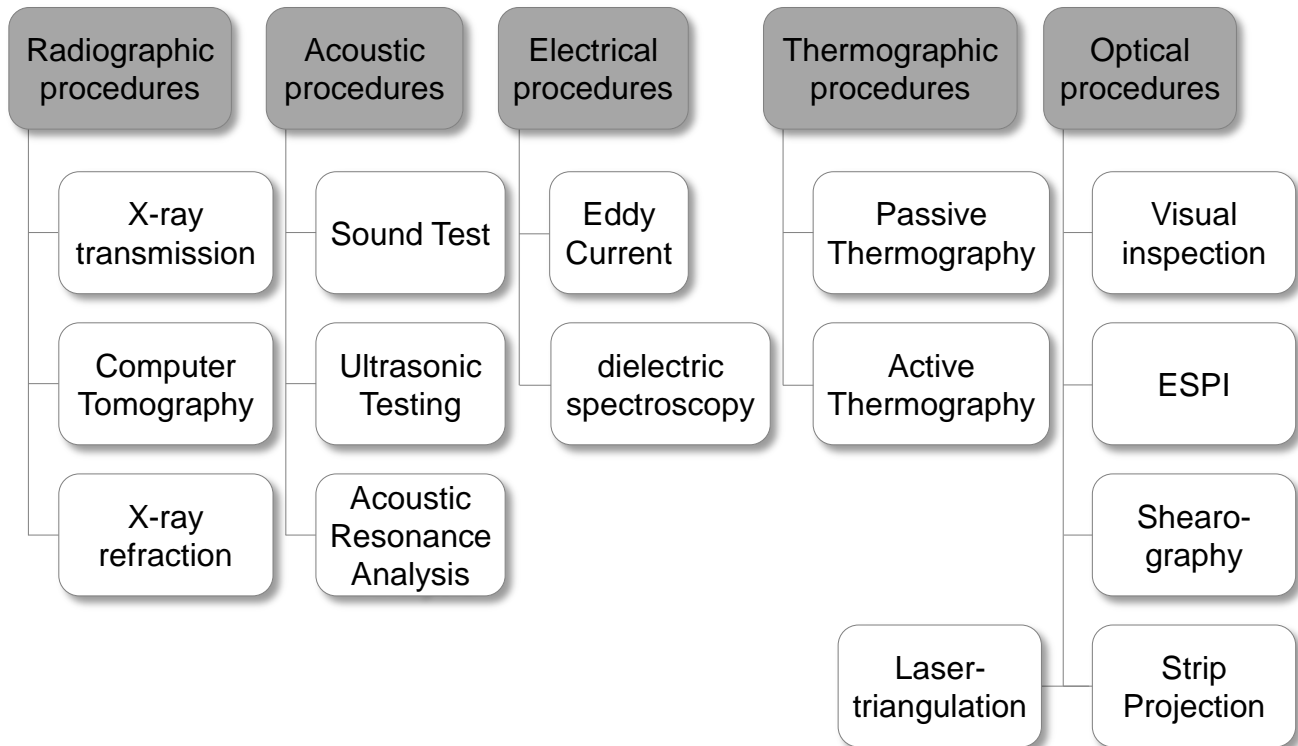
Figure 2-5: Overview of common NDT methods for defect detection according to (Kochan 2012)

In Appendix A 4 the individual procedures are elucidated in more detail and the method as well as the areas of application are explained.

2.3 Data Fusion

In the following chapter the concept of data fusion is explained as well as different fusion models, sensor configuration and fusion methods are presented.

2.3.1 Definition of Data Fusion

By using different sources of information, new or more precise knowledge is achieved. Knowledge about situations, physical quantities or events can be gained. This often happens in a much shorter time and at lower cost. Furthermore, the perceptive faculty can be extended and thus credibility of the results increased. In addition, quality and user-friendliness are to be improved. The data used are obtained both from raw sensor signals and verbally described properties of an object. (Beyerer 2006; Ruser & Puente León 2007; Weckenmann et al. 2009)

A distinction is made between the terms sensor integration and data fusion. In integration, the information from several sensors is used synergistically to solve detection, classification or identification tasks. Data fusion refers to the combination of data (time or location signals, parameters, statements) from the sensors used. (Luo & Kay 1989; Hall & McMullen 2004)

Focusing more on quality, data fusion can be described as a "set of methods, tools and means using data coming from various sources of different nature, in order to increase the quality (in a broad sense) of the requested information."(Wald 1999). Special properties of data fusion are the technical parameters and performance characteristics, effectiveness and benefit for the user.

Due to the advantages described, data fusion is used in many areas, for example in military technology, navigation and driver assistance systems or medical and production measurement technology (Beyerer 2006; Hall & Llinas 1997).

2.3.2 Fusion Models

Literature usually describes three fusion models, which are briefly explained below.

2.3.2.1 General Fusion Model

A general multi-sensor model is shown in Figure 2-6. All known objects in the detection zone as well as their status parameters (e.g. position and orientation to the sensor) are combined in a so-called world model. This is updated cyclically and according to requirements, enabling changes in the conditions or newly added objects to be recorded. With the help of sensor models knowing the sensor status, statistical statements about the sensor data can be made. (Ruser & Puente León 2007)

2.3.2.2 JDL-Model

Another model, mainly used in military technology, is the so called JDL model (Joint Directors of Laboratories). It is illustrated in Figure 2-7 and consists of five steps, whereby the preprocessing of the individual information represents level 0.

Level 1 contains of object recognition and change of state due to iterative fusion of sensor data, as well as registration, object detection or result allocation of different sensors. The outcome is the situation picture.
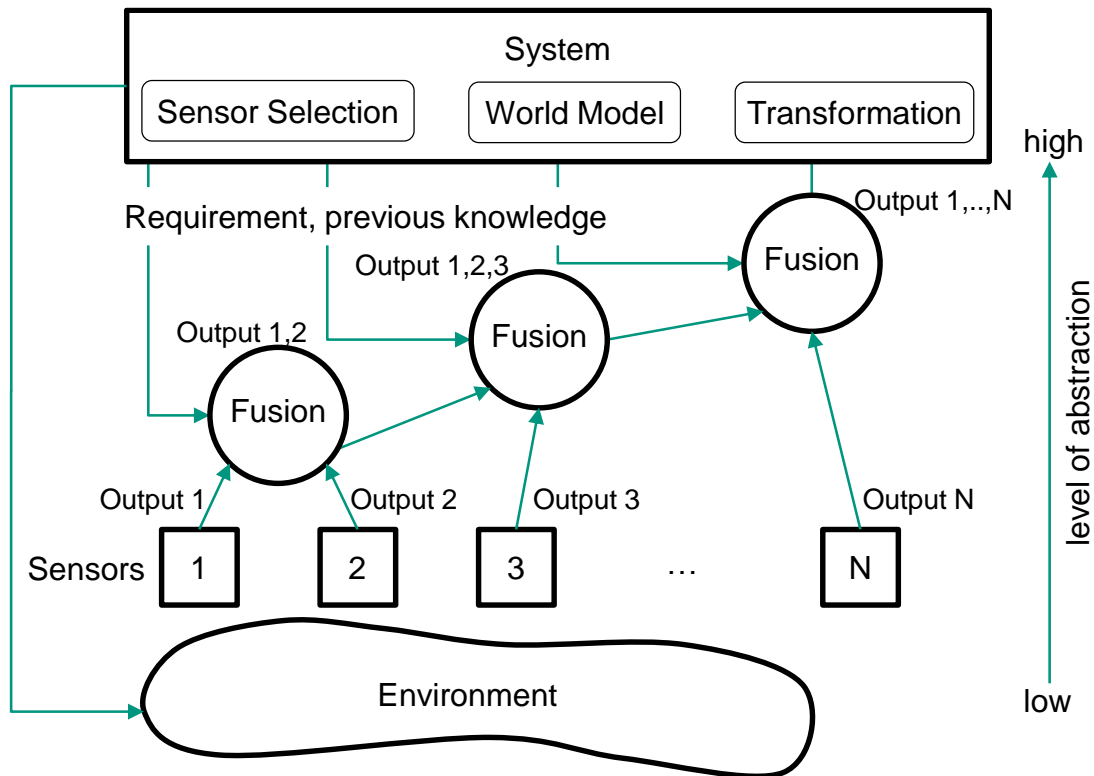
Figure 2-6: Principle of multi-sensor integration and data fusion according to (Luo & Kay 1989)
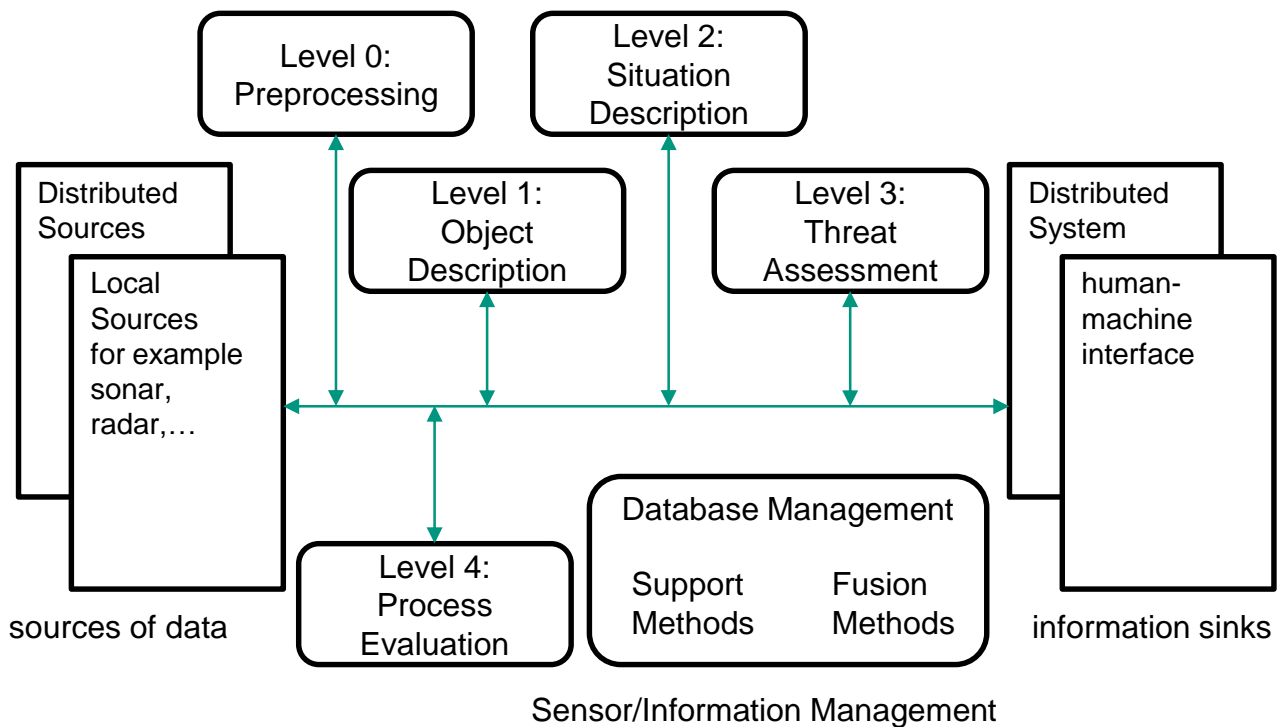
Figure 2-7: JDL model according to (Hall & Llinas 1997)

Level 2 is the situation analysis, allocating objects to a scenario. Therefore, the trajectories are temporally analyzed, allowing an interpretation of the movement pattern.

In the threat analysis (level 3), the fusion system assesses the options for action in order to minimize risk.

In the last step (level 4), the process is optimized through continuous evaluation of the overall process and interaction with the other levels.

The disadvantage of this model is not providing a description of data fusion, but rather making a hierarchical classification of information processing. Furthermore, it can be difficult to recognize the functions of levels 2 and 3 outside the military area. (Ruser & Puente León 2007; Beyerer 2006)

2.3.2.3 Omnibus Model

In the omnibus model, measurement is represented as a control loop, see Figure 2-8, with four tasks carried out in a control loop:

1. Measuring (signal processing)
2. Sounding (feature extraction, pattern recognition)
3. Deciding (context processing)
4. Action (control, use of resources, etc.)

The transitions between the individual tasks include different fusion stages (sensor data fusion, „soft-decision" fusion, „hard-decision" fusion and sensor management). (Beyerer 2006; Ruser & Puente León 2007)
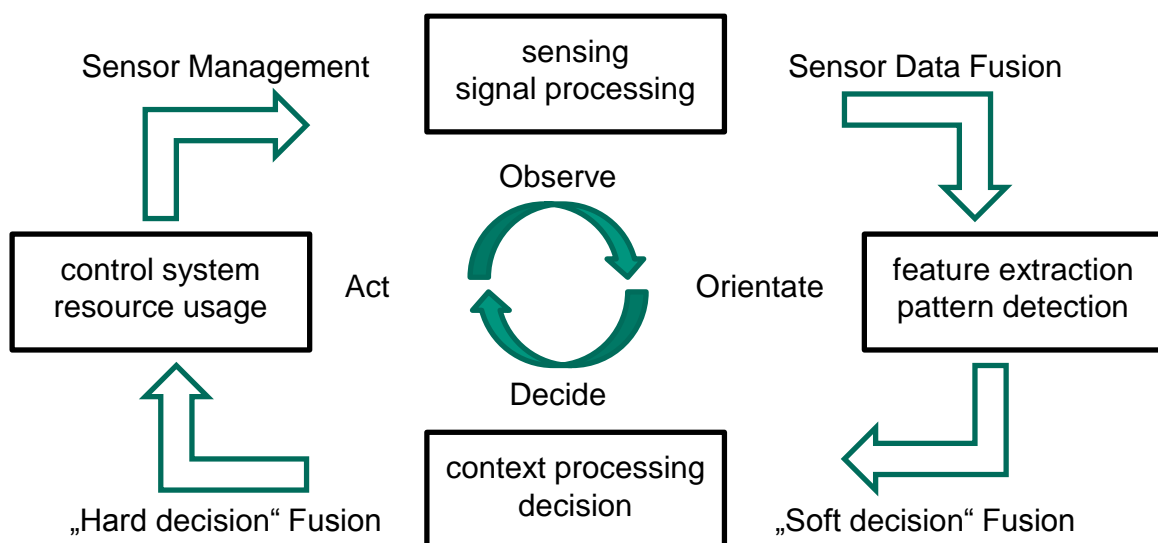
Figure 2-8: Omnibus model according to (Bedworth & O'Brien 2000)

2.3.3 Sensor Configuration

The integration concepts of individual sensors for a multi-sensor system depend on the location and the type of sensor data (Beyerer 2006). According to Durrant-Whyte (Durrant-Whyte 2016) a multi-sensor system can be divided into three basic configurations, based on sensor configuration. These three configurations are shown in Figure 2-9.
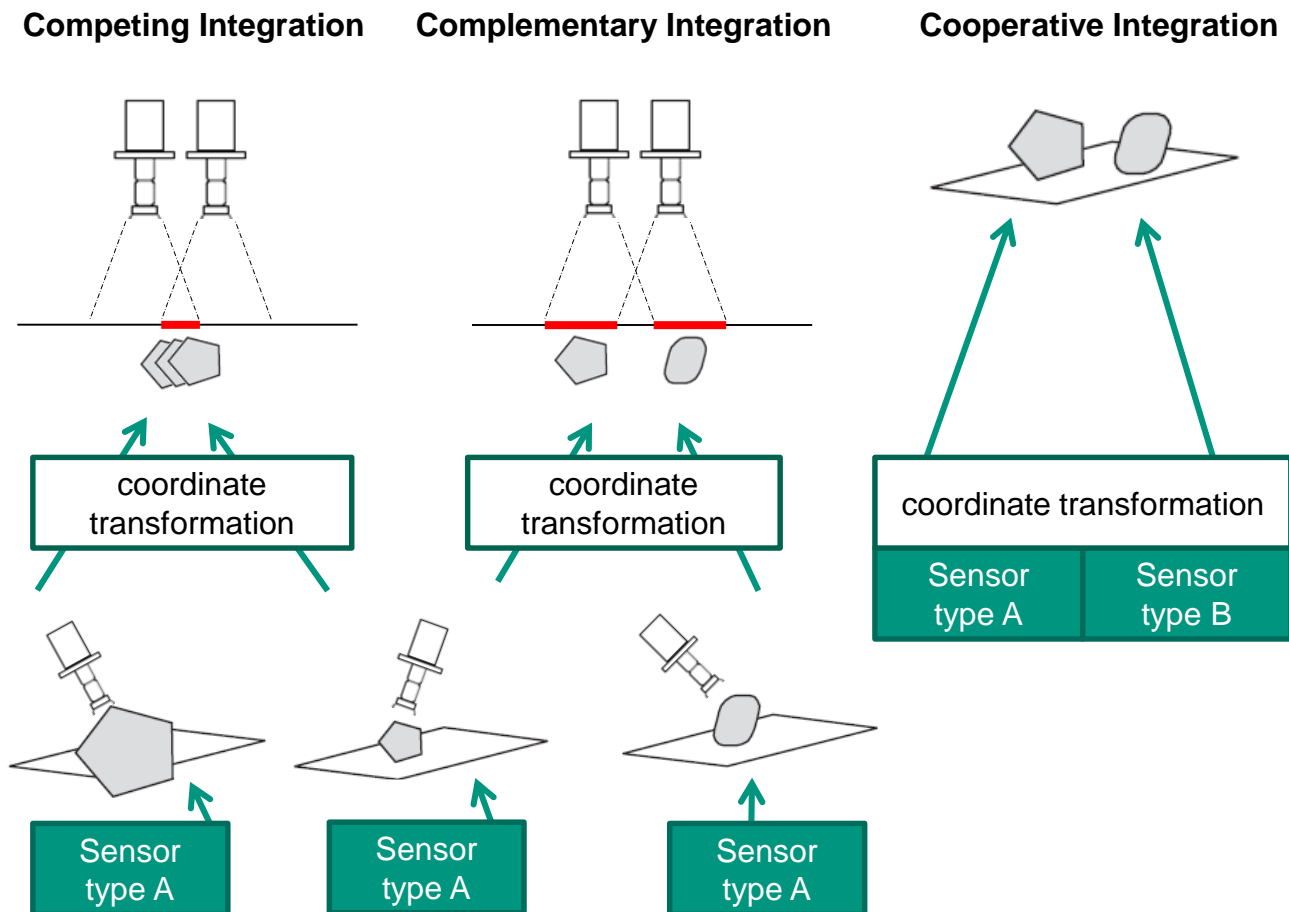
Figure 2-9: Concepts of sensor integration according to (Beyerer 2006)

With *competitive integration*, the same object is recorded with similar sensors in an independent measurement. The aim is to reduce uncertainty and susceptibility to errors.

For *complementary integration*, similar sensors are used independent of each other. The aim is to close information gaps and provide a complete picture of the test object.

The *cooperative integration* uses two or more independent sensors to generate information impossible to gather with a single sensor, since the useful information is distributed. (Beyerer 2006; Ruser & Puente León 2007; Weckenmann et al. 2009; Mitchell 2010; Mitchell 2007)

2.3.4 Fusion Methods

In the following, the data fusion process with focus on registration as well as different mathematical methods are explained.

2.3.4.1 Registration Methods in the Data Fusion Process

In general, the data fusion process can be represented schematically, as described in Figure 2-10.
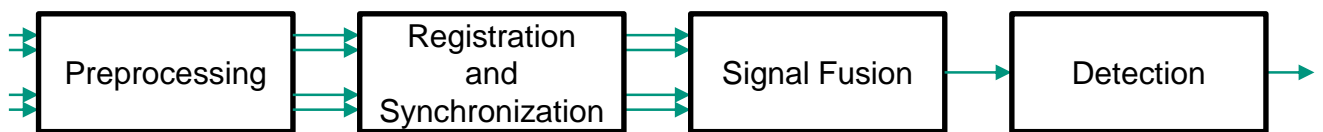
Figure 2-10: Data fusion procedure according to (Beyerer 2006)

After collecting the data by several sensors it is preprocessed, which means data amplification or noise suppression. This is followed by the registration, a spatial coordinate adjustment, or the synchronization of the individual sensors data. A distinction is made between rough and fine registration. (Beyerer 2006)

According to (Weckenmann & Gawande 2012) there are four different methods for rough registration:

1. **Interactive registration** The operator selects points or areas from different perspectives, which are present in different data sets. This method is very simple, but also very time-consuming.
2. **Registration via measured sensor positions** Sensors with very good positional accuracy are attached to the motion platform. This method is characterized by high accuracy.
3. **Registration via measured reference marks** Reference markers are placed on or close to the test object. The measurement allows automatic registration and is particularly suitable for the application of optical measurement data. Furthermore, fine registration is no longer necessary in many cases.
4. **Numerical registration approaches** In order to keep time to a minimum, the amount of data has to be reduced to a small amount of relevant and characteristic data. Corresponding measuring points are identified by feature extraction, for example at edges and corners.

During fine registration, the data is adapted even better to each other and existing deviations are minimized. This is done using various mathematical methods, such as correlation calculation, the Least Squares method or the Iterative Closest Point (ICP) algorithm. Problems can occur, if the exact same points are not represented, whereby wrong correspondences are found. Therefore, the rough registration has to ensure a not too large distance between the overlapping point clouds. (Weckenmann & Gawande 2012)

After registration, the data is merged and the result can then be interpreted (Weckenmann et al. 2009; Ruser & Puente León 2007).

2.3.4.2 Mathematical Methods for Data Fusion

After registration, the data are available in a common coordinate system. This is followed by the actual data fusion. For this, both grid-based and parameter-based approaches exist. Both approaches are briefly introduced below.

Grid-based fusion approaches are used for robot navigation and route planning (Abidi 1992). By combining simultaneous and sequential distance measurements of the same and different sensors, the occupancy probability of the grid can be determined. The grid occupancy is updated by sequential measurements of different positions. If high occupancy values are reached from different measurements at different points, the probability of an object located there increases. Opposing statements weaken the probability. (Ruser & Puente León 2007)

The parameter-based fusion methods can be divided into four groups:

- Feature-based approaches (weighted mean and the Kalman filter)
- Probabilistic approaches
- Fuzzy-Method
- Neuronal approaches

This thesis uses the feature-based fusion method, but is not comparable with known methods like Kalman filter or weighted average.

2.4 Uncertainty of Measurement

This chapter explains the principles of measurement uncertainty and their determination. The "Guide to the Expression of Uncertainty in Measurement" from Joint Committee for Guides in Metrology and other standards will be discussed.

2.4.1 Principles

The true value of a measured variable cannot be determined in practice, since a measurement result is influenced by many different influences, such as the environment or the personnel (Weckenmann & Knauer 1999). Therefore, each measurement result is associated with a measurement deviation, consisting of random and systematic deviations. The measurement uncertainty is therefore a parameter assigned to the measurement result, indicating the reasonable variation of the measurement variable, and thus given in addition to the measurement result. (JCGM 100; Keferstein, Marxer & Bach 2018)

However, the measurement uncertainty does not directly indicate a measurement error, but rather a range assumed to be greater than or equal to the actual measurement error (DIN 1319-1). Furthermore, it relates exclusively to a specific measurement task and therefore has to be recalculated for each measured characteristic (VDI/VDE 2617-8). Therefore, the entire measurement process has to be considered and all possible influencing variables with their uncertainty amounts taken into account (Weckenmann & Lorz 2001). An overview of influences on the measurement result is shown in Figure 2-11. The measurement uncertainty represents a quality parameter for the measurement result (Imkamp & Sommer 2009).
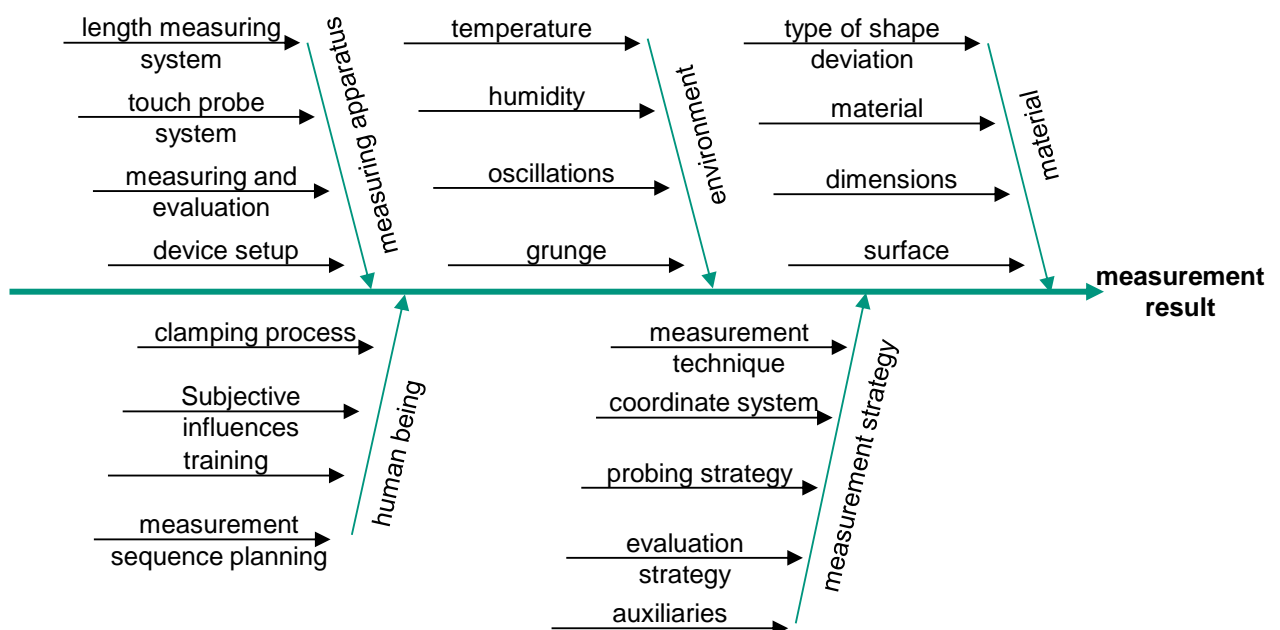
Figure 2-11: Influences on the measurement result according to (Keferstein, Marxer & Bach 2018)

The lower the manufacturing tolerances (specification range) of a test object, the more important is it to know the measurement uncertainty U in order to enable a statement for measurements near the specification limit (see Figure 2-12).
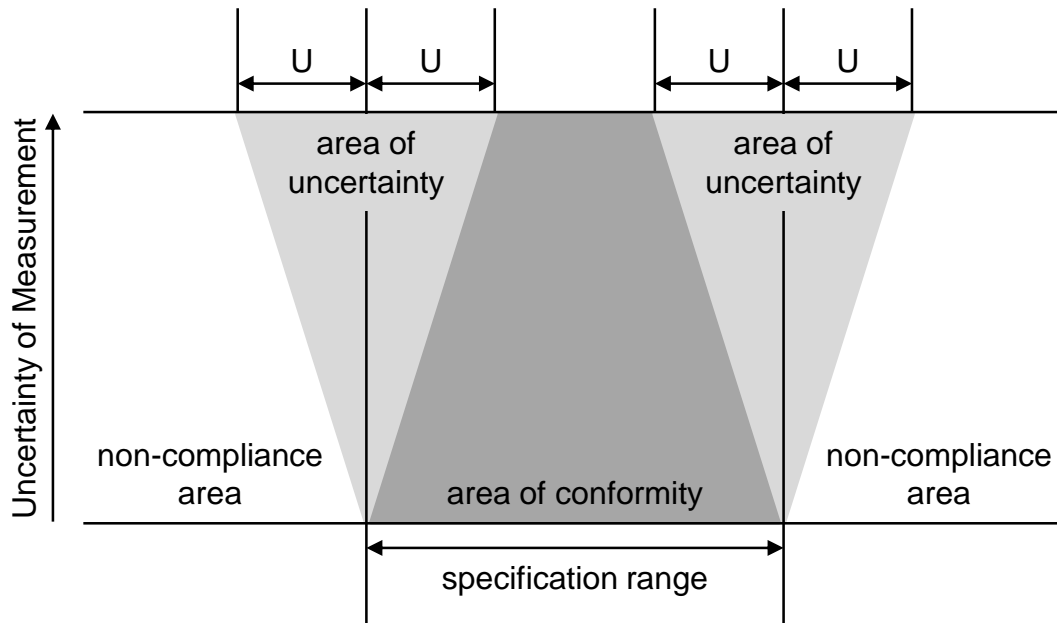
Figure 2-12: Uncertainty of measurement according to (DIN EN ISO 14253-1)

The internationally standardized procedure "Guide to the Expression of Uncertainty in Measurement" (GUM) was developed for the comparability of measurement results (JCGM 100) and is described in more detail in the following chapter.

2.4.2 Guide to the Expression of Uncertainty in Measurement

GUM was published in 1993 and reissued in 2008 in a slightly different form (JCGM 100), the German version entitled "Leitfaden zur Angabe der Unsicherheit beim Messen" in 1999 (DIN V ENV 13005).

According to GUM the measurement result is an estimated value for the measured variable (JCGM 100). GUM does not provide a specific procedure for carrying out an uncertainty of measurement determination, nor an evaluation standard to distinguish suitable measuring instruments from unsuitable ones (Dietrich & Schulze 2017).

However, GUM provides a general method for determining measurement uncertainty including several steps shown in Figure 2-13.

(1) Presentation of the knowledge about the measurement and identification of the influencing variables x_i

(2) Formulation of the model of measurement $y = f(x_i)$

(3) Determination of the standard uncertainty of the individual influencing variables u_i according to method A (experiment) or B (estimate) with the distribution factors z_i and preparation of the measurement uncertainty budget taking into account the sensitivity coefficients c_i

(4) Calculation of the combined standard uncertainty

$$u_c(y) = \sqrt{c_1^2 u_1^2 + c_2^2 u_2^2 + \cdots + c_i^2 u_i^2 + \cdots + c_n^2 u_n^2}$$

(5) Calculation of the expanded measurement uncertainty $U = k \cdot u_c(y)$

(6) Complete measurement result $y \pm U$

Figure 2-13: Procedure for determining the measurement uncertainty to GUM according to (VDI/VDE 2011)

In the first step, the knowledge of the measurement is presented and afterwards a model of the measurement is modeled in the second step. The functional relationship between the measured variable and all influencing factors, as well as the display, is established. This part is considered the most difficult to determine the uncertainty of measurement. The modeling is done according to the form

$$y = f(x_i) \hspace{4cm} \text{Equation 2-1}$$

The aim of this second step is to establish the functional relationship between the measured variable and all influencing variables. All factors x_1, x_2, x_n contributing to the measurement type y have to be identified. Due to variations, the factors are also subject to standard uncertainties u_i, which are included in the uncertainty balance (JCGM 100).

By assigning suitable probability distributions, an evaluation of the influencing variables is carried out in the third step with the aim to determine the best estimation and a (standard) uncertainty for each variable. There are two basic methods in this step, A and B.

Type A method is based on a statistical analysis of observation series, Type B contains all further possibilities for estimation, such as using values from literature, calibration values or manufacturer specifications (Sommer & Siebert 2004).

The next step four is to combine the estimated value of input variables and measurement uncertainty assigned to them on the basis of Gaussian uncertainty propagation. In a fifth step, the extended uncertainty of measurement is determined, specifying a confidence interval for expected value. For this purpose, the standard uncertainty $u_c(y)$ is multiplied by a coverage factor k for the expanded measurement uncertainty U:

$$U = k \cdot u_c(y)$$ Equation 2-2

The coverage factor $k = 2$ is selected to ensure a coverage probability of 95 % for a normal distribution. (JCGM 100)

In the last step, the complete measurement result is specified. This is calculated from the best estimate of the result variable and the associated expanded measurement uncertainty. (VDI/VDE 2011)

One disadvantage of GUM is the general formulation, making it difficult to use for many applications. The necessary functional relationships for the estimation is not always analytically describable so therefore the GUM method is not applicable. An alternative solution is numerical simulation according to the Joint Committee for Guides in Metrology for modeling the functional relationship (JCGM 101). The entire measuring process is represented virtually by means of a Monte Carlo simulation. Several hundred to thousand simulation runs are necessary for a high informative value (VDI/VDE 2011).

2.4.3 Other Standards

In addition to GUM, other standards deal with measurement uncertainty on a GUM basis. Although GUM offers an approach for determining the uncertainty of measurement, it does not fulfil all practical questions.

(DIN EN ISO 15530-3) is an established method for the experimental determination of measurement uncertainty in coordinate metrology and also refers to the GUM. A calibrated workpiece is measured repeatedly, whereby it is important to have similarities to the measuring workpiece. The similarity condition is a precondition for the determination of the measurement uncertainty according to (DIN EN ISO 15530-3) and refers to dimensional size, material, shape deviation, measuring strategy and probe configuration.

A minimum of 20 measurements is required. The influencing variables, such as operator, time of day or clamping, should be varied between measurements, as can happen in the normal measuring process. (DIN EN ISO 15530-3; Schwenke & Franke 2007)

The measurements are mainly based on four uncertainty contributions. The standard uncertainty from the uncertainty of calibration of calibrated workpiece stated in the calibration certificate (u_{cal}), the uncertainty from material and production variation (u_w), the standard uncertainty from the measurement method (u_p) and the standard uncertainty from systematic deviation (u_b). Systematic deviation is also called bias b and is a deviation from the calibration value. The extended measurement uncertainty is then calculated according to

$$U = k \sqrt{u_{cal}^2 + u_p^2 + u_w^2 + u_b{}^2}$$

Equation 2-3

The formula is adjusted according to (Schwenke & Franke 2007; Wendt, Keck & Schwenke 2007; Härtig & Krystek 2009; Härtig et al. 2009) to consider the systematic deviation as a random deviation. Therefore, applies

$$u_b = b$$

Equation 2-4

With the extended uncertainty U_{cal} specified in the calibration certificate, the standard uncertainty of the calibration process u_{cal} can be indicated:

$$u_{cal} = \frac{U_{cal}}{k}$$

Equation 2-5

The standard uncertainty of the measuring process u_p is determined as follows

$$u_p = \sqrt{\frac{1}{n-1} \sum_{i=1}^{n} (y_i - \bar{y})^2}$$

Equation 2-6

with

$$\bar{y} = \frac{1}{n} \sum_{i=1}^{n} y_i$$

Equation 2-7

where n is the number of measurements and y_i is the measured values.

The systematic deviation b is calculated as follows:

$$u_b = b = \bar{y} - x_{cal}$$

<div align="right">Equation 2-8</div>

x_{cal} represents the value of the measured variable of the calibrated workpiece or measurement standard. If the systematic deviation b can be compensated, this should be done and this contribution is eliminated in the extended measurement uncertainty. (DIN EN ISO 15530-3)

In determining the standard uncertainty from the production process u_w (DIN EN ISO 15530-3), only the variation of the thermal expansion coefficient of the measured workpiece is taken into account. If the similarity condition is met, this coefficient can be neglected. (DIN EN ISO 15530-3)

Another important study is the capability verification according to Measurement systems analysis (MSA) (AIAG 2010). This problem is taken into account by (DIN EN ISO 14253-1) and (DIN EN ISO 10012), as well as the evaluation of measuring and testing processes using the measurement uncertainty determination according to VDA Volume 5 (VDA Band 5), developed on basis of GUM. However, VDA Volume 5 does not allow universal calculation of measurement uncertainty and greatly simplifies procedures in industrial environment. Thus, VDA Volume 5 can only be used in the application area defined there. (Dietrich & Schulze 2017)

3 State of the Art

This chapter deals with the current state of research on quality assurance at FRP. The research project IRTG 2078 is presented, as well as the used material. Afterwards, possible defects and measuring techniques are discussed in more detail. Furthermore, relevant approaches for data fusion in lightweight construction and for quantitative evaluation using thermography are presented. The chapter concludes with a description of the resulting research deficit.

3.1 International Research Training Group

The project IRTG 2078 "Integrated engineering of continuous-discontinuous long fiber reinforced polymer structures", funded by the German Research Foundation (DFG), deals with lightweight material consisting of discontinuous long fiber reinforced polymer structures and local continuous fiber reinforcements. The material is examined by the different research areas characterization, simulation, design and technology. The developed quality assurance system for the complex material presented in this thesis belongs to the area technology. Additional parts of the area technology are further development and manufacturing of the material itself, which is also used for the investigations in the work and thus described in more detail below. (Böhlke & Wood 2014)

3.1.1 Material

The material used in this thesis is unsaturated polyester polyurethane hybrid (UPPH) produced at the Fraunhofer Institute for Chemical Technology (ICT) and is composed as shown in Table 3-1:

Table 3-1: Composition of materials according to (Ilinzeer 2018)

	DiCo-SMC	Co-SMC
UPPH flow resin with high viscosity	Daron ZW 14141	
UPPH no flow resin		Daron 41
Impregnation additive		BYK 9076
Release agent, flow additive	BYK 9085	BYK 9085
Inhibitor	pBQ	pBQ
De-airing	BYK A-530	

Peroxid (Initiator)	Trigonox 117	Trigonox 117
Isocyanat	Lupranat M20R	Lupranat M20R
Accelerator		BorchiKat0243
Styrene		Mono styrol
Glas fiber	EC 13,5 4800 272/80	
Carbon fiber		Panex 35, UD 300, UP sizing
Fiber content	41 wt.-%	60 wt.-%

The used material shows a special feature of the carbon fiber prepreg. In order to form and handle the continuous carbon fiber prepreg, it can be placed in an intermediate stage in which the material is already relatively rigid but not yet cured. This stage is called B-stage. (Bücheler 2018)

3.1.2 Production Process

The manufacturing process is as described in Chapter 2.1.1. A complete sequence of the entire process is shown in Figure 3-1.
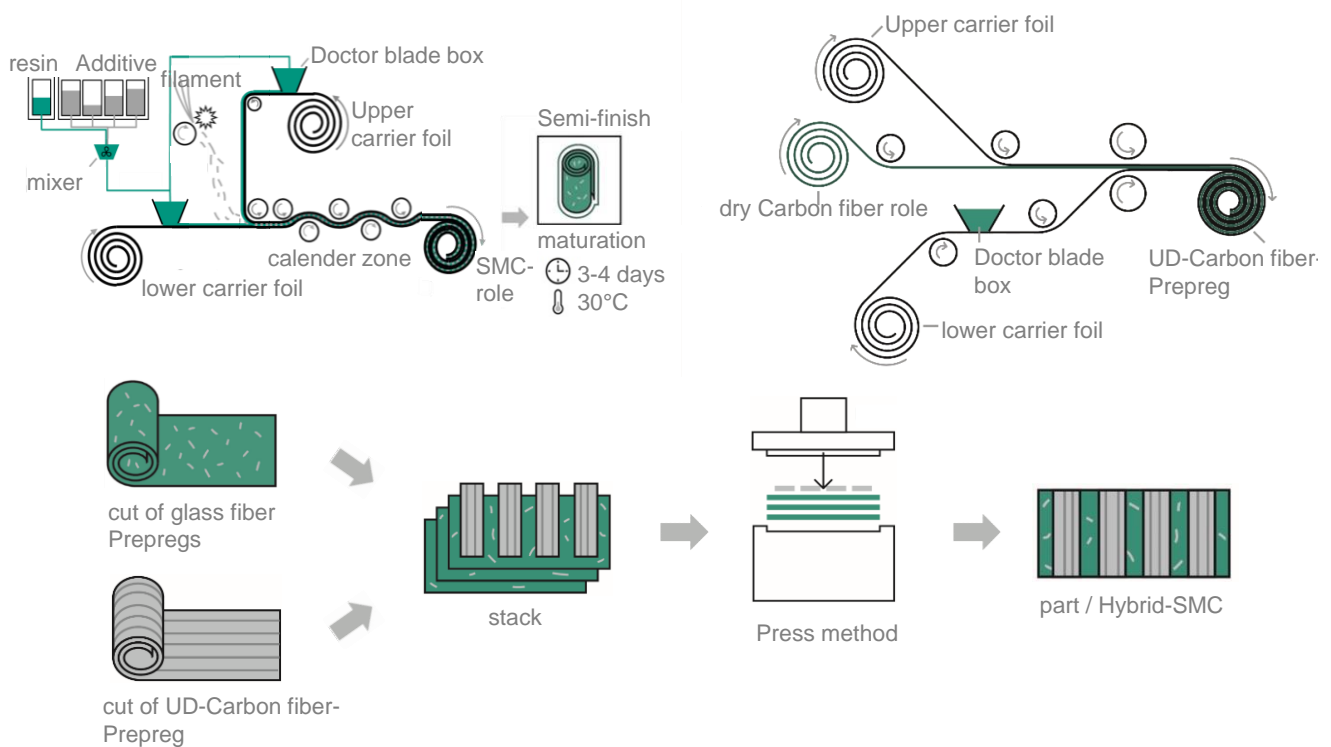

Figure 3-1: Production process of CoDiCo-SMC according to (Zaiß et al. 2017b)

To prevent the continuous carbon fiber prepregs from shifting, the tool has to be 100 % covered with material. In order to prevent this displacement even with smaller material deliveries, (Bücheler 2018) has developed a magnetic fixing process. Furthermore, the developed material has positive properties, which reduce the displacement. (Bücheler 2018)

During the manufacturing process, a large number of different defects can occur, evolving in different stages (see Chapter 2.1.2). To prevent defects at an early stage, testing and measuring techniques will be examined in the following chapter.

3.2 Testing and Measuring Techniques for Defects in Sheet Molding Compounds

According to (Eickenbusch & Krauss 2014), automation and quality assurance in FRP production are still at an early stage of development. Thus, the provision of testing and measuring methods for a complete quality assurance represents a great potential for the application of FRP components. (Eickenbusch & Krauss 2014)

This chapter describes the requirements for a testing and measuring system and selects the appropriate procedures in an interim conclusion.

3.2.1 Requirements for a Test and Measurement System for SMC

In order to avoid value-adding measures to be taken on defective components (Schmitt & Damm 2008) a process capable of examining components both in semi-finished and cured state has to be developed. Due to the sticky consistency of the semi-finished product, a non-contact systems is required. In addition, it has to be able to analyze a large number of different defects. The defects described in Chapter 2.1.2 can be divided into the two categories external and internal defects. Thus, the system must be able to detect defects on the surface, such as contour deviations or folds, but also internal defects, such as delaminations, foreign body or the incorrect orientation of the continuous carbon fiber material. Not only 2D geometries are considered, but also simple 3D geometries without undercuts. In addition, the system integration into the production process makes it necessary for the inspection time to be sufficient to evaluate the entire surface of large components within the same cycle time.

3.2.1.1 Approaches for External Defects in CoDiCo-SMC

In order to be able to evaluate geometries or external defects, (Bauer 2008) shows a comparison between confocal and strip projection methods, as well as the light section method.

The confocal system convinces with robust sensor heads, high data density, good measurability with deep structures and very good measurement resolution in the nm range. However, these methods require a long measuring time and are not suitable for inclined structures. (Bauer 2008)

The strip light projection has fast data acquisition and inspects large components within a short time. Operation and handling are simple and it has a low sensitivity to vibration and interference. However, it has difficulties with sharp edges, corners and cavities, as well as deep openings. For a successful measurement, the measuring room has to be darkened and the system is very sensitive to reflections. Therefore, the light output has to be adapted to the respective reflectivity of the surface and can only be carried out with stationary objects. (Bauer 2008)

The light section method has similar disadvantages as the strip light projection method. A single system also has difficulties with sharp edges and corners, as well as deep openings (Bauer 2008). For a good result it is also necessary to adjust the laser power to the reflectivity of the material. Furthermore, the coordinates of ceramics and plastics may be distorted by volume scattering. However, the system convinces with a high digitization speed and the simple and robust design of compact sensors. The individual systems are reasonably priced and a dense amount of data is possible. A measurement is possible on moving components as well as on inclined surfaces and is suitable for sensitive and filigree models. Furthermore, no darkening of the measuring room is necessary and the system is insensitive to changes in color and brightness. (Bauer 2008)

Computed tomography offers a method for examining wrinkles or fiber ripples (Lightfoot & Wisnom, M. & Potter, K. 2013). (Lightfoot & Wisnom, M. & Potter, K. 2013) investigates a complex shaped geometry and a preform of a propeller blade. By means of computed tomography it is possible to determine the fiber orientation and defects, as well as to carry out a layer-by-layer analysis of the preform. However, the measuring room is limited and the measuring and evaluation time is too long for inline testing. (Lightfoot & Wisnom, M. & Potter, K. 2013)

The detection of faults by means of eddy current is only possible with carbon fiber-reinforced plastics, since the materials electrical conductivity is used. Usually 2D components are examined for defects, such as fiber orientation or missing fiber bundles, both on dry semi-finished products and cured components. (Schulze et al. 2010; Heuer et al. 2015)

In the "3D-Fast" project, 3D geometries are examined using eddy current (Bardl et al. 2016). The component is scanned with aid of a 6-axis robot. An evaluation algorithm was developed making a statement about fiber orientation on the surface. Furthermore, the detection of large geometries is very time-consuming due to the small scan heads and could only be used for the continuous material with the existing material and is therefore not suitable for the entire component. (Bardl et al. 2016)

The investigation of geometry and the detection of external defects of carbon fiber preforms is currently the subject of various research activities. (Orth 2008) initially evaluates common test methods with respect to typical defect in FRP. X-ray radiation, computed tomography, 2D and 3D image processing, and 3D laser sensors all perform as good to very good for the detection of geometry and position. Computer tomography, 3D image processing and 3D laser sensor technology are 3D-capable. The aim of (Orth 2008) is to check the automatic production of textile preforms by a machine vision system. The focus is on material type, bond structure, alignment and geometry. A laser light section sensor is used for the machine vision system and its suitability is verified. Furthermore, the measurement uncertainty of the system is determined according to GUM. (Orth 2008)

Another system based on the optical principle, laser light section sensor guided by a robot, was developed by (Mersmann 2012). The application examines dry semi-finished fiber products as well as pre-impregnated fiber tapes and considers the geometry of the textile preform as well as the contour of the blanks. The uncertainty of measurement of the system is also considered in this work. (Mersmann 2012)

The study of (Schmitt et al. 2014) considers quality assurance of radial braiding processes already used for the production of longitudinal beams. The relevant quality characteristic for inline check is the fiber angle. For this purpose, optical inspection systems (Machine Vision System (MVS)) are available, convincing by their speed, non-destructiveness and contact-free operation. MVS enables statistical evaluations and process control (Jähne 1997). 2D camera data and 3D geometry data are fused for inspection.

For this purpose, a camera system with diffuse illumination and a laser light section sensor are used to capture the 3D geometry. Lighting has a significant influence on the quality of image analysis, using diffuse lighting minimizes reflection as far as possible. Through sensor data fusion, it is possible to determine the 3D braid angle with a measurement uncertainty of 0.2 degrees. Furthermore, it is a real-time system delivering results within cycle time, but only used for carbon fibers without matrix. (Schmitt et al. 2014)

(Fürtjes 2016) has developed an MVS whose main focus is on real-time capability and which is also designed for CFRP semi-finished products without matrix, but not for complex 3D geometries. The system is concerned with the quality assurance of fiber orientation and angle, using diffuse dome lighting and the Basler acA2040-180km camera. The measurement uncertainty is determined according to GUM. (Fürtjes 2016)

(Kosse et al. 2016) continue the above projects. (Kosse et al. 2016) for example, shows that a diode laser with line optics and an area scan camera working according to the laser light section principle can also be used to determine the waviness of fiber-thermoplastic composites. In this case the assembly is guided by a 6-axis robot. (Kosse et al. 2016)

The above research projects successfully examines simple 3D geometries, but there are problems with 3D geometries resulting in shading effects. This problem is addressed by (Brabandt 2018) by developing an integrated measurement system for the evaluation of carbon fiber preforms. First approaches are published in (Lanza & Brabandt 2012; Brabandt & Lanza 2015; Brabandt, Hettich & Lanza 2015) with the focus on investigating geometric deviations of flexible and highly reflective surfaces of carbon fiber preforms. For this purpose, a 3D measuring station based on the principle of laser light section sensors is developed and implemented. (Brabandt 2018) addresses problems with sharp edges and corners by merging two light section sensors to avoid shading effects. For inline use, a multi-stage procedure is proposed, first selecting regions of interest using a 2D inspection system and second carrying out the 3D measurement. (Brabandt 2018) points out that the investigations result is very dependent on material and fiber orientation. (Brabandt 2018)

The author of this thesis (Zaiß et al. 2017a) used the 3D-measuring station of (Brabandt 2018), optimal parameters for the SMC in cured condition and as semi-finished product are determined (Zaiß et al. 2017a). The parameters threshold, laser intensity, angle and

integration time are varied to evaluate different cloud of points, representing the 3D geometry of test object. Three results are shown: First, the selected parameters have great influence on the result. Second, a geometry detection of CoDiCo materials in cured as well as in semi-finished state is possible. Third, further investigations are necessary. (Zaiß et al. 2017a)

(Eitzinger et al. 2017) looks at the tape laying process, carried out with rollers with integrated sensors. The focus is on CFRP, available both as pure fiber products and as pre-impregnated materials, so-called prepregs. Errors investigated are placement errors, gaps between the carbon fiber tapes, overlaps, deformations, impurities and missing CFRP tapes. At least one radiation source or sensor shall be integrated into the roller, which is permeable to the radiation. It is not clearly stated which sensor is used, but a laser or diode is mentioned without further information. The roller with the sensor should be as flexible as possible. Material reflection and angle of surface inclination have an influence on the sensor, which can be used for the evaluation. (Eitzinger et al. 2017)

Also (Engel, Weimer & Orth 2016a) integrates a sensor into its system for FRP component production. It is mentioned that it can be a laser light section sensor, but not deepened further (Engel, Weimer & Orth 2016a; Engel, Weimer & Orth 2016b)

(Walton 2006a) has applied for a patent for a system dealing with the tape laying process. Several patents deal with the use of one or two lasers in combination with a camera. Thus, with a laser light section system avoiding shadowing effects, it should be possible to detect both gaps and wrinkles (Walton 2006b; Walton 2006a; Walton 2007)

No investigations or public documents are known about the presented patents, so that only a limited statement regarding their suitability is possible.

3.2.1.2 Approaches for Internal Defects in CoDiCo-SMC

For the examination of internal defects, a variety of different methods is available, which are introduced in Appendix A 4. In the following investigations, the suitability of these methods is examined in more detail.

According to (Hellier 2013) NDT methods are able to determine the internal structure of components without destroying or changing them. (Kochan 2012) systematically assesses the applicability of different non-destructive testing methods with focus on CFRP

components. The selected procedures are ultrasound, thermography and X-ray examination.

The X-ray method allows detailed imaging and good resolution of inhomogeneities such as cracks and pores. However, delamination is difficult to detect and the test surface at high resolution very small. Ultrasonic testing shows a very good resolution up to a depth of 10 mm, which cannot be confirmed for hollow sections. Lock-in thermography works without contact and a flat detection allows pores, inclusions, delaminations and near-surface defects to be detected well. However, the low penetration depth is a disadvantage. Furthermore, the poor heat conduction perpendicular to the carbon fiber is a further disadvantage, as the heat is quickly conducted into the tier, but not into the depth. Thus, defects in lower positions are strongly dampened by the environment. Short testing time makes thermography a superior method compared to ultrasound and X-ray methods. Within a minute it is possible to inspect a hood. (Kochan 2012)

(Oster 2012) achieved similar results by examining GFRP and CFRP components. In addition to the procedures to be investigated in (Kochan 2012), the shearography is included in the evaluation. (Oster 2012) makes it clear that NDT is not only carried out on final components, but has to be used early in the development process. This can lead to knowledge about defect types and their origin, as well as the effects on strength. Not every error has to be harmful or cause serious consequences. The following Table 3-2 presents the testability results of different defects according to (Oster 2012).

Table 3-2: Testability of defects according to (Oster 2012)

		non-destructive testing methods			
		computer tomography	ultrasound	thermography	shearography
Defect	Delamination	+	++	+	+
	Porosity	++	+	+	-
	Undulation	+	o	-	+
	Fiber crack	+	-	o	-

++ very good   + good   o limited   - not possible or unknown

The research project ReCarbonfit (Plank et al. 2013) introduces 15 typical defects in 100 x 100 x 0.8 mm^3 CFRP components. The defects are located between the middle

layers. These defects are supposed to be foreign objects, delaminations or air inclusions, as well as impact damages. The study tests various non-destructive testing methods, including visual inspection, computed tomography, radioscopy, active thermography and ultrasonic testing. 14 of 15 errors could be detected with computer tomography, ultrasonic testing and active thermography. (Plank et al. 2013)

In order to interpret and quantify error data correctly, computed tomography has the greatest potential, but also the disadvantages high costs, limited mobility and component size. Ultrasound is still a standard procedure, but thermography could become interesting for many users. It offers great advantages due to short inspection times, high mobility, clear costs and comparable defect detection. As disadvantages, however, high training effort and limited detectability of defects in test objects with high wall thickness (> 5 mm) have to be taken into account. (Plank et al. 2013)

The study by (Vaara & Leinonen 2012) gives an overview of different NDT methods and their suitability to detect defects in CFRP components. The following test methods were considered: Different ultrasonic methods, laser shearography, eddy current testing, different X-radiography methods, different thermography methods and acoustic impact testing. It turns out that thermography is a good way to detect a large number of errors. Ultrasonic methods are able to detect even more defects, but are much more time-consuming. Matrix cracks and fiber breaks are not detected by most NDT methods, the sound emission method is suitable for this. However, it is not suitable for many other defects. (Vaara & Leinonen 2012)

In the presentation of (Ullmann 2008), computed tomography, X-rays, ultrasound and lock-in thermography are compared and investigated for a ceramic fiber composite material. This shows that lock-in thermography is characterized by non-contact testing within a short time on large surfaces, as well as by mobile applicability. However, only 2D and blurred images are generated, not providing any depth information. Computed tomography, is also non-contact and has a good resolution on the one hand, but on the other hand is not mobile, very expensive and requires special safety measures due to radiation exposure. (Ullmann 2008; Fürtjes 2016) The work of (Lasagni et al. 2015) confirms the results so far.

Furthermore, there are first approaches to examine curved surfaces using thermography positioned by a robot and laser system (Schmidt & Dutta 2013). In order to be able

to make statements about the depth, an approach of (Ekanayake, Isenberg & Schmitt 2017) is developed, using frequency images for analysis.

Another method of NDT is the eddy current method, mainly investigated for the use in resin transfer molding (RTM) process and in processing of CFRP. As a basic requirement, the material has to be electrically conductive (Berger et al. 2016; Berger et al. 2017; Berger et al. 2018). It is regarded as a method that can be used along the entire process chain (Heuer et al. 2015). Since the examined material is not only carbon fiber material, this method is not considered further.

The works presented so far, dealing with approaches for external and internal defects, focus on carbon fiber materials in general or refer to the RTM processes. (Krämer et al. 2014) deals with the production of SMC semi-finished products and identifies three important errors: Air entrapping, fiber distribution and tearing of the carrier foil. To detect them in the manufacturing process, a thermographic camera was successfully installed. Thus, the defects can already be detected during production, but there are still weaknesses in resolution and process time. (Krämer et al. 2014)

The author of this thesis (Zaiß et al. 2017b) examines various ultrasound and active thermography methods regarding their suitability for quality control of SMC in the production process. The examination is carried out on semi-finished products as well as on cured components of CoDiCo-SMC. Active thermography is performed by using of a flash lamp. The water immersion bath, air coupling and ultrasonic spectroscopy are used for the ultrasonic examination. The aim is to demonstrate suitability for typical defects such as delamination, inclusions, porosity and fiber orientation. It is shown that ultrasonic methods cannot be used for semi-finished products due to too high damping of the material still in a limp state. Thermography is the best way to detect most faults quickly and contactless, making the method suitable for inline testing. An overview of the results is shown in Table 3-3 below. (Zaiß et al. 2017b)

Table 3-3: Comparison of NDT methods according to (Zaiß et al. 2017b)

	Capability of flaw detection						In-line process capability				
	Delamination	Inclusion	Porosity	Fiber/ matrix distribution	Fiber orientation	Degree of curing	Contact-less	Complex/ thick shapes	Cycle time	Imaging	Semi-finished material
Thermography	++	+	o	+	++	-	++	-	++	++	o
Water immersion bath	+	+	++	-	-	-	-	+	+	++	-
Air coupling	++	++	++	-	-	-	++	+	+/o	++	o
Ultrasonic spectroscopy	o	-	-	-	+	-	-	o	-	-	-

++ very high capability   + high capability   o good capability   - low capability

3.2.2 Interim Conclusion

Table 3-4 shows an evaluation of the presented approaches with regard to the requirements in Chapter 3.2.1. The approaches are divided into external and internal defects.

As a result of Table 3-4, currently there is no system fully meeting all requirements. Furthermore, some methods cannot be evaluated in terms of compliance with the requirements, which is why individual gaps exist. The eddy current method is excluded for selection as it is only suitable for electrically conductive materials, but not the examined DiCo-SMC.

For external defects, the laser light section system proves to be a suitable method able to examine large-area components within a short time. Investigations by (Zaiß et al. 2017a) show that it is possible to detect external defects on the examined material with the system of (Brabandt 2018).

Thermography is a suitable method for internal defects. Due to its fast, non-contact examination it is suitable for analyzing the existing material and a large number of defects. Up to now, 3D geometries can only be examined to a limited degree.

Table 3-4: Evaluation of existing approaches for detection of defects

Legend (evaluation unit):
- ● completely fulfilled
- ◕ nearly fulfilled
- ◐ partly fulfilled
- ◔ barely fulfilled
- ○ not fulfilled
- ☐ no statement possible

	Method	Reference	Contactless measurement	Semi-finished Material	Cured Material	Short measuring time	Simple 3D geometry	full-surface evaluation of large-area components
External Defects	Stripe projection method	(Bauer 2008)	●		●	◐	◔	◐
	Confocal method	(Bauer 2008)	●		●	◔	○	○
	Computer tomography	(Lightfoot & Wisnom, M. & Potter, K. 2013)	●		◕	○	◕	○
	Eddy Current	(Schulze et al. 2010; Heuer et al. 2015; Bardl et al. 2016)	◕	●	◕	○	◔	○
	Camera	(Fürtjes 2016)	●	◐		◕	○	◐
	Laser light section for simple geometries	(Mersmann 2012; Orth 2008; Kosse et al. 2016; Schmitt et al. 2014; Bauer 2008)	●	◐		◕	◐	◐
	Laser light section for complex geometries	(Zaiß et al. 2017a; Brabandt 2018; Bauer 2008)	●	◕	◕	◕	◕	◕
	Patents	(Walton 2006a; Walton 2006b; Walton 2007; Eitzinger et al. 2017)	●	◕	◕		◐	
Internal Defects	Thermography	(Kochan 2012; Oster 2012; Plank et al. 2013; Vaara & Leinonen 2012; Ullmann 2008; Schmidt & Dutta 2013; Krämer et al. 2014; Zaiß et al. 2017b; Lasagni et al. 2015; Ekanayake, Isenberg & Schmitt 2017)	●	●	◐	◕	◔	◕
	Ultrasound	(Kochan 2012; Oster 2012; Plank et al. 2013; Vaara & Leinonen 2012; Ullmann 2008; Lasagni et al. 2015)	◐	○	●	◔	◕	◔
	Computer tomography	(Kochan 2012; Fürtjes 2016; Oster 2012; Plank et al. 2013; Vaara & Leinonen 2012; Ullmann 2008)	●	●	●	○	●	○
	Eddy current	(Vaara & Leinonen 2012; Berger et al. 2016; Berger et al. 2018; Berger et al. 2017; Heuer et al. 2015)	◕	◕	◕	◐	◔	◔
	Shearography	(Oster 2012; Vaara & Leinonen 2012) (Sauerwein et al. 2012; Vaara & Leinonen 2012)	●		◕	◐	◕	◐
	Visual inspection	(Plank et al. 2013)	●	●	●	◔	●	○
	Acoustic testing	(Vaara & Leinonen 2012; Zaiß et al. 2017b)	○	○	◐	◔	○	○

Based on the current state of the art, the laser light section method of (Brabandt 2018) and thermography are preselected for further investigations. To enable a complete and fast examination of CoDiCo-SMC, a multi-sensor system with these methods is set up, requiring a joint evaluation of data by means of data fusion.

In the following chapter, the current state of research for data fusion in lightweight construction as well as more detailed requirements for the multi-sensor system and evaluation are discussed.

3.3 Multi-sensor System and Data Fusion

By setting up a multi-sensor system using laser light section and thermography, the data obtained has to be evaluated sensibly. The principle of data fusion is suitable for this, as it is used in many areas. For example in military technology, robotics, but also in production and measurement technology (cf. Chapter 2.3) (Beyerer 2006). In the following, requirements for the multi-sensor system and its evaluation by means of data fusion are discussed. Subsequently, the current state of research for data fusion in lightweight construction is presented and evaluated. Afterwards, the detailed evaluation of the thermographic examination is analyzed, because thermography provides an essential contribution to the complete quality assurance with the multi-sensor system.

3.3.1 Requirements for the Multi-sensor System and Evaluation

The use of data fusion offers various advantages. This includes more precise knowledge of physical quantities in a shorter time at lower costs, but also the reduction of uncertainty, as well as knowledge that cannot be obtained from one system alone (Beyerer 2006).

The complete quality assurance of presented CoDiCo-SMC requires a fast and intuitive user evaluation. The system has to be able to reliably inspect both semi-finished product and cured component. In order to assess the result correctly, the measurement uncertainty of the single systems and the multi-sensor system have to be known.

The use of thermography offers a quick way to check components for internal defects. However, a quantitative evaluation of the thermographic examination is necessary for the user in order to make defined statements regarding the defects. Furthermore, it is currently possible to use thermography to make a statement on whether a defect has occurred. It would be desirable if a clear assignment to defects could be made on the basis of characteristic features. This is currently only possible with the expert knowledge

of the operator. Also, the commercially available software programs for thermography offer only a two-dimensional evaluation without concrete depth information and 3D imaging. This would be useful for a more straightforward evaluation.

The following approaches for data fusion in lightweight construction and the evaluation methods of thermography are evaluated with regard to the requirements in Chapter 3.3.2 in order to subsequently identify the research deficit.

3.3.1.1 Multi-sensor System and Data Fusion in Lightweight Construction

The process of data fusion includes the measurement recording of different sensors, the subsequent extraction of information, the examination of commonalities and interfaces in order to then derive a decision (Raol 2010).

Already (Gros, Bousigue & Takahashi 1998) shows that one NDT method alone is not sufficient to completely evaluate a material. In order to solve this problem and avoid bad signal-to-noise ratio, the data fusion method is used. (Gros, Bousigue & Takahashi 1998) confirms the necessary requirement that visual data analysis can be interpreted more simply by displaying images of the tested areas. For the investigation of CFRP, data fusion of eddy current and thermography is performed at pixel level. The data fusion process is depicted in Figure 3-2.
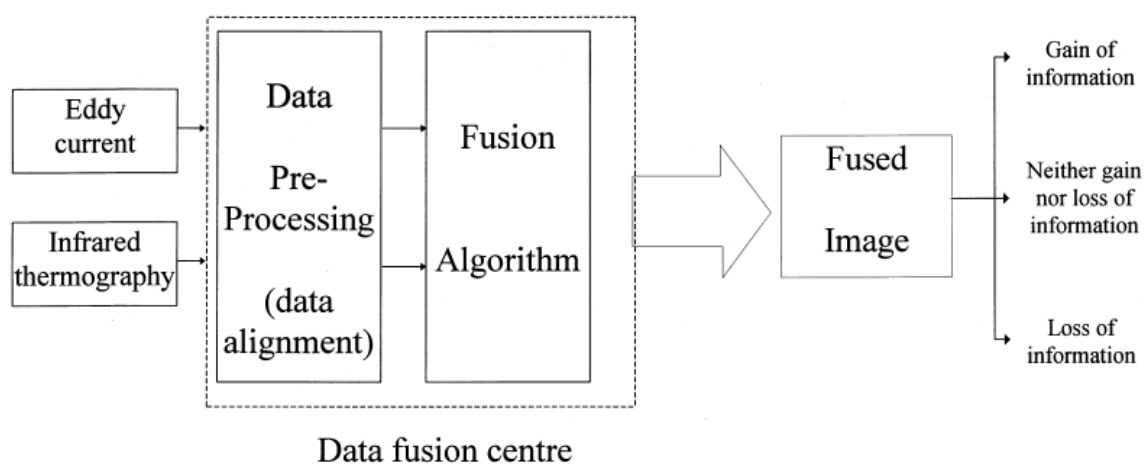
Figure 3-2: Schematic process of data fusion and possible results (Gros, Bousigue & Takahashi 1998)

For data reconciliation, each image represents the same view on the test object, defining a spatial reference into which the images are transformed. The images of both methods are combined on pixel level with statistical, arithmetic and probabilistic algorithms. In order to evaluate the different data fusion results, these are quantified. The fused

images are compared with a reference measurement of an ultrasound testing. The ultrasonic method is chosen for its reliability and recognition in the industry, although it can also provide incorrect information and the comparison can only be regarded as an estimation. The work shows potentials and limits of the merger, by also pointing out that further work is necessary to develop the optimal data fusion strategy including knowledge of the 3D structure. Data fusion is becoming increasingly important in order to better assess the reliability of NDT methods and reduce ambiguities. (Gros, Bousigue & Takahashi 1998)

Another area for using data fusion are CFRP preforms. The work of (Mersmann 2012), shows data fusion of a camera system and a light section sensor. The camera checks the texture and the light section sensor the 3D geometry (Mersmann 2012; Schmitt et al. 2008).

(Schmitt et al. 2015) develops a system, monitoring the production of multiaxial non-crimp fabrics and thus has an essential focus on fiber orientation. For quality assurance the machine vision system, consisting of a light section sensor and a camera system with diffuse dome lighting, has to monitor the production in real time. To achieve this, the algorithm for evaluation is divided into two areas and executed in parallel: First area is the calculation of segmentation, second area is the determination of fiber orientation with help of the structure tensor method. Also the uncertainty of measurement is determined. (Schmitt et al. 2015)

The work of (Brabandt 2018) also represents a data fusion system. The developed 3D measuring station contains two laser light section systems, fused to reduce shadowing effects and completely capture CFRP preforms. (Brabandt 2018)

In order to enable fast repair processes on CFRP components, the fusion of laser light section with ultrasound and thermography is discussed in (Schmitt, Ekanayake & Nienheysen 2018). As a result of accident frequency analysis, based on frequency, cause and type of damage, a hat profile with a sill-like geometry is considered more closely (Hopmann et al. 2017). For the investigation, a 3D CAD model of the component is required, on which the lock-in thermography images are then projected. A chessboard pattern, registered by laser scanner and thermography, is applied to the component as a marker for registration. In order to reduce calculation effort, the operator has to select several points independently with the support of instructions. As soon as the data sets are aligned, the defect information is projected onto the base model to calculate region

of interest (ROI) and error position. Registration takes place in the global coordinate system defined by the 3D model. The gray values of the phase image and the polygon mesh generated by the laser scanner are used to assign thermographic and geometric data. A merged image is depicted in Figure 3-3.

Figure 3-3: Sensor data fusion of geometry and thermographic data (Schmitt, Ekanayake & Nienheysen 2018)

After fusion of 3D model and thermographic measurement, the information about the maximum error rectangles is transmitted to the ultrasonic sensors and visualized. The line sensor of the ultrasonic sensor is guided meandering over the ROI. The running time of sound pulses, their intensity and the sound echo allow the geometry of the damaged area to be visualized in 3D. The effect of the damage on the mechanical properties can be estimated with the use of a finite element analysis. The presented examination offers data fusion of all repair steps, a digital mapping of damage to component and through the damage database also a fast and efficient damage assessment. (Schmitt, Ekanayake & Nienheysen 2018; Hopmann et al. 2017; Losch et al. 2016)

Within the research project "QualiFibre" a software enabling data fusion of different NDT methods is developed. For the quality assurance of GFRP and CFRP materials the methods computed tomography, dark-field X-ray hyperspectral imaging, thermography and ultrasonic testing are used. For investigation, a simple plate geometry with small curvatures is chosen, manufactured in the RTM process. As the methods used provide both 2D and 3D data, a NDT machine vision platform with intelligent and automatic analysis algorithm for both geometries is developed for data evaluation, making it possible to detect defects such as delamination or drying points. Subsequently, properties such as area and minimum/maximum extent of the defects are measured. In 3D data evaluation, errors such as porosity or fiber orientation are analyzed. All errors are

automatically registered and colored. In addition to the evaluation of individual proce-
dures, the software also contains fusion of thermography and ultrasound. The aim is to
detect as many errors as possible, as individual systems often do not detect all defects.
(Effenberger 2016b; Holstein et al. 2015; Effenberger 2016a)

(Soldan 2014) deals with data fusion in thermography with the aim to improve investi-
gations quality and to increase the amount of information available about the test object.
Three approaches are distinguished: First, quality improvement can only be achieved
with thermographic camera measurements and can lead, for example, to noise sup-
pression or an increase in dynamic range. Second, it is possible to change the camera
orientation to enlarge the field of view and improve geometric resolution. Third, the fu-
sion of thermograms with other imaging instruments allows more information to be ob-
tained for one measuring point as well as enables interpretation and analysis of meas-
urement data in a 3D model. (Soldan 2014)

The fusion in this approach takes place pixel by pixel, without making a concrete deci-
sion at the end, for example whether there is an error. The model of the pinhole camera
is used for registration. In addition to noise reduction, the use of filters and the extension
of depth of field, (Soldan 2014) fuse photographs and thermograms. In a rigid network
of cameras, the geometric relation between the coordinate systems is constant, or oth-
erwise have to be transformed. Furthermore, it is pointed out that the distortion of the
optics has to be determined and corrected, as well as the geometric relations between
the cameras. Registration is carried out using a calibration field made of screen-printed
cardboard. The recorded data are displayed as superimposed images as in Figure 3-4.
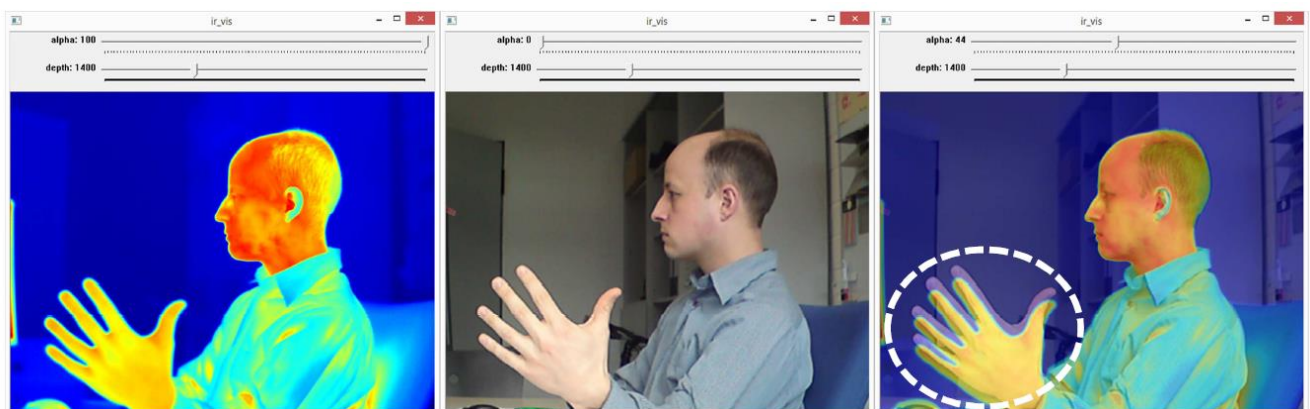
Figure 3-4: Data fusion of photography and thermogram (Soldan 2014)

The fusion leads to additional information, however for objects with other distances, for
example the hand in Figure 3-4, a registration error results, since the registration is

carried out only for a certain distance. Thus, the attachment should be combined with the depth of field. Based on these investigations, the conversion into a 3D thermography is now aimed for. This is based on mathematical camera models and registration is done by measuring external references with an optical motion tracking system. Different camera views are used to create a 3D thermographic model of the measured object. The 2D thermograms are assigned to 3D points and displayed in a global coordinate system. The fusion offers a realistic reality representation and thus facilitates the interpretation of measurements, since spatial proportions are present. Large and often redundant data volumes are a disadvantage. Great potential is attributed to the automatic evaluation of the measurements in a 3D model. (Soldan 2014) shows different fusion possibilities with thermographic cameras, which increases the quality of measurement data. The automated data evaluation and pattern recognition for errors due to the additional geometric properties in 3D thermograms are considered promising. (Soldan 2014)

These following investigations cannot be essentially assigned to lightweight construction, but are listed here for completeness. (Galovska, Petz & Tutsch 2012) investigates the uncertainty of measurement during dimensional measurement using cylindrical workpieces. In this paper, the investigation is examined by means of a Monte Carlo simulation. For the analysis of fused data there are different approaches, such as the probability theory (Bayes approach), Dempster-Shafer's evidence theory and the possibility theory using fuzzy sets. This paper shows that the transformation of data has a significant influence on the uncertainty of the merger result and therefore has to be carefully determined (Galovska, Petz & Tutsch 2012).

(Weckenmann et al. 2009) gives an overview of data fusion in dimensional measurement technology as well as examples from measurement technology such as image fusion and deflectometry. The work shows potentials of data fusion and points out the challenges to be mastered, such as automation or measurement uncertainty analysis. (Weckenmann et al. 2009)

(Bernstein 2011) develops an optical multi-sensor measuring method for a precise, real-time capable and complete measurement of extruded profiles. This system consists of a shadow casting method and several laser section systems and is evaluated according to scientific standards. An important part of the thesis is the experimental determination of the measurement uncertainty of the multi-sensor measurement method according to (VDI/VDE 2617-8). The measurement uncertainty is 20 µm. (Bernstein 2011)

3.3.1.2 Detailed Evaluation by thermography

Various options are available for the evaluation of thermographic examinations. In addition to the thermal cooling curve, also the phase and amplitude images generated by a Fourier transformation can be used for evaluation (see Appendix A 4.5). Especially the phase images are suitable for evaluation, because disturbing effects are suppressed and the depth range is larger (Spießberger, Gleiter & Busse 2008).

(Myrach et al. 2014) uses optical lock-in thermography to investigate the resolution limits and depth range. A CFRP plate (200 x 200 x 6 mm³), with a large number of flat-bottomed hole defects with different diameters and residual depths, is used. The following depths are detected during examination: ≥ 4.0 mm (Ø 23.8 mm), ≥ 3.5 mm (Ø 15.8 mm) and 3.0 mm (Ø 7.8 mm). Investigations are carried out on both unidirectional and quasiisotropic CFRP components. Unidirectional carbon fiber layers show a widening of defect contrast, which can be traced back to the higher thermal conductivity parallel to fiber direction. Thus, this work shows that the detection of the flat bottom hole depends on the size and that small diameter defects can only be detected at low depths due to the lateral heat flows. (Myrach et al. 2014)

(Maierhofer et al. 2014) uses the same samples and evaluates them after a flash excitation with the help of pulse-phase thermography (PPT). The phase images of PPT are evaluated and compared with the same frequencies as in lock-in thermography. The phase images hardly differ from each other, as shown in Figure 3-5.
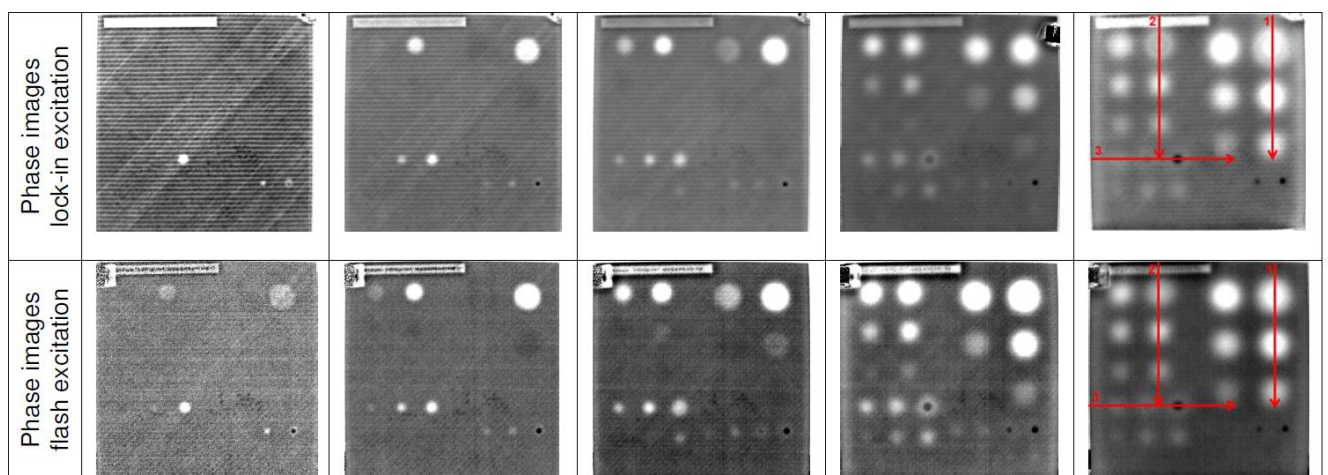
Figure 3-5: Comparison between pulse-phase and lock-in thermography (Maierhofer et al. 2014)

A comparison of both methods shows that lock-in thermography has a better signal-to-noise ration and the spatial resolution of the defects is higher. Therefore, it is suitable

for components with high thermal diffusivity. PPT, on the other hand, requires considerably less time and is well suited for components with low thermal diffusivity, including CFRP and GFRP components. (Maierhofer et al. 2014)

(Chiwu et al. 2014) is also conducting tests on a sample (135 x 100 x 10 mm^3) with 12 flat holes, examined by PPT. The diameters of the holes are 4, 6, 10 and 12 mm and the depth 0.5, 1.0 and 2.0 mm. The investigation shows that amplitude and phase images detect more defects than the pure thermogram. As the depth of the defect increases, the phase difference between the bore and the undamaged area decreases. The phase difference increases with increasing error diameters. Furthermore, the fuzzy C-means clustering algorithm is introduced, which performs edge detection in the phase image. (Chiwu et al. 2014)

(Hornfeck et al. 2015) demonstrates that different frequencies in lock-in thermography can reach different depths and thus enable a depth statement. The investigations are performed on GFRP with flat bores. However, long examination times are necessary in lock-in thermography in order to obtain a result. (Hornfeck et al. 2015)

Another method to analyze the depth is to determine the phase contrast. (Wallbrink, Wade & Jones 2007) use the determination of phase contrast for lock-in thermography on steel plates with round holes. In addition, it becomes clear that the size of the diameter has an influence on the phase angle, which also influences the depth analysis. (Ishikawa et al. 2013) use a similar method for PPT. The phase difference is used to determine the optimal frequency. (Ishikawa et al. 2013)

(Arndt 2007) also deals with the qualitative and quantitative evaluation of near-surface structures of rectangular pulse spectral thermography, but in the building industry. Rectangular pulse spectral thermography is an adaptation of PPT. In this work it becomes clear that phases are best suited for a qualitative evaluation and location of defects. (Arndt 2007) also points out that the amplitude, as far as it can be determined, provides more reliable and accurate quantitative values than the phase. The investigations determine that there is a correlation between the frequency at which a defect can be easily detected and its depth. The deeper the defect, the lower the respective frequency. Arndt's newly developed approach for quantitative detection using the characteristic frequency f_{ch} is suitable for defects between 3 and 10 cm size. However, the time required is very high and investigations have so far been limited to the construction industry without proof regarding FRP. (Arndt 2007)

Another quantitative examination of lock-in thermography is carried out by (Zöcke et al. 2007). The signal-to-noise ratio is used for defect detection, a digit is considered defective if it exceeds the threshold of 6 dB. Investigations are carried out on a CFRP plate with flat holes. For a local error depth determination, several thermographic images are taken at different frequencies. The area of interest is then selected and the signal-to-noise ratio is determined. The blind frequency f_b is determined for each defect. It represents the frequency a defect is no longer visible at. In order to avoid pre-selection, this paper presents a global procedure that uses all phase information. The procedures accuracy depends on the increment of lock-in frequencies. With increasing depth, defects become more blurred and difficult to detect due to heat diffusion. The work presented does not describe a solution to this problem. (Zöcke et al. 2007)

Based on the previous work, (Zöcke 2010) develops the process further. By fusion of the thermal images from optical lock-in thermography and ultrasound induced thermography deeper detections can be performed. Furthermore, the measurement of the defect size is more reliable. (Zöcke 2010)

(Ibarra Castanedo 2005) uses PPT and proposes a depth inversion technique based on the thermal diffusion length equation $\mu = \sqrt{\alpha / \pi \cdot f}$. An error is not detected above the blind frequency f_b, representing the limit frequency at which a defect at a certain depth still has sufficient phase contrast to be detected in the frequency spectrum. The phase contrast is proposed for the estimation of f_b. Furthermore, the work points out the well usability of PPT on curved components additional to flat ones. Phase evaluation reacts more to the difference between thermal material properties than geometric characteristics. Thus, no significant influence of sample geometry on quantitative results is observed. (Ibarra Castanedo 2005) also deals with possible uncertainties that could influence the investigations. Noise can be attributed to various forms, including environmental and structural forms as well as optical and electronic types. The use of non-homogeneous materials, such as FRP, also leads to uncertainties, as the thermal materials properties are not completely homogeneous. Furthermore, phase contrast calculations are subject to inaccuracies, as the non-defective surface is also not homogeneous. Other uncertainty factors mentioned include the impact of the selected sound area, time resolution, oversampling and thermal properties. The total measurement uncertainty is not calculated. (Ibarra Castanedo 2005)

Further procedures dealing with the quantitative analysis of defects, depth and size are mentioned in (Lahiri et al. 2012; Liu et al. 2015; Dudzik 2010).

(Mayr et al. 2008) examines the effect of PPT on curved geometries using CFRP components with Teflon strips inserted at different depths. Furthermore, a 3D finite element simulation is performed, taking into account anisotropic heat conduction and inhomogeneous heat excitation as well as orientation-dependent heat absorption to evaluate geometry effects. Measurements are used to create a model for the specific excitation conditions. This model also takes into account the energy distribution of the light source as well as distance and orientation dependence of the test objects with regard to energy absorption. The results are used in the finite element simulation, showing that defect size in curved area appears larger or smaller depending on heat flow direction. In real measurements, the diffusion images are strongly influenced by the geometry effect, but can be interpreted much better with the help of simulation. (Mayr et al. 2008)

(Gleiter 2011) is working intensively on the quantitative evaluation of dynamic thermography. The recorded infrared sequence is evaluated with mathematical methods. Lock-in thermography as well as PPT are part of dynamic thermography. The examinations are carried out with different FRP. With lock-in thermography, depth profiles can be created from phase images at different frequencies. The respective depth position is reconstructed from the frequencies of the phase maxima. In order to obtain a 3D image of inner interfaces, the phase images are arranged according to increasing frequency and put on top of each other. The frequency response at an intact location is used as reference. Other quantitative parameters determined by lock-in thermography are layer thickness, reflection coefficient and porosity determination. A layer thickness investigation is also carried out by PPT. The Decay Time Analysis (DTA) is used for this, in which a temporal averaging and a median filter smoothes the respective pixel time curve and eliminates outliers. A pulse-phase evaluation provides a better signal-to-noise ratio, but the layer thickness is not clearly linked to the phase value. With the DTA curve, the signal increases as the layer thickness increases, making it easy to determine the layer thickness. (Gleiter 2011)

To achieve a complete quantitative thermography evaluation, the measurement uncertainty of the system has to be known. This problem is addressed in a study by (Minkina, Duzik & Gryś 2010), examining components with high temperature and emissivity as well as objects with low temperature and emissivity. It is pointed out that at high tem-

peratures and emissivity, the greatest influence on the error in temperature measurement is due to the error associated with emissivity. In the other case, the ambient temperature and emissivity have the greatest influence. (Minkina, Duzik & Gryś 2010)

In the study by (Dudzik & Minkina 2008), standard uncertainty of thermography is attributed one of the greatest importance. The accuracy of the measurement method is determined with help of an acquisition interval. The following input variables are available for the Monte Carlo simulation used: Object emissivity, atmosphere temperature, ambient temperature, relative humidity, distance between infrared camera and object. The standard uncertainty increases with decreasing emissivity value. The assumption of the factor $k = 2$ for a 95 % confidence interval can be assumed as certain. The study confirms the results of (Minkina & Dudzik 2006). (Dudzik & Minkina 2008)

Accuracy determination also plays a role in (Ekanayake, Gurram & Schmitt 2018), examining a CFRP sample with blind holes of different size and depth. Lock-in Themography is used for the examination. A method to determine thermal properties and defect depth based on the complex wave field is presented. The focus is on minimized lateral heat flow and taking the contact resistances into account, which could be identified as significant factors influencing the accuracy of depth measurement. It is shown that the developed method shows a deviation of less than 0.5 mm in depth determination over a wide thickness range and blind hole diameter. The influence of contact resistance on repeatability, bias and linearity is less than the influence of lateral heat flow. (Ekanayake, Gurram & Schmitt 2018)

(Ekanayake, Isenberg & Schmitt 2017) also deals with the quantitative evaluation of 3D defect geometries analysis. The basis is a stack of thermographic images with different excitation frequencies in lock-in thermography, providing information about defect depth through the phase value. The analysis is performed on a sample with blind holes. The defect is extracted from each phase image and mapped into a 3D defect model. Four steps are carried out: Preprocessing, feature extraction, image analysis and depth calculation. With this method it is possible to show the 3D geometry of a defect from thermographic images. The correlation between excitation frequency, defect size in the thermal image and actual defect size are examined and compared with calibrated values. The next step is to further develop contour detection and algorithms for damage area detection. (Ekanayake, Isenberg & Schmitt 2017)

3.3.2 Evaluation of Existing Approaches

Table 3-5: Evaluation of existing approaches for multi-sensor systems in lightweight construction

evaluation unit

- ● completely fulfilled
- ◐ nearly fulfilled
- ◑ partly fulfilled
- ◔ barely fulfilled
- ○ not fulfilled
- □ no statement possible

concepts	Reference	Fast and intuitive evaluation	Determination of measurement uncertainty	Quantitative evaluation of internal defects	Characteristic features for defect identification	Depth analysis of the internal defects	3D image structure
Thermography and eddy current	(Gros, Bousigue & Takahashi 1998)	◐	○	◔			○
Laser light section and camera system	(Schmitt et al. 2008; Schmitt et al. 2015; Mersmann 2012; Brabandt 2018)	◐	◑	○		○	◔
Laser light section with ultrasound and thermography	(Schmitt, Ekanayake & Nienheysen 2018; Hopmann et al. 2017; Losch et al. 2016)	◑		◑			◑
Computer tomography, dark-field X-ray hyperspectral imaging, thermography and ultrasound	(Effenberger 2016a; Effenberger 2016b; Holstein et al. 2015)	◔			○		◔
Thermography Data Fusion	(Soldan 2014)	◐		◔	◔	○	◔
Dimensional Measurement	(Galovska, Petz & Tutsch 2012; Weckenmann et al. 2009; Mohammadikaji et al. 2016; Schulze et al. 2011)	◐	◔				
Optical multi-sensor measuring method	(Bernstein 2011)	◐	◑				

Table 3-5 and Table 3-6 show the evaluation of approaches presented in Chapters 3.3.1 with regard to the requirements of a multi-sensor system with data fusion evaluation and the evaluation of the thermographic investigations.

Table 3-6: Evaluation of existing approaches for thermographic evaluations

evaluation unit	
● completely fulfilled	◔ barely fulfilled
◑ nearly fulfilled	○ not fulfilled
◐ partly fulfilled	□ no statement possible

concepts	Reference	Fast and intuitive evaluation	Determination of measurement uncertainty	Quantitative evaluation of internal defects	Characteristic features for defect identification	Depth analysis of the internal defects	3D image structure
Resolution limits in lock-in thermography	(Myrach et al. 2014)			◐		◐	
Comparison between lock-in and pulse phase thermography	(Maierhofer et al. 2014)	◐		◐		◔	
Phase difference in pulse-phase thermography	(Chiwu et al. 2014; Ishikawa et al. 2013)			◐		◐	
Lock-in Thermography	(Hornfeck et al. 2015)	◔		◐		◐	
Phase contrast in lock-in thermography	(Wallbrink, Wade & Jones 2007)			◐		◐	
Rectangular pulse spectral thermography with characteristic frequency	(Arndt 2007)	◐		◐		◐	
Signal-to-noise ratio in lock-in thermography and fusion of optical lock-in and ultrasound induced thermography	(Zöcke et al. 2007; Zöcke 2010)			◐	◔	◐	
Pulse-phase thermography with blind frequency	(Ibarra Castanedo 2005)	◐	◔	◐		◐	◔
Pulse-phase thermography with complex thermal wave field	(Gleiter 2011)			◐		◐	
Lock-in thermography with complex thermal wave field	(Ekanayake, Gurram & Schmitt 2018)	◐		◐		◐	
Curved components	(Mayr et al. 2008; Ibarra Castanedo 2005)			◐		◔	◔
Stack picture with lock-in thermography	(Mayr et al. 2008; Gleiter 2011; Ekanayake, Isenberg & Schmitt 2017)			◐		◐	◐
Thermography in general	(Ekanayake, Gurram & Schmitt 2018; Minkina & Dudzik 2006; Dudzik & Minkina 2008)	◔	◐				
Further approach	(Lahiri et al. 2012; Liu et al. 2015; Dudzik 2010)			◔		◔	

3.4 Deficit in Research

After showing the approaches for quality assurance of external and internal defects in CoDiCo-SMC, it becomes clear that a single system is not sufficient. Therefore, two systems have to be integrated in a multi-sensor system. Laser light section and thermography are chosen for this purpose.

Several requirements are set up for this multi-sensor system. The focus is on a fast and clear evaluation for the user, in order to make a statement about the components condition within a short time. Table 3-5 and Table 3-6 depict that there are already multi-sensor systems for lightweight construction applications fulfilling this requirement. Nevertheless, there is no focus on evaluation of external and internal defects, but rather an exact measurement of defined criteria, such as the fiber angle or the shape. Furthermore, demonstrators are used mostly for one criterion only. Determination of measurement uncertainty lacks in most works, as it is only determined for a few systems and is not available for a system consisting of laser light section and thermography. Thus, the aim of the present thesis is to set up a multi-sensor system, which examines the external and internal defects using a demonstrator component made of CoDiCo-SMC. The system provides the user with a fast result and can evaluate this on the basis of the determined measurement uncertainty of the system.

Furthermore, the state of the art shows that thermography offers great potential for quantitative evaluation. It is proven that depth information can be given, depending on the material. Thus, the depths and areas of defects are determined for the existing material and a defined layer structure. For easy evaluation, a 3D visualization of the component and the thermographic results has to be available. The present investigations deal in simple approaches with a 3D representation, but mostly with the use of lock-in thermography. Thus, a further goal of this work is to extend the established multi-sensor system with a depth evaluation and 3D analysis of CoDiCo-SMC components. A defect characterization is not investigated in any of the research work, which is why a characterization for selected defects on CoDiCo-SMC materials is carried out with help of thermography.

4 Solution Approach

In order to achieve the objectives described in Chapter 1.2 and to solve the research deficit described in Chapter 3.4, a solution approach is presented in this chapter. It is segmented to three parts, as illustrated in Figure 4-1.

First Part – Defects and their Effects on the Mechanical Properties

To answer the first research questions, the used CoDiCo-SMC has to be examined in detail, especially regarding possible defects occurring during the production steps stacking and pressing. These critical defects are evaluated to obtain their effects on the mechanical properties. In this first part, represented by chapter 5, also the basis for all subsequent investigations is set.

Second Part – Methods to Detect and Characterize the Critical Defects

As shown in chapter 3, to perform quality assuring measurements on the new hybrid material CoDiCo-SMC in both semi-finished and cured state, different systems are required. Thus, a method to detect external defects plus another method to detect internal defects have to be selected and described in the second part. This also includes the determination of optimum parameters for a defined test object and a measurement uncertainty analysis.

Chapter 6 describes the laser light section system, for which no measurement uncertainty analysis method is available so far. Thus, such a method has to be developed and carried out exemplarily.

Due to given premises, the second system has to be integrated into the portal, already used by the first system. Hence, the portal interfaces have to be investigated in detail, supporting the selection of pulse-phase thermography. This method, including its more comprehensive investigations are described in chapter 7. To provide detailed information about internal defects, their depth has to be determined. As a method doing so is not available so far, it has to be developed.

Third Part – Implementation of a Holistic Measurement System

To obtain a holistic view and thus enable quality assurance for a complete part, the two methods have to be combined to a multi-sensor system in the third part, represented by chapter 8. This also requires to fuse the obtained data, in order to ensure a user-friendly system operation. As an exemplary representation, the layer model is developed. Similar to the single system, the measurement uncertainty is also determined for the multi-sensor system.

5 | Defects and their Effects

- Used Material
- Layer Structure and Test Objects

- Defect Identification and Selection
- Effects of Defects

6 | Laser Light Section System

- Parameter for Laser Light Section System
- Laser Light Section System Measurement Uncertainty

7 | Active Thermography

- Portal Interfaces
- Selection of suitable Active Thermography
- Parameter for Pulse-Phase Thermography
- In-depth Analysis
- Characterization of Defects
- Pulse-Phase Thermography Measurement Uncertainty

8 | Multi-sensor System

- Design of the Multi-Sensor System
- Data Fusion

- Added Value and Data Fusion Layer Model
- Data Fusion Measurement Uncertainty

Figure 4-1: Structure of the own approach

5 Defects and their Effects

This chapter describes the used material and explains it in more detail. Subsequently, an overview of the layer structure used in this thesis is presented. This is followed by an outline of the possible defects occurring during and after the manufacturing process and a classification into categories. Finally, the possible defects are limited and evaluated in order to show their effects and to explain the selection.

5.1 Used Material

The used material developed at ICT is described in Chapter 3.1.1. The DiCo-SMC (see Table 3-1) is used for all of present investigations. This material is referred as DiCo-SMC in the following. This material is always reinforced with glass fibers.

The semi-finished Co-SMC of the ICT can only be used in this thesis for a few test objects because it has to be further processed within one hour and is therefore not practicable for own tests. Thus, the continuous carbon fiber prepreg is replaced in most tests by the material UDCarbon 24/60 12 K 1090 from Polynt Composites Germany GmbH. This material consists of vinyl ester resin with 60 wt % continuous carbon fibers (Polynt Composites Germany GmbH 2016) and is recommended to be used by ICT. A material datasheet is provided in Appendix A 5. This material can also be assigned to a SMC and is therefore referred as Co-SMC in the following because the carbon fibers are continuously there. The use of the material from Polynt is indicated in the appropriate place. All tests on the semi-finished product are carried out with the material from Polynt and are rarely used even for finished components.

5.2 Layer Structure of used Material

In principle, two different layer structures are used in this thesis differing regarding thickness of the test object. The Co-SMC layer in both cases is placed between DiCo-SMC layers. The thickness is only varied by the number of DiCo-SMCs. The two layer structures are illustrated in Figure 5-1.
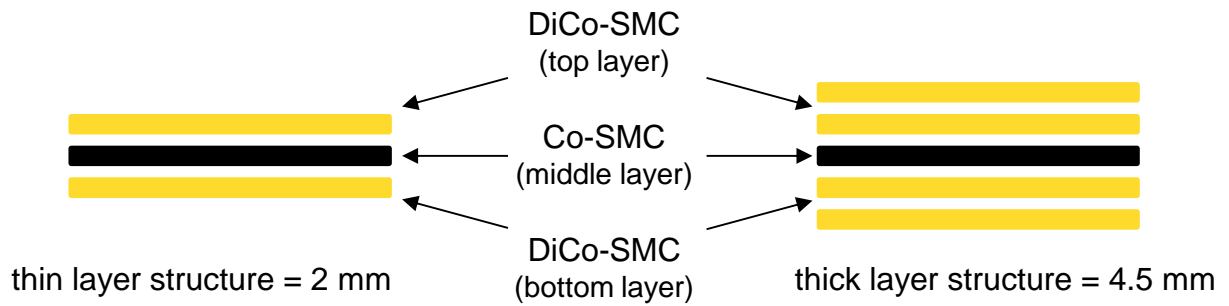
Figure 5-1: Layer structure of thin (left) and thick (right) test objects

In exceptional and noted cases, the Co-SMC is attached on the surface to investigate its optical properties.

5.3 Used Test Objects

The investigations of the present work are carried out on basis of different test objects. The two most important, as mostly used, demonstrators are briefly described below.

5.3.1 IRTG Demonstrator

Within the IRTG projects framework, a demonstrator with the external dimensions 230 mm x 180 mm x 18 mm is developed. The short side's slopes have an angle of 135° to the lower plane. The slops on the long sides have an angle of 120° on one side and 140° on the other side (A_Schwende 2017). These different slopes allow an investigation in the present thesis, whereby the demonstrator fulfils the necessary requirements. Figure 5-2 illustrates the geometry.
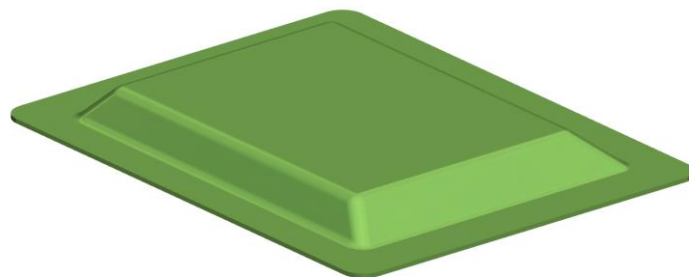
Figure 5-2: IRTG demonstrator according to (A_Schwende 2017)

The IRTG demonstrator's technical drawings are depicted in Appendix A 6.

5.3.2 Small Demonstrator

The other test object is similar to the IRTG demonstrator, but reduced in its outer dimensions. This enables measurements with CT, as there are restrictions regarding the part dimensions. Thus, this small demonstrator has the external dimensions 94 mm x 120 mm°x°18 mm, but the same slopes as the IRTG demonstrator. The small demonstrator is depicted in Figure 5-3. (A_Schwende 2017)

Figure 5-3: Small demonstrator according to (A_Schwende 2017)

A technical drawing of the component is provided in Appendix A 7.

5.4 Defect Identification and Selection

In order to develop a suitable measuring and testing system for the material described in Chapter 3.1.1 and 5.1, the possible defects have to be identified, selected and limited in the first step. In the second step, the selected defects are explained in more detail and divided into categories.

5.4.1 Selection of Relevant Defects

Figure 5-4 depicts possible defects, occurring for each individual production step. The individual production steps can be seen in the background of the figure (cf. Chapter 3.1.2). An example is resin accumulation or air inclusion in production of semi-finished products. Another example is the penetration of foreign body, such as foil or impurities, into the material. This defect happens directly before inserting the material in press. A short description of the most common defects is provided in Appendix A 3.
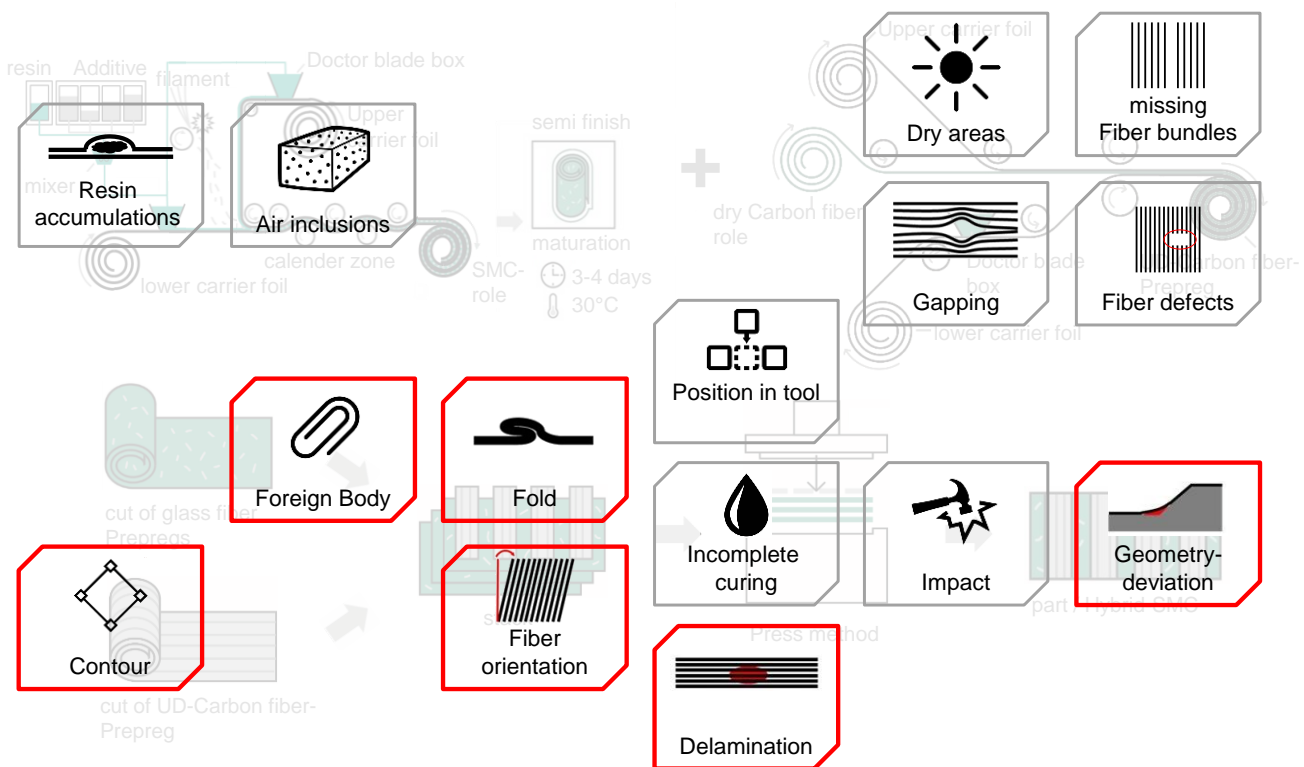
Figure 5-4: Origin of the defects in the different manufacturing steps (Defect-image according to (Egloff 2017))

In order to cover a wide range of investigated defects, but to reduce the number of possible defects to a reasonable number, the following assumptions are made:

- The semi-finished material is supplied in a flawless condition. Thus, the production of the semi-finished material is excluded and defects such as air inclusions or missing fiber bundles are not considered.
- Due to 100 % inlay of material in the mold, displacement can be prevented. Thereby, the position in the mold does not matter.
- Test object manufacturing and parameter controlling prevents incomplete curing of test objects.
- Subsequent test object handling avoids impact damage.

On the basis of these assumptions, it is possible to focus on an essential production step and the possible defects are limited to: Contour of Co-SMC, foreign body, fold, fiber orientation, delamination and geometrical deviation of whole test object. These six defects are selected for further evaluation in the thesis at hand and therefore form the basis for following analyzes.

5.4.2 Description of the Selected Defects

Delaminations, as occurring in reality, cannot be reproduced for examination, as the processes leading to this defect are too complex. However, they can be simulated with foils, separating the layers. As this foil is also a foreign body, the defects foreign body and delamination are handled as one defect (orange frame in Figure 5-5).

Contour errors in the investigated material always refer to Co-SMC. Furthermore, the fiber orientation, which also refers to Co-SMC, is investigated. Thus, the contour and orientation can be analyzed with one method and is therefore summarized in this thesis (blue frame in Figure 5-5).

The two remaining defects fold and geometrical deviation of cured test objects have to be analyzed separately. As described in Chapter 1.1 it is necessary to avoid value adding process steps to later scrap parts. Therefore, the described defects are examined in semi-finished material and cured test objects.

The selected defects can be divided into external and internal defects as depicted in Figure 5-5. The fold can arise both inside and on the surface and is therefore allocated to both categories.
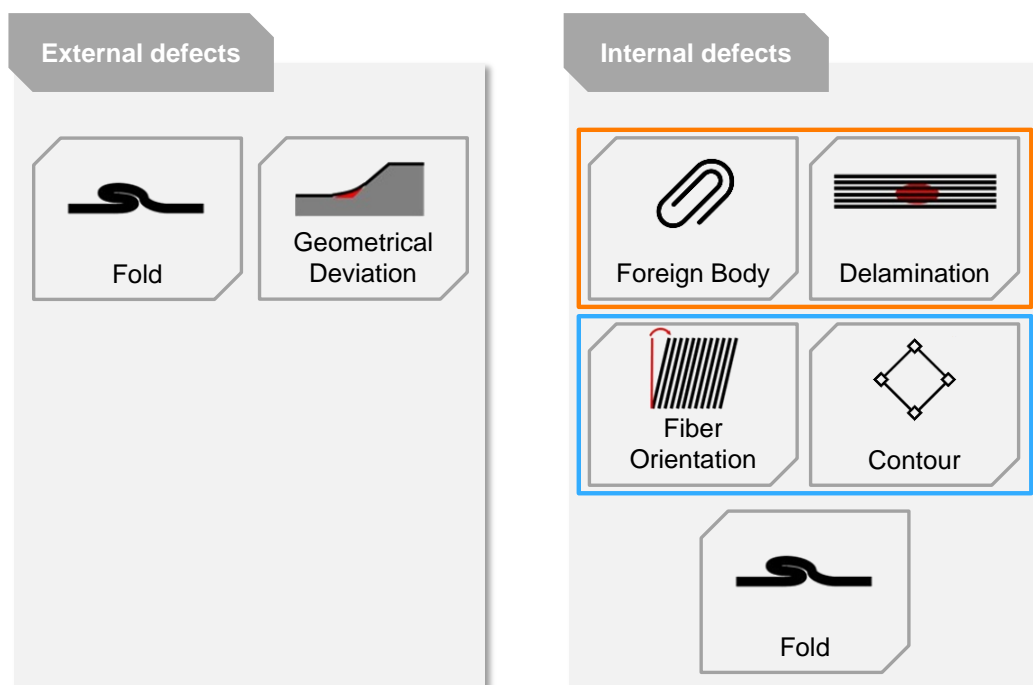
Figure 5-5: Defects to be examined in this work, as well as their division into external and internal defects (defect-image according to (Egloff 2017))

Thus the first research question (cf. Chapter 1.2) can be answered, which critical defects have to be examined in CoDiCo-SMC.

5.5 Mechanical Properties of Defective Components

The presented defects reduce the components mechanical properties. The "Effect of Defect" (EoD) is always determined if a tolerable defect size is to be defined or if permissible limit values are exceeded in NDT. (Oster 2012)

By determining EoD it is possible to define kinds of defects, size and position which NDT methods have to detect in order to be able to make statements about the effects. For this reason, the selected defects in Chapter 5.4 have to be inserted into the test objects to measure their effects on the mechanical properties. This investigation proves the necessity of quality assurance methods without claiming to analyze the different defects regarding size and position. Two series of tests are carried out in order to obtain an estimation as complete as possible.

5.5.1 First Test Series

The test objects layer structure for the first series consists of glass fiber SMC, carbon fiber SMC and glass fiber SMC (cf. Figure 5-1 left), all produced at ICT. This tests series investigates the following defects (A_Sadic 2017):

- Fold (Co-SMC folded without more detailed specification)
- Foreign Body (foil as foreign body without size specification in specimen middle, also represents delamination)
- Angular Deviation (5°, 10°, 15°)

The fold is placed in Co-SMC in the middle of the specimen by folding the material. The foil as a foreign body is located on one side of the Co-SMC. The angular deviation is achieved by cutting test objects at different angles from plates. These tensile specimens have a size of 20 mm x 210 mm and are cut out by using water jet cutting (A_Sadic 2017). The test is carried out with the Zmart.Pro universal testing machine from Zwick-Roell, featuring a load cell capacity of 200 kN. The nominal loading rate is 2 mm min^{-1}. The initial measuring length equals 60 mm. (A_Sadic 2017)

The following Table 5-1 depicts the number of tensile specimens pulled in the first test series as well as the number of centrally fractured specimens, which is required for determination of tensile strength. All specimens of a plate were either tested or until at least four specimens were broken in the middle. Due to the angle, the plate with the angular deviation has a smaller number of samples. The resulting evaluation, including Young's modulus and standard deviation, is illustrated in Figure 5-6.

Table 5-1: Number of tensile tests (A_Sadic 2017)

	Number of specimens	Number of centrally fractured specimens
Reference	22	9
Fold	13	9
Foreign Body (foil)	22	4
Angle 5°	13	3
Angle 10°	16	4
Angle 15°	10	4
Total	96	33
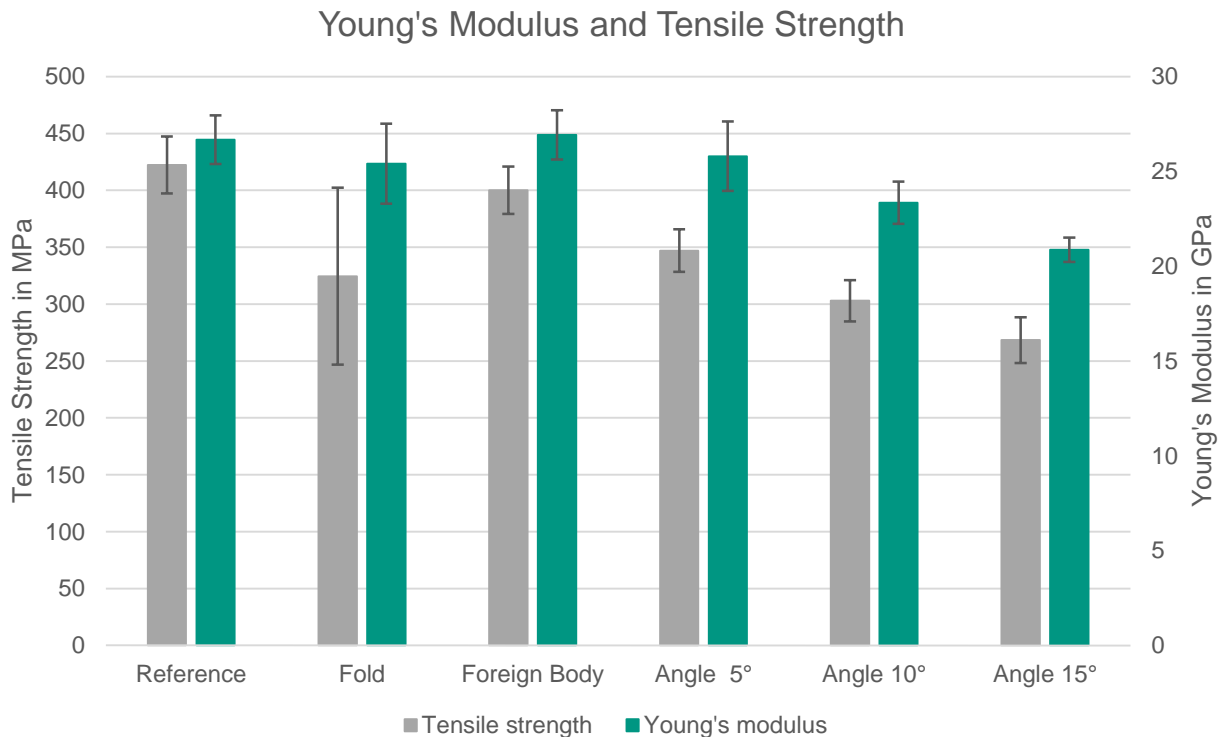
Figure 5-6: Evaluation of Young's modulus and tensile strength of first test series

As result, all investigated defects have a negative effect on tensile strength. The fold has a major influence with a reduction of the tensile strength by 23.15 % in relation to the reference test specimen. However, the large standard deviation of ± 77.76 MPa is conspicuous and has to be observed. The stiffness of test specimens with foreign body is 0.95 % higher in its mean value than the reference test specimens, but also in this case the standard deviation has to be considered. The mechanical impact of angular

deviation strongly depends on the angle. It can be expected that the proven reduction further increases by scaling up the angle.

The following Table 5-2 gives an overview of the determined average values. In the case of defects, the percentage rate of change of the respective characteristic values in relation to the reference value is also given in parentheses. (A_Sadic 2017)

Table 5-2: Overview of mechanical properties according to (A_Sadic 2017)

	Average Young's modulus in GPa (difference in %)	Average Tensile Strength in MPa (difference in %)
Reference	26.67	422.29
Fold	25.4 (-4.77 %)	324.51 (-23.15 %)
Foreign Body (foil)	26.93 (+0.95 %)	400.12 (-5.25 %)
Angle 5°	25.8 (-3.28 %)	347.05 (-17.83 %)
Angle 10°	23.35 (-12.47 %)	303.03 (-28.24 %)
Angle 15°	20.86 (-21.79 %)	268.4 (-36.44 %)

5.5.2 Second Test Series

To address these ambiguous results, a second tests series with precisely defined defects is carried out validating the first results. Layer structure remains like in first series, only the Co-SMC is changed to UDCarbon 24/60 12 K 1090 from Polynt Composites Germany GmbH. This tests series investigates the following, more detailed defects:

- Fold (Co-SMC folded, 10 mm)
- Foreign Body (Foil as foreign body, 20 mm wide)
- Angular Deviation (5°, 10°, 15°, 90°)

In order to illustrate the defects fold and foreign body, these are presented schematically in Figure 5-7.
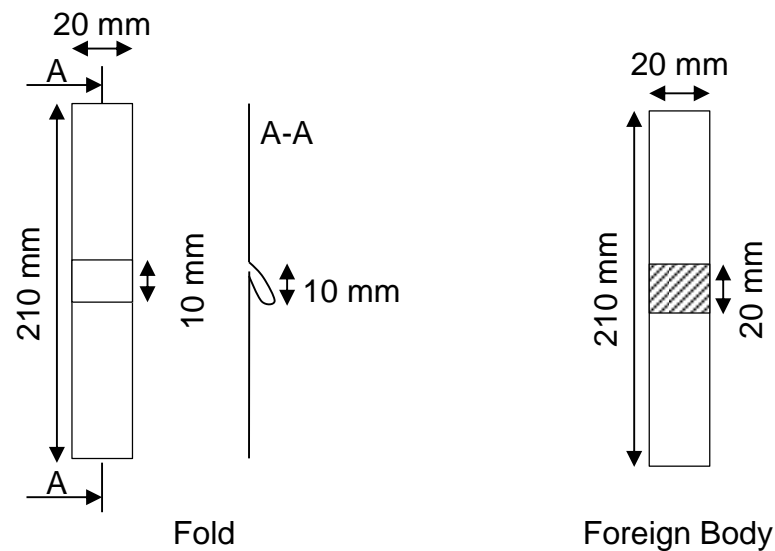
Figure 5-7: Schematic illustration of the defect fold (left) and foreign body (right)

The tests were performed by Dr. Michael Thompson in the Department of Chemical Engineering at McMaster University in Hamilton, Canada using the MTS Criterion® Universal Test Systems, with a load cell capacity of 50 kN and a nominal loading rate of 10 mm min^{-1}. As a restriction, only the tensile strength can be evaluated with this device, but not the Young's modulus. Table 5-3 provides an overview of the values of the second test series and the change rate in relation to the reference test specimens.

Table 5-3: Overview of the tensile strength of the second test series

	Number of test parts	Average Tensile Strength in MPa (difference in %)
Reference	18	401.1
Fold	24	124.9 (-68.86 %)
Foreign Body (foil)	14	363.1 (-0.48 %)
Angle 5°	12	273.6 (-31.78 %)
Angle 10°	10	220.8 (-44.96 %)
Angle 15°	6	191.3 (-52.31 %)
Angle 90°	8	99.8 (-75.11 %)

Mean values and standard deviations are illustrated in Figure 5-8.
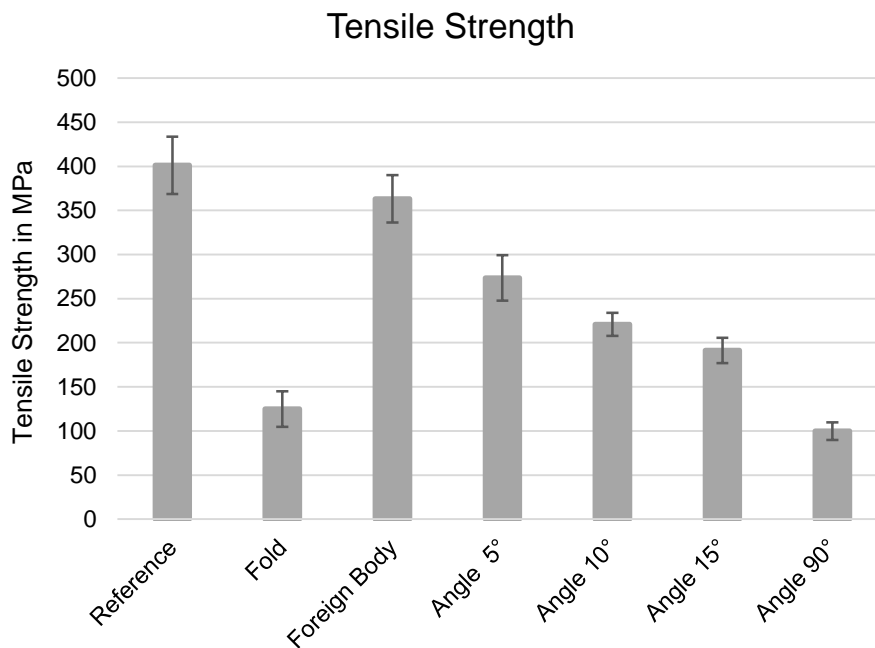
Tensile Strength

Figure 5-8: Evaluation of tensile strength of second test series

The obtained results from the second test series confirm and refine those of the first series. The folds influence is clearly shown in comparison to the first series, where the large standard deviation presumably results from undefined defect geometry. Also for foreign body, the impact on mechanical properties is made clear. In the first series the undefined defect size in average was too small to achieve an expressive result. The result of the angular deviation is simply confirmed. The deviation of the values can be traced to the other used Co-SMC.

Both test series prove, that the selected defects lead to a reduction of mechanical properties. In order to avoid unnecessary value-adding production steps, defects have to be detected early in the production process. As described in Chapter 5.4.2, these selected defects are internal as well as external and have to be detected in semi-finished as well as cured state. Referring to Chapter 3.4, this requires a multi-sensor system that reliably detects the different defects early in the process. With this chapter, the Effects of Defects on the mechanical properties are described and thus the second research question (cf. Chapter 1.2) can be answered.

As shown in Chapter 3.2.2 and confirmed by experiments (Zaiß et al. 2017a), the methods laser light section and active thermography selected in the interim conclusion are suitable for quality assurance of the investigated material. Both methods are described in more detail in the following chapters.

6 Laser Light Section System

In this chapter, a parameter analysis for evaluating CoDiCo-SMC with the laser light section system (LLSS), as displayed in Figure 6-1, is performed. Afterwards, the measurement uncertainty of this system is determined.
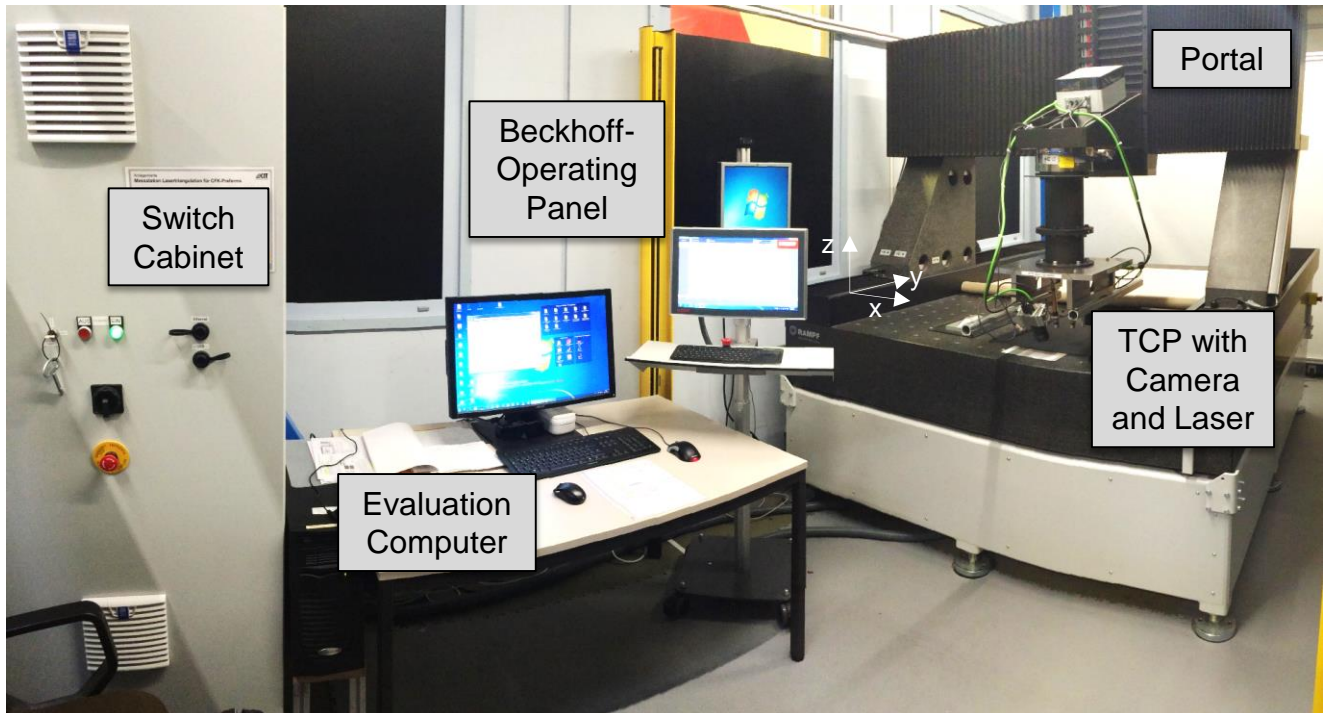
Figure 6-1: Design of the LLSS according to (Brabandt 2018; A_Demmerle 2016)

All LLSS components are explained in more detail in Appendix A 8 and the LLSS Data Processing in Appendix A 9.

6.1 Parameter for LLSS

As optical reflection is material dependent, the variable parameters of LLSS have to be determined and adapted accordingly. For this purpose, the calibration of the LLSS is explained in more detail and an overview of the adjustable parameters is given. Afterwards the description of the fixed parameters follows. Finally, the variable parameters for the CoDiCo-SMC are determined, in both semi-finished and cured state.

6.1.1 Calibration of LLSS

In order to achieve optimum geometry results with the aid of the LLSS, the system has to be calibrated in advance. A differentiation is made between the camera setting and the laser setting. The laser setting involves the correct alignment of the laser line as well as the width and sharpness of the laser line with a reference line. Subsequently,

the focusing of the camera is set correctly. The calibration is carried out with a calibration body, which consists of a defined material, is fixed to the portal and can be scanned with one path. This calibration body is illustrated in Figure 6-2. (A_Oergele 2017)
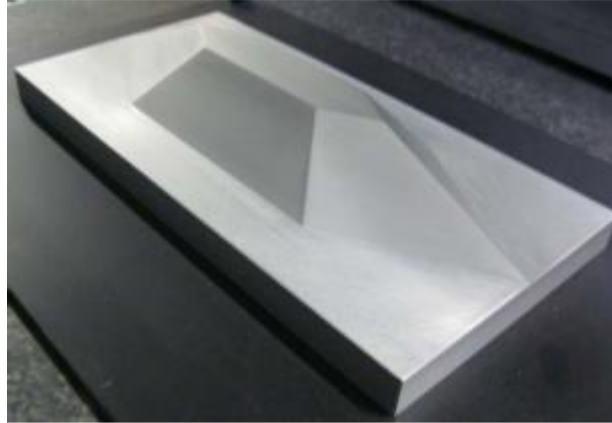
Figure 6-2: Calibration body for the LLSS (A_Oergele 2017)

An exact geometry of the calibration body is stored in a software program, serving as a reference. It is used to calculate the metrically correct, three-dimensional CoP and to store the conversion factors for scanning unknown geometries in the system. Calibration is performed individually for each set of LLSS. As soon as a modification is made to the system, a new calibration has to be carried out. (A_Oergele 2017)

6.1.2 Overview of the Adjustable Parameters of the LLSS

Table 6-1 lists all adjustable parameters according to (Brabandt 2018) and thus gives an overview. A distinction is made between the portal and the LLSS.

The large number of variable parameters leads to a number of possible combinations that cannot be fully investigated. Thus, recommendations from system providers, findings from (Brabandt 2018) and preliminary tests are used and described in the following chapters.

Table 6-1: Overview of parameters according to (Brabandt 2018)

	Adjustable parameters	Unit
Portal	trigger interval	μm
	traverse speed	mm/min
	path distance	mm

Continuation on the next page

	Adjustable Parameters	Unit
LLSS	camera	
	• screen	-
	• exposure time	µs
	• focus point	-
	• slope mode	-
	• threshold	-
	• type of 3D camera algorithm (e.g. COG)	-
	• f-number	-
	laser	
	• laser intensity	V
	• exposure time	µs
	• focus point	-
	configuration	
	• geometric arrangement	-
	• camera angle α	°
	• laser angle β	°
	• triangulation angle φ	°
	• lateral tilting (side panel angle 0°, 5°, 10°, 15°) γ	°

6.1.3 Fixed Parameters of LLSS

The arrangement "Specular" and "Look-away" (see Figure A-3) are identified as suitable geometric arrangements. However, the "Specular" arrangement shows clear deficits with regard to shading on strongly curved surfaces. Therefore, the "look-away" arrangement is used for all tests.

Further shading effects are to be avoided by the lateral tilting. Thereby it is shown that with a tilting of γ = 15° the quality of the image decreases strongly. Preliminary tests indicate that a tilting of γ = 5° is favorable and is therefore kept constant throughout all tests. (Brabandt 2018; A_Pohlmann 2017)

Depending on the size of the component, several scans over the component at different path distances are necessary. However, the path distance is not taken into account in the parameter selection. A suitable scanning speed is defined with 500 mm/min and an alternating trigger distance of 50 µm (A_Pohlmann 2017; Brabandt 2018).

The system supplier recommends $k_{Cam} = 5.6$ for f-number, representing an optimum with regard to aberration blur and diffraction blur. Therefore, this value is kept constant in all tests. The working distance of the objective is fixed at 250 mm. (Brabandt 2018)

Due to different reflection behavior, it is possible to completely saturate pixels during an exposure. The Multi Slope Function of the camera checks the pixels saturation at defined times during exposure time and resets it to the limit level if exceeding the saturation limit. The Triple Slope Mode, in which saturation is reset twice, first time after 60 % and second time after 90 % of exposure time, is used in this thesis. (A_Pohlmann 2017)

Furthermore, the cameras can be operated in different modes. A saturation threshold has to be defined for each mode. If this is reached, a pixel is included in the image processing. In the Center of Gravity Mode (COG) the center of gravity of the surface is determined, defined by the threshold value and the intensity distribution. This mode is considered to be the most precise and therefore it also provides the most accurate results and is used for all measurements in this thesis. (A_Pohlmann 2017)

Both cameras and lasers of the two used LLSS sets have to be focused on one focus point in order to minimize blurs at local height differences of the geometry. For this purpose, both systems are focused on the same point. (Brabandt 2018)

6.1.4 Variable Parameters of LLSS

The variable parameters are experimentally determined. For this purpose, the test objects and the evaluation criteria are presented. Subsequently, the experiments and their results are described in more detail in order to define the optimum parameters for the material and test object at hand.

6.1.4.1 Test Objects for Parameter Analysis

The demonstrator developed in the IRTG project (cf. Chapter 5.3.1), illustrated in Figure 6-3 on the right, is used to determine the suitable parameters. The semi-finished material is applied to a carrier body, representing the IRTG demonstrators mold shape, see Figure 6-3 on the left. The attached plastic balls serve as a reference for the alignment in CAD comparison.

Figure 6-4 on the left depicts the semi-finished material on the carrier body with the usually used Co-SMC from Polynt Composites Germany GmbH. The right side illustrates the cured test object. It consists of two layers DiCo-SMC with the Co-SMC as an exception produced at ICT. For both test objects, the Co-SMC is attached to the surface.
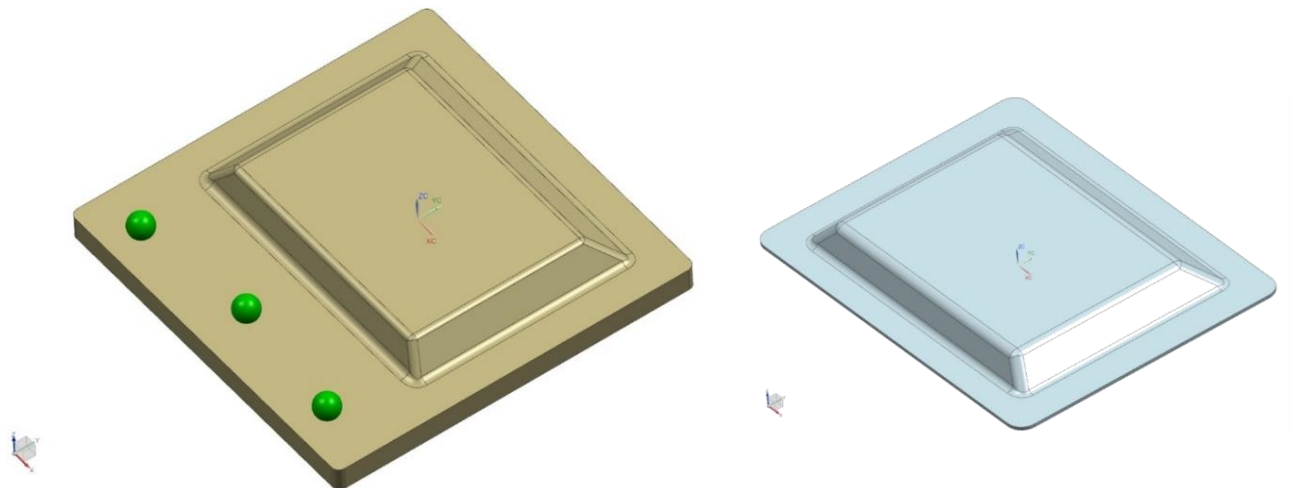
Figure 6-3: 3D model of the carrier body (left) and IRTG demonstrator (right) (A_Pohlmann 2017)
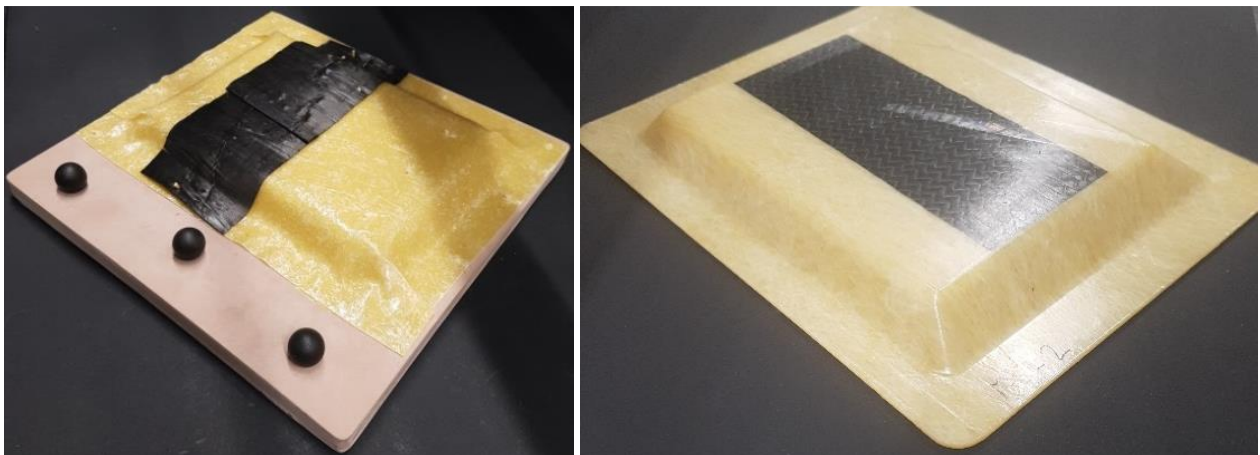
Figure 6-4: Semi-finished test object (left) and cured test object (right) (A_Pohlmann 2017)

6.1.4.2 Evaluation Criteria and Experimental Design

For evaluating the parameter combinations, the four following, equally weighted criteria are defined. The subsequent Table 6-2 lists the criteria's "Quality of CoP" and "CAD Comparison" values (A_Pohlmann 2017). The attributes listed in Table 6-2 are evaluated by a visual analysis of the operator.

- **Quality of the CoP:** The geometric elements planes, front and rear slope, balls and edges are detected error-free in one measuring path, meaning there are no outliers, artifacts or voids. The lateral slopes are partly located outside the sharpness range, as no height tracking is possible at the given scan path.

- **CAD Comparison:** Comparing measured geometry and CAD model offers the possibility to recognize deviations of individual geometric elements. The criterion is the deviation of these two geometries, aligned by the referring balls.
- **Laser Penetration Depth:** The laser beam penetration results in a measurement uncertainty, which cannot completely be evaluated. The depth is determined at the line between Co-SMC and DiCo-SMC by a section through the test object.
- **NaN Content:** The content of undetected areas (Not-a-Number = NaN) should be as low as possible to ensure a reliable defect detection. NaN is determined over the complete geometry's evaluation using the MATLAB® tool MapAnalyse-GUI.

Table 6-2: Evaluation scale for quality of CoP according to (A_Pohlmann 2017)

Evaluation	Attribute of the quality of the CoP
1	no artifacts and outliers; balls are well detected; geometric elements uniformly well detected
2	no artifacts and outliers; balls are well detected; geometric elements outside the depth of field not well detected
3	scattered artifacts and outliers; point density of the balls decreases; geometric elements outside the depth of field area are more difficult detected
4	more artifacts and outliers; point density of balls low; also geometry elements in the depth of field area poorly recognized
5	increased artefacts and outliers; balls rarely recognizable; Poor recognition of all geometric elements

Table 6-3: Evaluation scale for CAD comparison according to (A_Pohlmann 2017)

Evaluation	Attribute of the CAD comparison
1	deviations predominantly in the green range
2	deviations from roundings; other areas predominantly green
3	deviations from roundings; scattered spots in the yellow/blue area
4	deviations from roundings; increased yellow/blue deviations
5	strong deviations over the entire test object

6.1.4.3 Experiments for Parameter Analysis

As parameters are kept constant on basis of empirical values, manufacturing information and preliminary tests, the tests for optimum parameter determination are based on the variation of exposure time, laser intensity and threshold. This parameters can be changed without recalibration of the LLSS (A_Oergele 2017). The threshold represents a level value influencing the noise of the measured values significantly. According to (Brabandt 2018) a value of 150 should not be undercut.

Furthermore, (A_Pohlmann 2017) is able to prove that the laser beam penetrates the used material due to its low filler density, making the penetration depth of the laser beam a further factor, especially for the used material. Consequently, a suitable laser angle has to be identified. Investigations show that a flat incident angle of the laser beam leads to the lowest penetration depth at a plane. Thus, the initial aim is to achieve the largest possible laser angle with the limitation of scanning the complete calibration body in one path. Therefore, the maximum laser angle is $\beta = 10°$ and the camera angle $\alpha = 40°$ with a resulting constant triangulation angle $\varphi = 30°$. (A_Pohlmann 2017)

On basis of preliminary tests (A_Oergele 2017), test plans (cf. Table A-1 and Table A-2 in Appendix A 10) are developed for semi-finished and cured test objects, including the mentioned parameters exposure time, laser intensity and threshold.

Results for the Semi-Finished Test Object

The results are displayed in Table 6-4 and figures for the semi-finished test object can be found in Appendix A 11.

Table 6-4: Results for the semi-finished test object according to (A_Pohlmann 2017)

Parameters		First tests				Additional tests			
Threshold		600		800		600			
Exposure time [µs]		900				600		1200	
Laser intensity [V]	2.5	4	0.89	5	0.707				
		4	42.92	4	68.39				
	3.5	2	1.139	4	0.879	4	0.979	2	1.197
		2	9.23	3	33.81	4	48.08	2	3.32

top left	Quality of the CoP (scale 1-5)
top right	Laser penetration depth (in mm)
bottom left	CAD comparison (scale 1-5)
bottom right	NaN content (in %)

The following trends are observed for the semi-finished product: With low laser intensity, the NaN content increases, but the penetration depth of the laser decreases. An increasing laser intensity improves the quality of the CoP. However, it can be observed that artifacts occur at the steep slope with 120°. This may arise due to the clearly different angular relationships between surface, laser and camera. A threshold of 600 is considered optimal because a higher value does not give better results. The last parameter, the exposure time, also affects the number of NaNs. The NaN increases with lower exposure time. Increasing the exposure time leads to a slight increase in penetration depth, but reduces the NaN content from 9.23 % to 3.32 % and the lateral slopes are better captured. The determined parameters for the semi-finished product are a threshold of 600, an exposure time of 1200 µs, and a laser intensity of 3.5 V. This is also marked in Table A-1. Figure 6-5 depicts CoP and CAD comparison with these parameters.
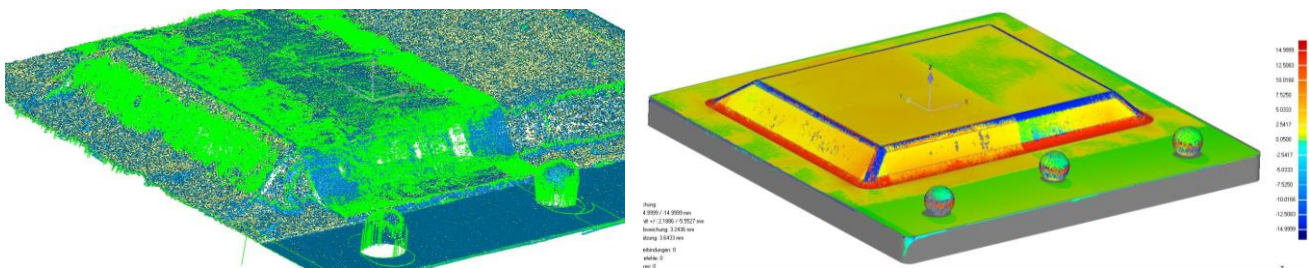
Figure 6-5: CoP (left) and CAD comparison (right) with optimum parameters for the semi-finished product (A_Pohlmann 2017)

It is noticeable that deviations occur at the roundings during the CAD comparison. The noticeable deviations, occurring at roundings, cannot be prevented with any parameter combination in this thesis.

Results for the Cured Test Object

The results are listed in Table 6-5 and figures of tests are illustrated in Appendix A 12.

The occurring tendencies in semi-finished test object can be transferred to the cured one. Due to the different reflection behavior, a lower exposure time is selected. With a laser intensity of 2.5 V, it is not possible to determine the laser penetration depth because too few data points are available. However, the result for semi-finished products at 3.5 V is confirmed. In general, the penetration depth of 0.19 mm is much less significant than for semi-finished products.

Table 6-5: Results for the cured test object according to (A_Pohlmann 2017)

Parameters		First tests								Additional tests			
Threshold		600				800				600		800	
Exposure time [μs]		300		600		300		600		900			
Laser intensity [V]	2.5	5	ND	3	ND	5	ND	5	ND				
		4	74.25	4	39.39	5	88.46	4	75				
	3.5	3	0.083	2	0.225	4	0.089	2	0.035	1	0.386	2	0.073
		3	38.15	2	3.3	3	64.74	3	27.66	2	0.57	3	11.57

top left	Quality of the CoP (scale 1-5)
top right	Laser penetration depth (in mm)
bottom left	CAD comparison (scale 1-5)
bottom right	NaN content (in %)
ND	Not detected

As a result, geometry of the cured test object can be measured better than for the semi-finished product. A threshold of 600 W, an exposure time of 900 μs and a laser intensity of 3.5 V are identified as optimum parameters for the cured test object. I is highlighted in Table A-2. This combination has a NaN content of only 0.57 %. The determined CoP and the CAD comparison are illustrated in Figure 6-6. As with the semi-finished product, the roundings show deviations in the CAD comparison. Again, the roundings show deviations, which cannot be prevented in this thesis. (A_Pohlmann 2017)
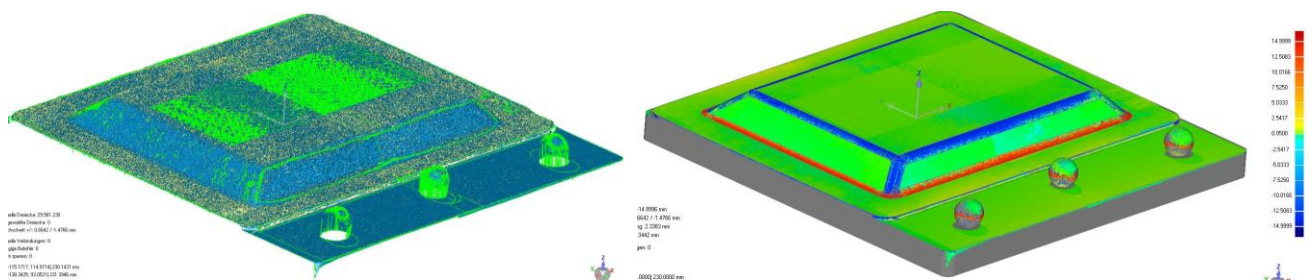
Figure 6-6: CoP (left) and CAD comparison (right) with optimum parameters for the cured test object (A_Pohlmann 2017)

6.1.4.4 Extension of the Test Series

The used CoDiCo-SMC is neither painted nor contains fillers, allowing the laser to penetrate into the material. The geometric variable responsible for penetration depth is the so-called incidence angle, which is defined the smaller angle between laser beam and material surface. A lower laser incidence angle results in a lower penetration depth.

With a measurement taken at a slope, the laser alignment remains the same, but the incidence angle changes. This is sketched in Figure 6-7 with overstated angles to increase recognizability. It is obvious, that a laser angle of 10° on the plane has a smaller incidence angle than a laser angle of 3°. However, this is reversed at a slope.
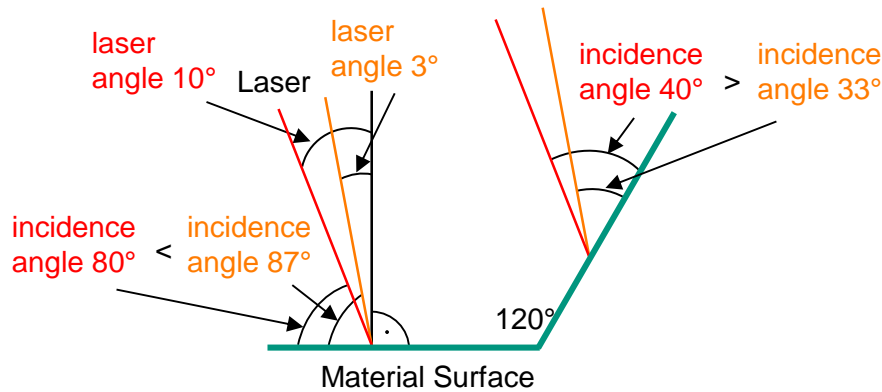
Figure 6-7: Relationship of laser and incidence angle at flat (left) and sloped surfaces (right) (A_Pohlmann 2017)

The previous test series mainly focused on the plane and hence resulted in a favorable setup with a laser angle of 10° and a camera angle of 40°. As an alternative, a laser angle of 3° and a camera angle of 33° have also proved positive results in previous tests (A_Oergele 2017). For this reason, the alternative setup is evaluated with the determined optimal parameters for threshold, exposure time and laser intensity (cf. Chapter 6.1.4.3).

Results for the Semi-Finished Test Object

Table 6-6 lists the results for the semi-finished test object with the alternative angles.

Table 6-6: Result for laser angle of 3° and camera angle of 33° for semi-finished test object

Semi-finished test object		Extension	
Threshold		600	
Exposure time [µs]		1200	
Laser intensity [V]	3.5	2	1.276
		2	2.68%

top left	Quality of the CoP (scale 1-5)
top right	Laser penetration depth (in mm)
bottom left	CAD comparison (scale 1-5)
bottom right	NaN content (in %)

Compared to the previous setup with a laser angle of 10° and a camera angle of 40° (cf. Table 6-4), CoP quality and CAD comparison remain constant. The penetration depth of the laser has increased minimally from 1.197 mm to 1.276 mm, whereby the number of NaNs has slightly improved from 3.32% to 2.68%. CoP and CAD adjustment are depicted in Figure 6-8.
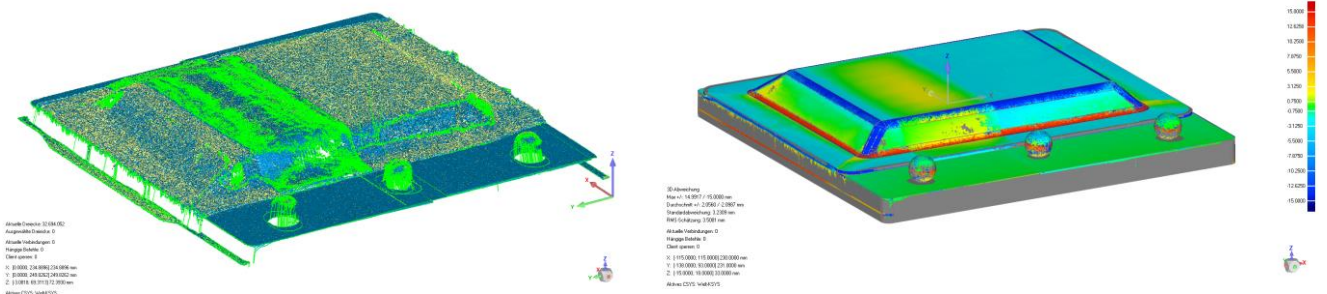
Figure 6-8: CoP (left) and CAD comparison (right) with alternative angles for semi-finished test object

Results for the Cured Test Object

For the cured test object, the results with alternative angles are listed in Table 6-7.

Table 6-7: Result for laser angle of 3° and camera angle of 33° for cured test object

Cured test object		Extension	
Threshold		600	
Exposure time [µs]		900	
Laser intensity [V]	3.5	1	0.4162
		2	0.2%
top left	Quality of the CoP (scale 1-5)		
top right	Laser penetration depth (in mm)		
bottom left	CAD comparison (scale 1-5)		
bottom right	NaN content (in %)		

Again compared to the previous setup (cf. Table 6-5), CoP quality and CAD comparison have the same values. The laser penetration depth increases from 0.386 mm to 0.4162 mm, similarly to the semi-finished test object. However, the number of NaNs is reduced again from 0.57 % to 0.2 %. Figure 6-9 depicts CoP and CAD comparison.
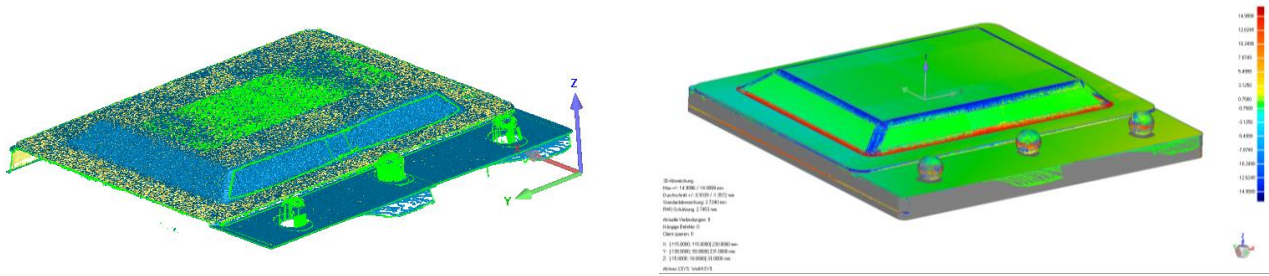
Figure 6-9: CoP (left) and CAD comparison (right) with new optimum parameters for cured test object

Despite the fact of an increased laser penetration depth, the laser angle of 3° and camera angle of 33° are selected for the following investigations. Two explanations:

1. The lower number of NaNs is particularly important for data fusion (cf. Chapter 8.2.1).
2. The values for laser penetration depth are measured on the plane, whereby the test object for following investigations is the small demonstrator with a high slope share (cf. Chapter 5.3.2). As demonstrated in Figure 6-7, a steeper laser angle is favorable on slopes.

Thus, all further investigations are carried out with laser angle of 3° and camera angle of 33° and the following parameters:

Table 6-8: Parameters of the LLSS for all further investigations

	Semi-finished test object	Cured test object
Threshold	600	600
Exposure time [µs]	1200	900
Laser intensity [V]	3.5	3.5

6.2 LLSS Measurement Uncertainty

In order to assess a measurements quality, the determination of the measurement uncertainty is used as a scientific basis, see Chapter 2.4 (Sommer & Siebert 2004). In this chapter, the measurement uncertainty analysis for the LLSS is performed. Initially, the test components are introduced and the selected features defined. Subsequently, the general procedure is presented in order to demonstrate and discuss the results for cured and semi-finished test objects.

6.2.1 Test Objects and Features for Measurement Uncertainty of LLSS

The test object used for determination of the measurement uncertainty consists of DiCo-SMC from ICT and Co-SMC from Polynt Composites Germany GmbH. Its geometry is described in Chapter 5.3.2.

The cured test object consists of two layers DiCo-SMC with a strip of Co-SMC on the surface and an overall wall thickness of 2 mm. The two different surface materials enable the investigation to include different reflection properties. (A_Karwan 2018)

The test object in semi-finished state consists of only one layer DiCo-SMC with a Co-SMC strip on the surface. The part is glued onto a mold, made of Ureol®, reproducing the geometry of the demonstrators lower mold part. Thus, it is possible to evaluate the same geometrical features on both cured and semi-finished test object, depicted in Figure 6-10. (A_Karwan 2018)

One of the characteristics to be investigated is geometric deviation (cf. Chapter 5.4.2). Therefore, the features selected for measurement uncertainty analysis are the distance between the lower and upper plane as well as the slopes with the angles 120° and 140°. (A_Karwan 2018)
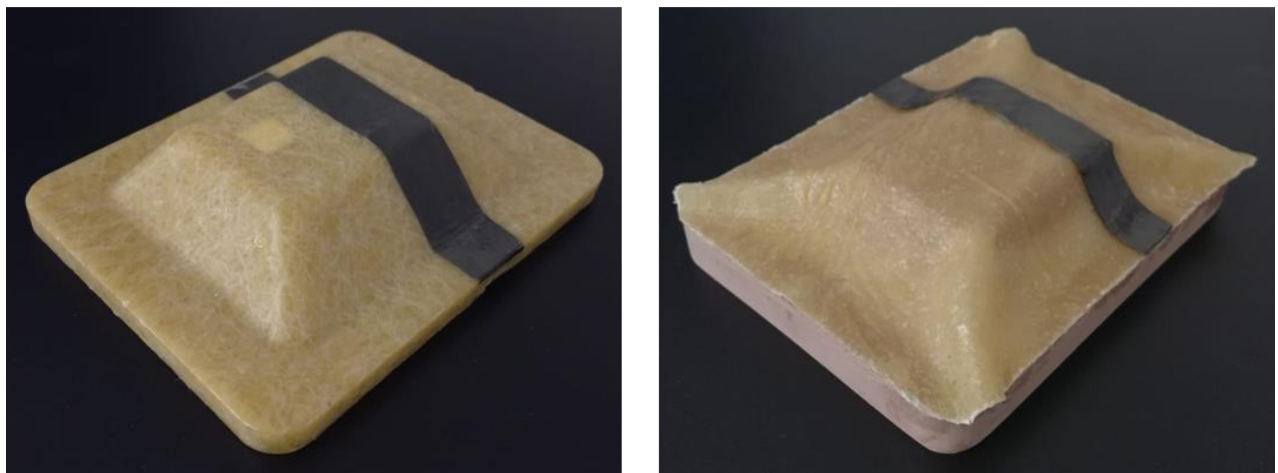
Figure 6-10: Cured test object (left), semi-finished test object on Ureol® (right)
(A_Karwan 2018)

6.2.2 General Procedure of LLSS Measurement Uncertainty Analysis

There is no procedure defined in literature for determining the measurement uncertainty of a LLSS. On basis of research regarding current methods, the procedure according to (DIN EN ISO 15530-3) is used to determine the measurement uncertainty, which is considered GUM-compliant (cf. Chapter 2.4.3). (A_Pohlmann 2017)

According to (DIN EN ISO 15530-3) the calibration uncertainty u_{cal}, the standard uncertainty from the measurement method u_p, and the standard uncertainty from systematic deviation u_p are included in the expanded measurement uncertainty calculation U of a measurement system.

$$U = k \sqrt{u_{cal}^2 + u_p^2 + u_b^2}$$ Equation 6-1

The standard uncertainty from the production process u_w is additionally used for a deviation of the thermal expansion coefficient (cf. Chapter 2.4.3). If the similarity conditions are observed, u_w can be neglected, as in the presented thesis.

Determination of the factors u_p and u_b are taken from standards and transferred directly to LLSS. u_{cal} is usually determined by checking the calibration certificate of used measurement standard. As this is not available for the present work, a traceable approach for the calculation of u_{cal} has to be developed.

Therefore, reference measurements with other measuring methods are performed. Thus, a reference value of the measured variable for u_b and u_{cal} are determined. In this thesis, computer tomography (CT) is chosen as reference method, because it can generally be regarded more accurate than LLSS. With CT, it is possible to calibrate both cured and flexible semi-finished material. (A_Pohlmann 2017) The CT METROTOM 800 from ZEISS is used for the measurements, with the setting parameters listed in Appendix A 13.

A disadvantage of CT is the number of still unknown uncertainty factors, influencing its measurement uncertainty. To tackle this issue, additional tactile measurements with a coordinate measuring machine (CMM) are carried out on the cured test object. The determination of an U_{CMM} is well researched and therefore, its factors are largely known and calculable. Furthermore, CMM is considered a very accurate measuring method. The tactile investigation is carried out with the CMM PRISMO from ZEISS by scanning the test object surface. The number of contact points is listed in Table 6-9.

The obtained tactile mean value is compared with the mean value of CT measurement results. The resulting difference is u_{b_CT}, beeing an indicator of the unknown uncertainty influences of CT. Due to the similar material behavior of semi-finished and cured material, this value is used for both conditions.
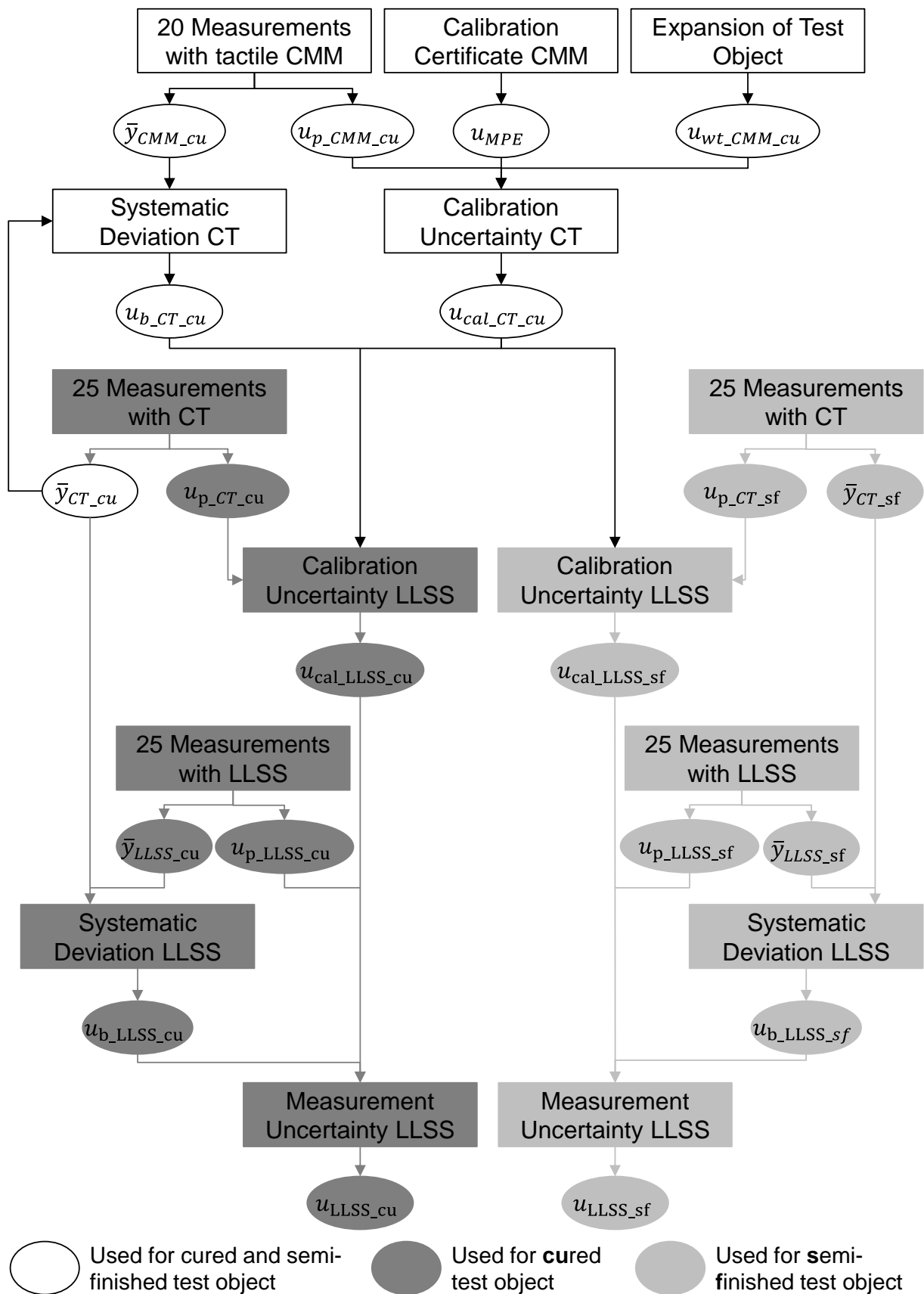
Figure 6-11: Determination of the measurement uncertainty for LLSS according to (A_Pohlmann 2017)

Table 6-9: Number of contact points of the cured component during CMM measurement (A_Karwan 2018)

Plane	Number of contact points
upper plane	5154
lower plane	1511
slope 120°	975
slope 140°	652

As a result, for the calculation of u_{CT}, u_{cal_CT}, is determined from the u_{CMM}. Thus, the determination of u_{LLSS} consists of a multi-stage procedure for semi-finished and cured test objects, illustrated in Figure 6-11. In addition to the uncertainty designation, the index contains used measuring method and test object condition.(A_Pohlmann 2017)

The following chapters detailed explain the determination of individual factors for the calculation of U_{LLSS}.

6.2.2.1 Determination of the LLSS Calibration Uncertainty u_{cal_LLSS}

CT is used as reference method for the determination of u_{cal_LLSS}, resulting in a calculation according to the following Equation 6-2:

$$u_{cal\_LLSS} = \sqrt{\underbrace{u^2_{cal\_CT\_cu}}_{(1)} + \underbrace{u^2_{p\_CT}}_{(2)} + \underbrace{u^2_{b\_CT\_cu}}_{(3)}} \qquad \text{Equation 6-2}$$

For reference measurements, the same test objects in both semi-finished and cured state are used. Thus, the similarity condition according to (DIN EN ISO 15530-3) is fulfilled. To determine the calibration uncertainties, it is assumed that the variables do not correlate with each other.

As described in the previous chapter, CT uncertainties are tackled by tactile reference measurements on the cured test object. This results in $u_{cal\_CT\_cu}$ (cf. (1) in Equation 6-2) being calculated according to the following uncertainty balance equation with its single components explained in detail below (DIN EN ISO 15530-3):

$$u_{cal\_CT\_cu} = \sqrt{\underbrace{u^2_{p\_CMM\_cu}}_{(1.1)} + \underbrace{u^2_{K\_CMM}}_{(1.2)} + \underbrace{u^2_{MT\_CMM}}_{(1.3)} + \underbrace{u^2_{wt\_CMM\_cu}}_{(1.4)} + \underbrace{u^2_{MPE}}_{(1.5)}} \qquad \text{Equation 6-3}$$

$u_{p\_CMM\_cu}$ (cf. (1.1) in Equation 6-3) is the uncertainty caused by the measurement process. For its determination, 20 tactile measurements are performed. To include the operator influences, the position in the measuring room and the clamping are varied after

five measurements. The mean value of these measurements represents the best esti-mator for the true value of measured quantity. $u_{p\_CMM\_cu}$ results from the standard devi-ation of the 20 measurements whose results are given in Appendix A 14.

The CMM probe is calibrated to an officially calibrated ball standard to ensure tracea-bility. As this standard is part of the measuring system, diameter and uncertainty are already stored in the evaluation software. Therefore, the uncertainty of the measuring ball diameter u_{K_CMM} (cf. (1.2) in Equation 6-3) is omitted and does not have to be con-sidered further. Probe deviation and uncertainty are also stored in the evaluation soft-ware and thus, taken into account when calibrating the measuring system. Hereby, the uncertainty of the probe u_{MT_CMM} (cf. (1.3) in Equation 6-3) is negligible either. (A_Pohl-mann 2017)

The uncertainty balance also includes the test object expansion $u_{wt\_CMM\_cu}$ (cf. (1.4) in Equation 6-3). Therefore, the temperature deviation during measurement has to be known. The measuring room is air-conditioned to 20°C, but the temperature fluctuates during measurements due to supply of fresh air or door opening. Therefore, the OPUS 20 temperature measuring instrument is used for temperature monitoring, having an accuracy of 0.3°C in the range 0-40°C. The average room and thus workpiece temper-ature of 23.3°C is used to determine workpiece expansion and the accuracy of the tem-perature measuring instrument is added. The uncertainty of workpiece expansion is calculated according to the Equation 6-4

$$u_{wt\_CMM\_cu} = (T - 20°C) \cdot u_a \cdot l \hspace{3cm} \text{Equation 6-4}$$

with the workpiece temperature T, the standard uncertainty of the expansion coefficient u_a, which can be assumed to be 20 % of its value, and the measured variable length l (VDI/VDE 2617). The CoDiCo-SMC expansion coefficient is not known, therefore the value $14 \cdot 10^{-6} K^{-1}$ from (Mathes & Witten 2014) is used. It is assumed that the test object expands equally in all directions and thus, the surfaces geometric relationships do not change. Therefore, u_{wt_CMM} is set to zero for the angles. (A_Pohlmann 2017; A_Karwan 2018)

The length measurement uncertainty u_{MPE} (Maximum Permissible Error) (cf. (1.5) in Equation 6-3) is taken from the calibration certificate of the measuring instrument. For the CMM PRISMO from ZEISS length measurement uncertainty is

$$u_{MPE\_plane} = \left(1,2 + \frac{l}{350}\right)\mu m \qquad\qquad\qquad \text{Equation 6-5}$$

l corresponds to the length of the measured variable in mm (Carl Zeiss Industrielle Messtechnik GmbH 2015). According to (VDI/VDE 2617), the length measurement accuracy can be converted into a geometry deviation for angles according to the following Equation 6-6:

$$u_{MPE\_angle} = \frac{2}{K} \cdot \sin^2(\alpha_E) \qquad\qquad\qquad \text{Equation 6-6}$$

K corresponds to the denominator of the length measurement accuracy, in this case 350 and α_E to the nominal angle. The result is available in radian measure.

The described simplifications in combination with Equation 6-3 results in the measurement uncertainty balance for $u_{cal\_CT\_cu}$, which in turn is part of the LLSS calibration uncertainty u_{cal_LLSS} (cf. Figure 6-11 and Equation 6-2). $u_{cal\_CT\_cu}$ is calculated both for the feature distance between planes and angles.

$$u_{cal\_CT\_cu\_plane} = \sqrt{u_{p\_CMM\_cu}^2 + u_{wt\_CMM\_cu}^2 + u_{MPE\_plane}^2} \qquad \text{Equation 6-7}$$

$$u_{cal\_CT\_cu\_angle} = \sqrt{u_{p\_CMM\_cu}^2 + u_{wt\_CMM\_cu}^2 + u_{MPE\_angle}^2} \qquad \text{Equation 6-8}$$

To determine u_{p_CT} (cf. (2) in Equation 6-2) 25 calibration measurements of each semi-finished and cured test object, are carried out via CT. The subsequent evaluation is carried out with the VG Studio Max 2.2 software from the company Volume Graphics. The results are listed in Appendix A 15 and A 16.

For calculation of $u_{b\_CT\_cu}$ (cf. (3) in Equation 6-2), the mean value difference of the 20 tactile measurements and the 25 CT measurements, both on the cured test object, is used. $u_{b\_CT\_cu}$ represents an indicator of the unknown uncertainty influences on CT and is therefore used for investigation of both semi-finished and cured test objects.

6.2.2.2 Determination of the LLSS Standard Uncertainty u_{p_LLSS}

For determination of the standard deviation (DIN EN ISO 15530-3) it is recommended to perform 25 repeated measurements. Therefore, the determined optimal parameters (cf. Chapter 6.1.4) and the same NC program are used for all LLSS measurements.

The evaluation for LLSS is done with the program Geomagic Control 2014.4.0 from the company 3D Systems. The software offers the possibility to import the CoP in the .ply format for subsequent measuring. For this purpose, the test object is virtually cut in five defined planes to determine the geometric dimensions and to obtain dimensions over a certain area of test object. In Figure 6-12, a test object with the five cuts and a cross-section is displayed. The planes are placed equally in all 25 tests. The results are presented in Appendix A 17 and A 18.
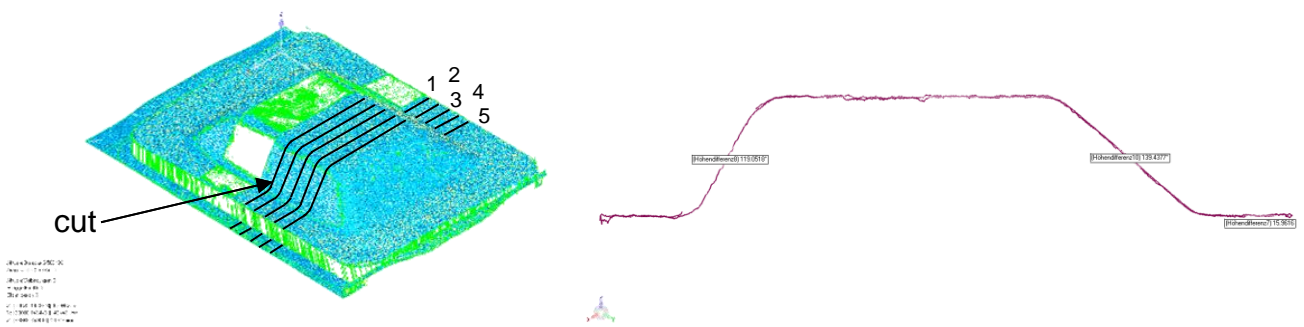
Figure 6-12: Cured test object with five defined planes (left) and cross-section (right)

For the evaluation of the CT measurements it is possible to create with the program VG Studio Max 2.2 virtual planes from manually selected points of the CoP, for instance on the surface of the object. With help of these planes, the measured values of the features to be determined can be calculated. Depending on the surface size, up to 1,000 contact points per plane are selected for the most accurate result. The vertically averaged distance is used to determine the distance between the upper and lower plane of the test object. It is calculated as follows: From each point of one plane a perpendicular is dropped onto the other plane and the arithmetic mean value formed from maximum and minimum distance of the perpendiculars. The angle is measured from the lower plane to the respective slope. (A_Karwan 2018)

The CALYPSO program from ZEISS is used to determine distance and angle for tactile reference measurements. The distance is the perpendicular length from center of one plane to the other plane. The angle between the lower plane and respective slope is selected for angle determination. (A_Karwan 2018)

6.2.2.3 Determination of the LLSS Systematic Deviation Uncertainty u_{b_LLSS}

(DIN EN ISO 15530-3) calculates the uncertainty from systematic deviation u_b according to Equation 2-8. Therefore, the following applies to the LLSS

$$u_{b\_LLSS} = \bar{y}_{LLSS} - \bar{y}_{CT}$$

Equation 6-9

Thereby $\bar{y}_{CT} = x_{cal}$ applies. x_{cal} is the measured variable value of the calibrated work-piece and $\bar{y}$ the arithmetic mean of the measured values. u_{b_LLSS} is assumed small, otherwise it has to be corrected at the measuring system. The calculation of the LLSS measurement uncertainty is carried out according to

$$U_{LLSS} = k\sqrt{u_{cal\_LLSS}^2 + u_{p\_LLSS}^2 + u_{b\_LLSS}^2}$$

Equation 6-10

6.2.3 LLSS Measurement Uncertainty for Cured Test Object

Using the procedure presented in Figure 6-11, the measurement uncertainty of the cured test object u_{LLSS_cu} can be determined for the features plane distance, angle 120° and angle 140°. The individual uncertainty factors are listed in Table 6-10 below. The factor $k = 2$ is selected for the calculation of the expanded measurement uncertainty. (A_Karwan 2018)

Table 6-10: Determination of the measurement uncertainty of LLSS for the cured test object (A_Karwan 2018)

Uncertainty factor	Distance between planes [mm]	Angle 120° [°]	Angle 140° [°]
$u_{p\_CMM\_cu}$	0.0002	0.0002	0.0003
$u_{wt\_CMM\_cu}$	0.0002	0.0	0.0
u_{MPE}	0.0012	0.2456	0.1353
$u_{p\_CT\_cu}$	0.0144	0.0545	0.0330
$\left|u_{b\_CT\_cu}\right|$	0.0326	0.5209	0.0544
$u_{cal\_CT\_cu}$	0.0013	0.2456	0.1353
$u_{p\_LLSS\_cu}$	0.0896	0.4162	0.1331
$\left|u_{b\_LLSS\_cu}\right|$	0.0654	0.1667	0.0788
$u_{cal\_LLSS\_cu}$	0.0357	0.5784	0.1495
$\boldsymbol{u_{LLSS\_cu}}$	**0.1166**	**0.7318**	**0.2151**
$\boldsymbol{U_{LLSS\_cu}}$	**0.2331**	**1.4637**	**0.4302**

6.2.4 LLSS Measurement Uncertainty for Semi-Finished Test Object

The uncertainty of measurement for the semi-finished test object u_{LLSS_sf} has to be determined according to the same procedure (cf. Figure 6-11). The results are listed in Table 6-11. (A_Karwan 2018)

Table 6-11: Determination of the measurement uncertainty of LLSS for the semi-finished test object (A_Karwan 2018)

Uncertainty factor	Distance between planes [mm]	Angle 120° [°]	Angle 140° [°]
$u_{p\_CMM\_cu}$	0.0002	0.0002	0.0003
$u_{wt\_CMM\_cu}$	0.0002	0.0	0.0
u_{MPE}	0.0012	0.2456	0.1353
$u_{p\_CT\_sf}$	0.0310	0.4927	0.3687
$\left|u_{b\_CT\_cu}\right|$	0.0326	0.5209	0.0544
$u_{cal\_CT\_cu}$	0.0013	0.2456	0.1353
$u_{p\_LLSS\_sf}$	0.0498	1.3376	1.7451
$\left|u_{b\_LLSS\_sf}\right|$	0.0795	0.1449	0.2855
$u_{cal\_LLSS\_sf}$	0.0450	0.7579	0.3964
$\boldsymbol{u_{LLSS\_sf}}$	**0.1041**	**1.5442**	**1.8122**
$\boldsymbol{U_{LLSS\_sf}}$	**0.2081**	**3.0884**	**3.6244**

6.2.5 Evaluation of LLSS Measurement Uncertainty

In the following, the minimum achievable tolerances and the measurement system resolution are discussed in more detail. The arithmetic mean values and the measurement deviations are then evaluated. Finally, the individual factors of the measurement uncertainty balance are assessed and a sensitivity analysis is performed.

6.2.5.1 Minimum Tolerances and Resolution of the LLSS

No tolerance values are known for CoDiCo-SMC in order to verify the measuring systems suitability. According to (VDA Band 5) the following is valid:

$$Q_{MS} = \frac{2 \cdot U_{MS}}{TOL} \cdot 100 \ \% \ \leq 15 \ \%$$
<div align="right">Equation 6-11</div>

As a result, the minimum tolerance is as follows

$$TOL_{min} = \frac{2 \cdot U_{MS} \cdot 100\%}{15\%}$$

Equation 6-12

The minimum tolerances for the features of semi-finished and on cured test objects, resulting from the determined uncertainty values are listed in Table 6-12.

Table 6-12: Minimum tolerances for semi-finished and cured test objects (VDA Band 5; A_Karwan 2018)

Feature	Cured test object	Semi-finished test object
Distance between planes [mm]	3.11	2.77
Angle 120° [°]	19.52	41.18
Angle 140° [°]	5.74	48.33

The minimum tolerances of the cured test object are still very high, especially at the angle of 120°. Thus, they are assumed to be insufficient for industrial use. The minimum tolerances for semi-finished test object are very high as well but lower for the feature distance between planes. This can be attributed to the unevenness of the semi-finished material and the only five measured positions. However, semi-finished products get their final shape in the extrusion process, which makes larger tolerances acceptable. (A_Karwan 2018)

In addition, according to (VDA Band 5) the measurement system resolution has to be taken into account. It has to be less than 5 % of the feature tolerance. According to (Brabandt 2018), the lateral resolution is 49 µm, whereby the measuring system resolution is 0.9 % and thus fulfills the requirement of (VDA Band 5). This can also be assumed for the angle tolerance, because the angles are only a different representation of vertical and horizontal description.

6.2.5.2 Arithmetic Mean and Distribution

In the following, the mean values as well as the individual measurements deviations are examined in more detail. Figure 6-13 displays the arithmetic mean value of cured and semi-finished test objects.

For the cured test object, both CMM and CT show deviations from the drawing specification. This can be attributed to the pressing process with unknown dimensional tolerances. Therefore, CMM is used as reference, as it is considered the most accurate

measuring method. The much higher LLSS distance mean value is again explained by the laser beam penetrating the material and thus, influencing interaction between surface and laser (cf. Chapter 6.1.4.4).
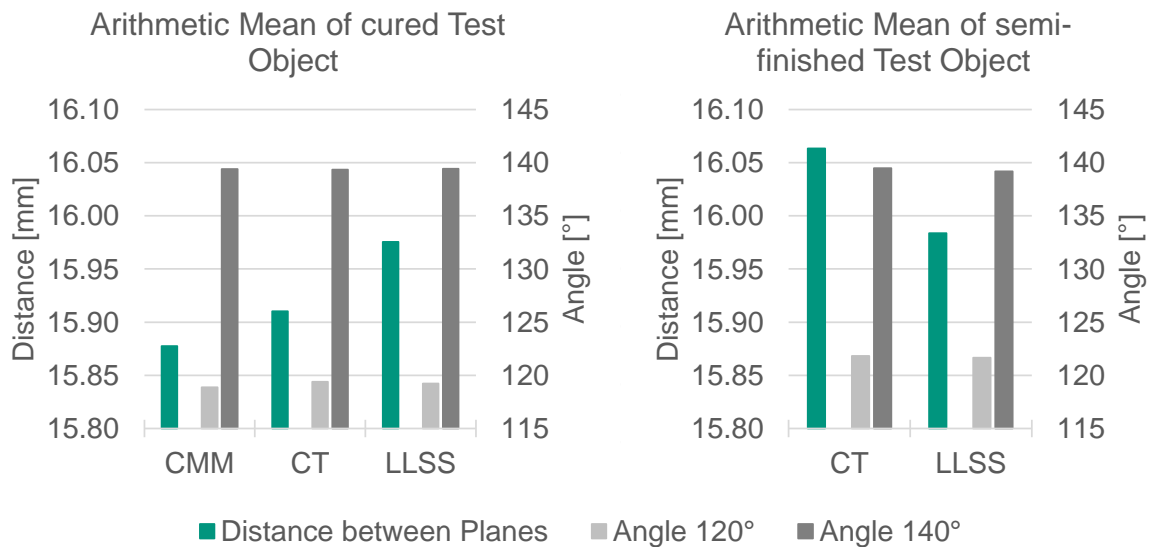
Figure 6-13: Arithmetic mean of cured (left) and semi-finished (right) test objects according to (A_Karwan 2018)

Considering the cured test objects angles, the LLSS measured values are very close to the CMM and CT values. The deviations can only be attributed to system deviations.

For semi-finished test object, the LLSS distance mean value is smaller than the CT value. For both measurement methods, the angle of 120° is larger and the angle of 140° smaller. This results from the semi-finished test object being manually adapted to the carrier body's shape, which is impossible at the roundings, and thus having a high likelihood of unevenness and inaccuracies. As investigation result, LLSS differs from reference measurements only for the distances. The angles however, show similar results.

Table 6-13 summarizes the standard deviations of the individual measuring systems for features on the cured and semi-finished test objects. The scattering of CT manly results from the manual data points selection for creating the virtual plane, which cannot always be placed at the same position. With LLSS, the evaluation of cross-sections can lead to deviations, as the ranges are selected manually. In addition, the uneven surface of the semi-finished test object has a high influence although measured correctly. It is noticeable that the standard deviations for the angles are considerably higher than for the planes distance, particularly for LLSS. (A_Karwan 2018) This can also be attributed to the interaction between the measuring system and the test object.

Table 6-13: Standard deviations of cured and semi-finished test objects according to (A_Karwan 2018)

	Standard Deviation	CMM	CT	LLSS
cured Test Object	Distance between Planes	0.0002	0.014	0.090
	Angle 120°	0.0002	0.055	0.416
	Angle 140°	0.0003	0.033	0.133
semi-finished Test Object	Distance between Planes		0.031	0.050
	Angle 120°		0.493	1.338
	Angle 140°		0.369	1.745

6.2.5.3 Factors of the Measurement Uncertainty

The determined LLSS measurement uncertainty consists of three factors. The relative uncertainty factor ε is inserted (A_Karwan 2018) in order to evaluate the influence of each individual factor. The following applies:

$$\varepsilon_{CAL\_LLSS} = \frac{\varepsilon^2_{CAL\_LLSS}}{\varepsilon^2_{CAL\_LLSS} + \varepsilon^2_{p\_LLSS} + \varepsilon^2_{B\_LLSS}} \qquad \text{Equation 6-13}$$

$$\varepsilon_{EVR\_LLSS} = \frac{\varepsilon^2_{p\_LLSS}}{\varepsilon^2_{CAL\_LLSS} + \varepsilon^2_{p\_LLSS} + \varepsilon^2_{B\_LLSS}} \qquad \text{Equation 6-14}$$

$$\varepsilon_{B\_LLSS} = \frac{\varepsilon^2_{B\_LLSS}}{\varepsilon^2_{CAL\_LLSS} + \varepsilon^2_{p\_LLSS} + \varepsilon^2_{B\_LLSS}} \qquad \text{Equation 6-15}$$

$$\varepsilon_{CAL\_LLSS} + \varepsilon_{p\_LLSS} + \varepsilon_{B\_LLSS} = 1 \qquad \text{Equation 6-16}$$

Initially, Figure 6-14 displays the absolute values of the individual measurement uncertainty factors for all features.

The respective relative uncertainty factors for each measurement and test object are presented in Figure 6-15, illustrating the individual shares and thus influences.
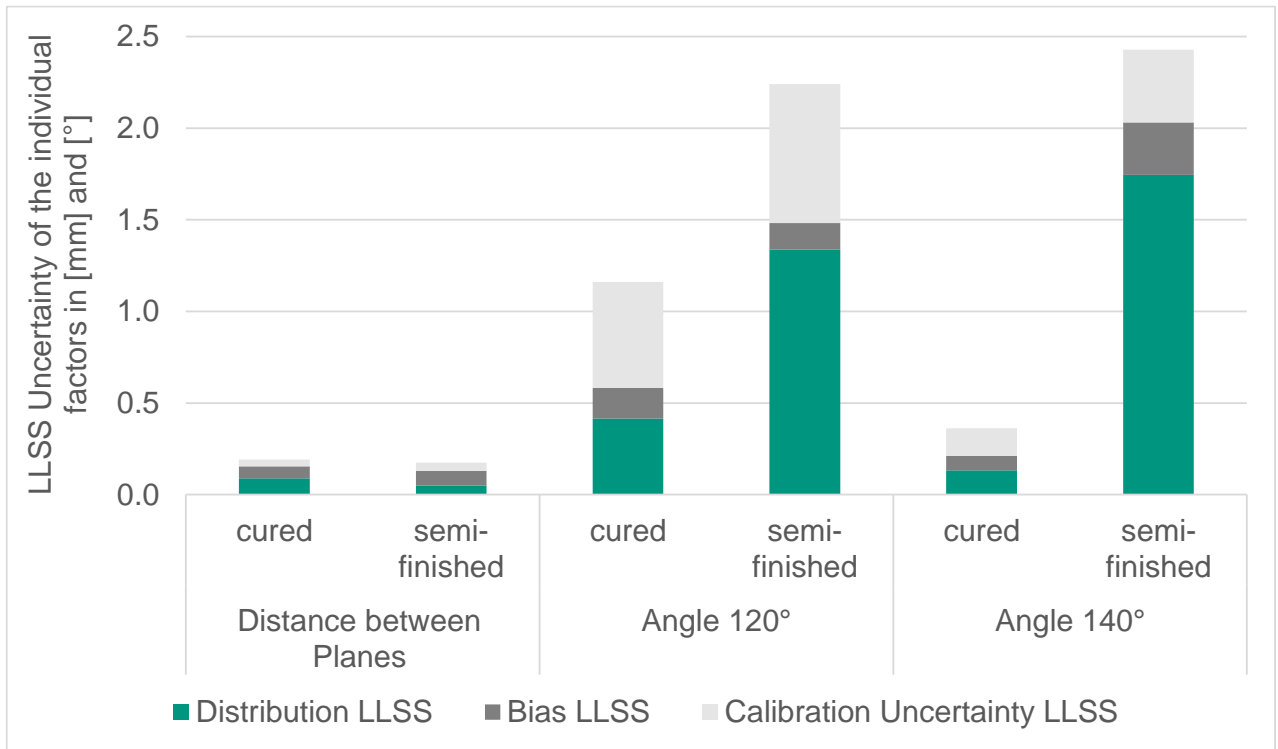
Figure 6-14: Absolute uncertainty factors of LLSS on cured and semi-finished test objects
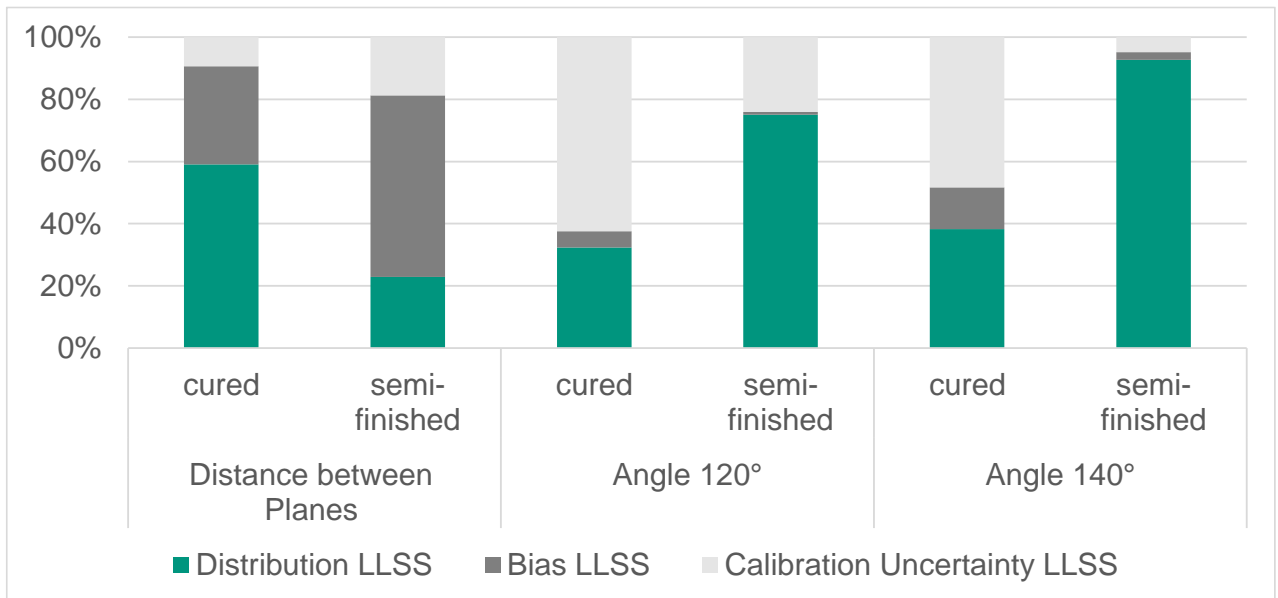
Figure 6-15: Relative uncertainty factors of LLSS on cured and semi-finished test objects according to (A_Karwan 2018)

LLSS Calibration Uncertainty

A clear influence tendency of the calibration uncertainty cannot be inferred from the measurements. This factor is lowest for the distance between planes for both cured and semi-finished test objects. However, this factor increases with the angles, especially on

the cured test object. It is noticeable that at an angle of 140° on the semi-finished test object the calibration uncertainty share is almost as low as at the distance between planes on cured test object.

For both test objects, the calibration uncertainty is primarily influenced by the systematic deviation between CT and CMM. This can be explained by the different evaluation strategies for calculating the planes at CMM and in CT. One possible solution would be to adapt the evaluation strategy to one system. (A_Karwan 2018)

The influence on the calibration uncertainty of the semi-finished product is due to the dispersion of the CT. The reason for this is the surface determination in VG Studio. A multi-material surface determination would be conceivable, which is, more computationally intensive than the manual surface determination. (A_Karwan 2018)

LLSS Standard Uncertainty

Distribution is an essential factor in the measurement uncertainty balance, especially for semi-finished products. The deviation influence of semi-finished test object is greater due to the uneven surface shape compared to the cured test object, with the exception of the distance between planes. The semi-finished material can be very well adapted to the planes compared to the slopes and thus the deviation is lower. With the angles, a smaller deviation can be observed on the cured test object than with the distance of the plane. As a result, the selected angle settings are well suited for the slopes.

LLSS Systematic Deviation Uncertainty

In addition to distribution, systematic deviation is another important factor influencing the determined measurement uncertainty. According to (JCGM 100) it is necessary to identify the systematic deviations in order apply a correction.

The systematic deviation has a particularly large influence on the distance between planes. Possible reasons are the manual selection of data points during evaluation as well as the optical properties of CoDiCo-SMC. Thus, the influence of the laser incidence angle is very important for a measurement. The determination of the systematic deviations is not further pursued in this thesis, because a multitude of influencing factors can be responsible and this represents another field of research.

As a result of the whole evaluation in chapter 6, research question three (cf. Chapter 1.2 is partially answered: The LLSS is suitable for geometric deviations as well as the measurement uncertainty is presented for cured and semi-finished test objects.

7 Active Thermography

This chapter describes the active thermography system. Integration of the active thermography system into the existing portal, already carrying the LLSS, is a requirement. Therefore, the existing portal interfaces and boundary conditions are explained to enable the selection of one active thermography system.

Similar to LLSS, a parameter analysis is carried out to determine the suitable parameters for CoDiCo-SMC. In addition, an in-depth analysis is an essential part of the present investigations, providing a basis for later evaluation. Furthermore, characterization of defects and determination of the systems measurement uncertainty is examined.

7.1 Portal Interfaces

To integrate active thermography into the existing portal, the available interfaces, installation space and maximal payload have to be taken into account.
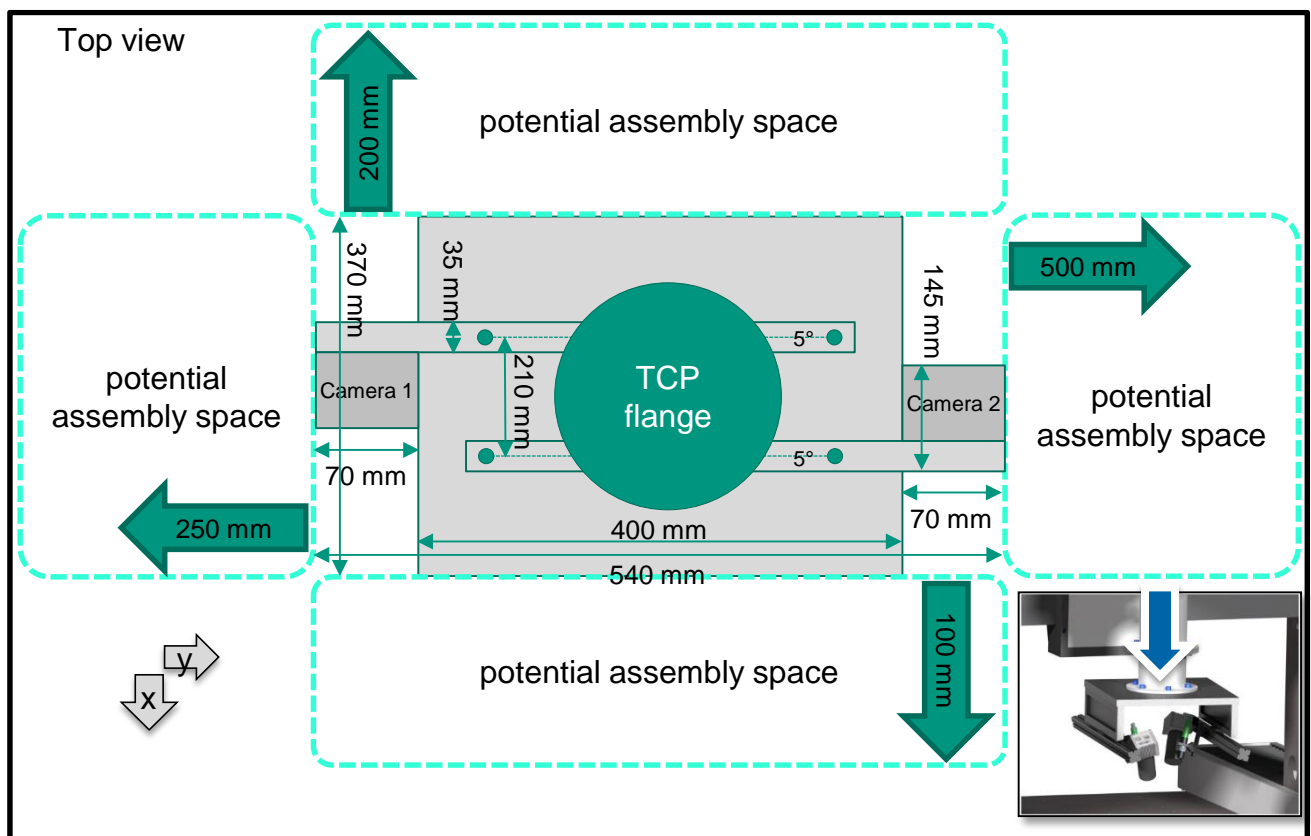
Figure 7-1: Schematic illustration of possible assembly spaces for the active thermography system according to (A_Demmerle 2016)

The portal is designed for a load of 40 kg on TCP. The steel adapter plate used by (Brabandt 2018) is replaced by an aluminum plate due to its high weight. This results in

an LLSS weight of 18.4 kg, including the adapter plate and the side panel angle. Thus, approx. 21 kg are available for the active thermography system.

As the LLSS is already mounted to TCP, different areas around it are available for installation of the active thermography system. Figure 7-1 provides a schematically overview of these possible installation spaces on the right and left as well as in front and behind of LLSS. The most suitable installation space can be determined after selection of the thermography system (cf. Chapter 7.2).

In order to realize an automated examination, it is necessary to integrate the new thermography system into the existing CNC control. This involves the Beckhoff TwinCAT 3 controller with a machine tool module. (DIN 66 025; Brabandt 2018) A connection to MATLAB® has to be established for subsequent evaluation and data consolidation.

7.2 Selection of suitable Active Thermography

Criteria have to be defined in order to identify a suitable active thermography method for the present application. These and the degree of fulfilment are listed in Table 7-1.

Table 7-1: Evaluation criteria and the meaning of the evaluation according to (A_Demmerle 2016; Zaiß et al. 2017a)

Evaluation criteria	- -	+ +
Process time	A lot of time required	Fast process
Flexibility	Only small and simple geometries	Simple and complex geometries of various sizes
Evaluation effort	Numerous additional steps required; Complex evaluation	No additional reworking steps required than with conventional methods
Safety	System represents a hazard to personnel; elimination of the hazard is not possible	system poses no hazard; no additional safety necessary
Space & weight	Required installation space is too large for the portal (collision); Weight exceeds 21 kg	Compact system (small assembly space required); Very light system
Costs	Extremely high acquisition costs with high maintenance costs; cost-intensive adjustments to the portal may be necessary	Low acquisition costs with low maintenance costs

Four different excitation modes for active thermography, considered useful, are evaluated according to the above criteria. These are pulse-phase thermography (PPT) with

flash lamp excitation, lock-in thermography with halogen lamp excitation, laser thermography and thermography with infrared heater. Table 7-2 provides an overview of the individual methods and their fulfilment of the requirements.

Table 7-2: Evaluation of different excitation modes for active thermography regarding defined criteria according to (Zaiß et al. 2017a)

	Process time	Flexibility	Evalua-tion effort	Safety	Space & weight	Costs
Pulse-phase thermography	+ +	+	+ +	o	-	+
Lock-in-ther-mography	-	-	+ +	+ +	o	+
Laser-thermography	o	o	-	- -	+ +	- -
Thermogra-phy with infra-red heater	o	-	o	+ +	+	-
Legend	-- very low degree of fulfilment, o good degree of fulfilment, ++ very high degree of fulfilment					

Due to the high costs and the additional required safety measures caused by the hazard to personnel by using lasers, laser thermography is not used. Thermography with an infrared heater also has high costs and requires long process times. Therefore, this procedure is also excluded. (A_Demmerle 2016)

Thus, the remaining systems are PPT and lock-in thermography, each with advantages and disadvantages. The PPT system is selected for the present thesis. Significantly shorter process and evaluation times are decisive. Furthermore, the system is more flexible with regard to test object size, while costs of both systems do not differ much. The required installation space for the PPT system is available and the maximum permitted mass is not exceeded. The safety disadvantage compared to lock-in thermography can be eliminated by simple remedy. (A_Demmerle 2016)

A PPT system is integrated into the existing portal and is installed in front of the LLSS to ensure the greatest possible freedom of movement (cf. Chapter 8.1.2).

The selected thermography system was developed by edevis GmbH. The infrared camera from InfraTec GmbH is integrated into the system. The individual components are explained in detail in Appendix A 19. The test procedure for PPT is also explained in Appendix A 20. Figure 7-2 depicts an overview of the PPT system and its components.

1	Infrared Camera
2	Workstation
3	Signal Generator
4	Flash Generator
5	Flash Lamp
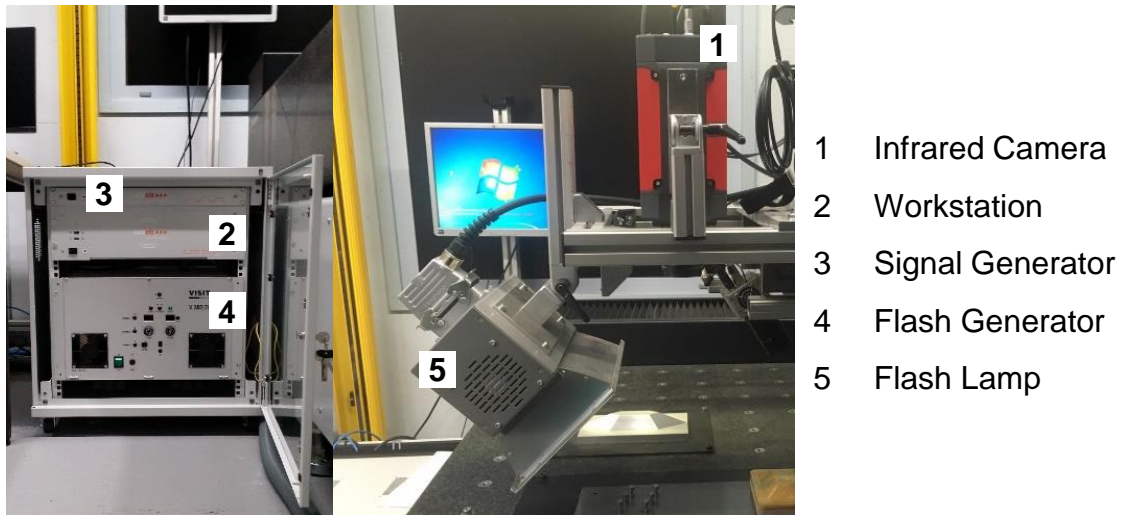
Figure 7-2: Component overview of PPT system according to (A_Pohland 2017)

7.3 Parameter for PPT

The parameters for PPT can be distinguished in fixed parameters, constant for semi-finished and cured test objects, and variable parameters, differing for semi-finished and cured test objects.

7.3.1 Fixed Parameters of PPT

For all experiments, the reflection method is used as an arrangement, where flash lamp and infrared camera are located on the same side of the test object.

After the camera is connected to the software, the calibration data set "FF 25 mm (0-60) 851 µs" is selected in all tests. '0-60' means that the test objects temperature is in the range between 0-60°C during testing. The last number specifies the optimal integration time of 851 µs. In this case, the integration time is to be equated with the exposure time of conventional cameras.

With a low incidence of light, this leads to an increase in black or noisy image areas. The thermal sensitivity rises with longer integration time. This can lead to an overexposure of the detector at high temperatures, due to quickly dropping temperatures in the cooling phase, the few images with overexposure can be discarded (Gleiter 2011). By

means of the integration time, the maximum possible frame rate is also determined, representing the number of recorded frames per second. The higher the frame rate, the better the examination quality. The maximum possible frame rate at an integration time of 851 μs is 341 frames per second.

When recording the live images, the so-called digital levels is output, which can also be displayed as temperature after a calibration. However, no exact temperature values but temperature differences are required for investigations, making a camera calibration in relation to the exact temperature unnecessary.

According to the test object thickness and the required evaluation frequency, the recording time has to be varied. A recording time of 60 s has proven to be sufficient, covering a wide spectrum of frequencies and guaranteeing a short measurement time, and is thus not exceeded in this thesis. Longer recording times allow the detection of deeper defects, but provide a blurred picture due to lateral heat flows.

A pulse delay of 0.1 s is selected for all experiments. Thus, the flash lamp triggers 0.1 s after the infrared camera has started recording (A_Griener 2018; A_Lorenz 2017).

The excitation must not damage the test object but should be as homogeneous as possible, depending on flash energy and geometrically parameters. The flash generator is adjustable up to the maximum energy output of 6 kJ, which is ideal according to preliminary tests and therefore used for this thesis (A_Griener 2018). Flash distance and angle, have to be changed according to size and geometry of test object and therefore belong to the variable parameters.

7.3.2 Variable Parameters of PPT

In addition to the fixed parameters, the variable parameters have to be adjusted according to the test object geometry.

The distance from camera to test object is adjusted to the capture image area. A distance of at least 30 cm is considered optimal. At a distance of 35 cm, an image field measuring 13 cm x 11 cm is recorded (InfraTec GmbH 2018). The selected camera distance is specified in the test descriptions. Once the camera is aligned with the test object, its focus has to be adjusted manually the lens.

The flash distance varies between 21 cm and 23 cm depending on the test object geometry. A flash lamp inclination around 45° is considered optimal. However, it has to be slightly adjusted according to test object structure and geometry. (A_Griener 2018)

All variable parameters are specified in the respective test descriptions. The basic structure is shown schematically and as a real illustration in Figure 7-3.
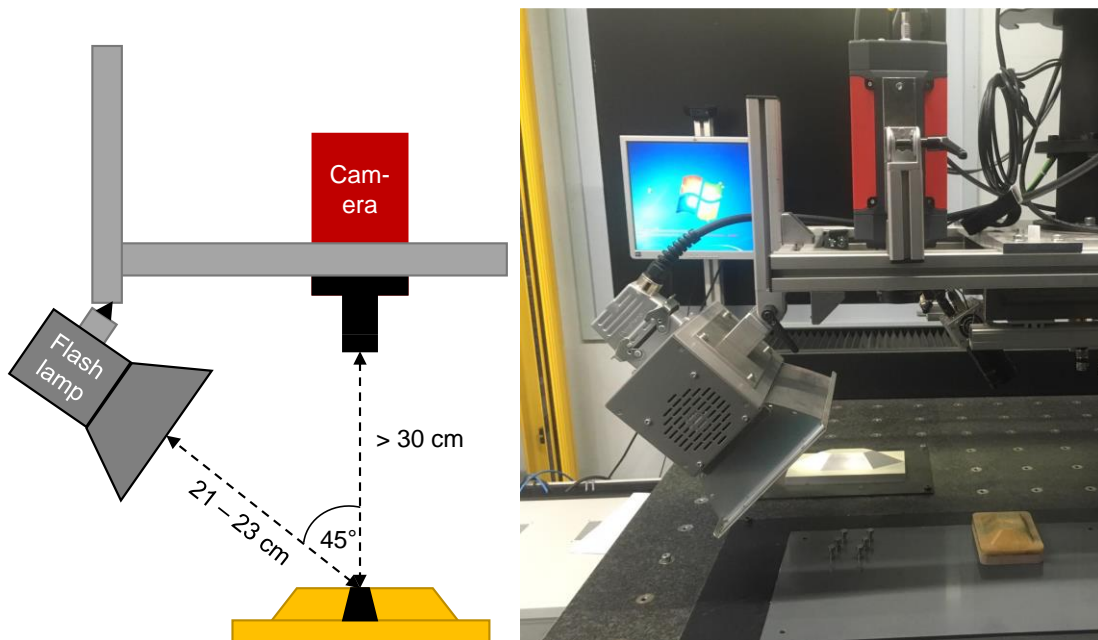
Figure 7-3: Schematic and real test setup according to (A_Griener 2018)

7.4 In-depth Analysis of PPT

The discrete Fourier Transform converts the thermograms into phase and amplitude images (cf. Appendix A 4.5). The phase images contain information about the depth of the respective defects. (cf. Appendix A 4.5). As the recording time of the thermography measurement increases, lower excitation frequencies are generated and the penetration depth rises. Thus, at lower frequencies it is possible to detect deeper defects in comparison to higher frequencies (Zöcke 2010). With longer measurements, it has to be taken into account that the lateral heat flow increases and edges are imaged continuously instead of discretely. This is due to the desired temperature compensation at temperature difference. Thus, a clear separation between defect and good region is impossible. Furthermore, the image contrast decreases.

With succeeding damages, the deeper damages are not detected as the thermal wave is reflected at the first thermal boundary layer. (Gleiter, Spießberger & Busse 2007)

In the following, test performance and analysis method for the so-called in-depth analysis are explained. Afterwards, the results are evaluated and interpreted.

7.4.1 Test Execution and Analysis Method of the In-Depth Analysis for PPT

(Zöcke 2010) and (Wallbrink, Wade & Jones 2007) show that the size of a defect, be-side its depth, has an impact on the in-depth analysis. This is confirmed by preliminary tests (A_Ibach 2018). Therefore, in-depth analyses of large pockets milled into cured plates are performed in this thesis. The pocket size of approximately 160 mm x 40 mm should prevent the influence of the defect size on depth determination due to the fact that this defect is unrealistically large and therefore only the depth is considered. How-ever, it has to be taken into account that the depth analysis is strongly dependent on the respective layer structure of the test objects. Thus, tests with both layer structures described in Chapter 5.2 are performed. In both cases, the test object is a plate with the dimensions 450 mm x 450 mm, varying in thicknesses with 4.5 mm for the thick structure and 2.8 mm for the thin structure. Milling different deep pockets into the plates, results in the availability of various residual wall thicknesses illustrated in Figure 7-4. The thin plate allows less deep pockets, resulting in a reduced number of residual wall thicknesses.
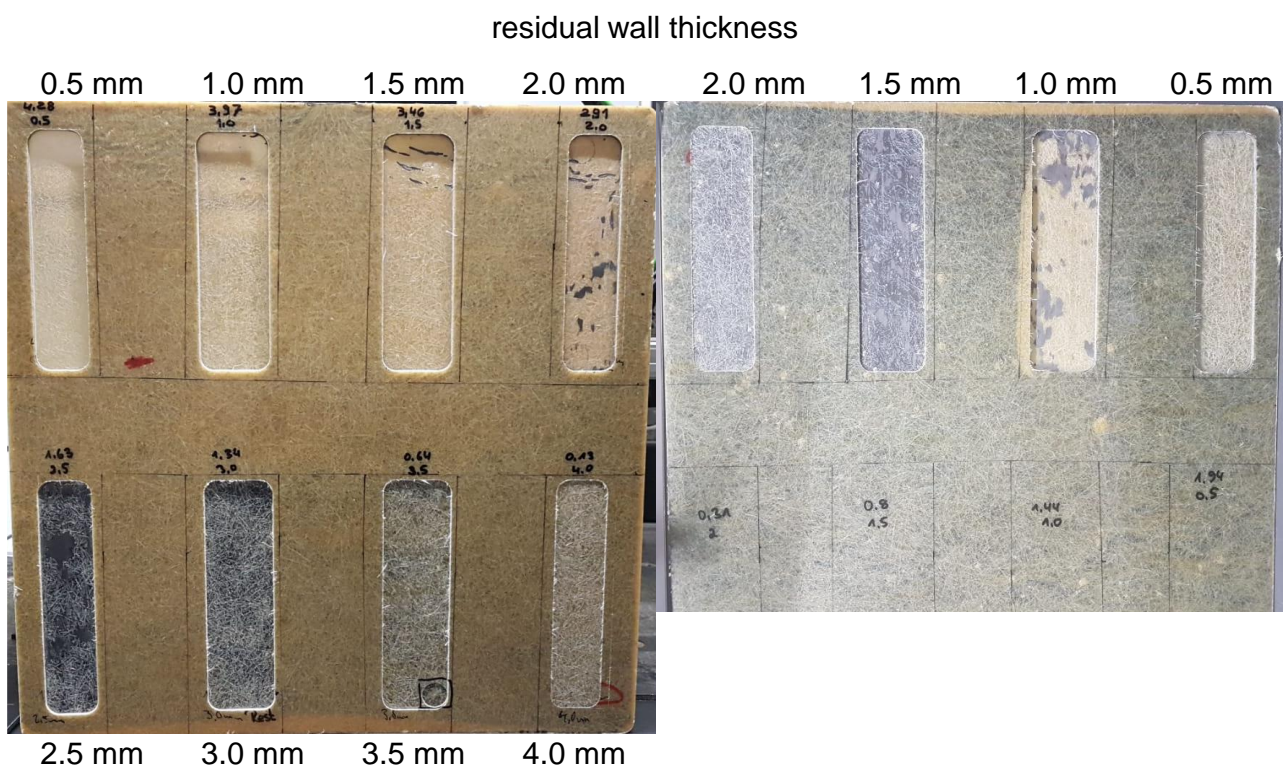
Figure 7-4: Thick plate (left) and thin plate (right) with milled pockets and different residual wall thickness (in mm)

To validate the remaining wall thickness, they are measured five times with a caliper gauge. The results are listed in Table 7-3.

Table 7-3: Defined residual wall thicknesse compared to caliper measured values

Defined residual wall thickness [mm]	Mean value thick plate [mm]	Mean value thin plate [mm]
0.5	0.628	0.47
1.0	0.996	0.93
1.5	1.522	1.54
2.0	1.988	2.018
2.5	2.52	-
3.0	2.984	-
3.5	3.586	-
4.0	4.018	-

For thermographic investigation, the distance camera to plate is 35.7 cm, the flash distance 22.5 cm. 60 s are selected for the recording time and five tests are carried out for each pocket.

Two lines with a length of 83 pixels each are set and used for evaluation. One line is placed in the center of the pocket (defect), the other in the assumed defect free area (plate). The line value for each frame is the average value of this frames 83 pixels. All line values are plotted in a Phase-Frequency diagram as depicted in Figure 7-5.
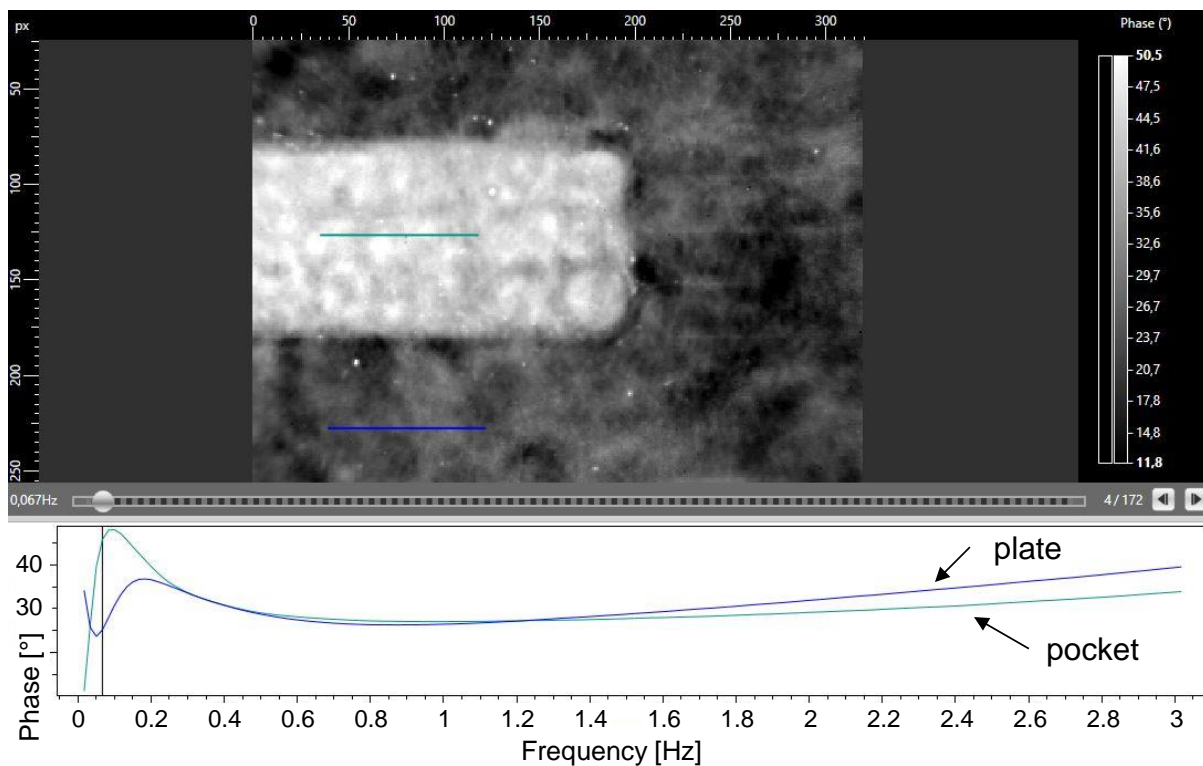
Figure 7-5: Example for first evaluation step, using the thick plate with a residual wall thickness of 1.5 mm

In the first evaluation step, the maximum phase difference, at the lines, is selected as evaluation criterion for determining the frequency assigned to a corresponding depth. Therefore, the recording with the highest phase difference is used, which also has the highest contrast. This recording and the maximum phase difference indicated by the vertical line in the Phase-Frequency diagram are illustrated in Figure 7-5.

Phase difference analysis has already been applied in (Wallbrink, Wade & Jones 2007) and (Ishikawa et al. 2013) (cf. Chapter 3.3.1.2).

In the second step, the maximum phase difference is determined for each recording, including selection of the corresponding frequency. Table 7-4 and Table 7-5 give an overview of the remaining residual wall thicknesses and the identified optimum frequencies, as well as the associated standard deviations. The relationship between frequency and penetration depth is described in Equation A-3 in Appendix A 4.5.

Table 7-4: Depth evaluation of thick plate

Residual wall thickness [mm]	Frequency mean value [Hz]	Standard deviation
0.5	1.762	1.026
1.0	0.117	0.011
1.5	0.067	0
2.0	0.050	6.939E-18
2.5	0.083	0
3.0	0.073	0.008
3.5	0.043	0.008
4.0	not detectable	

Table 7-5: Depth evaluation of thin plate

Residual wall thickness [mm]	Frequency mean value [Hz]	Standard deviation
0.5	0.331	0.025
1.0	0.281	0.019
1.5	0.385	0.015
2.0	0.445	0.017

7.4.2 Evaluation of the In-Depth Analysis for PPT

As the results for thick and thin layer structure differ considerably, they are separated and listed in the following two chapters.

7.4.2.1 Evaluation of the In-Depth Analysis for Thick Layer Structure

The analysis of the determined frequencies for the thick plate shows, that the frequency continuously decreases with increasing residual wall thickness up to 2.0 mm. This corresponds to the assumption that lower frequencies are required to detect deeper defects (cf. Chapter 7.4).

It is conspicuous, that with a further increase of the residual wall thickness, the frequency increases at 2.5 mm and then decreases again. This contradicts Equation A-3 and the assumption in Chapter 7.4.

However, Equation A-3 includes the thermal conductivity k_{th}, varying for each material. With knowledge of the layer structure (cf. Chapter 5.2) it can be stated, that at a residual wall thickness of 2.5 mm the Co-SMC is added. Carbon fibers have a 17 times higher thermal conductivity ($17\ W/m \cdot K$) than glass fibers ($1\ W/m \cdot K$) (Suter Kunststoffe AG 2018), whereby the heat of active excitation is conducted faster through the material. Thus, from a residual wall thickness of 2.5 mm there is a new material combination with new thermal conductivity, conducting heat better. As a result, the optimum frequency increases once again and then decreases with increasing residual wall thickness.

7.4.2.2 Evaluation of the In-Depth Analysis for Thin Layer Structure

The analysis of the thin plate initially presents a similar picture as already described for the thick plate: The frequency decreases with increasing residual wall thickness. As soon as the Co-SMC material is added, the frequency rises again.

In addition, at a residual wall thickness of 1.5 mm, a phase jump is recognizable as illustrated in Figure 7-6.
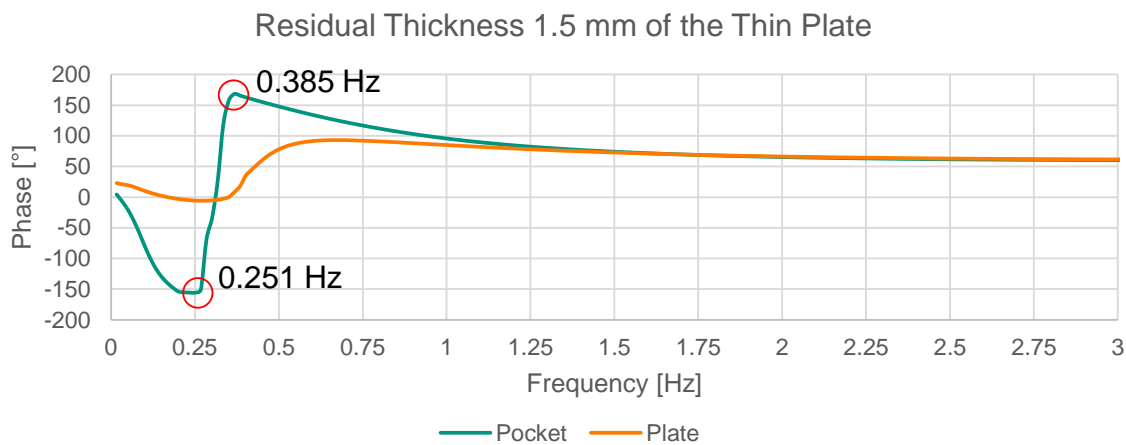
Figure 7-6: Phase sequence of pocket and plate with 1.5 mm residual wall thickness

The phase jump of approximately -150° to 150° occurs in the course of the pocket and thus exceeds 180°. In the phase jump area, no exact statement is possible. Therefore, in this case it is not useful to select the maximum phase difference at 0.368 Hz, but the starting position of the phase jump at 0.251 Hz, because an exact statement is still possible and corresponding depths are reached at the low frequency.

With further increase of the remaining wall thickness, the curves of pocket and residual wall thickness align, as illustrated in Figure 7-7. For the analysis of the suitable frequency for a residual wall thickness of 2.0 mm, the minimum phase value of the pocket is selected. Following this procedure, the optimum frequency again decreases with increasing residual wall thickness.
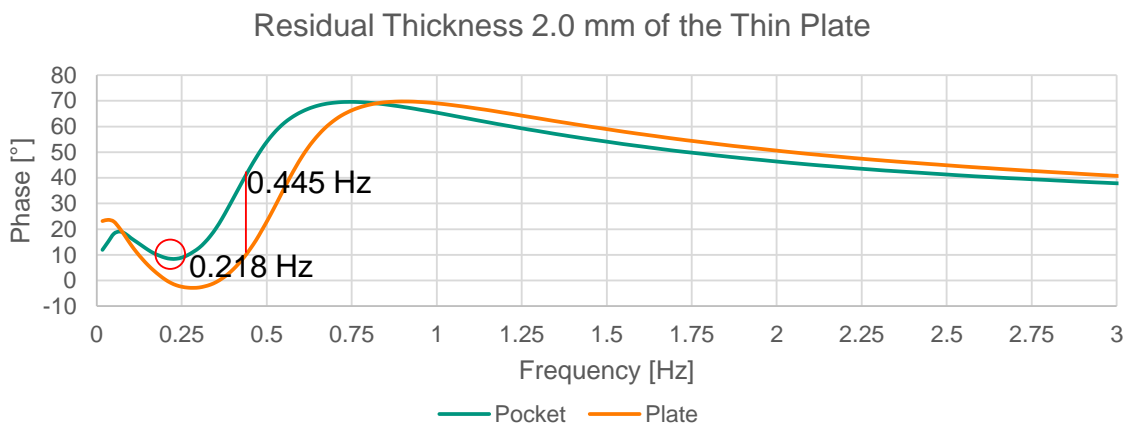
Figure 7-7: Phase sequence of pocket and plate with 2.0 mm residual wall thickness

As a result, the optimal frequencies for in-depth analysis of the thin plate have to be adjusted as listed green in Table 7-6.

Table 7-6: Corrected depth evaluation of thin plate

Residual wall thickness [mm]	Frequency mean value [Hz]	Standard deviation
0.5 mm	0.331	0.025
1.0 mm	0.281	0.019
1.5 mm	0.238	0.012
2.0 mm	0.218	5.55E-05

This investigation shows, that the analysis of phase images allows an evaluation of depth information. However, the obtained frequencies have to be checked for plausibility. Therefore, due to the phase jump in comparison to the thick plate, the thin plate is adapted. Furthermore, only the method can be transferred to other layer structures, but

not the result, since it varies depending on the layer structure. In addition, defects can be covered by boundary surfaces or other defects located in front of them (Gleiter, Spießberger & Busse 2007).

The determined frequencies are also used in measurement uncertainty analysis (cf. Chapter 7.6) and layer model (cf. Chapter 8.4).

7.5 Characterization of Defects

Chapter 5.3 explains that different defects can occur in the considered CoDiCo-SMC, with various effects on the mechanical properties (cf. Chapter 5.5). So far it is only possible, to make a statement whether a defect is existing or not. A great benefit for the user could be generated by obtaining information about the defect type. Thus this chapter deals with the characterization of different defects.

Preliminary tests indicate the occurrence of different characteristics for surface and depth defects, recommending both types for further investigation and analysis. Thus, the defects fold in Co-SMC, foil as a foreign body and divergent Co-SMC orientation are investigated as surface defects as well as depth defects. The tests are performed on cured and semi-finished test objects. (A_Griener 2018)

For examination, the small demonstrator (cf. Chapter 5.3.2), with corresponding layers listed from top to bottom in Figure 7-8, is used. For the first tests, an 80 mm x 20 mm Co-SMC strip is used, resulting in a significant expansion through the pressing process by the factor 1.5 of the Co-SMC strip on the surface, transverse to fiber direction. With the strip on the inside, the expansion is negligible. This turns out to be problematic when evaluating the angular deviation, because a large part of the area to be evaluated is covered and therefore cannot be evaluated. For this reason, a strip width of 10 mm is selected for the surface defects and 20 mm for the depth defects. (A_Griener 2018)

For the examination of semi-finished product, the same layer structure is used. The DiCo-SMC has a size of 120 mm x 94 mm and the Co-SMC strip has a width of 10 mm. All tested components are shown in Appendix A 21.

The defect foreign body is realized by a strip of DiCo-SMC carrier foil, which remains on the material. It has the dimensions 94 mm x 20 mm and is directly covered by the Co-SMC strip. With the depth defect, the foil is applied once under the Co-SMC and once above it. This is not possible with the surface defect series, and therefore the foil is only placed under the Co-SMC. See Figure 7-8. (A_Griener 2018)
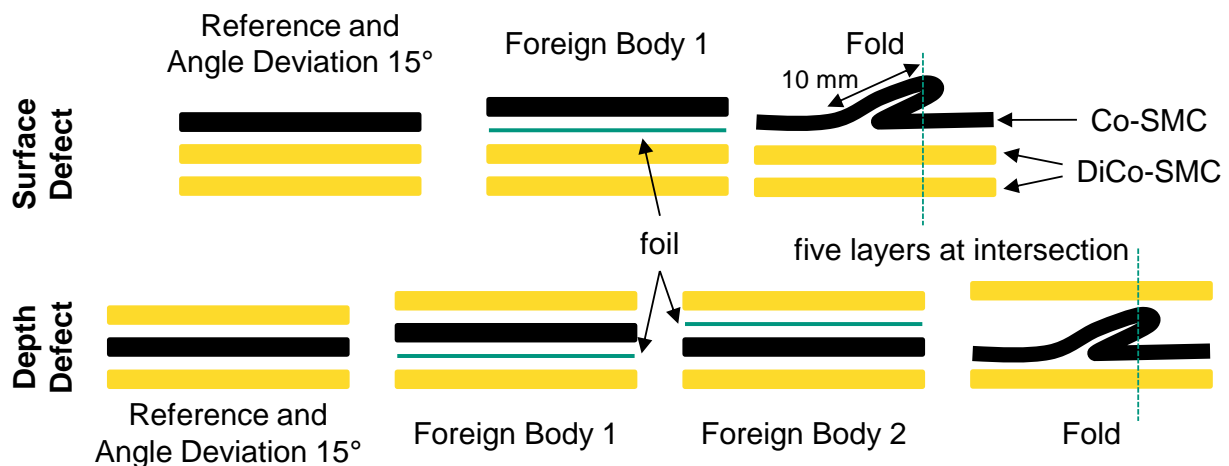
Figure 7-8: Overview of the layer structure of the individual test specimens according to (A_Griener 2018)

The defect fold is realized by a Co-SMC excess, whereby the material bulges upwards. During the pressing process, it turns over resulting in a fold-like accumulation of material. This changes the layers order and, especially in semi-finished state, the test object thickness. For defect generation a fold with a height of 10 mm is realized and convolved afterwards. (A_Griener 2018)

The defect angular deviation is realized by the inclined insertion of Co-SMC. The deviation angle is 15°, whereby it can shift slightly due to the pressing process. The detection of angle deviations is particularly important for structural components, because a change in fiber orientation affect the mechanical properties in force direction and lead to early component failure. (A_Griener 2018)

During the examination, the distance between camera and test object is 22 cm. This is due to a change in the mounting of the camera. As a result, the flash distance to the object is 22 cm with an angle of 35°. For the cured test objects, each test is repeated three times to detect distribution, which is determined to be very small. Thus, only minor deviations are expected for the semi-finished test objects either and therefore, the analysis is only performed once.

After a discrete Fourier transformation, thermograms as well as phase and amplitude images are available for evaluation. Three different methods are used: Evaluation in thermogram, in frequency spectrum as well as in location-related phase and amplitude spectrum.

The evaluation is carried out in so-called regions of interest (ROI), whereby point, line and rectangle are available as ROI for this investigation. Using the rectangular ROI

results in a strong averaging of all measured values, resulting in a distorted measure-ment. The point ROI shows large standard deviations since even small ambient disturb-ances have an influence and strongly falsify the result. The line ROI prevents strong averaging of the measured values by allowing complete observation of the defect area.

In the frequency spectrum, line ROI is placed in the middle over the defect in Co-SMC. This results in a length of 55 or 65 pixels. In the location-related phase and amplitude spectrum, the line ROI is laid over the entire length of the Co-SMC. (A_Griener 2018)

The individual evaluation methods are explained in more detail in the next chapters followed by the results and a summary.

7.5.1 Evaluation Methods for Thermographic Analysis

As mentioned before, three different thermographic evaluation methods are used for defect characterization. These three methods are explained in more detail below and the evaluation parameters for the present investigation are defined more precisely.

7.5.1.1 Evaluation in the Thermogram

Surface Defects - Thermogram

	0.1 s	0.5 s	1 s	3 s	5 s	10 s	30 s	60 s
Reference	70.40	35.24	32.26	29.24	28.33	27.76	27.27	26.85
Foreign Bodies	69.30	36.37	33.06	29.81	28.82	28.12	27.65	27.24
Fold	69.72	35.38	32.37	29.64	28.85	28.31	27.75	27.30
Angle Deviation	70.55	36.28	33.30	30.30	29.37	28.66	28.16	27.78

time of measurement [s]

Reference —— Foreign Bodies —— Fold —— Angle Deviation
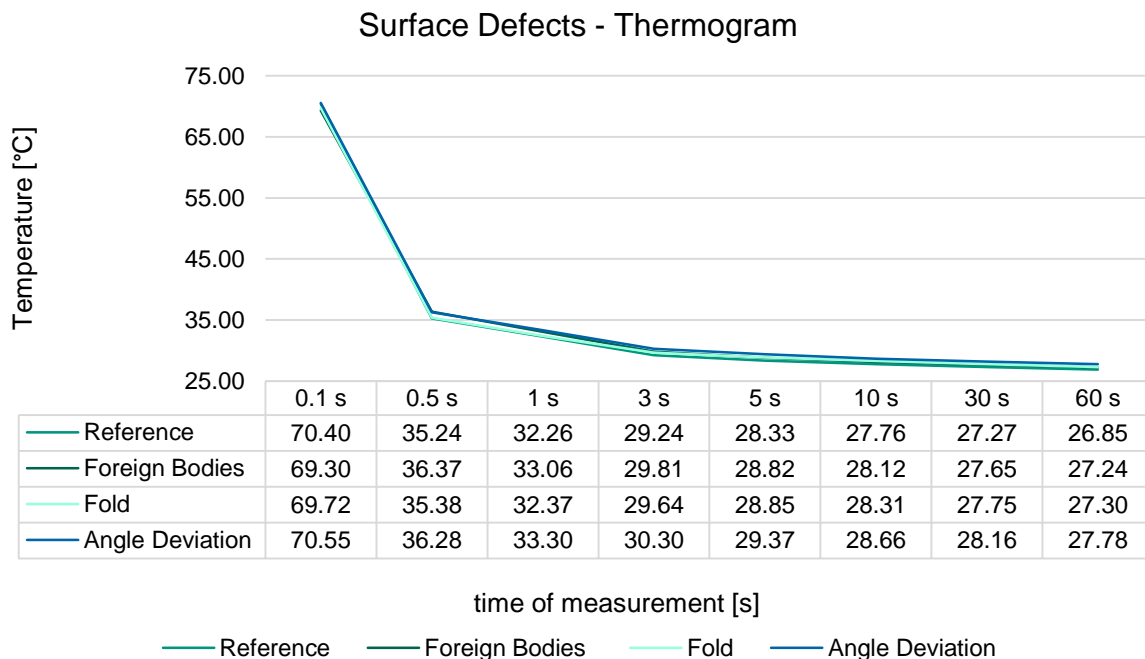
Figure 7-9: Thermogram of surface defects of the cured test objects according to (A_Griener 2018)

In a thermogram, temperature curves are plotted over time. The thermograms are eval-uated with the observation times $t_1=0.1\ s$, $t_2=0.5\ s$, $t_3=1\ s$, $t_4=3\ s$, $t_5=5\ s$, $t_6=10\ s$,

t_7=30 s and t_8=60 s. The objective of thermogram evaluation for defect characterization is to compare defects on basis of specific temperature curves. (A_Griener 2018)

For evaluation, all defects plus a defect free expected reference for cured test objects are plotted in one diagram. The surface defect curves are displayed in Figure 7-9. Due to overlap of all temperature curves, no difference can be detected.

Depth Defects - Thermogram

	0.1 s	0.5 s	1 s	3 s	5 s	10 s	30 s	60 s
Reference	31.52	30.51	30.57	30.10	29.83	29.59	29.02	28.29
Foreign Body 1	30.38	29.28	29.31	28.72	28.39	28.12	27.75	27.31
Foreign Body 2	42.22	30.20	30.01	29.05	28.65	28.41	28.05	27.56
Fold	45.95	31.46	30.69	29.33	28.97	28.76	28.32	27.77
Angle Deviation	32.31	30.76	30.74	30.05	29.71	29.47	29.00	28.38

time of measurement [s]
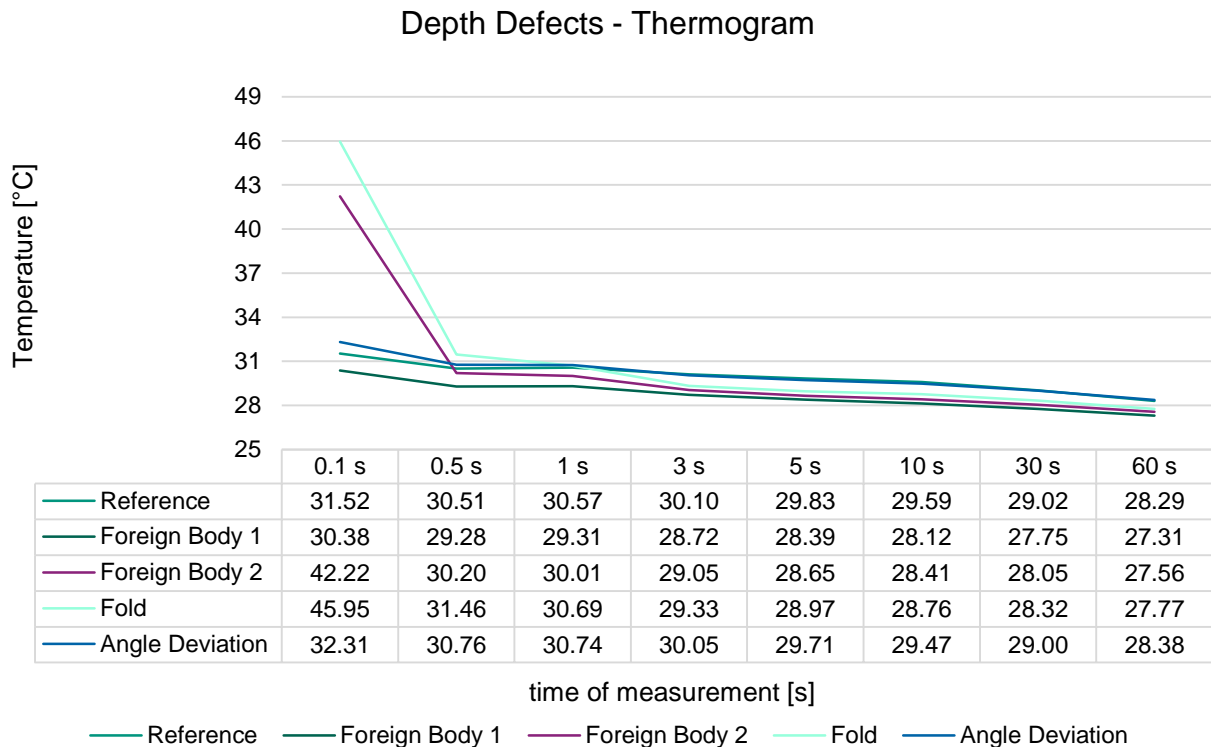
Figure 7-10: Thermogram of depth defects for the cured test objects according to (A_Griener 2018)

The depth defect curves are displayed in Figure 7-10. Investigating the curves shows deviations, but does not allow a clear defect differentiation. For this reason, thermogram evaluation is not further pursued and not applied to examine semi-finished test objects either.

7.5.1.2 Evaluation in the Frequency Spectrum

The thermogram image sequences are transferred to frequency domain by means of a discrete Fourier Transform. The resulting phase and amplitude images are less susceptible to interference and offer better contrast than the thermogram. In this thesis, the images are examined for their specific characteristics with regard to phase angle and amplitude. For evaluation, the line ROI is located across the defect on Co-SMC strip, which is illustrated in Figure 7-11. (A_Griener 2018)
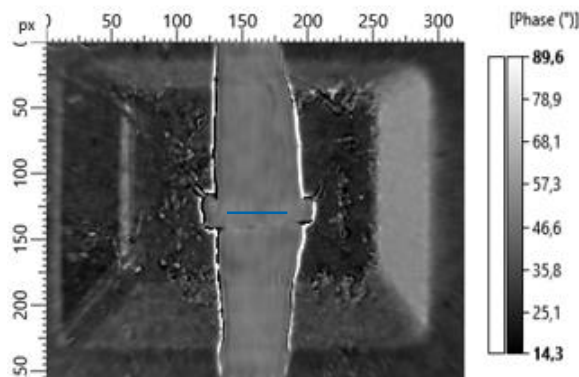
Figure 7-11: Phase image of the surface fold defect for the cured test object at 0,802 Hz according to (A_Griener 2018)

Investigation results for the individual defects are presented in Chapters 7.5.2 and 7.5.3.

7.5.1.3 Evaluation in the Location-Related Phase and Amplitude Sequence

The location-based evaluation in phase and amplitude spectrum considers single pixel values, located next to each other in one line with a line ROI. The measured values therefore are not averaged. For each frequency increment, a special value curve is determined. The line ROI with a length of 255 pixels is placed on the center of the Co-SMC in fiber direction. Pixel 0 is located at the test objects upper edge and the entire vertical component length is covered. This offers the possibility to find defects in the cross-section of one direction and to view the values of different frequencies. (A_Griener 2018)

Figure 7-12 represents the amplitude image of a reference test object with the 255-pixel long, green line ROI placed centrally over the Co-SMC strip. The areas a) and c) represent the test object slope. All evaluations take place in section b) from pixels 40 to 180, which includes the defect area.
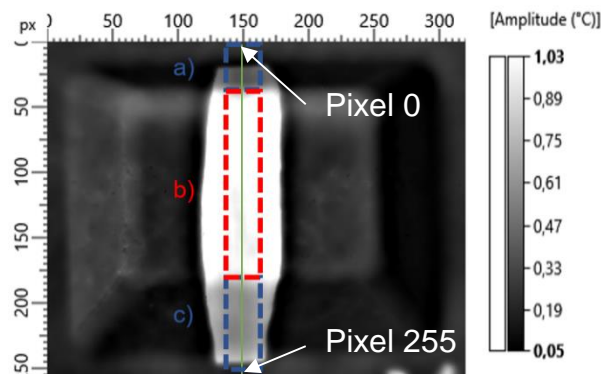
Figure 7-12: Evaluation ranges in the location-related frequency sequence of a good test object according to (A_Griener 2018)

The analysis of 218 displayed frequencies is time-consuming and not target-oriented, therefore specific evaluation frequencies have to be defined. It has to be ensured that the value curve development from low-frequency to high-frequency range is taken into account.

The frequency range between $0 < f < 1\,Hz$ should contain the largest number of different frequencies, since a high dynamic range results in the frequency range between 0.033 Hz and 0.4 Hz. Therefore, an observation distance of approx. 0.1 or 0.2 Hz between different frequencies is defined. The smallest possible frequency of 0.017 Hz is not considered due to the recognizable values jump to the next higher frequency. At a frequency of 0.017 Hz, the test object is completely traversed by the thermal wave due to the high depth range. The jump in value can be explained by the thermal wave reflection at boundary layers of the test object. In the frequency range between $1 < f < 3\,Hz$ an observation distance of approx. 0.4 Hz is choosen. Above 3 Hz, there are only minor deviations in the values, resulting in 3.018 Hz being defined as the maximum frequency. Thus the following 10 evaluation frequencies are defined: 0.033 Hz; 0.1 Hz; 0.2 Hz; 0.401 Hz; 0.802 Hz; 1.205 Hz; 1.608 Hz; 2.00 Hz; 2.401 Hz; 3.018 Hz. (A_Griener 2018)

The semi-finished test object shows no behavior at the upper frequencies, therefore only the following eight frequencies are used the evaluation: 0.033 Hz; 0.1 Hz; 0.2 Hz; 0.401 Hz; 0.802 Hz; 1.205 Hz; 1.608 Hz; 2.00 Hz.

Subsequently, the defects are evaluated in cured and semi-finished state. Foreign body and fold are analyzed in frequency spectrum as well as in the location-related phase

and amplitude sequence. Due to its clear detectability, the angle deviation is only investigated in the frequency spectrum images.

7.5.2 Analysis of Surface Defects

In this chapter, surface defects of both semi-finished and cured test object are analyzed. Plots of the frequency spectrum, including a defect free expected reference, as well as of the location-related phase and amplitude spectrum are provided for each defect. To ensure comparability also for location-related phase and amplitude spectrum, the plots of reference objects are provided in the following. Figure 7-13 illustrates both plots for the cured reference object with Co-SMC on the surface.
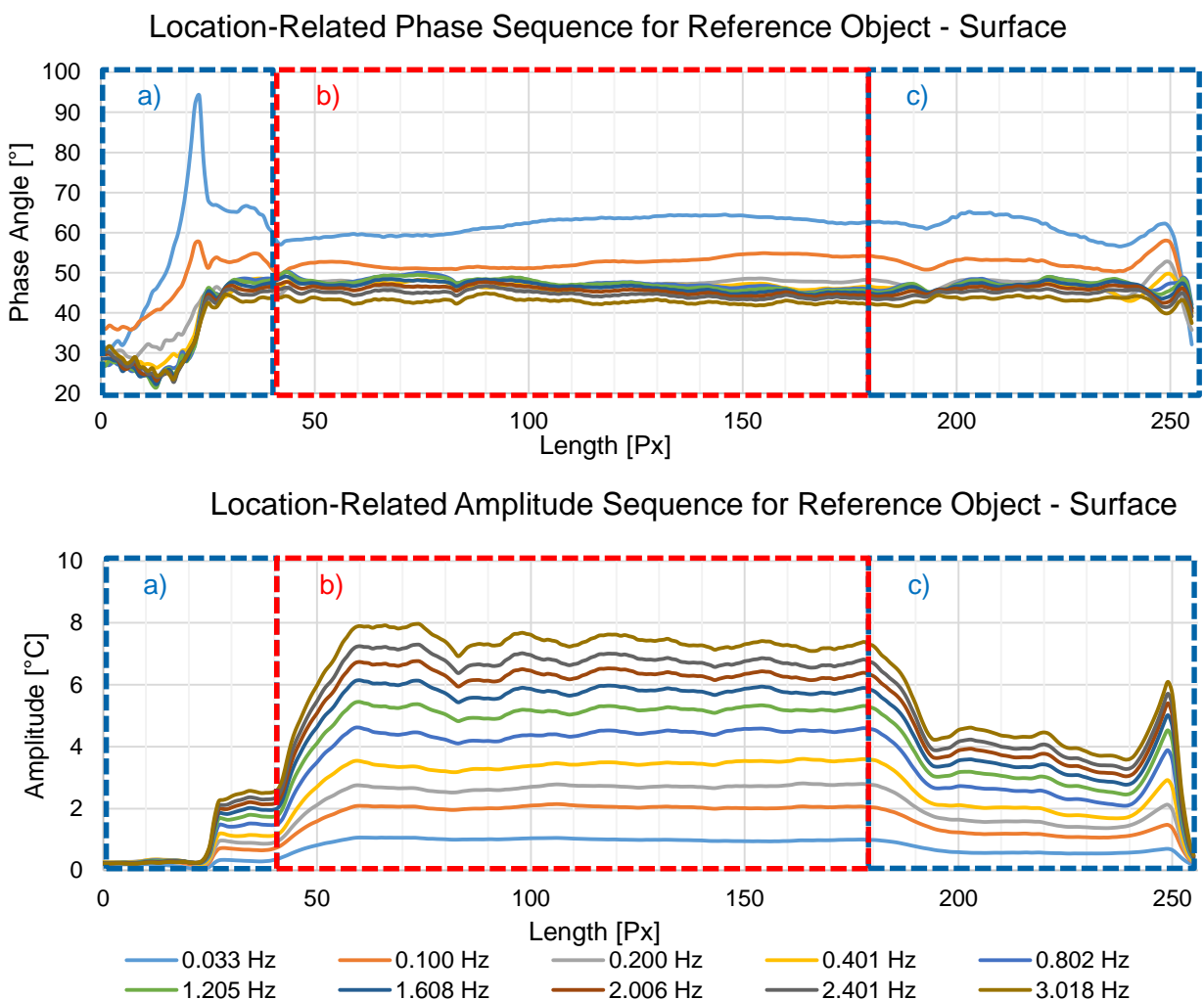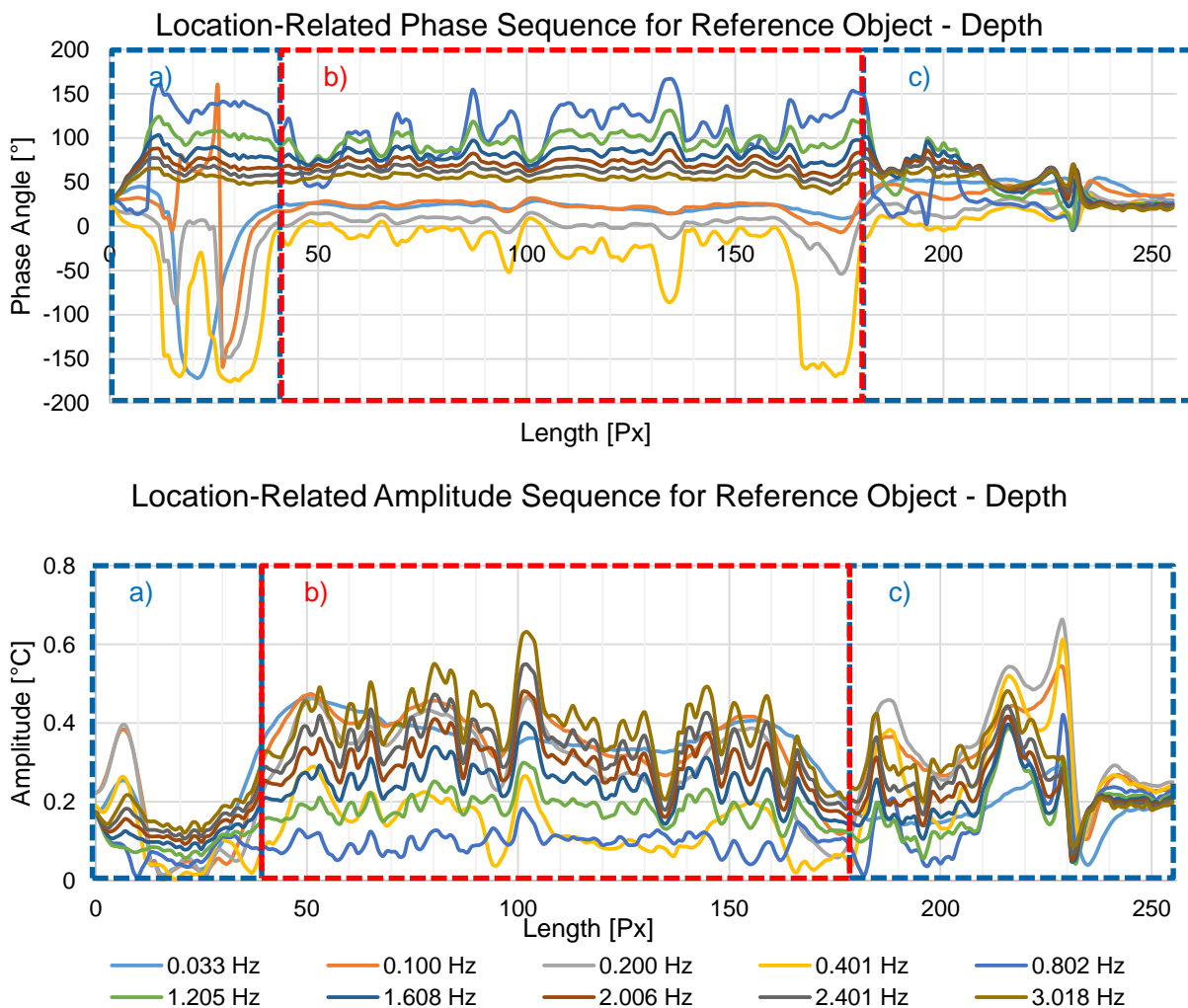

Figure 7-13: Location-related phase and amplitude sequence for cured surface reference object according to (A_Griener 2018)

The location-related phase and amplitude curves for the semi-finished reference object are depicted in Figure 7-14.

Location-Related Phase Sequence for Reference Object - Surface

Location-Related Amplitude Sequence for Reference Object - Surface
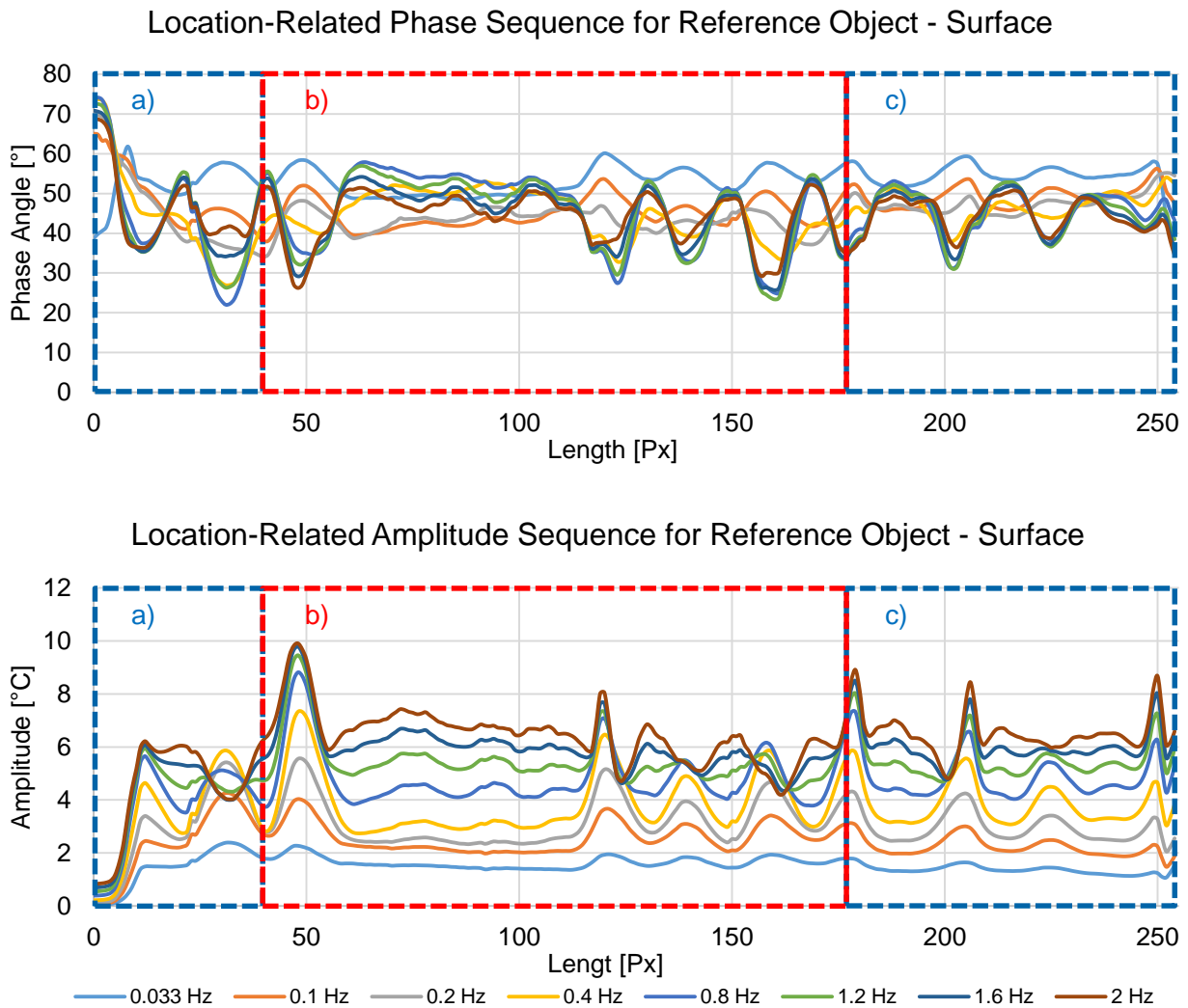
Figure 7-14: Location-related phase and amplitude sequence for semi-finished surface reference object

The curves peaks result from inhomogeneities, occurring in form of air inclusions in the semi-finished reference object.

7.5.2.1 Foreign Body

Cured Test Object

Figure 7-15 depicts both amplitude and phase in the frequency spectrum of the defect foreign body. As a result of the evaluation, no clear deviations from the reference object are noticed. From approx. 0.35 Hz, a flattened course in the phase spectrum can be observed. The average phase angle difference between reference and test object is approximately 2°.

Surface Defect Foreign Body
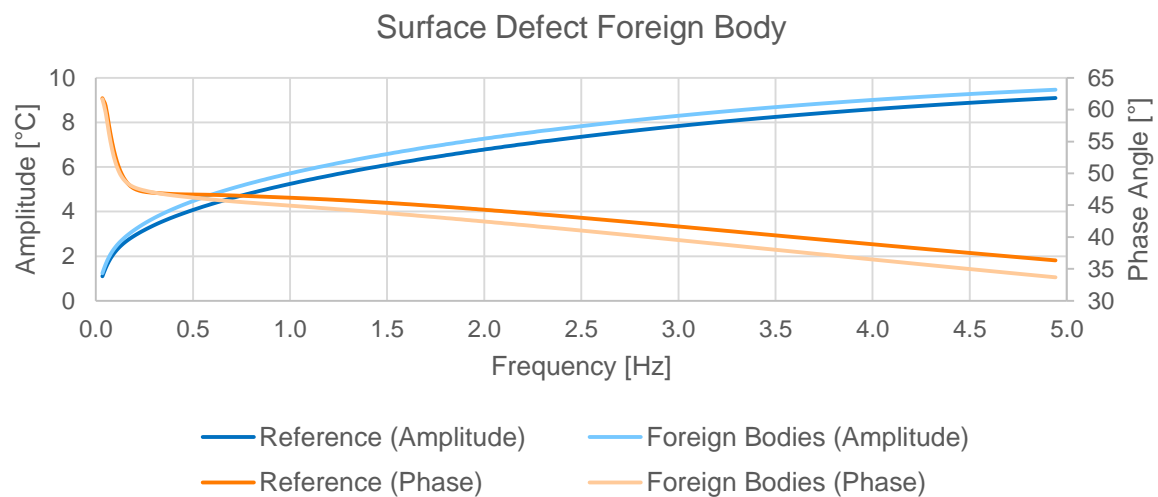
Figure 7-15: Frequency spectrum of the cured surface defect foreign body according to (A_Griener 2018)

This curve suggests, that the foreign body interacts with the thermal diffusion due to own thermal properties of the foil. Furthermore, this defect can also be considered as delamination (cf. Chapter 5.4.1). In this context, the consideration of contact resistance is an essential point. Defect boundaries are rough, so that heat transfer can only take place at microscopically small points, resulting in the entire heat flow passing through this reduced contact area. Delamination leads to a complete layer replacement and thus to a high contact resistance. This accumulates heat, becoming visible in a higher amplitude curve. (A_Griener 2018)

The divergent phase and amplitude curves indicate an existing defect, without providing specific characteristics to identify the defect. Thus, the following analysis is carried out in the location-related frequency spectrum. The location-related phase and amplitude sequence for foreign body is displayed in Figure 7-16.

In comparison to Figure 7-13, there is barely any difference in the location-related phase sequence. Changes can be observed above all in the marginal area. This can be attributed to surrounding perturbations and inhomogeneous excitation.

In the location-related amplitude spectrum, an increase in value range can be observed. Each frequency has an amplitude value 0.5°C higher than the reference component. This suggests that the heat is accumulated on the foreign body and the amplitude value increases. (A_Griener 2018)

Location-Related Phase Sequence for Foreign Body Test Object -
Surface

Location-Related Amplitude Sequence for Foreign Body Test Object -
Surface
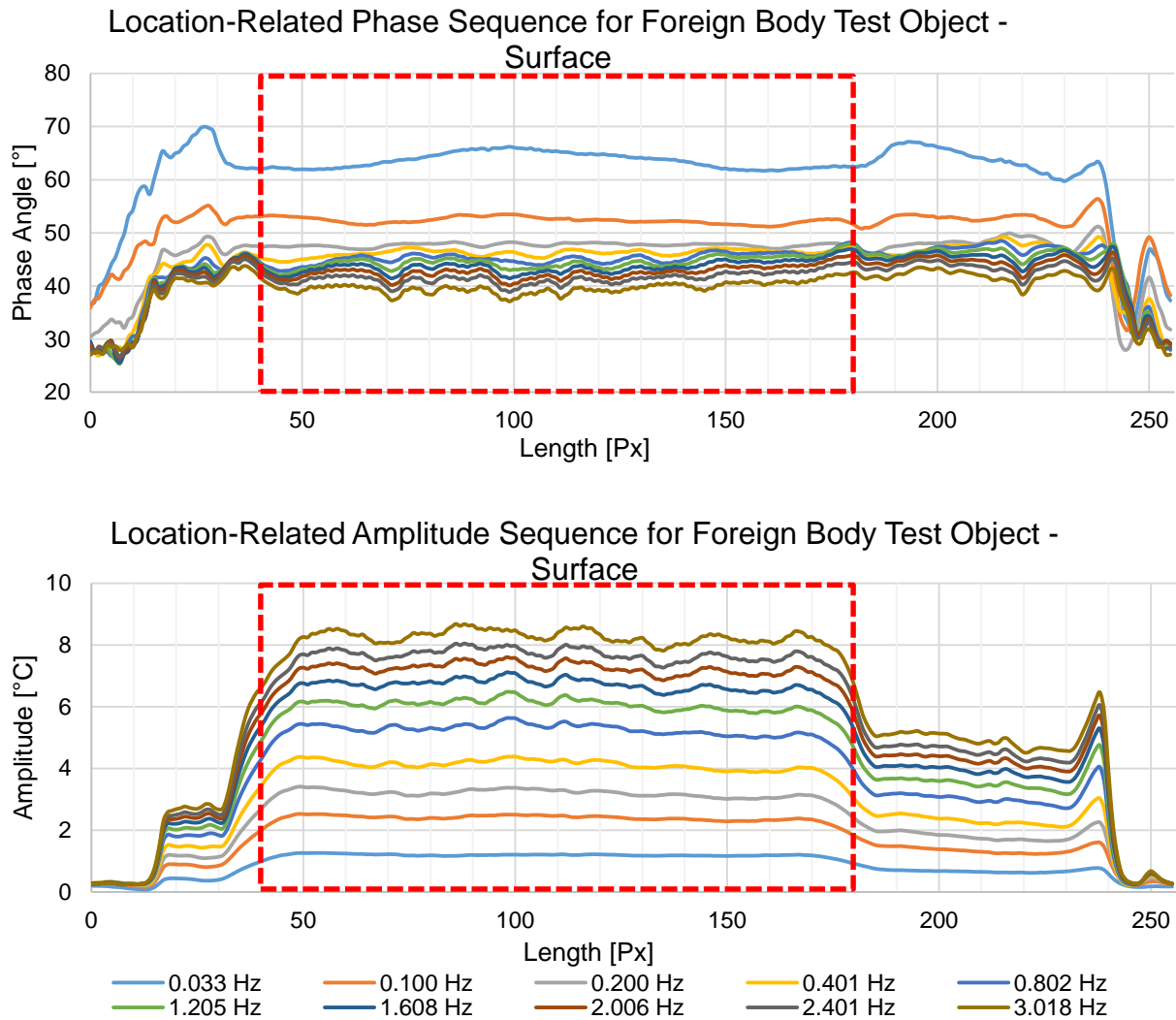
*Figure 7-16: Location-related phase and amplitude sequence for cured surface
foreign body test object according to (A_Griener 2018)*

Semi-Finished Test Object

The frequency spectrum of the semi-finished test object displays a deviation from the
reference object, illustrated in Figure 7-17. Both amplitude value and phase angle differ
from the reference object in the low-frequency range. The phase angle adjusts with
increasing frequency, since the foil is under Co-SMC and therefore not directly on the
surface. In contrast to the cured test object, this adjustment is justified by air inclusions
in the semi-finished product, acting as delamination. These are also present in the reference object so that no difference is discernible here. Therefore, the location-related
phase and amplitude sequence is also considered in Figure 7-18.

Surface Defect Foreign Body
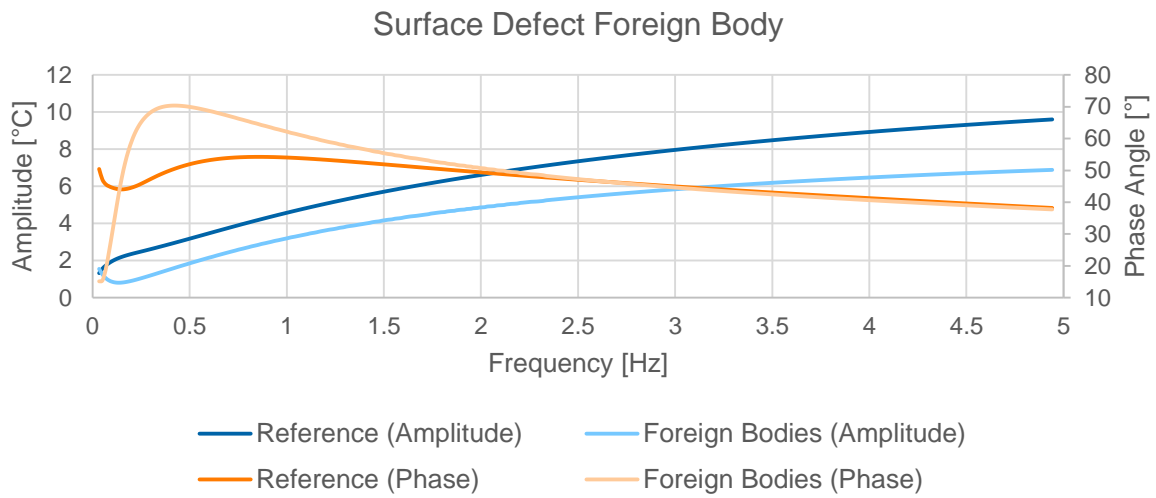
Figure 7-17: Frequency spectrum of the semi-finished surface defect foreign body according to (A_Griener 2018)
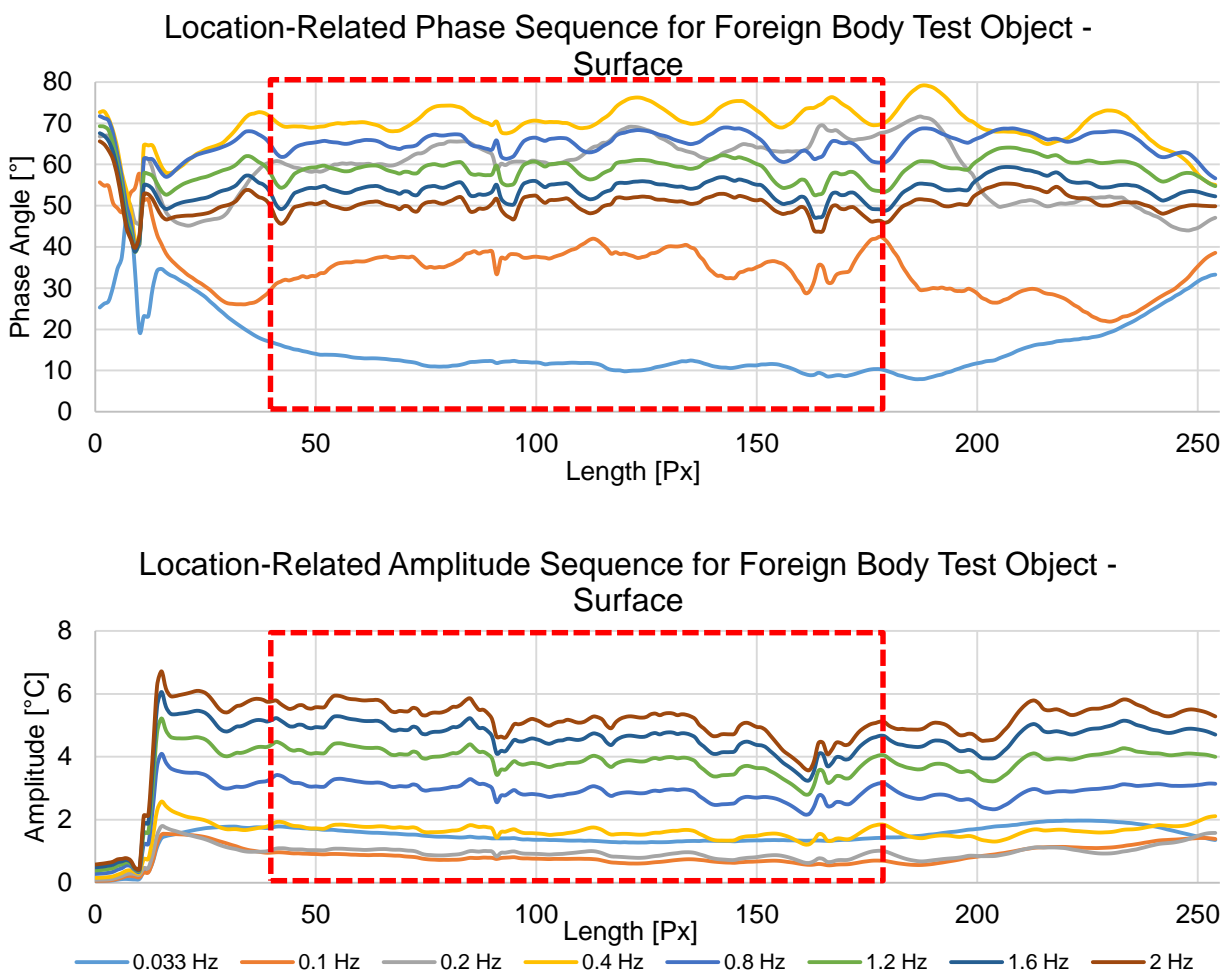
Figure 7-18: Location-related phase and amplitude sequence for semi-finished surface foreign body test object

The phase response comprises a much larger range of phase angles than the reference object, indicating a defect. For the amplitude values, the range is similar to the reference object. This is again justified by the air inclusions, similar to delamination and thus hindering the diffusion process in the same way as the foil. Therefore, the surface defect foreign body on semi-finished test objects cannot clearly be determined.

7.5.2.2 Fold

Cured Test Object

The frequency spectrum for the surface defect fold is illustrated in Figure 7-19.
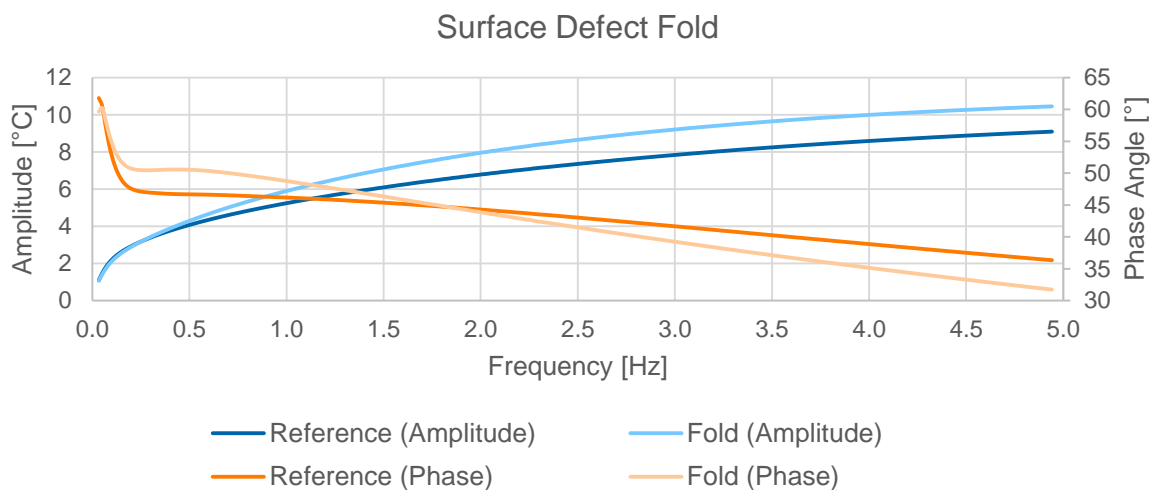
Figure 7-19: Frequency spectrum of the cured surface defect fold according to (A_Griener 2018)

The defect fold changes the layer structure, as there is a local accumulation of material. Thus, in the folded area there are five layers of material lying on top of each other, followed by DiCo-SMC - DiCo-SMC - Co-SMC - Co-SMC - Co-SMC, see Figure 7-8. Therefore, the thermal waves have to pass not only through the three usual layers, but also through the additional ones. Thereby, each layer has to be regarded as a resistance for the thermal diffusion process, which also increases the phase shift of the defect compared to the reference. In addition, the phase shift also increases due to interference effects, since the thermal waves are reflected at each individual layers boundary surfaces. (A_Griener 2018)

In the low-frequency range (up to 0.1 Hz), the folds phase response is similar to the reference object. However, a vertical shift towards higher phase values is recognizable at 0.41 Hz, with a phase angle difference of almost 4°, which can be explained by the

more difficult diffusion process due to the larger number of layers. From 0.5 Hz a digressive phase progression is visible at the fold, intersecting the reference progression approx. 2.0 Hz. Thus, from 0.5 Hz the depth range of the thermal wave is no longer sufficient and the diffusion process disturbed, resulting in a lower phase angle. As the frequency increases, the phase difference between reference and folded test object increases as well. (A_Griener 2018)

A uniform increase over the entire spectrum can be observed for the amplitude. From 0.5 Hz a strong value deviation compared to the reference object can be detected. A significantly higher amplitude value indicates a fold defect, but requires further evaluation. Thus, the local frequency range, which is depicted in Figure 7-20, is analysed subsequently. (A_Griener 2018)
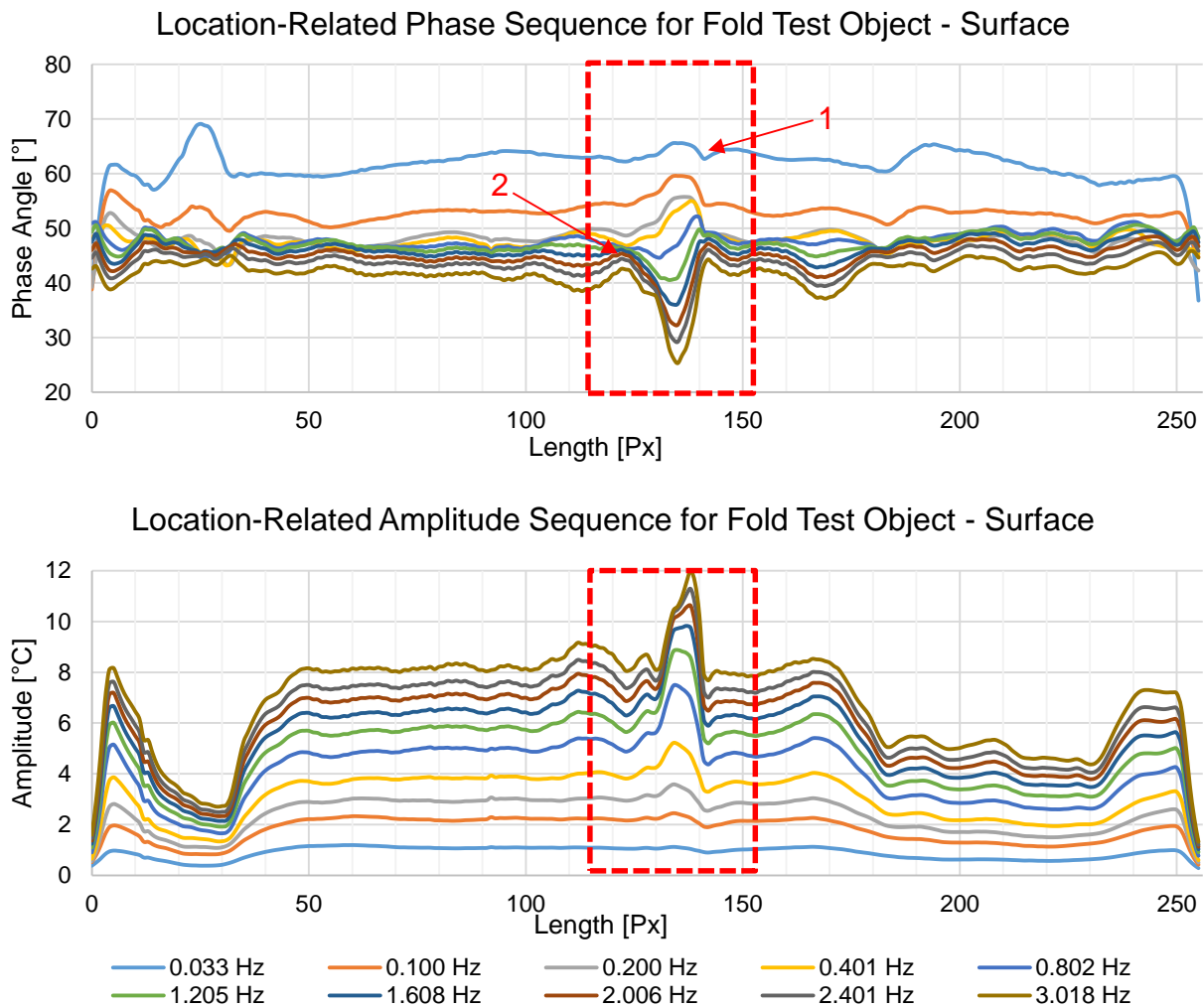
Figure 7-20: Location-related phase and amplitude sequence for cured surface fold test object according to (A_Griener 2018)

A clear characteristic feature can be seen in the location-related phase sequence. In the low-frequency range, the phase values increase. The fold boundary can also be seen in the diagram. A bend in the value (1) represents the transition from the single-layer Co-SMC to the three-layer Co-SMC. Since the defect is on the surface, it also has an influence on all the considered frequency characteristics. The second pleat edge (2), located under the top Co-SMC layer, is only detected at higher frequencies, i.e. at a lower depth. With the location-related amplitude curve, only a minimal increase in amplitude can be detected at low frequencies. As the frequency increases, the amplitude values rise. A global maximum in the fold area is reached with the amplitude values. The defect of the fold on the surface can be clearly characterized by the evaluations. (A_Griener 2018)

Semi-Finished Test Object

The frequency spectrum of the surface defect fold is displayed in Figure 7-21.
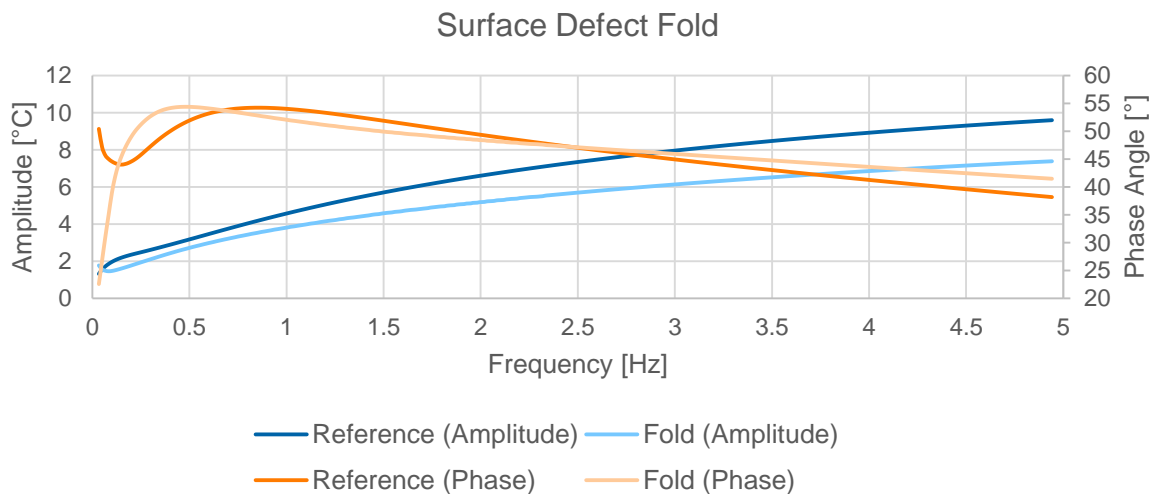
Figure 7-21: Frequency spectrum of the semi-finished surface defect fold

It is noticeable in Figure 7-21 that, in contrast to the cured test object, the reference amplitude is greater than the folded test object's. The phase angle courses also differ, intersecting three times. The cause of this behavior is the impossibility to compress the folded Co-SMC, resulting in the fold standing up and having air between the individual layers as illustrated by Appendix A 21 . Thus, no clear statement can be made about the defect. Therefore, the location-related phase and amplitude sequence in Figure 7-22 is also considered.

Location-Related Phase Sequence for Fold Test Object - Surface

Location-Related Amplitude Sequence for Fold Test Object - Surface
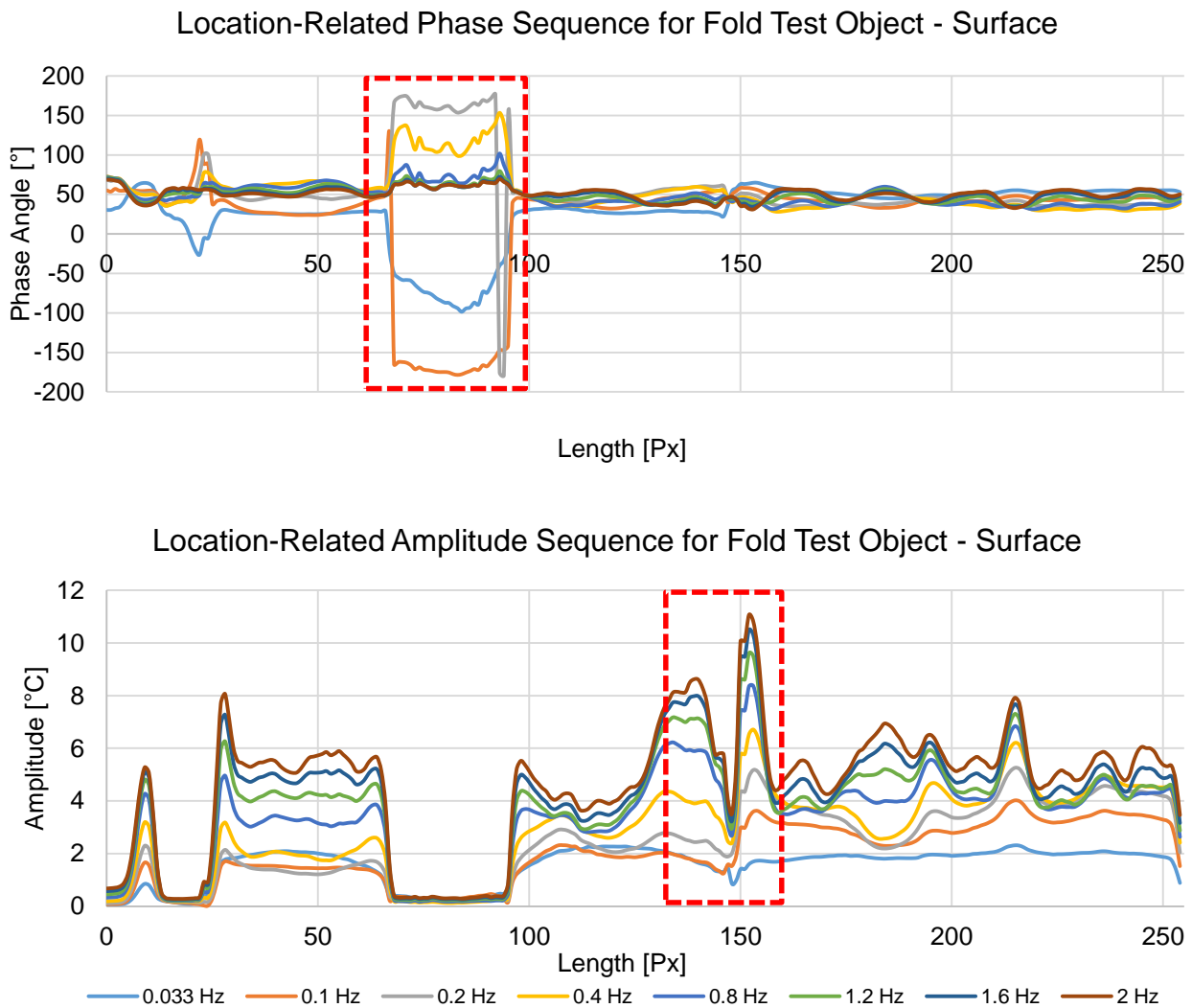
Figure 7-22: Location-related phase and amplitude sequence for semi-finished surface fold test object

The fold is located approximately in the range between pixel 130 and 150, where no characteristic is recognizable in the location-related phase sequence. The conspicuous deflections between pixels 70 and 90 result in the additionally attached DiCo-SMC to fix the Co-SMC (cf. Appendix A 21). This is also recognizable in the location-related amplitude curve. Furthermore, the amplitude value covers a larger value range between pixels 130 and 150. This is also caused by the disturbed diffusion process, indicating a defect, although it is not possible to clearly characterize the defect fold.

7.5.2.3 Angle Deviation

Cured Test Object

A different procedure is used to investigate the angular deviation. In the case of this defect, only the images in the frequency spectrum are considered, ensuring fast and

easy evaluation. For the measurement, the component is placed directly at a stopper whereby the edges lie parallel to the captured image. This means that no alignment of the image is necessary for a correct angle measurement. The evaluation of the angular deviation on the cured test object is based on the phase image.

At a frequency of 0.15 Hz, the test object surface is displayed and the evaluation is carried out with a line ROI, which is depicted as a red line in Figure 7-23. Due to the pressing process, the Co-SMC strips edge recognizably does no longer form a straight line. Therefore, the line ROI is placed directly on the outermost strip edge on the test object's upper plane. The DisplayIMG Professional software outputs the angle value of the line ROI. An angle of 12.5° is measured, deviating from the intended 15°, as well due to extrusion forces shifting the Co-SMC strip during the pressing process.
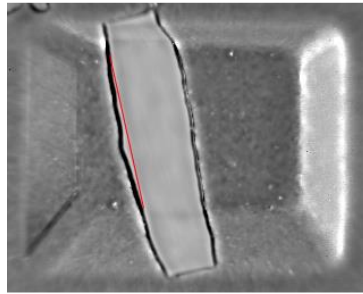
Figure 7-23: Phase image at 0.15 Hz of the cured surface test object with an angular deviation of 15°

Using frequency evaluation and line ROI, angular deviations can clearly be analyzed.

Semi-Finished Test Object
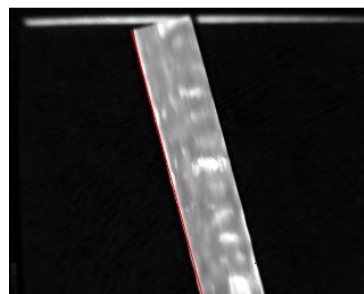
Figure 7-24: Amplitude image at 0.15 Hz of the semi-finished surface test object with an angular deviation of 15°

The amplitude image is considered more suitable for the evaluation of a semi-finished test object, as it provides a much better contrast. The Co-SMC edge is not yet distorted, so that the line ROI can be placed on the entire edge. The evaluation takes place at the same frequency of 0.15 Hz as for the cured component. The software supplies the value

15° and thus confirms the angular deviation at the semi-finished test object's surface. The image for evaluation is depicted in Figure 7-24.

7.5.3 Analysis of Depth Defects

This chapter deals with the same defects as the previous one, except these defects are in depth instead of on the surface.

Again, the evaluation methodologies frequency spectrum as well as in location-related phase and amplitude spectrum are carried out for each defect. Therefore, the plot of the frequency spectrum includes a defect free expected reference curve. In addition, the location-related phase and amplitude sequence are provided individually for each defect. Figure 7-25 and Figure 7-26 provide the cured and semi-finished reference object's location-related phase and amplitude spectrum to ensure comparability.

Figure 7-25: Location-related phase and amplitude sequence for cured depth reference object according to (A_Griener 2018)

Location-Related Phase Sequence for Reference Object - Depth

Location-Related Amplitude Sequence for Reference Object - Depth
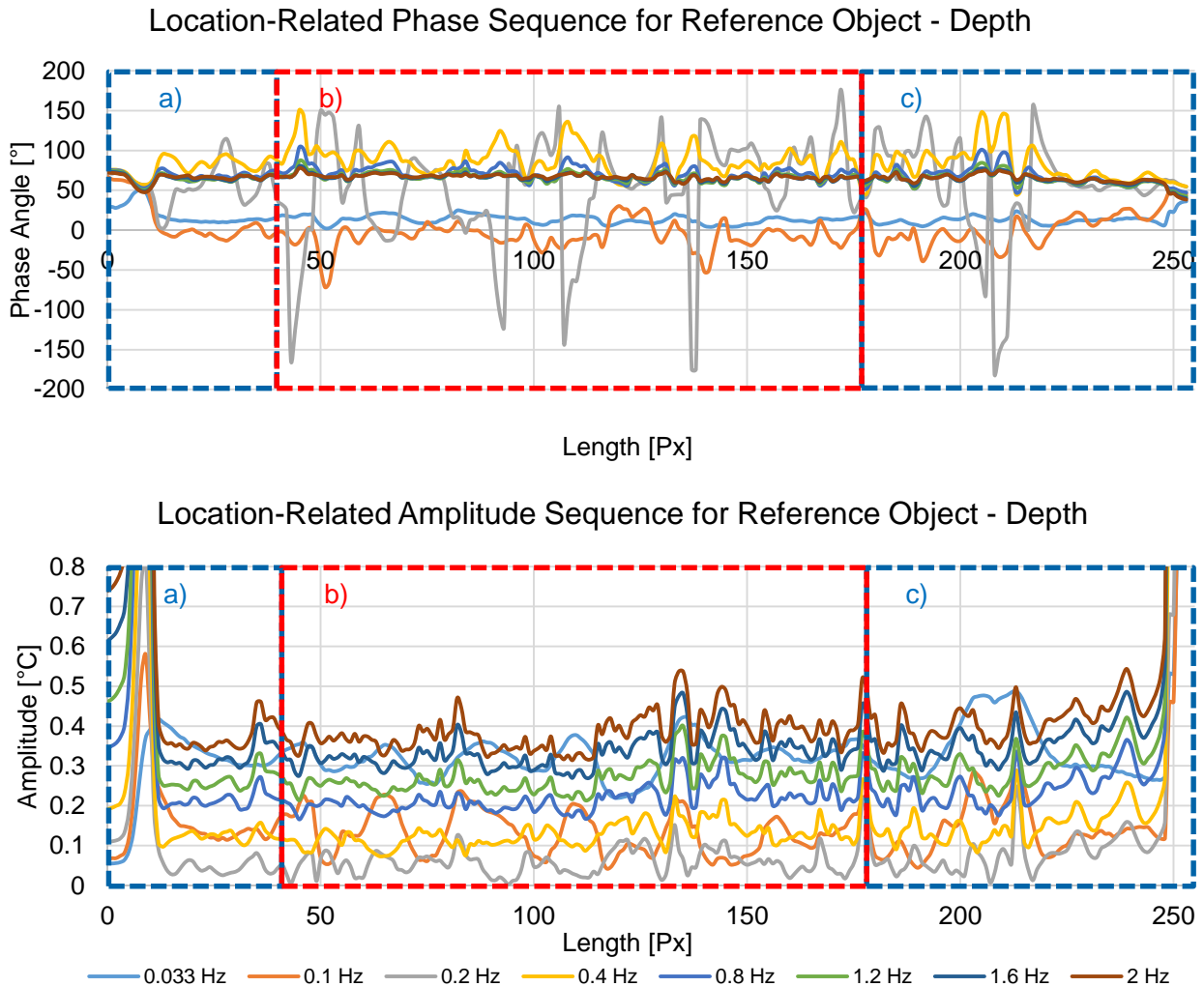
Figure 7-26: Location-related phase and amplitude sequence for semi-finished depth reference object

7.5.3.1 Foreign Body

Cured Test Object

A distinction is made between two variants of the depth defect foreign body. In case of foreign body 1, the foil is located under the Co-SMC strip. In case of foreign body 2 it is above the Co-SMC strip. The frequency spectrum curves are plotted in Figure 7-27.

The phase spectrum at the depth defect includes phase angles from - 40° to approx. 120°. A phase jump occurs between 0.3 Hz and 1.0 Hz. Negative phase angles of up to 0.6 Hz are detected. The following range shows a fast change to a high positive phase shift. Such a phase reversal has occurred with all examined test specimens of the depth defect series and can be evaluated as a characteristic feature for internal Co-

SMC. The phase jump can also be detected in the amplitude spectrum by a local minimum. (A_Griener 2018)

Depth Defect Foreign Body
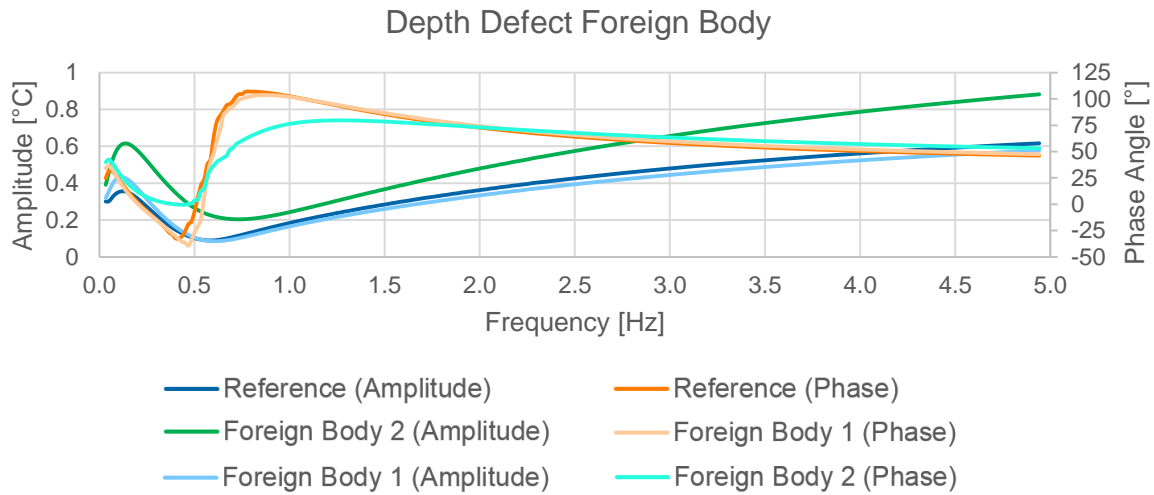
Figure 7-27: Frequency spectrum of the cured depth defect foreign body according to (A_Griener 2018)

Considering the phase characteristics, a clear difference between foreign bodies 1 and 2 is noticeable. The course of foreign bodies 1 is almost identical to the reference object, only in the range between 0.1 Hz and 0.5 Hz deviating phase values are measured. This conforms to the assumption that only low-frequency thermal waves are able to reach a sufficient depth range. With foil on Co-SMC (foreign body 2), clear phase angle differences up to 40° are visible. With increasing frequency, all phase values equalize, since a smaller depth range is achieved and the foreign body has no influence on the thermal wave. (A_Griener 2018)

Also in the amplitude spectrum, the course of foreign body 1 is similar to the reference object, only in low-frequency range below 0.3 Hz higher amplitude values are visible. Foreign body 2 has a considerably higher amplitude spectrum, which is nearly parallel to the reference until 1.0 Hz and increases progressively above. As a result, this defect on top of Co-SMC interferes with the heat diffusion process. (A_Griener 2018)

This investigation indicates characteristic effects in the phase and amplitude image. In addition, the location-related frequency sequence is considered. Figure 7-28 illustrates only foreign body 2, since no conspicuous values are detected for foreign body 1.

No characteristic features can be detected in the location-related phase spectrum. The compressed value range compared to the reference object can be attributed to the disturbed heat diffusion.
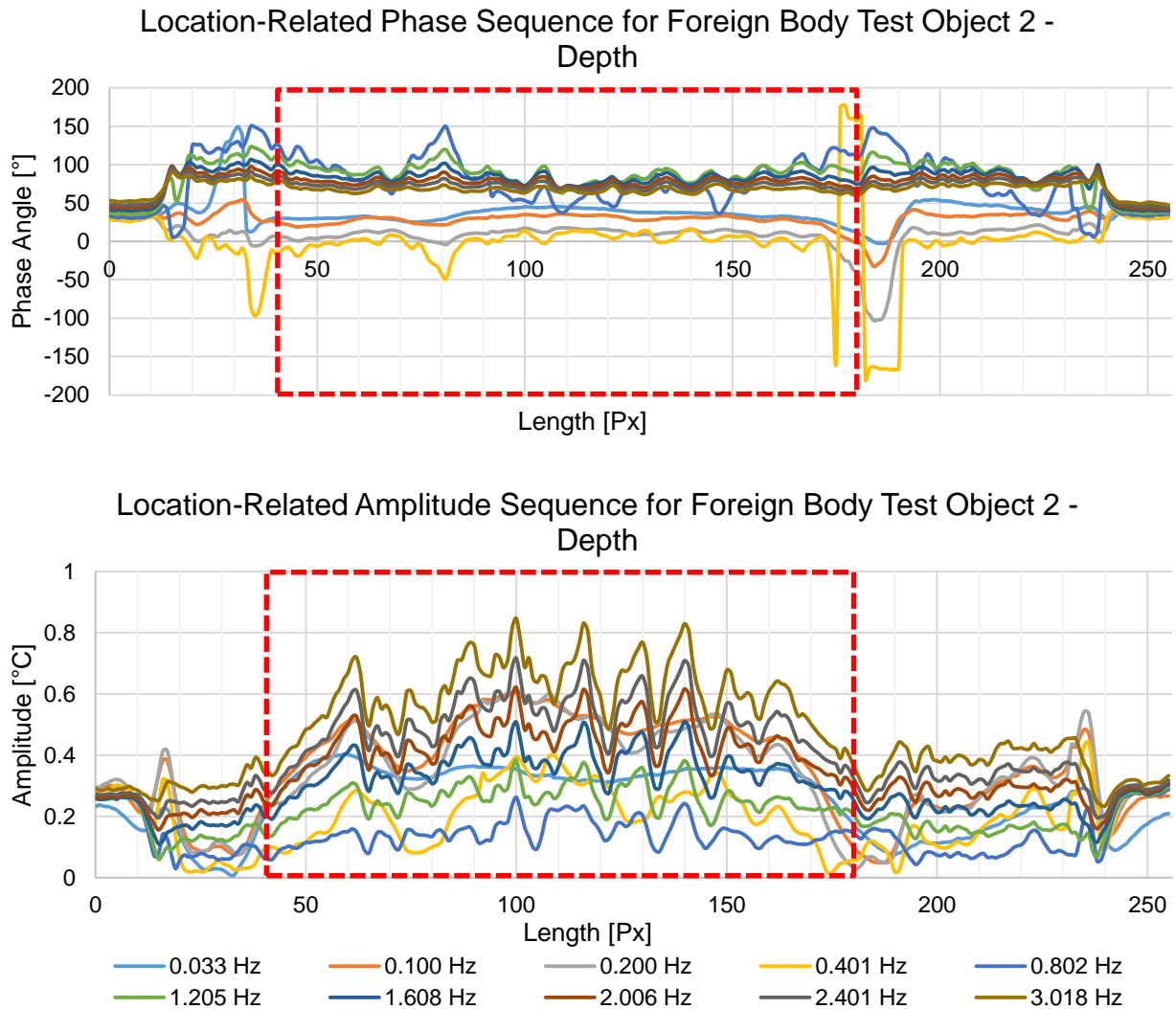
Figure 7-28: Location-related phase and amplitude sequence for cured depth foreign body 2 test object according to (A_Griener 2018)

The location-related amplitude curve again shows clear effects. The frequencies considered have increased amplitude values and an unsteady course. (A_Griener 2018)

Especially through the frequency spectrum analysis, the defect can be attributed to foreign bodies. The location-based evaluation scarcely provides any added value.

Semi-Finished Test Object

For the semi-finished test object, the same foil placement variants are examined as described for the cured test object. The evaluation in the frequency spectrum is presented in Figure 7-29.

Depth Defect Foreign Body
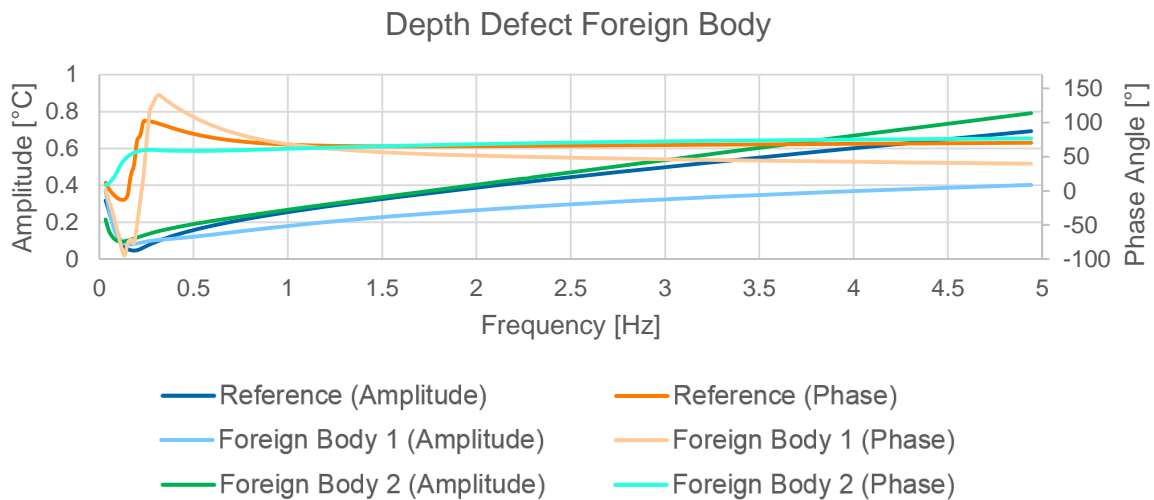
Figure 7-29: Frequency spectrum of the semi-finished depth defect foreign body

The behavior differs from the cured objects. Foreign body 2, located closer to the surface, is very similar to the reference object regarding the amplitude curve. Only in the low-frequency range below 0.5 Hz as well as at frequencies above approx. 2.5 Hz, the curves drift apart. In this low-frequency range, foreign body 1 and the reference object are similar, but diverge at approx. 0.4 Hz.

Both phase courses shows clear deviations from the reference object, for example in the phase jump of foreign object 1. Foreign object 2 is similar to the reference object from a frequency of 1 Hz. With this component, the foil is almost on the surface. Due to air inclusions, the reference object behaves similarly to the test object. The evaluation of the semi-finished test object also shows that there is a defect, but no characterization is possible.

The investigation in location-related phase and amplitude sequence is presented below. The location-related phase sequence is plotted for both foreign bodies, since they differ significantly. The location-related amplitude curve is similar for both foil placement variants, therefore only foreign body 2 is plotted.

Location-Related Phase Sequence for Foreign Body Test Object 1 - Depth

Location-Related Phase Sequence for Foreign Body Test Object 2 - Depth

Location-Related Amplitude Sequence for Foreign Body Test Object 2 - Depth
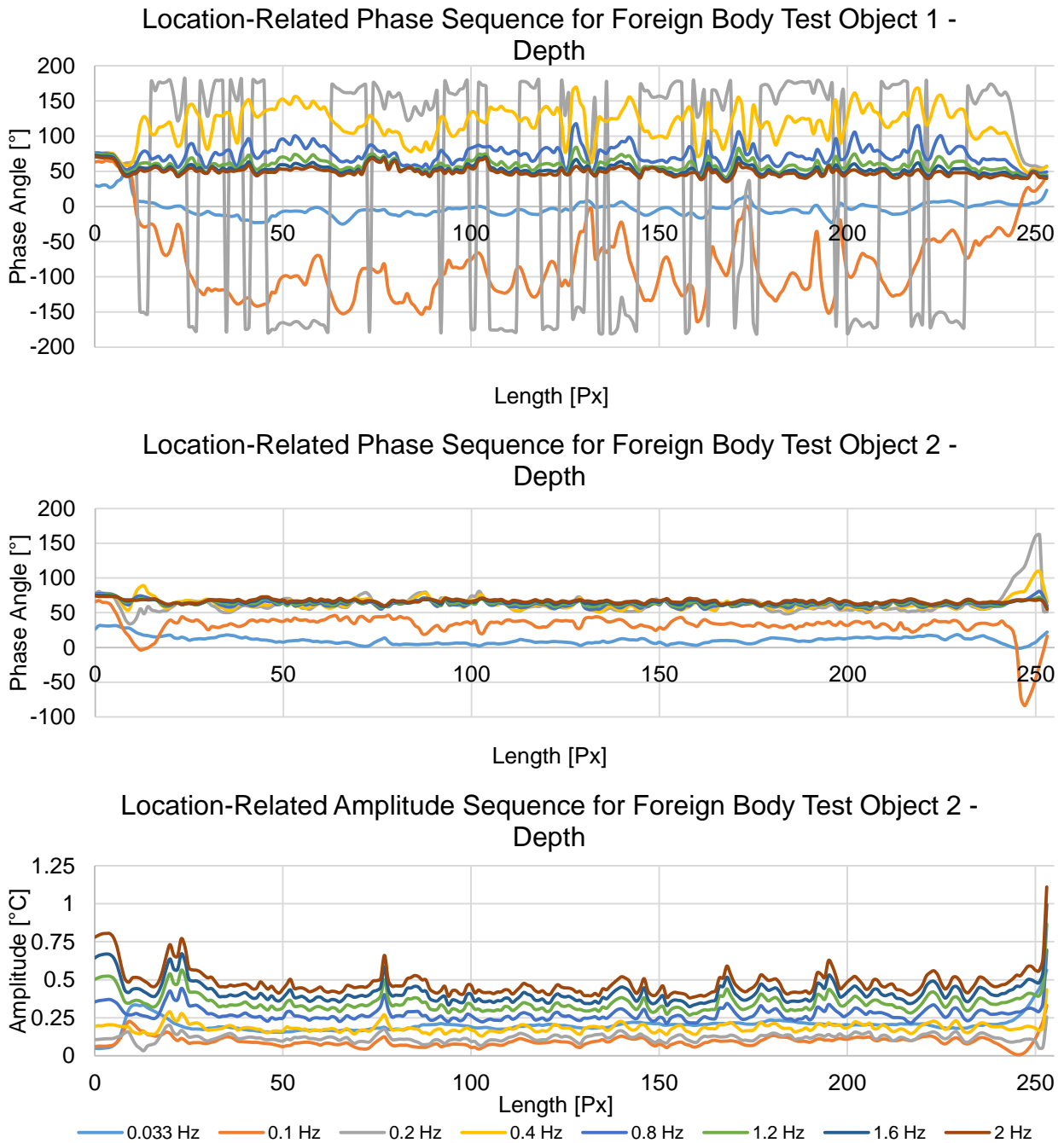
Figure 7-30: Location-related phase and amplitude sequence for semi-finished depth foreign body test object

Foreign bodies 1 is very unsteady in the local phase progression, covering a much larger value range than the reference object. This is a first indication of a foreign body in the semi-finished test object and can be explained by air inclusions between the foil and the Co-SMC. Foreign body 2 shows rather a compressed behavior and has a smaller value range than the reference object. This is due to the disturbed diffusion processes, but cannot be clearly defined.

In the location-related amplitude curve, foreign body 2 is only insignificantly higher than the reference. Thus, it does not allow any statement about defect characterization.

7.5.3.2 Fold

Cured Test Object
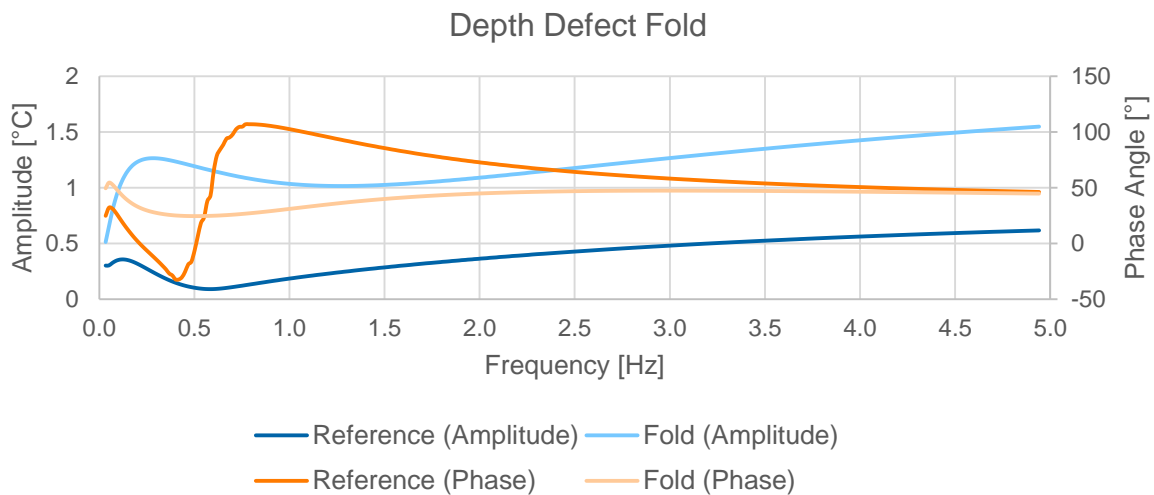
Figure 7-31: Frequency spectrum of the cured depth defect fold according to (A_Griener 2018)

As illustrated in Figure 7-31, the fold's phase spectrum is strongly attenuated compared to the reference, including the missing phase jump. Between reference and test object, phase differences up to 90° are achieved in the range of 0.5 – 1 Hz. From approx. 4.0 Hz on, the phase values equal the reference object.

A characteristic curve is recognizable in the amplitude spectrum, because the defect fold causes a significant increase in amplitude values. Again, this is explained by the disturbed heat flow due to the new layer structure. (A_Griener 2018)

In addition, an investigation in the location-related frequency spectrum, which is illustrated in Figure 7-32, is also carried out.

At high frequencies, global maxima and minima caused by layer boundary effects are recognizable in the location-related phase and amplitude sequences. The low phase angle in the fold area between pixels 110 and 150 indicates a multi-layer structure. Higher values in the fold area are noticeable in the amplitude progression. Thus, the local phase and amplitude curves confirm the presence of a fold. (A_Griener 2018)
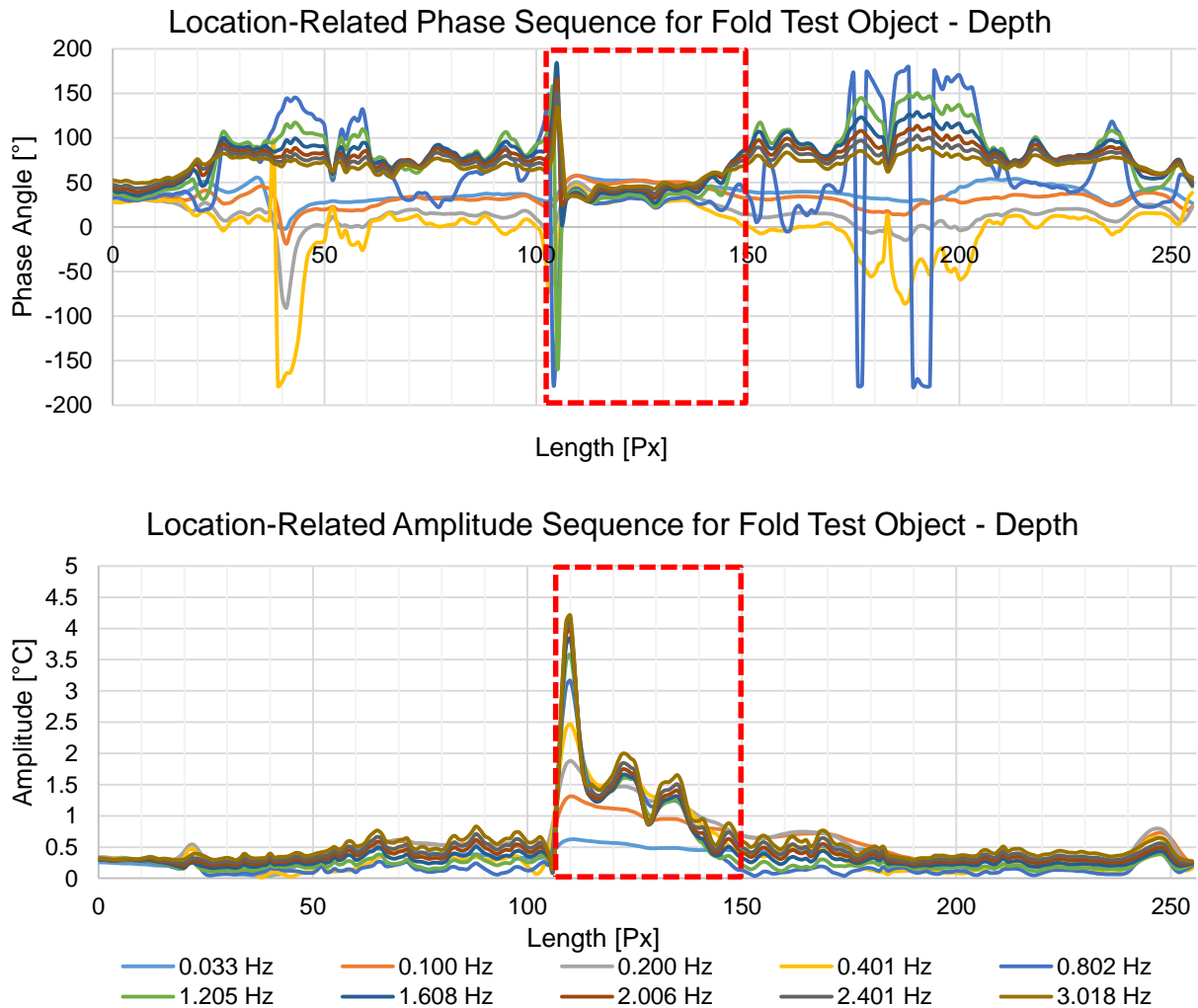
Figure 7-32: Location-related phase and amplitude sequence for cured depth fold test object according to (A_Griener 2018)

Semi-Finished Test Object

Figure 7-33 depicts the phase and amplitude progression of fold and reference object.

As in the previous investigations, at higher frequencies the amplitude value of the test object is lower than the reference. This is justified by air inclusions in the semi-finished material. In the low-frequency range (< 0.5 Hz), the fold has a stronger amplitude effect, since it is a depth defect accumulating heat at the additional layers. Also in the low-frequency range, the phase angle covers a larger value range than the reference, which indicates a defect. The location-related evaluation is presented in Figure 7-34.
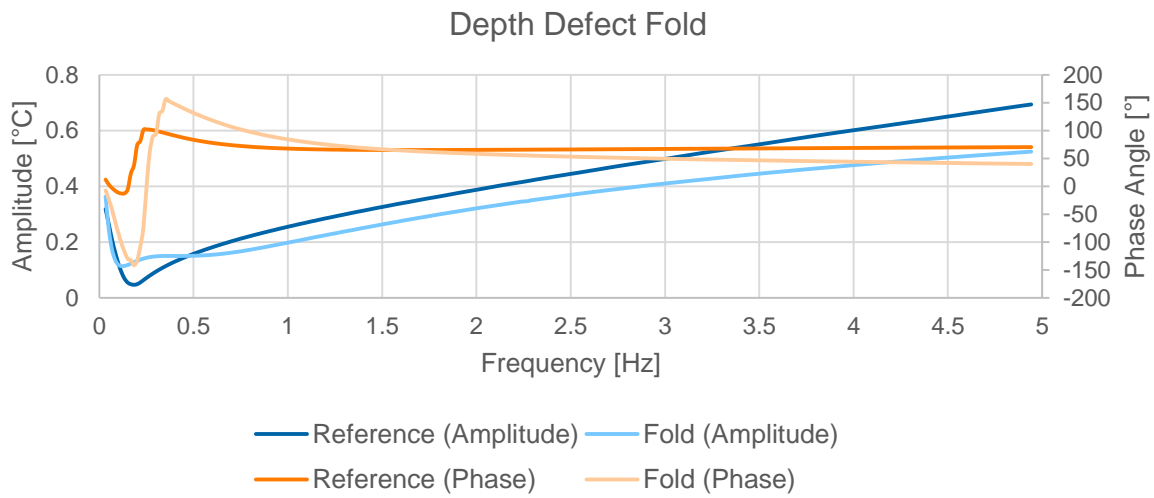
Figure 7-33: Frequency spectrum of the semi-finished depth defect fold
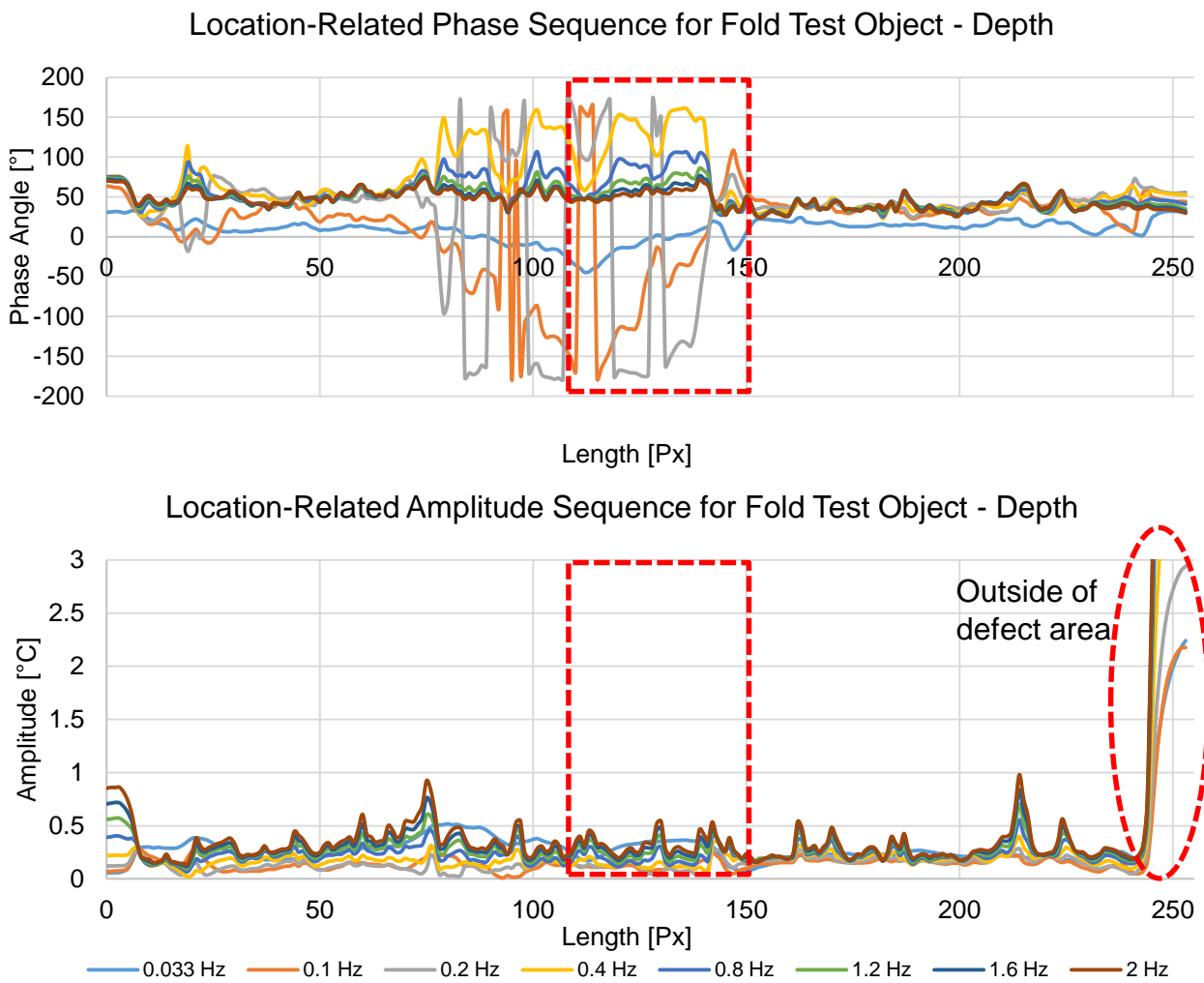
Figure 7-34: Location-related phase and amplitude sequence for semi-finished depth fold test object in state

No defect can be inferred from the location-related amplitude sequence. The jump around pixel 240 is due to the missing Co-SMC besides DiCo-SMC at the end of the test object (cf. Appendix A 21). The fold is located between pixels 120 and 150. In this area, clear deflections are recognizable at the frequencies 0.1 Hz and 0.2 Hz. These indicate a deeper range and a disturbance of the diffusion process. This can be regarded a characteristic feature of the depth fold defect in semi-finished test object.

7.5.3.3 Angle Deviation

Cured Test Object

The frequency 0.05 Hz is selected for evaluation of the depth defect due to the good contrast, as illustrated in Figure 7-35. The edges are slightly blurred. However, it is possible to place a line ROI. The measurement results in an angle of 14.8°. Thus, evaluation in the frequency domain enables the determination of the depth defect angular deviation of Co-SMC.
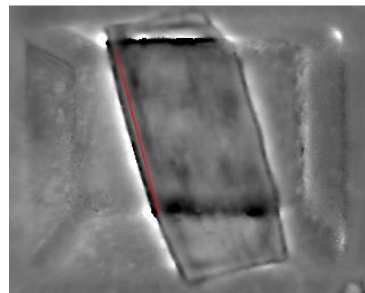
Figure 7-35: Phase image at 0.05 Hz of the depth test object in cured state with an angular deviation of 15°

Semi-Finished Test Object
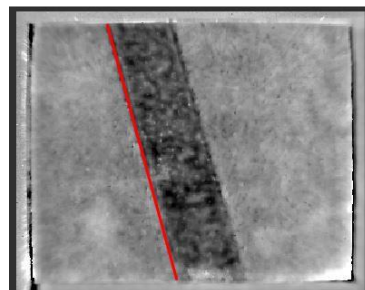
Figure 7-36: Phase image at 0.05 Hz of the depth test object in semi-finished state with an angular deviation of 15°

Contrary to the assumption made in Chapter 7.5.2.3, the phase image for a depth defect is more suitable for the evaluation of semi-finished test object. The evaluation takes place at 0.05 Hz, resulting in the image, as depicted in Figure 7-36. The measured

angle is 15.2°. Thus an angle determination can also be carried out on the semi-finished test object in the case of a depth defect.

7.5.4 Summary and Evaluation of Defect Characterization

The presented investigation indicate, that evaluating the cured test object with a thermogram does not allow clear conclusions to be drawn regarding the defect type or its characteristics. Therefore, a defect classification is carried out with help of the phase and amplitude images, since noticeable defect describing characteristics are determined. Thus, it is possible to clearly deduce a defect by evaluating the frequency spectrum and the location-related value sequence. A two-stage analysis of the available evaluation possibilities is recommended, as illustrated in Figure 7-37.
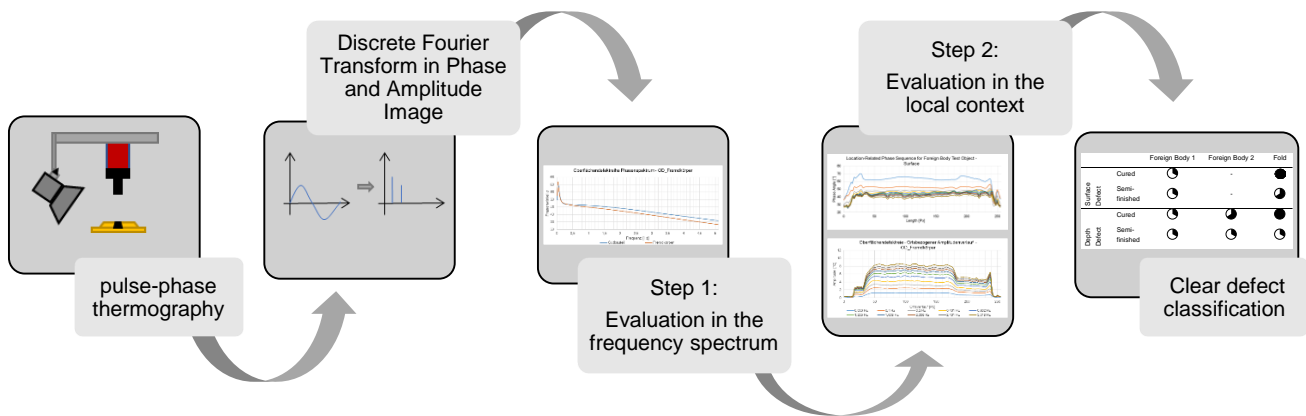
Figure 7-37: Schematic sequence for the unambiguous detection of defects for cured test objects according to (A_Griener 2018)

For the cured test objects, the findings from the observations of the defect processes are summarized in Appendix A 22 in Table A-10 and consolidated for a defect characterization in a two-stage analysis. For each defect, the optimum reason for consideration in the frequency spectrum and in the location-related sequence of values is selected. Table 7-7 lists, how good a defect can be characterized in cured and semi-finished test objects.

Examining the semi-finished test object indicates, that it is impossible to assign unambiguous characteristic features to this condition. The damping of the semi-finished material is too high and the number of air inclusions too large to enable detection of clear differences with the individual evaluations. Only the defect presence is demonstrated with the described procedures. The angle evaluation is possible for the cured as well as for the semi-finished test object in the frequency spectrum (cf. Table A-11 in Appendix A 22). Thus, the fourth research question (cf. Chapter 1.2) for the semi-finished test

object can be answered. Furthermore, the investigation shows that layer structure and material have to be known in order to determine and characterize a defect.

Table 7-7: Evaluation of defect characterization

		Foreign Body 1	Foreign Body 2	Fold	Angle
Surface Defect	Cured	(first indications)	-	(clear)	(clear)
Surface Defect	Semi-finished	(first indications)	-	(recognizable, not characterizable)	(clear)
Depth Defect	Cured	(first indications)	(first indications)	(clear)	(clear)
Depth Defect	Semi-finished	(recognizable, not characterizable)	(first indications)	(first indications)	(clear)

Legend:	◯ No characterization possible	◔ First indications of defect visible
	◕ Defect clearly recognize-, but not characterizable	● Clear defect characterization

Nevertheless, it is possible to make a statement about the selected defects in cured test objects by linking individual thermographic evaluations. With the procedure described in Figure 7-37, defects on cured test objects can be characterized by thermography, answering the fourth research question (cf. Chapter 1.2) for these components.

7.6 PPT Measurement Uncertainty

As for LLSS, the measurement uncertainty is also determined for PPT. For this analysis, a new test object is used both for cured and for semi-finished state. Initially, these test objects are introduced and the procedure for the measurement uncertainty analysis is described. The results for cured and semi-finished test objects are then presented. Finally, an evaluation of the determined measurement uncertainty is carried out.

7.6.1 Test Objects and Features for PPT Measurement Uncertainty

DiCo-SMC from ICT and Co-SMC from Polynt Composites Germany GmbH are used for both cured and semi-finished test objects. For the cured test object, the thick layer structure (cf. Chapter 5.2) is pressed to a plate. Five blind holes with different diameters and residual wall thicknesses are drilled into this plate, as illustrated in Figure 7-38 on the left and listed in Table 7-8. The residual wall thicknesses are checked with the CMM

O-INSPECT from ZEISS, the resulting values are also listed in Table 7-8. The values approve that 1.0 mm, 2.0 mm and 2.5 mm can be assumed the residual wall thickness.
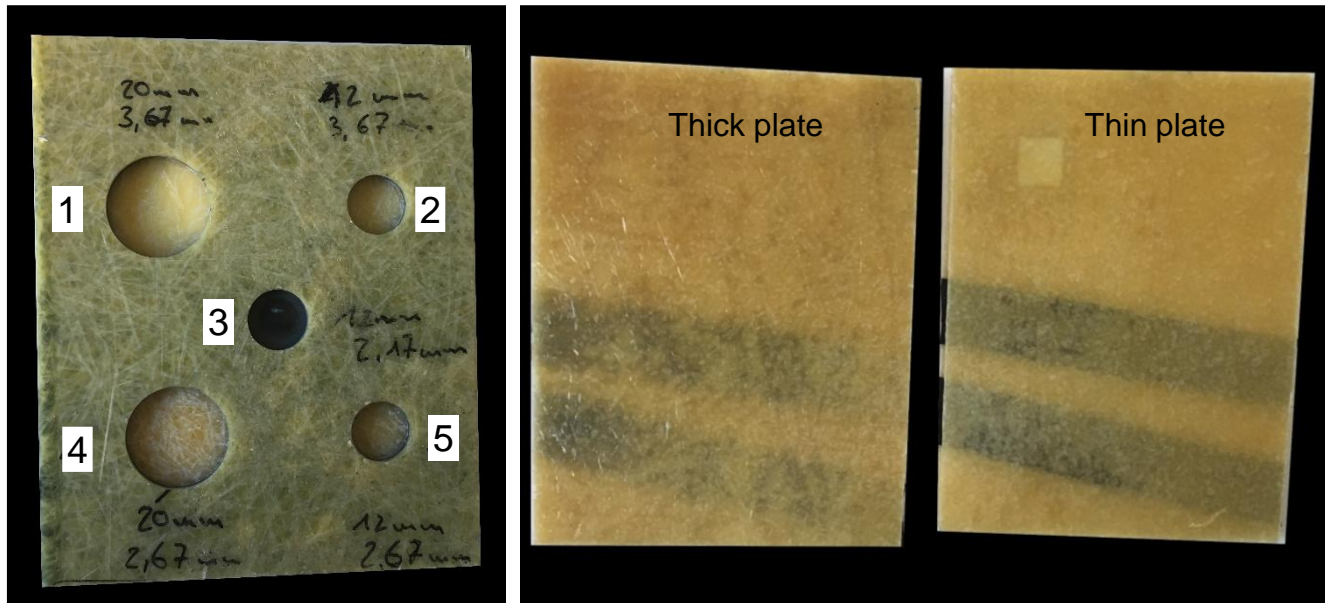
Figure 7-38: Cured test object (left), two semi-finished test object (right) for measurement uncertainty

Two test objects are used for the semi-finished product, both depicted in Figure 7-38 on the right. For this purpose, both layer structures from Chapter 5.2 are used. Two Co-SMC strips with different angles are inserted between the DiCo-SMC layers: 8° and 14° for the thick plate as well as 8° and 12° for the thin plate.

Table 7-8: Characteristic parameters attribution and comparison of residual wall thickness with CMM

Feature number	Diameter [mm]	Residual wall thickness [mm]	Comparison measurement with CMM [mm]
1	20	1.0	0.96
2	12	1.0	0.94
3	12	2.5	2.42
4	20	2.0	1.94
5	12	2.0	1.91

7.6.2 General Procedure of PPT Measurement Uncertainty Analysis

Different characteristics are defined for the test objects. Characteristics and procedure are explained below for the cured and the semi-finished test objects.

7.6.2.1 Cured Test Object

For the perforated plate made of cured material, the diameter is the defined feature. The measurement uncertainty determination is performed on basis of the known residual wall thickness and the depth analysis described in Chapter 7.4.

25 measurements are carried out for each blind hole. The recording time is 60 s, the camera distance 37.0 cm and the flash distance 22.3 cm. The subsequent discrete Fourier Transform is performed at the frequencies 0.117 Hz, 0.05 Hz and 0.083 Hz, which correspond to the residual wall thicknesses 1.0 mm, 2.0 mm and 2.5 mm according to Table 7-4 in Chapter 7.4.

Afterwards, each hole is evaluated with the blob analysis (Binary Large Object) in the DisplayIMG Plus software. This analysis captures contiguous areas of the binary image and can be evaluated with respect to various criteria, such as the area (Brabandt 2018), as in this thesis. For the evaluation, the unit 'Pixel' has to be converted to 'mm'. This is done by calibrating the camera image using a chessboard pattern. The calibration procedure is described in Figure 7-39.
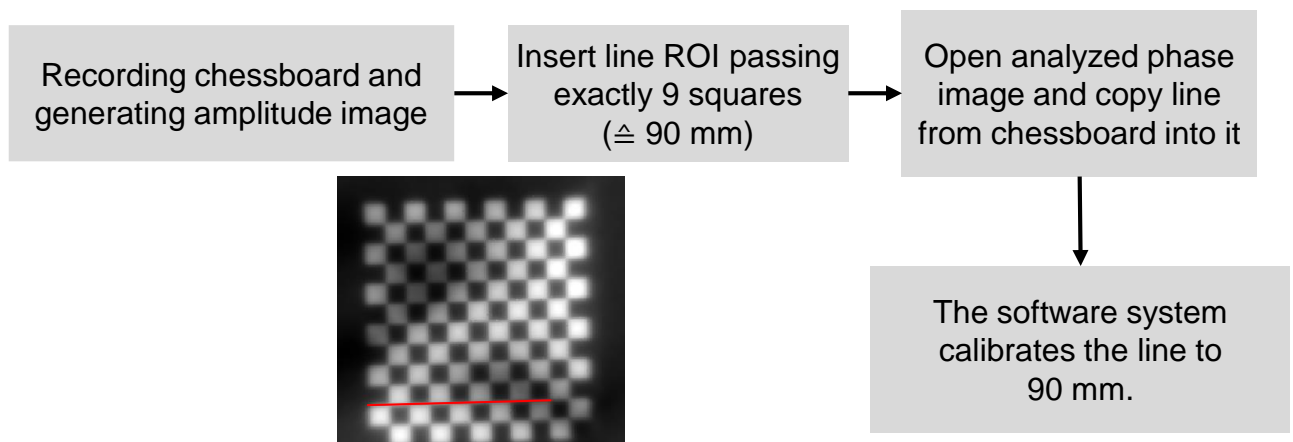
Figure 7-39: Procedure for calibrating a thermographic measurement from 'Pixel' to 'mm' according to (A_Ibach 2018)

After measurement, a rectangular ROI is drawn around the hole at the appropriate frequency for the remaining wall thickness, cf. Figure 7-40. Subsequently, the blob analysis is performed in this ROI. This evaluation step is exemplarily illustrated in Figure 7-40 for all five blind holes. With the 25 measurements the standard uncertainty from the measurement method of cured test object $u_{p\_PPT\_cu}$ can be calculated according to Equation 2-6 on page 24.
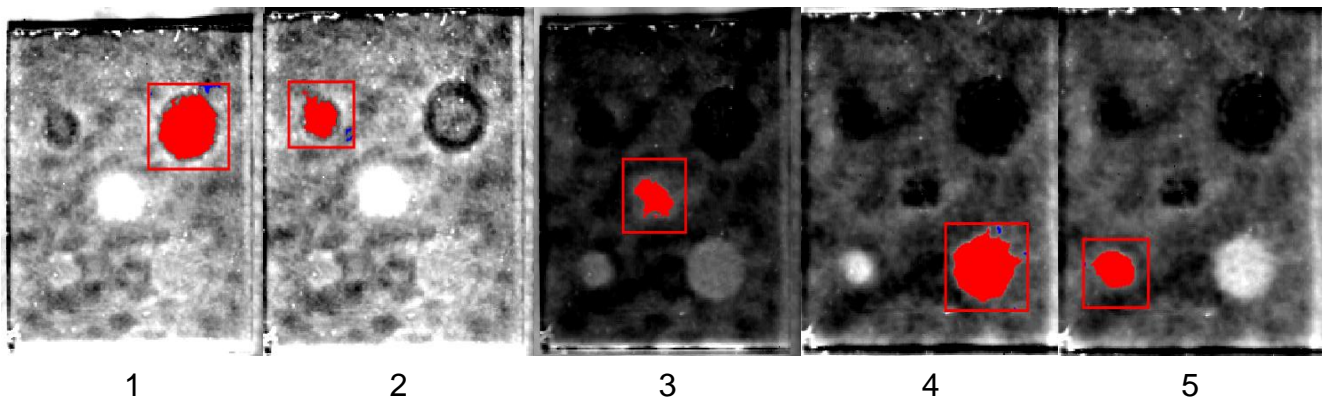
Figure 7-40: Blob analysis for all five blind holes

In addition, for a complete measurement uncertainty balance according to Equation 2-3, u_{cal}, u_w and u_b have to be determined. u_w can be neglected according to (DIN EN ISO 15530-3), since the conditions for scattering of thermal expansion coefficients and the similarity conditions are met.

To determine $u_{cal\_PPT\_cu}$, five reference measurements are carried out with the CT ZEISS METROTOM 800, similar to the measurement uncertainty analysis for LLSS. The measurement parameters are listed in Appendix A 23. $u_{p\_CT\_cu}$ is calculated from the five measurements (cf. Appendix A 24). In order to indicate the accuracy, the test uncertainty can be used according to (DIN ISO/TS 23165). This is 1.2 µm according to (Carl Zeiss Industrielle Messtechnik GmbH 2011). Therefore, $u_{cal\_CT\_cu}$ and $u_{b\_CT\_cu}$ are set to zero. Thus, CT can be assumed to be much more accurate than thermography, especially since thermography up to now is not regarded as a measuring system but as a testing system and therefore no information on accuracy is given.

Thus, $u_{p\_CT\_cu}$ is included as $u_{cal\_PPT\_cu}$ in the measurement uncertainty balance of thermography. The mean value of the five CT measurements is x_{cal} for bias calculation. In the present thesis, the uncertainty from systematic deviation is determined according to Equation 2-8. Thus, for thermography the measurement uncertainty balance for the cured test object equates according to the following:

$$U_{PPT\_cu} = k \sqrt{u_{p\_CT\_cu}^2 + u_{p\_PPT\_cu}^2 + u_{b\_PPT\_cu}^2} \qquad \text{Equation 7-1}$$

7.6.2.2 Semi-finished Test Object

The features for determining the measurement uncertainty of the semi-finished test objects are the different angles of the Co-SMC, located between the DiCo-SMC. The angle always refers to the short edge closest to the Co-SMC strip. 25 thermographic measurements are carried out per test object, with a subsequent discrete Fourier Transform. The evaluation of the thin test object, with two layers DiCo-SMC, is performed at a frequency of 0.151 Hz. For the thick test object, with four layers of DiCo-SMC, the frequency 0.05 Hz is used. One line ROI is always applied to the test object edge as a reference (green line) plus a second line ROI to the Co-SMC strip (red and blue line). The DisplayIMG Plus software provides the angle of the respective second line ROI. Figure 7-41 illustrates the evaluation for both thick and thin test object.
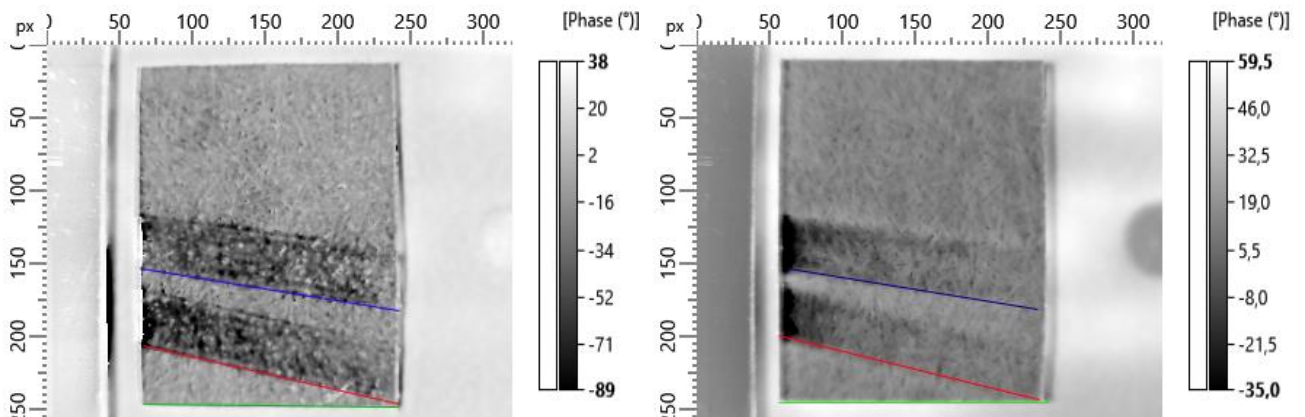
Figure 7-41: Thin (left) and (right) thick test object of semi-finished material
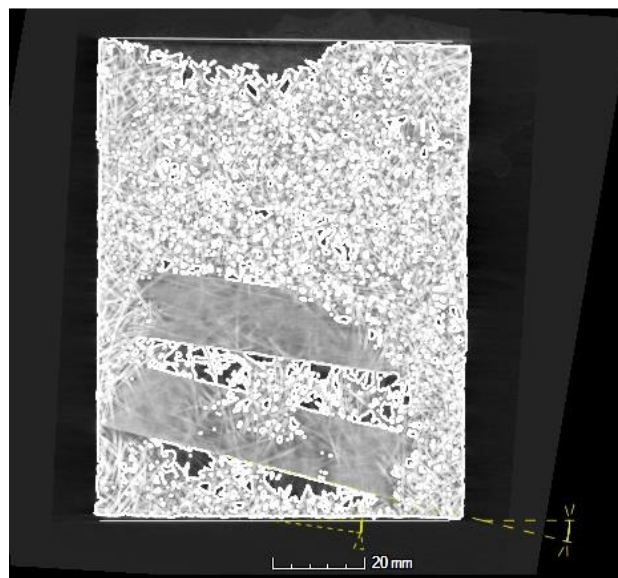
Figure 7-42: Angle evaluation for the semi-finished test object with CT

For reference, five measurements are carried out with the CT as described for the cured test object (appendix A 26). For the subsequent evaluation, the surface is automatically determined and the so called 3-2-1 registration is done. Therefore VG Studio Max 2.2 is using three levels for registration. The angle can be calculated by defining the line over at least four points at the test object's bottom edge and at the edges of the Co-SMC strips. This evaluation, exemplary for the thick semi-finished test object, is depicted in Figure 7-42.

Also here $u_{p\_CT\_sf} = u_{cal\_PPT\_sf}$ is valid and the mean value of the CT measurement is used as reference for the calculation of $u_{b\_PPT\_sf}$. This results in the measurement uncertainty balance for the semi-finished product for thermography:

$$U_{PPT\_sf} = k\sqrt{u_{p\_CT\_sf}^2 + u_{p\_PPT\_sf}^2 + u_{b\_PPT\_sf}^2}$$
<div align="right">Equation 7-2</div>

7.6.3 PPT Measurement Uncertainty for Cured Test Object

The procedure described in Chapter 7.6.2.1 can be used to determine the measurement uncertainty for the cured test object with blind holes. The results of the individual measurements is listed in Appendix A 24 and A 25. Table 7-9 lists all uncertainty factors for the individual blind holes. The factor $k = 2$ is used for the expanded measurement uncertainty (cf. Chapter 2.4.2).

Table 7-9: Determination of PPT Measurement Uncertainty for cured test object

Uncertainty factor	Area of blind hole 1 [mm²]	Area of blind hole 2 [mm²]	Area of blind hole 3 [mm²]	Area of blind hole 4 [mm²]	Area of blind hole 5 [mm²]
$\bar{y}_{CT\_cu} = x_{cal}$	310.90	110.92	110.03	310.65	110.55
$u_{p\_PPT\_cu}$	7.44	7.28	6.64	4.04	3.54
$\left| u_{b\_PPT\_cu} \right|$	11.94	4.37	3.33	5.16	3.82
$u_{cal\_PPT\_cu}$	0.47	0.37	0.43	0.31	0.37
$\boldsymbol{u_{PPT\_cu}}$	14.07	8.50	7.45	6.56	5.22
$\boldsymbol{U_{PPT\_cu}}$	28.15	17.00	14.89	13.13	10.44

7.6.4 PPT Measurement Uncertainty for Semi-Finished Test Objects

The measurement uncertainty for the semi-finished test objects is carried out according to the same procedure as for the cured test object and der measurement procedure

described in Chapter 7.6.2.2. All results of the individual measurements are listed in Appendix A 26 and A 27. The following Table 7-10 summarizes the results with the expanded measurement uncertainty with the factor $k = 2$.

Table 7-10: Determination of PPT Measurement Uncertainty for semi-finished test objects

	Thin test object		Thick test object	
Uncertainty factor	Angle 8° [°]	Angle 12° [°]	Angle 8° [°]	Angle 14° [°]
$\bar{y}_{CT\_sf} = x_{cal}$	8.10	12.05	8.00	13.95
$u_{p\_PPT\_sf}$	0.23	0.19	0.32	0.21
$\left\|u_{b\_PPT\_sf}\right\|$	0.19	0.03	0.15	-0.49
$u_{cal\_PPT\_sf}$	0.20	0.11	0.15	0.10
$\mathbf{u_{PPT\_sf}}$	**0.36**	**0.22**	**0.38**	**0.55**
$\mathbf{U_{PPT\_sf}}$	**0.72**	**0.44**	**0.76**	**1.09**

7.6.5 Evaluation of PPT Measurement Uncertainty

In this chapter, the minimum tolerances and resolutions of PPT are presented. Also the determined measurement uncertainty of the cured and the semi-finished test objects are evaluated. The individual results are compared in order to give the user an initial benchmark for the thermographic system.

7.6.5.1 Minimum Tolerances and Resolution of the PPT

For internal defects in CoDiCo-SMC, there are no known tolerances which can be used to evaluate the determined measurement uncertainty. However, as already described in Chapter 6.2.5.1, the minimum tolerances can be calculated according to Equation 6-12. The minimum tolerances are listed in Table 7-11 and Table 7-12.

Table 7-11: Minimum tolerances of PPT for cured test object (VDA Band 5)

	Blind hole 1 [mm²]	Blind hole 2 [mm²]	Blind hole 3 [mm²]	Blind hole 4 [mm²]	Blind hole 5 [mm²]
Minimum tolerances of cured test object [mm²]	375.29	226.64	198.57	175.05	139.20

Table 7-12: Minimum tolerances of PPT for semi-finished test objects (VDA Band 5)

	thin test object		thick test object	
	Angle 8°	Angle 12°	Angle 8°	Angle 14°
Minimum tolerances of semi-finished test objects [°]	9.55	5.91	10.11	14.54

The minimum tolerances for the cured test object are very high. This is due to the heat flow, penetrating not only into depth, but also laterally. Furthermore, the result is influenced by defect size and defect depth. The measurement uncertainties are smaller for measuring the angles in the semi-finished test objects. However, the determined minimum tolerances are too large for use in industry, especially since even a small angle deviation of 5° considerably deteriorates the mechanical properties (cf. Chapter 5.5).

The resolution of the measuring system has to be considered for a complete examination according to (VDA Band 5) (cf. Chapter 6.2.5.1). At a camera distance of 35 cm, an area of 13 cm x 11 cm is detected (InfraTec GmbH 2018). The detector size corresponds to 320 x 256 pixels (InfraTec GmbH 2016a), whereby a resolution of 0.4 mm in x-direction and 0.42 mm in y-direction is achieved. Thus the requirements according to (VDA Band 5) are fulfilled.

7.6.5.2 Evaluation of the Measurement Uncertainty for Cured Test Object

According to Table 7-9, blind hole 1 has the largest measurement uncertainty. The absolute values are also plotted in Figure 7-43.
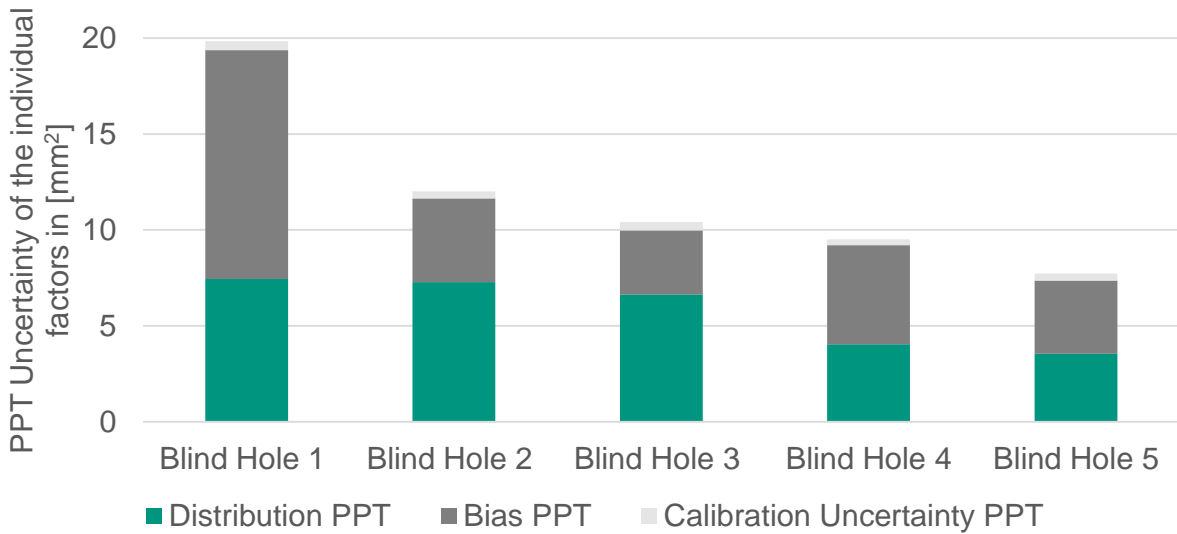
Figure 7-43: Absolute uncertainty factors of PPT on cured test object

It is the hole with the largest diameter of 20 mm and the smallest residual wall thickness of 1 mm. Figure 7-44 depicts the influence of the individual measurement uncertainty contributions on the determined measurement uncertainty. It is noticeable that the calibration uncertainty influence is negligible with a maximum of 0.49 %.
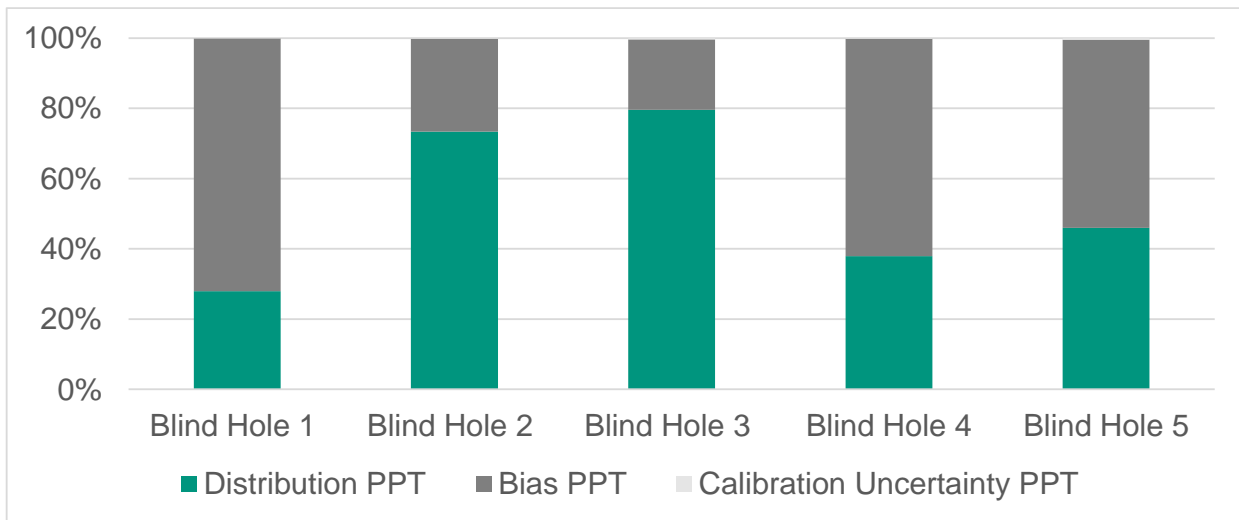
Figure 7-44: Relative uncertainty factors of PPT on cured test objects

Performing the measurements, it was noticeable that the determined area for blind hole 1 is usually measured larger than it actually is. Blind hole 2 has a smaller diameter than blind hole 1, resulting in a larger influence of the distribution. However, blind hole 2 has an overall lower measurement uncertainty than blind hole 1. This result confirms the statement in Chapter 7.4, that the size of defect influences the measurement result.

Blind holes 4 and 5 have the smallest measurement uncertainties, but differ in the determined measurement uncertainty despite the same residual wall thickness. For blind hole 3, the deviation of the system is the decisive factor. Figure 7-40 illustrates that the blob analysis does not detect a circle, but rather an ellipse. With a residual wall thickness of 2.5 mm, the Co-SMC is present. Its unidirectional alignment also influences the heat transport, resulting in the detected ellipse having its maximum expansion in fiber direction.

The investigation shows that the determined measurement uncertainty for the same residual wall thickness depends on defect size. For the same defect size, but different residual wall thicknesses, no correlations are discernible.

7.6.5.3 Evaluation of the Measurement Uncertainty for Semi-Finished Test Objects

The measurement uncertainty of the semi-finished test objects is considerably lower than that of the cured test object. The absolute values for semi-finished test parts listed in Table 7-10 are presented in Figure 7-45.
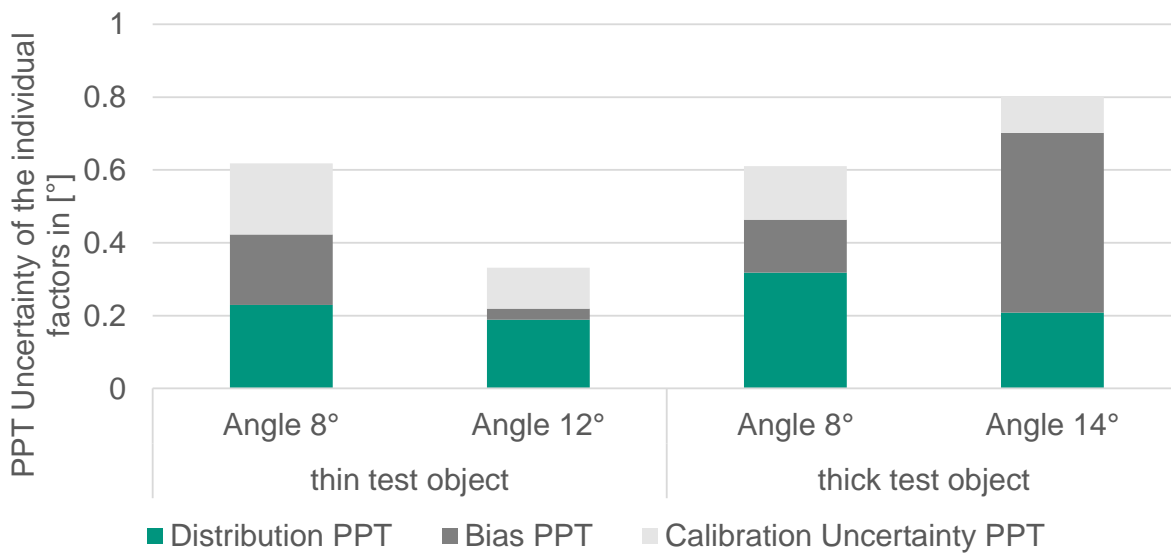
Figure 7-45: Absolute uncertainty factors of PPT semi-finished test objects

Figure 7-46 demonstrates that the factor of calibration uncertainty now also has an influence on the result.
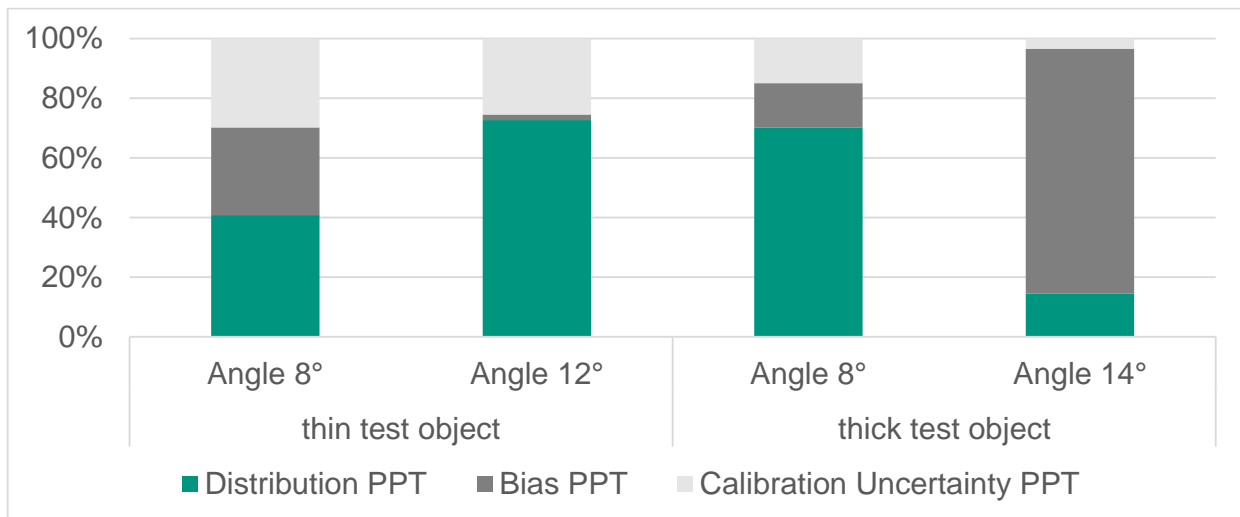
Figure 7-46: Relative uncertainty factors of PPT on semi-finished test objects

In principle, the distribution of the measurement using PPT has the greatest influence. The systematic deviation is only decisive when examining the thick sheet at an angle of 14°.

The evaluation process is not automated but carried out manually by the operator. In a phase or amplitude image, the operator manually generates a line ROI, which is used by the software to calculate the angle. This influence has to be conscious when considering the measurement uncertainty and explains the influence of the distribution of the system.

LLSS and PPT can be used to detect geometric deviations and internal defects and therefore are suitable for investigating CoDiCo-SMC. With the measurement uncertainty determination of LLSS in Chapter 6.2 and of PPT in this chapter, the third research question (cf. Chapter 1.2) is answered completely. Both systems are already applicable, but the determined measurement uncertainty shows that there is still potential for system improvement.

8 Multi-sensor System

Due to the great defect variance (cf. Chapter 5.4), one system is not sufficient for investigation. By using a multi-sensor system (MSS) consisting of LLSS and PPT, it is possible to analyze both internal and external CoDiCo-SMC defects as well as to determine dependencies between those defects.

In the first step, the interfaces described in Chapter 7.1 are considered for design and connection towards a complete LLSS and PPT system integration. The related data fusion process is presented subsequently. In the third step, added value of the presented data fusion is highlighted and subsequently demonstrated by a layer model. Finally, the measurement uncertainty of the entire MSS is determined.

8.1 Design of the Multi-Sensor System

The portal interfaces including the selection of a suitable thermography system is described in Chapter 7.1. Thus, the connection of the control systems and a security system have to be realized. Subsequently, the constructive MSS realization takes place.

8.1.1 Connection of the Control System

Programming for controller connection is carried out using the TwinCAT 3 development environment from Beckhoff Automation GmbH & Co. KG. A local network is set up via Ethernet for data exchange between PPT and LLSS. The OPC-UA interface controls the PPT system. The network structure is illustrated in Figure 8-1. (A_Kretsch 2017)
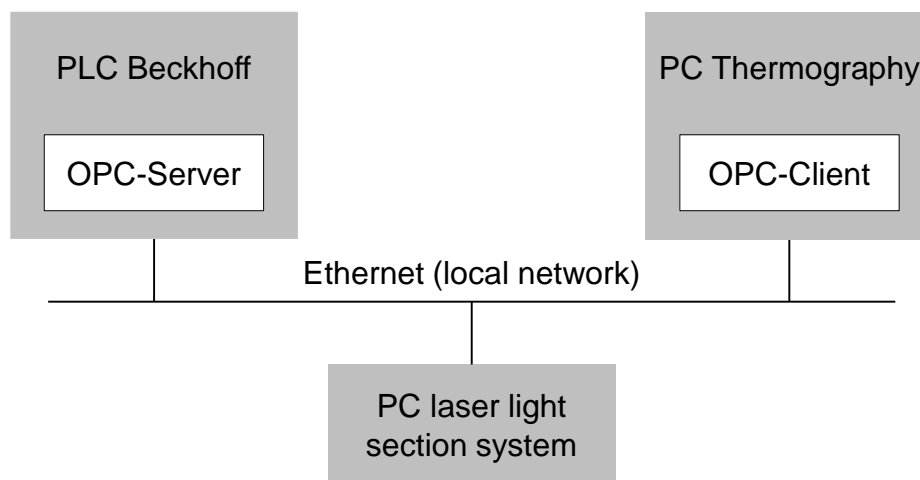
Figure 8-1: Local network structure (A_Kretsch 2017)

With the local network and the PLC control from Beckhoff it is possible to exchange data, to implement a program sequence via a M command, which can be integrated

into a continuous NC program, to transfer portal coordinates and to select datasets. To abort the process and thus avoid endless loops in the PLC, a timeout is implemented for measurements. (A_Kretsch 2017)

Furthermore, a safety concept is implemented in order to avoid danger from the high-energy flash. Therefore, the flash lamp is turned away from the user. In addition, a curtain forms a protective separation around the portal, avoiding outsiders to look into the flash. A further warning light, installed outside the area, warns of an impending thermographic flash and subsequent measurement. In addition, an emergency stop function is integrated. (A_Kretsch 2017)

8.1.2 Realization of the Construction

With the existing LLSS and PPT components as well as the control system integration, the multi-sensor system is set up (cf. Figure 8-2). As the whole system can move in x, y, and z direction, it can be adapted to variable geometries. (A_Weinhardt 2017)

To avoid electromagnetic coupling between individual system's wires, the current-carrying cable of the flash unit has to be positioned separated from the signal-carrying cables. Otherwise, the magnetic field generated by the pulsed current can impair the signals in other wires.
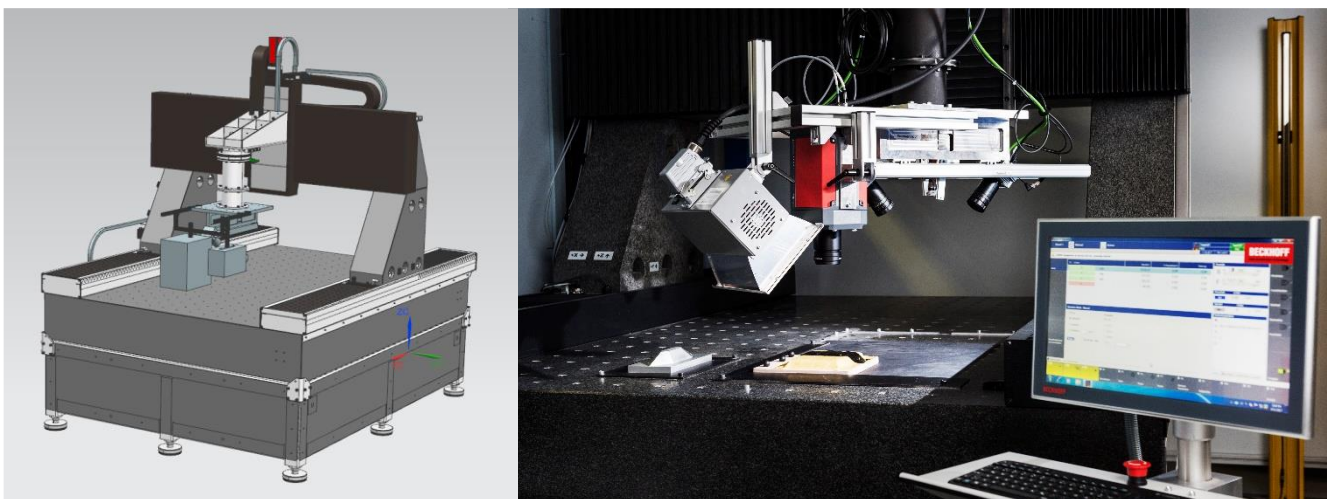
Figure 8-2: MSS CAD design (left) (A_Weinhardt 2017) and implementation (right) (Figure with kind permission of Sandra Göttisheim/KIT 2017)

Thus, the first part of research question five (cf. Chapter 1.2) is answered: A testing and measuring system for CoDiCo-SMC quality assurance can be implemented by a MSS,

consisting of laser light section and pulse-phase thermography. The question regarding measurement uncertainty of the MMS is answered in Chapter 8.5

8.2 Data Fusion

The MSS fuses LLSS and PPT data to obtain further information than attainable with two separate systems (cf. Chapter 2.3). The pinhole camera model, explained in Appendix A 28, is used to work up data and thus enable data fusion. Subsequently, the data fusion process is explained in detail, in order to apply it to the small demonstrator test object afterwards.

8.2.1 Data Fusion Process

The data fusion developed in this thesis, is initially performed using a simple hat profile as pictured in Figure 8-3. This is produced with DiCo-SMC from ICT and Co-SMC from Polynt Composites Germany GmbH
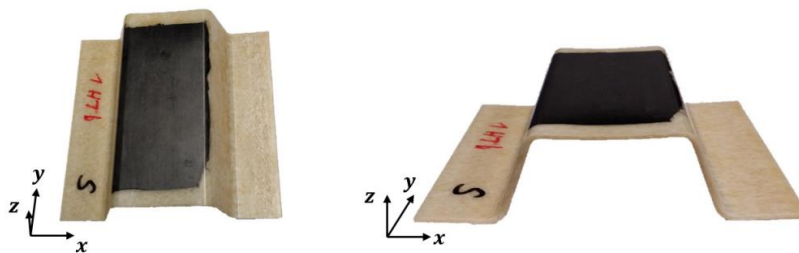
Figure 8-3: Hat profile for data fusion development according to (A_Pohland 2017)

The data fusion concept in this thesis is developed according to the procedure in Figure 2-10 and completely implemented in the software MATLAB®. The individual steps are illustrated in Figure 8-4 and explained below.

Initially, the LLSS and PPT raw data has to be recorded sequentially in order to avoid system interference. To create the CoP (cf. Figure A-11 in Appendix A 9), the LLSS scans both test object and registration bodies consisting of matt metal cylinders. The optimum parameters for cured material are used (cf. Chapter 6.1.4.4).

Before the test object is thermographicaly investigated, parameters for the infrared camera have to be set. To determine distortion and intrinsic parameters, several images of a chessboard pattern are taken, differing in orientation. As 10 to 20 images are recommended, at least 10 images are used for the present investigations. The amplitude images are processed with the *Single Calibration App* of MATLAB®'s *Computer Vision*

System Toolbox. As soon as the camera is calibrated, changes made to the lens result in a necessary recalibration. (A_Pohland 2017)
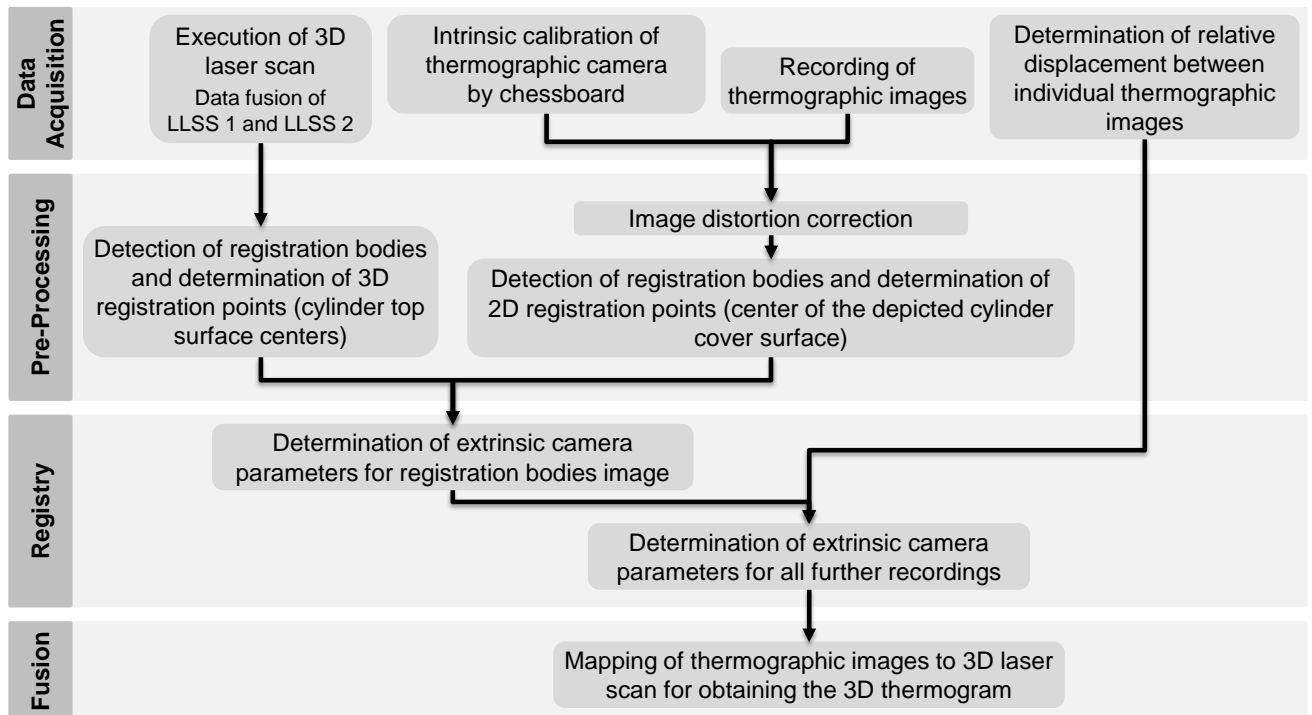
Figure 8-4: Data fusion process of LLSS and PPT (Schäferling et al. 2018)

For PPT, a recording time of 30 s and a frame rate of 200 Hz are selected, because the parameters in Chapter 7.3 were not known at the time of these experiments. However, this selection of parameters has no negative effect on the quality of the recordings. Several thermographic images for a complete acquisition are recorded of both, test object and registration bodies. The image x- and y-position are derived from the portal position input. In addition, the portal moves in z-direction, following the test object's height profile in order to keep camera distance and thus focus constant. The component illustrated in Figure 8-3 for instance has two planes and thus requires thermographic images in two heights. (A_Pohland 2017)
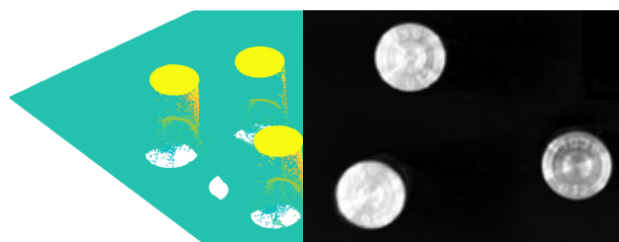
Figure 8-5: Cylinder detection by LLSS (left) and PPT (right) (Schäferling et al. 2018)

A further step in data pre-processing is the registration bodies detection. Figure 8-5 depicts the cylinder recording as 3D data using LLSS and as 2D data using PPT.

For both, LLSS and PPT the center point of the cylinder top surface is determined in order to register the two systems by merging the cylinder centers of the individual images. (A_Pohland 2017)

This registration involves two essential points. First, the extrinsic infrared camera position and orientation are determined with the help of the registration bodies, requiring the congruence of at least four 3D world and 2D image points derived from cylinder centers. Six registration bodies are used in the present thesis. In the 2D images of the PPT, phase images are used at different frequencies, because the phase images differ strongly in quality.

It is impossible to capture both registration bodies and test object in one thermographic image. Therefore, the extrinsic parameters for all further images are expressed by the portal position, still based on the registration bodies position, as visualized in Figure 8-6. As this is a simple translation, only the translational parts of the extrinsic parameters in Equation A-18 need to be adjusted. As the portal TCP position is known, the relative displacement of x, y and z, describing the displacement translation vector, can be determined. This is identical to the translational vector of the infrared camera, as infrared camera is fixed to the portal. (A_Pohland 2017)
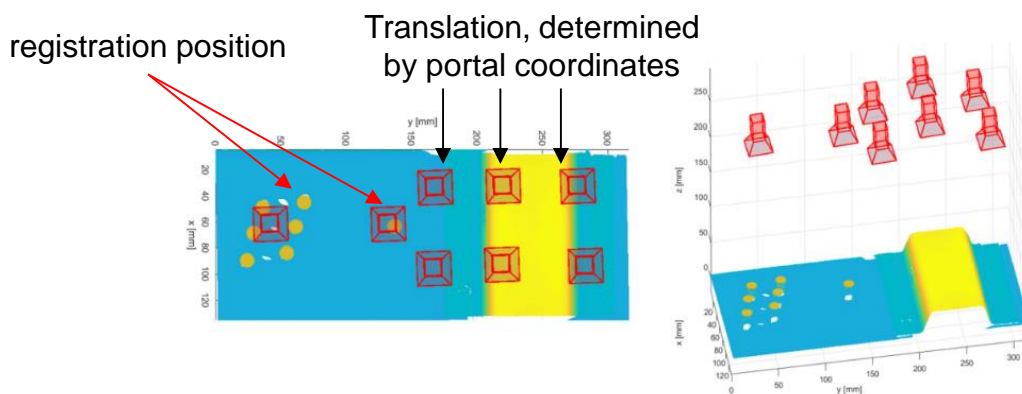
Figure 8-6: Visualization of the infrared camera position (Schäferling et al. 2018)

In the last step, the data fusion takes place by mapping 2D thermographic image to 3D LLSS CoP. To do so, each CoP point is projected onto the image plane by using the camera model equation (cf. Equation A-18). Thus, each 3D CoP point is allocated to one image pixel including its color. This color is taken over to the 3D geometry. Thus, purpose, the NaN number in the CoP has to be as low as possible (cf. Chapter 6.1.4.4).

As multiple images are required, the images are captured overlapping to avoid image gaps. Due to the hat profile, the overlap areas are imaged with different sharpness. For this reason, only the sharp image area is selected for coloring the 3D data. The fusion and a 3D thermogram are illustrated in Figure 8-7. (A_Pohland 2017)

CoP

2D Thermographic Picture

Fusion
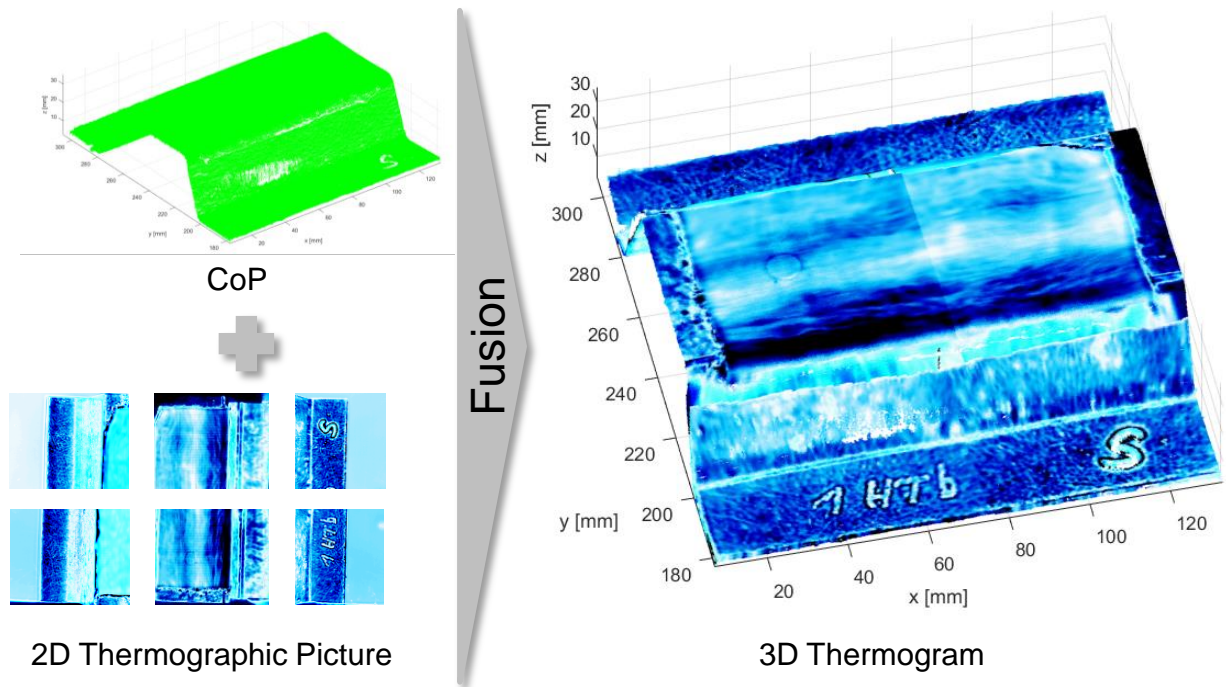
3D Thermogram

Figure 8-7: Elements of data fusion and 3D thermogram according to (A_Pohland 2017; VDI/VDE-Gesellschaft Mess- und Automatisierungstechnik 2018)

8.2.2 Demonstration of Data Fusion

The developed data fusion method is applied to the small demonstrator used in this thesis (cf. Chapter 5.3.2). The DiCo-SMC is from ICT and the Co-SMC from Polynt Composites Germany GmbH. The thick layer structure as presented in Chapter 5.2 is used. The test object is presented in Figure 8-8.

Figure 8-8: Small demonstrator as test object for data fusion

For the data fusion of the small demonstrator only one thermographic image is sufficient. This is possible as no difference in sharpness can be detected in the thermographic images due to lower height than the hat profile in Chapter 8.2.1, which also reduces the computing effort. Figure 8-9 compares two images focused on different planes to demonstrate no visible differences.

Focused on this plane
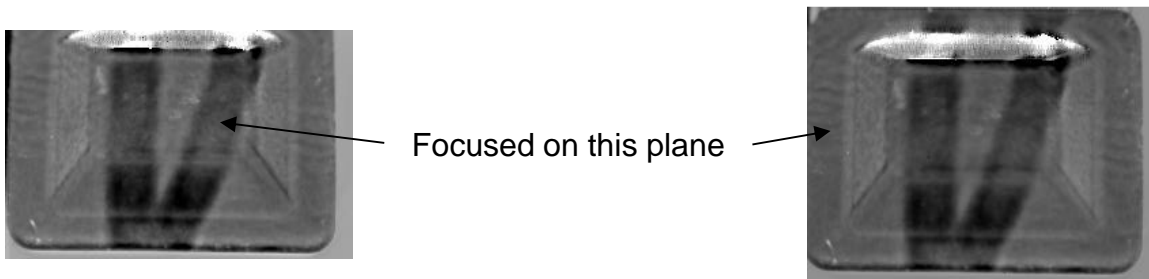
Figure 8-9: Phase images with focus on different planes

Figure 8-10 depicts data fusion with a phase image. The geometry of the small demonstrator and the Co-SMC strips are clearly visible.
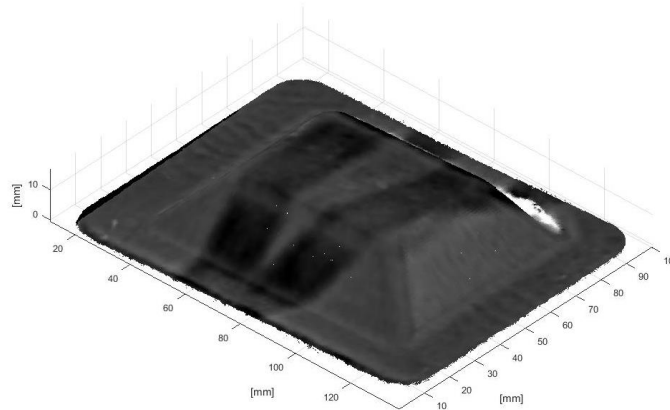
Figure 8-10: Data fusion of the CoP with a phase image at 0.05 Hz

8.3 Added Value of Data Fusion

Data fusion provides several added values: In the presented case, it provides the possibility to relate internal defects or Co-SMC orientation to the test object's geometry. Furthermore, it is possible to analyze distances between external and internal defects and to show effects of individual defects on others. For instance in case of a dent with an internal defect beneath, the depth information of the internal defect alone would lead to a wrong estimated location. With the additional deep information of the dent, provided by the LLSS, the internal defect depth has to be adjusted deeper, as in Figure 8-11.
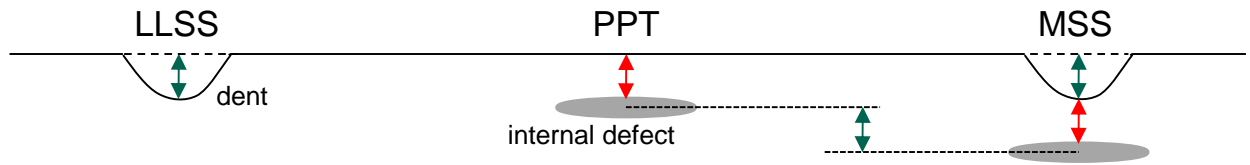
Figure 8-11: Exemplary added value of data fusion using dent and internal defect

Furthermore, geometric relationships can be identified by data fusion. For example, it is possible to determine the distance from an internal Co-SMC to an external test object edge, as displayed in Figure 8-12, or the angle of a Co-SMC in relation to the external test object edge. The angle analysis is depicted in Figure 8-13.
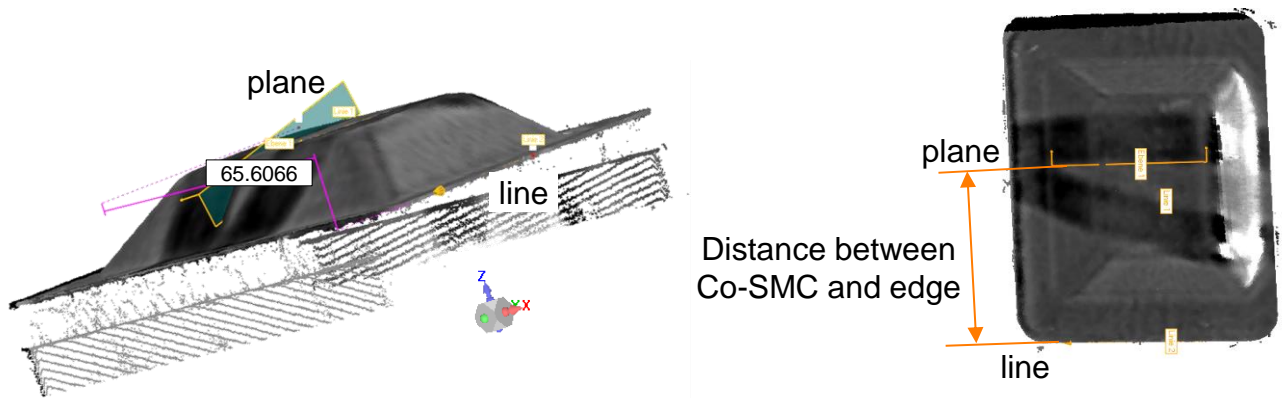
Figure 8-12: Data fusion to analyze distance between Co-SMC and test object edge
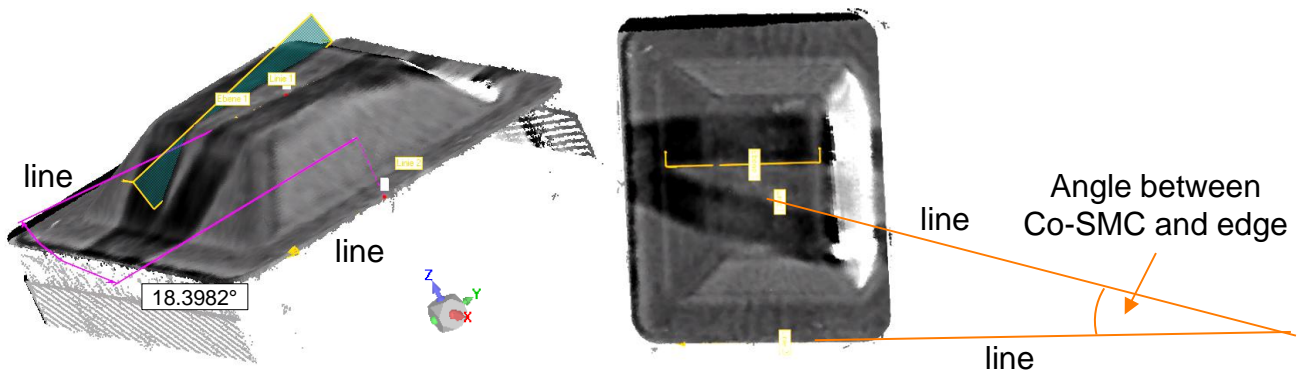
Figure 8-13: Data fusion to analyze angle between Co-SMC and test object edge

For the simple demonstrator geometry, used in this thesis, the examples illustrated in Figure 8-12 and Figure 8-13 could also be evaluated based on PPT only. This becomes impossible, already for simple geometries, by adding the third dimension. Figure 8-14 illustrates an example, where the internal Co-SMC has to cover a component edge according to a certain specification. To ensure quality, this overlap has to be measured by relating the Co-SMC position to the test object's geometry.
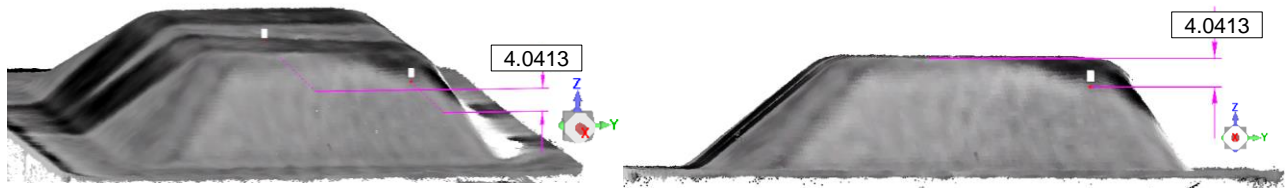
Figure 8-14: Data fusion to analyze Co-SMC covering test object edge

In addition, data fusion can be used to create a layer model that provides the operator with a quick overview of the individual layers and depth information. This model is presented in the following chapter.

8.4 Data Fusion Layer Model

By extending the developed data fusion to a layer model, it is possible to provide the user with a view on the different test object layers. Thus, a fast evaluation is possible.

The layer model is based on the frequencies determined in Chapter 7.4, providing depth information according to the discrete Fourier Transform. There are seven frequencies available for the used layer structure, representing the depths 0.5 - 3.5 mm in 0.5 mm steps. Therefore, the presented layer model consists of seven evaluation layers in total, as depicted in Figure 8-15. It is also possible to view single layers, as illustrated in Figure 8-16, representing the fourth layer at a depth of 2.0 mm, with the clearly visible Co-SMC. Both figures also provide a section through the layer model.
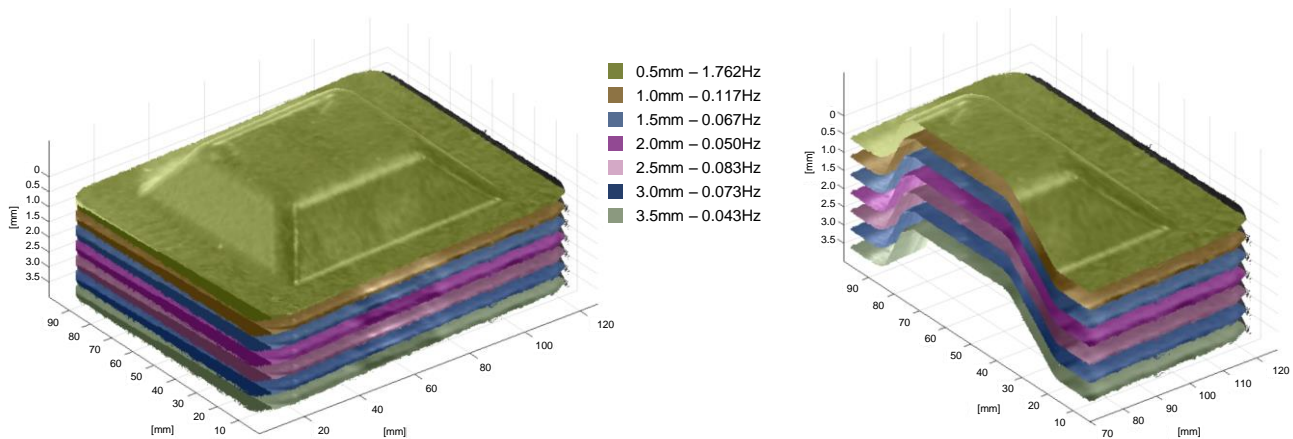
Figure 8-15: Data fusion layer model for small demonstrator

With this layer model, the sixth research question (cf. Chapter 1.2) is answered: A layer model enables the user to perform a quick and practicable evaluation.
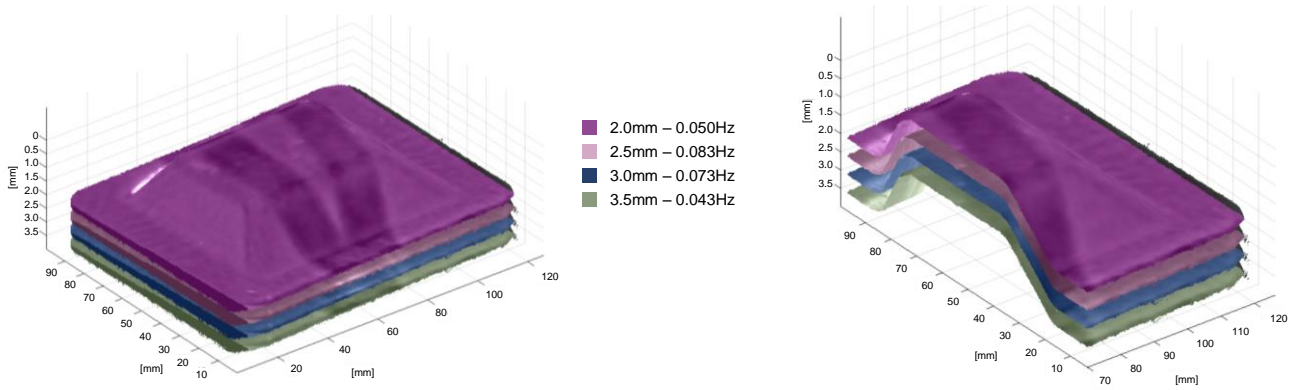
Figure 8-16: Layer model of the data fusion with less layers

8.5 Data Fusion Measurement Uncertainty

The data fusion used in this thesis can be attributed to cooperative integration (cf. Chapter 2.3.3). As illustrated in Figure 8-17 the target is gaining additional information by using different sensors. Thus, it can be assumed that the data fusion measurement uncertainty is in the same range as the single systems. Therefore, improving LLSS and PPT would also lead to a reduction of data fusion measurement uncertainty.
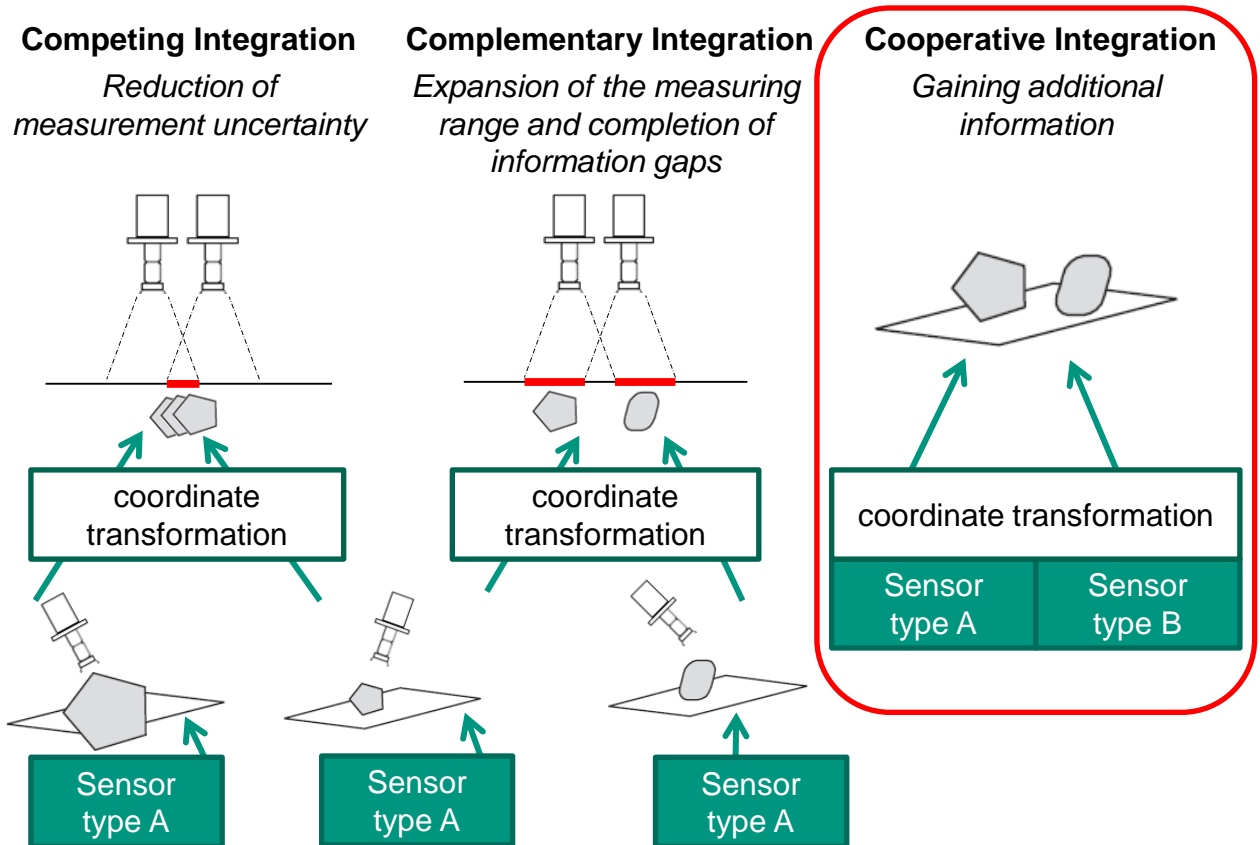
Figure 8-17: Targets of sensor integration concepts according to (Beyerer 2006)

The measurement uncertainty is determined for the developed MSS including data fusion, as already for the individual systems (cf. Chapter 6.2 and 7.6). In the following, test object and feature for the measurement uncertainty analysis are briefly explained. Subsequently, the measurement uncertainty analysis procedure is explained and the results presented. These results are finally discussed.

8.5.1 Test Object and Features for Measurement Uncertainty of Data Fusion

The measurement uncertainty is only carried out on the cured test object, because the pressing process can change the semi-finished product in such a way that an investigation using data fusion does not provide any added value. As a result of CoDiCo-SMC component production a displacement of the Co-SMC often is observed, such as deviating angles and positions of the Co-SMC. Thus, the component's mechanical properties are influenced. Therefore, the distance of one Co-SMC strip in relation to test object geometry is the feature used to determine the measurement uncertainty.

The data fusion measurement uncertainty is performed on the small demonstrator already described in Chapter 8.2.2. The component has a thickness of 4.5 mm. The feature is illustrated in Figure 8-12.

8.5.2 General Procedure of Data Fusion Measurement Uncertainty Analysis

To determine the measurement uncertainty, 25 data fusion measurements are performed. Since the feature refers to the Co-SMC strips, representing the test object's middle layer, the analysis is performed on the phase image at a frequency of 0.05 Hz, corresponding to a residual wall thickness of 2 mm. (cf. Chapter 7.4.2.1). The fusion is performed according to Chapter 8.2.2. The feature is evaluated with the program Geomagic Control 2014.4.0 from the company 3D Systems. The distance is measured in x-direction between a plane applied to the Co-SMC strip using three points and a line attached to the edge using two points. The evaluation procedure is depicted in Figure 8-12. With 25 measurements, it is possible to calculate the measurement method's standard uncertainty u_{p_DF}. Thus, only u_{p_DF}, u_{cal_DF} and u_{b_DF} have to be determined, where u_w can be neglected as before (cf. Chapter 7.6.2). (DIN EN ISO 15530-3).

The reference method used to calculate u_{cal_DF} is CT measurement, again performed with the CT ZEISS METROTOM 800. The applied parameters are listed in Appendix A 29. 25 CT measurements are carried out, the subsequent evaluation is performed in VG Studio Max 2.2. The surface is automatically created and a 3-2-1 registration is

done over 3 levels. For point selection on the upper plane, the z-value 13.5 mm is selected for all measurements. u_{p_CT} is determined by the 25 measurements. u_{cal_CT} and u_{b_CT} are set to zero, because CT can be assumed to be much more accurate than the individual procedures laser light section as well as thermography and thus also data fusion (cf. Chapter 7.6.3). Thus $u_{p\_CT} = u_{cal\_DF}$ is included in the data fusion measurement uncertainty balance. The CT measurements mean value is used to define x_{cal}, u_{b_DF} is calculated according to Equation 2-8. Therefore, the total data fusion measurement uncertainty is determined according to the following equation:

$$U_{DF} = k \sqrt{u_{p\_CT}^2 + u_{p\_DF}^2 + u_{b\_DF}^2} \qquad\qquad \text{Equation 8-1}$$

8.5.3 Data Fusion Measurement Uncertainty for Cured Test Object

The described procedure is used to determine the data fusion measurement uncertainty. The individual evaluation results are presented in Appendix A 30 and A 31. Table 8-1 lists all uncertainty factors as well as the determined measurement uncertainty and expanded measurement uncertainty. The factor $k = 2$ is used for the expanded measurement uncertainty.

Table 8-1: Determination of the Data Fusion Measurement Uncertainty

Uncertainty factor	Distance between Co-SMC and edge [mm]
$\bar{y}_{CT}$	65.57
u_{p_DF}	0.49
u_{b_DF}	0.30
u_{cal_DF}	0.04
$\mathbf{u_{DF}}$	**0.58**
$\mathbf{U_{DF}}$	**1.15**

8.5.4 Minimum Tolerances and Resolution of the Data Fusion

The minimum tolerance for the feature Co-SMC distance to test object edge according to (VDA Band 5) is determined to be $TOL_{\min\_DF} = 15.33\ mm$. Obviously, the determined tolerance is still very large. Since the individual systems already fulfill the resolution of the measuring system according to (VDA Band 5), the MSS also fulfills this resolution.

Previous tests with an additional feature, the angle between Co-SMC strip and test object edge, indicate similar values for the measurement uncertainty. Therefore, a measurement uncertainty investigation based on an additional feature is reasonable, if on the one hand the individual systems, LLSS and PPT, are improved. One the other hand it is possible to improve the data fusion as suggested in the following.

8.5.5 Suggestions for Improvement

To improve MSS with data fusion and thus reduce the measurement uncertainty, three levers are suggested: Automation, improved registration and ROI determination.

The standard deviation u_{p_DF} represents the largest part of data fusion measurement uncertainty (cf. Table 8-1). One influencing factor is the measurement with Geomagic Control, as points for evaluation are be set manually leading to large operator influence. Therefore, an automated evaluation with image recognition would reduce distribution.

Another influencing factor for the standard deviation u_{p_DF} is registration bodies detection. Since the flash excitation occurs from one side only, there are exceptions where the cylinders are not displayed round but with a tail. This results in a deviating location determination and thus reduced congruence of the individual system's coordinate systems related to test object position. To tackle this problem, two approaches are conceivable, which could also augment each other:

On the one hand, the registration method (cf. Chapter 2.3.4.1) could be changed. An appropriate alternative could be the numerical registration approach, using characteristic features of the test object. This leads to a higher number of features and reduces possible movements within the measuring system through minimized movements. On the other hand, using more than one flash lamp for excitation would reduce shadowing.

To retain the system target of a fast evaluation for inline application but simultaneously increase the measuring time seems to be a conflict of objectives. Solving this would be possible by defining a region of interest (ROI) for the slower PPT process. Taking the example illustrated in Figure 8-14, only the test object edge plus surrounding is of interest regarding internal properties. Thus, it is possible to spend the evaluation time originally intended for the whole test object on this ROI and hence gain better results.

With the determination of the data fusion measurement uncertainty, research question five is completely answered.

9 Discussion and Outlook

This chapter first aims to discuss the thesis at hand's own approach critically, with regard to the research questions asked in chapter 1.2. Secondly, it tries to provide needs for actions and an outlook for further research projects continuing this work.

9.1 Discussion

This work's aim is to develop a multi sensor system, based on data fusion, for the quality assurance of continuous-discontinuous-Sheet Molding Compound (CoDiCo-SMC) components, able to detect and possibly characterize defined critical defects.

9.1.1 First Part – Defects and their Effects on the Mechanical Properties

The first part of the thesis focuses on defects occurring in CoDiCo-SMC and their effects on the mechanical properties. By limiting those and classifying them into external and internal defects, it is possible to obtain a good overview. The selected defects cover different kinds of errors, ensuring a wide range of applications and are therefore sufficient for the present thesis. Nevertheless, the investigated defects are a selection and thus do not include all possible errors and process steps. The investigations carried out to determine the Effects of Defects provide clear evidence that even small defects, occurring at an early production step, influence the mechanical properties. To avoid waste, quality assurance has to be conducted before adding value to scrap parts. Therefore, both semi-finished and cured test objects are investigated and research questions one and two are clearly answered in this thesis.

9.1.2 Second Part – Methods to Detect and Characterize the Critical Defects

In the second part, the research questions deal with suitable systems for quality assurance of internal and external defects in semi-finished and cured test objects as well as the measurement uncertainty of these systems. In addition, the possibility of an extended evaluation is focused. Using a detailed state-of-the-art analysis, laser light section system (LLSS) and pulse-phase thermography (PPT) are identified as suitable systems. LLSS is characterized by a quick examination of large components' complete surface. In addition, there are already existing investigations indicating good suitability. PPT fulfils existing boundary conditions by a fast and also large-scale investigation. Thus, a first part of the research questions is answered.

9.1.2.1 LLSS

Examining the existing LLSS in more detail, reveals only partial suitability. The large number of setting parameters have strong influence on the measurement quality. Only tendencies, for example that a certain threshold must not be undercut, but no clear connections regarding the different parameter combinations are recognizable. Therefore, parameter determination is an important part of the present thesis, whereby not all evaluation criteria can be completely fulfilled. For instance, it is impossible to prevent laser penetration into the material without more fillers in or lacquer on the material. By reducing the exposure time, the penetration depth is also reduced. This comes at the expense of a larger NaN number, which is essential for later data fusion and therefore higher rated, resulting in a deeper accepted penetration depth. With a constant laser incidence angle to component surface, it would be possible to calculate the penetration depth. The parameters determined in this thesis only apply to the described material combination and cannot automatically be transferred to other materials. In addition, the interaction with complex geometries is unknown.

For measurement uncertainty determination, an approach is developed and applied to test objects. This approach offers an accurate reference by using CT and provides a good basis for the different measurement uncertainty factors through traceability to tactile measurements. Besides using different measuring methods, the presented approach is GUM-compliant and includes a variety of factors. The exemplary determined measurement uncertainties $U_{\mathrm{LLSS\_cu}} = 0.2331\ mm$ and $U_{\mathrm{LLSS\_sf}} = 0.2081\ mm$ for the distance between two planes deviate due to different standard uncertainties. These values are too large for an industrial application, but provide a first reference point for using LLSS on CoDiCo-SMC components.

Chapter 6.2.5.3 describes the factors influencing the measurement uncertainty most, providing a basis to reduce them in further investigations. As the factor's share differs noticeably for each feature and material state, only nonuniform statements are possible. The manual evaluation process is assumed to have an influence on the measurement uncertainty. Therefore, an automatic evaluation is recommended for further investigations. Furthermore, calibration by an accredited laboratory would be another possibility to reduce uncertainty. By developing the method for LLSS measurement uncertainty determination and executing it exemplary, a reference point for the system quality is obtained and thus research question three for LLSS completely answered.

9.1.2.2 PPT

PPT is set to be the system for internal defects detection, as it meets all necessary requirements for CoDiCo-SMC investigation and is characterized by a fast recording time. In addition, PPT is already used as an industrial test method, providing qualitative analyses. However, quantitative values are required for the application in this thesis.

An experimental PPT method providing in-depth information is developed, which can be applied to different layer structures and thus offers a good possibility for expansion towards other materials and layer structures. Nevertheless, the current distance of 0.5 mm between the evaluation layers and a maximum test object thickness of 3.5 mm are insufficient for a precise measurement application. Decisive factor is the unknown course of the thermal wave, currently not allowing any discrete values for an in-depth analysis. A first workaround, weakening but not solving the problem, is to improve the resolution. This would require to reduce the distance between camera and test object, narrowing the field of view. However, the optimum distance of 0.3 m specified by the manufacturer would be undercut.

In addition, PPT is expanded from detecting internal defects, to characterizing them. This is an important step towards linking detected defects to their effects on mechanical properties. However, the present investigation requiring further investigations for validation. Thus, the fourth research question is answered, as defects have clear characteristics detected by a single system.

Similar to LLSS, an experimental method for determining the PPT measurement uncertainty is developed. The exemplary determined uncertainties $U_{\mathrm{PPT\_cu}} = 14.89 \ mm^2$ for a blind hole (diameter = 12 mm; residual wall thickness = 2.5 mm) and $U_{\mathrm{PPT\_sf}} = 0.72°$ for an 8° angle are too large for an industrial application, but provide a first reference point for using PPT on CoDiCo-SMC components. One reason for the high values is the mentioned course of the thermal wave. This is amplified by the hybrid material, consisting of several individual components with different thermal conductivities. In addition, the manually performed evaluation influences the uncertainty, which could be mitigated by an automated evaluation. Nevertheless, the determined measurement uncertainty enables a quantitative statement for thermography measurements on CoDiCo-SMC components. Thus, the third research question for PPT is answered completely, since the system potentials and its measurement uncertainty are determined.

9.1.3 Third Part – Implemention of a Holistic Measurement System

The last research questions deal with the multi-sensor system (MSS) implementation as well as the measurement uncertainty and a complete user-friendly evaluation. The pinhole camera model is used to develop a method for data fusion, which has not yet been used in this way. It offers the possibility to quickly perform a complete investigation for all selected defects and to evaluate geometric dependencies between the defects, partially answering research question five. The system could be extended by further methods, providing great potential for further research.

As the MSS consists of LLSS and PPT, it is also limited to their specifications, as described above. Furthermore, it is only tested with one CoDiCo-SMC layer structure, requiring further test with different materials and layer structures. The exemplary determined measurement uncertainty $U_{\mathrm{DF\_Distance}} = 1.15 \, mm$ for the distance is higher compared to the single systems, due to detection of registration bodies and manually evaluation process. Although it is pointed out that investigations relating internal to external properties are only possible based on data fusion.

The first influencing factor, registration via measured reference marks using the metal cylinders, could be tackled by reduced shadowing through more than one flash lamp for excitation. Furthermore, the registration method could be changed to the numerical registration approach, using more features and reducing possible movements within the measuring system. The manual evaluation process is the second influencing factor and could be mitigated by using automated evaluation based on image recognition. The presented investigation completely answers research question five, but also indicates further potential in terms of accuracy.

To provide a user-friendly evaluation, data fusion and the PPT in-depth analysis are extended to a layer model, offering the possibility to view and analyze several evaluation layers, representing different depths. Nevertheless, the existing model provides no information regarding the relationship of the single evaluation layers. By connecting the defect expansion information of the single layers, it would be possible to provide the volume of internal defects. This would also be supported by reducing the evaluation layer distance of currently 0.5 mm. However, an approach for the user-friendly evaluation is presented, whereby research question six is answered.

9.2 Outlook

As illustrated in the previous chapter, research activities with focus on further development of the MSS and the individual systems remain open for the future.

In the present thesis, only simple geometries with slopes are considered. Thus, it makes sense to extend the system to complex 3D geometries. As material penetration by the laser is angle dependent, repositioning the laser only longitudinal and especially height direction is insufficient. Therefore, a contour following system has to be developed, that also adjusts the laser angle and thus ensures a constant optimum angle between surface and laser. In addition, other surface scanning systems, like a strip light projection system, should be evaluated for more complex geometries. The existing portal is suitable to carry other systems.

To improve defect detection with the MSS, it could be supplemented by further systems. For instance an ultrasonic system is conceivable, as it is able to achieve greater depths at higher precision. Since ultrasonic is time-consuming, it cannot be applied to the entire test object. Nevertheless, a two-step approach is possible: First, the test object is examined with the current LLSS and PPT to define potential critical areas. In the second step, these areas are evaluated in detail with ultrasonic testing.

Fully-automated evaluation using image and pattern recognition, as discussed above, can enable faster evaluation and less uncertainty. The in-depth analysis would be more precise by using more evaluation layers for the same test object thickness. In addition, a defects outer contour can be interpolated by connecting the respecting results of single evaluation layers. Thus, not only the defect area, but also its volume is determined.

The data fusion execution can be optimized by developing a more precise registration method, leading to a positive effect on measurement uncertainty.

To evaluate more complex geometries, an additional measurement after rotation around the z-axis is recommended, in order to minimize the NaN number at lateral slopes.

10 Summary

Fiber-reinforced plastics are becoming increasingly important and the production of Sheet Molding Compound (SMC) is growing steadily. Since the mechanical properties of discontinuous-SMC (DiCo-SMC) are low, it is locally reinforced with carbon continuous-SMC (Co-SMC). This results in a large number of possible defects occurring in the manufacturing process. Thus, early detection is required in order to avoid value-adding steps on defective components.

In this thesis, a defect limitation as well as a classification to external and internal defects are carried out initially. The subsequent Effects of Defects examination clearly demonstrates their impact on mechanical properties and thus substantiates the necessity of defect detection.

Due to the defect distinction, one measuring system alone is insufficient. Therefore, a multi-sensor system, consisting of laser light section and active thermography, is designed. For both individual systems, optimal parameters for the investigated continuous-discontinuous-SMC (CoDiCo-SMC) are determined and methods for measurement uncertainty calculations are developed. Furthermore, the thermography method is extended to an in-depth analysis, assigning defects to certain depths and thus forming the basis for the data fusion layer model. In addition, it is pointed out that defects have characteristic sequences related to their type.

The multi-sensor system's data fusion offers the possibility, to identify geometric relationships between external and internal defects. Furthermore, the layer model offers a quick view on evaluations layers within the test object. The system's quality is demonstrated by determining the measurement uncertainty.

Thus, a multi-sensor system for the quality assurance of CoDiCo-SMC is presented in this thesis. The developed methods for measurement uncertainty analysis offer the possibility to determine the quality of this multi-sensor system, consisting of laser light section and thermography, for the first time.

11 References

Literature sources according to the scheme A_Name (year) refers to student projects at the wbk Institute for Production Science, which were supervised by the author of this thesis.

IIA_Demmerle, J. (2016), *Konzeptentwicklung eines Multisensor-Messsystems zur Untersuchung faserverstärkter Kunststoffe durch Thermographie und Lasertriangulation*. Masterarbeit, Karlsruher Institut für Technologie (KIT), Karlsruhe, wbk Institut für Produktionstechnik.

A_Griener, J. (2018), *Untersuchung von SMC-UD-Bauteilen zur Klassifizierung von spezifischen Defekten mittels Puls-Phasen-Thermografie*. Bachelorarbeit, Karlsruher Institut für Technologie (KIT), Karlsruhe, wbk Institut für Produktionstechnik.

A_Ibach, D. (2018), *Untersuchung zur Tiefenbestimmung von SMC-UD-Bauteilen mittels Puls-Phasen-Thermografie*. Masterarbeit, Karlsruher Institut für Technologie (KIT), Karlsruhe, wbk Institut für Produktionstechnik.

A_Karwan, F. (2018), *Messunsicherheitsbestimmung eines Lasertriangulationssystem bei der Untersuchung von Sheet Moulding Compund*. Bacheloararbeit, Karlsruher Institut für Technologie (KIT), Karlsruhe, wbk Institut für Produktionstechnik.

A_Kretsch, D. (2017), *Programmierung einer Steuerung für ein Multisensorensystem*. Bachelorarbeit, Karlsruher Institut für Technologie (KIT), Karlsruhe, wbk Institut für Technologie.

A_Lorenz, M. (2017), *Untersuchung von defekten SMC-UD-Bauteilen mittels Lasertriangulation und Puls-Phasen-Thermographie*. Bachelorarbeit, Karlsruher Institut für Technologie (KIT), Karlsruhe, wbk Institut für Produktionstechnik.

A_Oergele, J.-N. (2017), *Parameterbestimmung eines Laserlichtschnittsystems zur Erfassung von SMC-Bauteilen*. Bachelorarbeit, Karlsruher Institut für Technologie (KIT), Karlsruhe, wbk Institut für Produktionstechnik.

A_Pohland, P. (2017), *Entwicklung eines Vorgehens zur Fusion eines 3D Laserscans und Bildaufnahmen der Puls-Phasen-Thermographie*. Masterarbeit, Karlsruher Institut für Technologie (KIT), Karlsruhe, wbk Institut für Produktionstechnik.

A_Pohlmann, P. (2017), *Parameteroptimierung zur Validierung der Messunsicherheit eines Lasertriangulationssystems bei der Untersuchung faserverstärkter Kunststoffe.* Masterarbeit, Karlsruher Institut für Technologie (KIT), Karlsruhe, wbk Institut für Produktionstechnik.

A_Sadic, E. (2017), *Defektanalyse in carbonfaserverstärkten SMC- Materialien und der Einfluss auf die mechanischen Eigenschaften.* Bachelorarbeit, Karlsruher Institut für Technologie (KIT), Karlsruhe, wbk Institut für Produktionstechnik.

A_Schwende, B. (2017), *Betrachtung und Gestaltung der vollständigen Prozesskette zur Entwicklung eines Werkzeuges für die Herstellung eines SMC-Bauteils.* Bachelorarbeit, Karlsruher Institut für Technologie (KIT), Karlsruhe, wbk Institut für Produktionstechnik.

A_Weinhardt, T. (2017), *Konstruktive Zusammenführung eines Multi-Sensor-Messsystems.* Studienarbeit, Karlsruher Institut für Technologie (KIT), Karlsruhe, wbk Institut für Produktionstechnik.

Abidi, M. A. (1992), *Data Fusion in Robotics & Machine Intelligence,* Elsevier Science, Oxford. ISBN: 0-12-042120-8.

AIAG (2010), *Measurement systems analysis. Reference Manual,* Automotive Industry Action Group, Southfield, Michigan. ISBN: 978-1-60-534211-5.

Ambrozinski, L.; Piwakowski, B.; Stepinski, T. & Uhl, T. (2012), 'Application of air-coupled ultrasonic transducers for damage assessment of composite panels', *6th European Workshop on Structural Health Monitoring.*

Arndt, R. (2007), *Rechteckimpuls-Thermografie im Frequenzbereich. Adaption der Puls-Phasen-Thermografie für die qualitative und quantitative zerstörungsfreie Prüfung oberflächennaher Strukturen im Bauwesen.* Dissertation, Universität Berlin, Berlin.

AT - Automation Technology GmbH (2014), *Hardware reference manual. C4-2040-GigE Camera.* Rev 1.8.

Bardl, G.; Nocke, A.; Cherif, C.; Pooch, M.; Schulze, M.; Heuer, H.; Schiller, M.; Kupke, R. & Klein, M. (2016), 'Automated detection of yarn orientation in 3D-draped carbon fiber fabrics and preforms from eddy current data', *Composites Part B: Engineering,* vol. 96, pp. 312–324.

Bargel, H.-J. & Schulze, G. (eds.) (2018), *Werkstoffkunde,* Springer Vieweg, Berlin. ISBN: 978-3-662-48629-0.

Bauer, N. (ed.) (2008), *Handbuch zur industriellen Bildverarbeitung. Qualitätssicherung in der Praxis,* Fraunhofer IRB-Verl., Stuttgart. ISBN: 978-3816773863.

Bedworth, M. & O'Brien, J. (2000), 'The Omnibus model. A new model of data fusion?', *IEEE Aerospace and Electronic Systems Magazine*, vol. 15, no. 4, pp. 30–36.

Berger, D.; Egloff, A.; Summa, J.; Schwarz, M.; Lanza, G. & Herrmann, H.-G. (2017), 'Conception of an Eddy Current In-process Quality Control for the Production of Carbon Fibre Reinforced Components in the RTM Process Chain', *Procedia CIRP*, vol. 62, pp. 39–44.

Berger, D.; Zaiß, M.; Krämer, A.; Häfner, B. & Lanza, G. (2016), 'Bewertung von Mess-systemen für den Leichtbau. Untersuchung verschiedener Messsysteme für faserver-stärkte Kunststoffe', *wt Werkstattstechnik online*, vol. 106, no. 11, pp. 787–793.

Berger, D.; Zaiß, M.; Lanza, G.; Summa, J.; Schwarz, M.; Herrmann, H.-G.; Pohl, M.; Günther, F. & Stommel, M. (2018), 'Predictive quality control of hybrid metal-CFRP components using information fusion', *Production Engineering*, vol. 12, no. 2, pp. 161–172.

Berndt, D. & Bauer, N. (eds.) (2003), *Leitfaden zu Grundlagen und Anwendungen der optischen 3-D-Messtechnik,* Fraunhofer-Allianz Vision, Erlangen. ISBN: 3-8167-6297-2.

Bernstein, J. (2011), *Optisches Multi-Sensor-Messverfahren zur dimensionellen in-line Messung von Strangprofilen im Fertigungsprozess,* Shaker. ISBN: 3844003452.

Beyerer, J. (ed.) (2006), *Informationsfusion in der Mess- und Sensortechnik,* Universi-tätsverlag, Karlsruhe. ISBN: 9783866440531.

Beyerer, J.; Puente León, F. & Frese, C. (2016), *Automatische Sichtprüfung. Grundla-gen, Methoden und Praxis der Bildgewinnung und Bildauswertung,* Springer Vieweg, Berlin. ISBN: 9783662477861.

Bledzki, A. K.; Kurek, K. & Gassan, J. (1995), 'Mikroporen in Faserverbundwerkstoffen. Beeinflussung des mechanischen Verhaltens', *Kunststoffe*, vol. 85, no. 12, pp. 2062–2065.

Böhlke, T. & Wood, J. (2014), *Integrated engineering of continuous-discontinuous long fiber reinforced polymer structures. Integrierte Entwicklung kontinuierlich-diskontinuierlich langfaserverstärkter Polymerstrukturen,* submitted research proposal to DFG for project GRK 2078.

Brabandt, D. (2018), *Qualitätssicherung von textilen Kohlenstofffaser-Preforms mittels optischer Messtechnik,* Shaker, Herzogenrath. ISBN: 978-3-8440-6070-6.

Brabandt, D.; Hettich, S. & Lanza, G. (2015), 'Messtechnik für die Qualitätssicherung von Carbonfaser-Preforms', *Lightweight Design*, vol. 8, no. 6, pp. 20–25.

Brabandt, D. & Lanza, G. (2015), 'Data Processing for an Inline Measurement of Preforms in the CFRP-Production', *Procedia CIRP*, vol. 33, pp. 269–274.

Bruderick, M.; Denton, D.; Shinedling, M. & Kiesel, M. (2002), *Applications of Carbon Fiber SMC for the 2003 Dodge Viper*. https://www.quantumcomposites.com/pdf/papers/Viper-SPE-Paper.pdf [21.06.2018].

Bücheler, D. (2018), *Locally continuous-fiber reinforced sheet molding compound*. Dissertation, Fraunhofer Verlag, Stuttgart. ISBN: 978-3-8396-1300-9.

Busse, G. & Eyerer, P. (1983), 'Thermal wave remote and nondestructive inspection of polymers', *Applied Physics Letters*, vol. 43, no. 4, pp. 355–357.

Busse, G. & Solodov, I. (2013), *Neue Materialien auf dem Prüfstand. Innovative zerstörungsfreie Prüfung für Luftfahrtanwendungen*. https://www.uni-stuttgart.de/presse/archiv/themenheft/09/busse.pdf [21.06.2018].

Carl Zeiss Industrielle Messtechnik GmbH (2011), *Zeiss METROTOM® 800. Technische Daten,* Oberkochen, Germany.

Carl Zeiss Industrielle Messtechnik GmbH (2015), *Kalibrierschein Zeiss Prismo,* Oberkochen, Germany.

Cherif, C. (2011), *Textile Werkstoffe für den Leichtbau. Techniken - Verfahren - Materialien - Eigenschaften,* Springer-Verlag Berlin Heidelberg, Berlin, Heidelberg. ISBN: 978-3-642-17992-1.

Chiwu, B.; Qingju, T.; Junyan, L. & Yang, W. (2014), 'Inspection on CFRP sheet with subsurface defects using pulsed thermographic technique', *Infrared Physics & Technology*, vol. 65, pp. 117–121.

Christoph, R. & Neumann, H. J. (2011), *Röntgentomografie in der industriellen Messtechnik. Präzise, wirtschaftlich und universell,* Süddeutscher Verlag onpact, München. ISBN: 978-3-86236-009-3.

Deutsch, W. A. K. (2000), *Automated Ultrasonic Inspection.* https://www.ndt.net/article/wcndt00/papers/idn197/idn197.htm [26.06.2018].

Dietrich, E. & Schulze, A. (2017), *Eignungsnachweis von Prüfprozessen,* Hanser, München. ISBN: 978-3-446-45124-7.

DIN (54192), *DIN 54192:2010-11: Zerstörungsfreie Prüfung – Aktive Thermografie,* Beuth, Berlin, 2010.

DIN (65673), *DIN 65673:1999-04: Luft- und Raumfahrt - Faserverstärkte Kunststoffe - Garn-, Gewebe- und Prepregfehler; Definitionen,* Beuth, Berlin, 1999.

DIN (66 025), *DIN 66 025 Teil 1:1983: Programmaufbau für numerisch gesteuerte Arbeitsmaschinen,* Beuth, Berlin, 1983.

DIN (1319), *DIN 1319-1:1995-01: Grundlagen der Meßtechnik Teil 1: Grundbegriffe,* Beuth, Berlin, 1995.

DIN EN (13018), *DIN EN 13018:2016-06: Zerstörungsfreie Prüfung – Sichtprüfung – Allgemeine Grundlagen,* Beuth, Berlin, 2016.

DIN EN (16714-3), *DIN EN 16714-3:2016-11: Zerstörungsfreie Prüfung – Thermografische Prüfung – Teil 3: Begriffe,* Beuth, Berlin, 2016.

DIN EN ISO (10012), *DIN EN ISO 10012:2004-03: Messmanagementsysteme - Anforderungen an Messprozesse und Messmittel,* Beuth, Berlin, 2004.

DIN EN ISO (14253-1), *DIN EN ISO 14253-1:2013-04: Geometrische Produktspezifikationen (GPS) – Prüfung von Werkstücken und Meßgeräten durch Messen – Teil 1: Entscheidungsregeln für den Nachweis von Konformität oder Nichtkonformität mit Spezifikationen,* Beuth, Berlin, 2013.

DIN EN ISO (15530-3), *DIN EN ISO 15530-3:2018-09: Geometrische Produktspezifikation und -prüfung (GPS) - Verfahren zur Ermittlung der Messunsicherheit von Koordinatenmessgeräten (KMG) - Teil 3: Anwendung von kalibrierten Werkstücken oder Normalen,* Beuth Verlag, Berlin, 2012.

DIN EN ISO (15549), *DIN EN ISO 15549:2011-03: Zerstörungsfreie Prüfung – Wirbelstromprüfung – Allgemeine Grundlagen,* Beuth, Berlin, 2011.

DIN ISO/TS (23165), *DIN ISO/TS 23165:2008-08: Geometrische Produktspezifikation (GPS) – Leitfaden zur Ermittlung der Testunsicherheit von Koordinatenmessgeräten (KMG),* Beuth, Berlin, 2008.

DIN V ENV (13005), *DIN V ENV 13005:1999-06: Leitfaden zur Angabe der Unsicherheit beim Messen,* Beuth, Berlin, 1999.

Dobmann, G. (2005), *Zerstörungsfreie Prüfverfahren – Überblick.* https://www.qz-online.de/qualitaets-management/qm-basics/messen_pruefen/thermographie/artikel/zerstoerungsfreie-pruefverfahren-ueberblick-157123.html [26.06.2018].

Domininghaus, H.; Elsner, P.; Eyerer, P. & Hirth, T. (eds.) (2012), *Kunststoffe. Eigenschaften und Anwendungen,* Springer, Berlin, Heidelberg. ISBN: 978-3-642-16173-5.

Donges, A. & Noll, R. (2015), *Laser Measurement Technology. Fundamentals and Applications,* Springer, Heidelberg. ISBN: 978-3-662-43633-2.

Döring, D. (2011), *Luftgekoppelter Ultraschall und geführte Wellen für die Anwendung in der zerstörungsfreien Werkstoffprüfung.* Dissertation, Universität Stuttgart, Stuttgart, Institut für Kunststofftechnik.

Dudzik, S. (2010), 'Approximation of Thermal Background Applied to Defect Detection using the Methods of Active Thermography', *Metrology and Measurement Systems*, vol. 17, no. 4, p. 758.

Dudzik, S. & Minkina, W. (2008), 'Application of the numerical method for the propagation of distributions to the calculation of coverage intervals in the thermovision measurements', *QIRT 2008 9th International Conference on Quantitative InfraRed Thermography*, Krakow, Poland.

Durrant-Whyte, H. F. (2016), 'Sensor Models and Multisensor Integration', *The International Journal of Robotics Research*, vol. 7, no. 6, pp. 97–113.

edevis GmbH (2016), *EDEVIS Leistungsbeschreibung und Angebot 19124459. PTvis Prüfsystem.* Submitted via E-Mail.

Effenberger, I. (2016a), 'Datenfusion. Software kombiniert Thermographie, Ultraschall und CT', *inVISON.* https://www.invision-news.de/allgemein/datenfusion-2/ [28.06.2018].

Effenberger, I. (2016b), *Final Report Summary - QUALIFIBRE (Qualification and Diagnosis of Carbon and Glass Fibre-Reinforced Composites with Non-Destructive Measurement Technologies)*, Fraunhofer IPA. https://cordis.europa.eu/result/rcn/176989_de.html [28.06.2018].

Effenberger, I.; Martinez, H. V.; Schloske, A. & Klieber, A. (2013), 'Kombination etablierter und neuer Methoden. Messen und Prüfen von Faserverbundbauteilen', *QZ*, vol. 58, no. 10, pp. 38–41. https://www.ipa.fraunhofer.de/content/dam/ipa/de/documents/UeberUns/Leitthemen/Leichtbau/Messen_und_Pruefen_von_Faserverbundbauteilen.pdf [30.06.2018].

Egloff, A. (2017), *Entwicklung eines automatisierten Prüfstands zur systematischen Ermittlung von Zusammenhängen und Wechselwirkungen zwischen Faserhalbzeugen und der Wirbelstromprüfung*. Masterarbeit, Karlsruher Institut für Technologie (KIT), Karlsruhe, wbk Institut für Produktionstechnik.

Ehrenstein, G. W. (2006), *Faserverbund-Kunststoffe. Werkstoffe - Verarbeitung - Eigenschaften,* Hanser, München, Wien. ISBN: 9783446227163.

Eickenbusch, H. & Krauss, O. (2014), *Werkstoffinnovationen für nachhaltige Mobilität und Energieversorgung.* Verein Deutscher Ingenieure e.V. (ed.), Düsseldorf.

Eitzinger, C.; Engel, F.; Orth, T. & Weimer, C., *Patent: Devices and Methodsfor depositing reinforcing fiber tapes and detecting laying errors* (2017), US US 2017/0001384 A1.

Ekanayake, S.; Gurram, S. & Schmitt, R. H. (2018), 'Depth determination of defects in CFRP-structures using lock-in thermography', *Composites Part B: Engineering*, vol. 147, pp. 128–134.

Ekanayake, S.; Isenberg, C. & Schmitt, R. H. (2017), 'Method for Quantitative 3D Evaluation of Defects in CFRP Using Active Lock-in Thermography', *Procedia CIRP*, vol. 66, pp. 254–258.

Engel, F.; Weimer, C. & Orth, T., *Patent: Laying unit and method for producing a fibre composite component* (2016a), US 2017/0144386 A1.

Engel, F.; Weimer, C. & Orth, T., *Patent: Laying unit, device and method for producing a fiber composite component* (2016b), US 2017/0144384 A1.

Erhard, A. (2007), *Aufgaben und Abgrenzung der Zerstörungsfreien Prüfung,* DGZfP-Jahrestagung 2007. https://www.ndt.net/article/dgzfp07/Inhalt/v11.pdf.

Erhard, A. (2014), *Verfahren der zerstörungsfreien Materialprüfung. Grundlagen,* DVS Media, Düsseldorf. ISBN: 9783871556135.

Europaparlament und Europarat (2009), *Zur Festsetzung von Emissionsnormen für neue Personenkraftwagen im Rahmen des Gesamtkonzepts der Gemeinschaft zur Verringerung der CO2-Emissionen von Personenkraftwagen und leichten Nutzfahrzeugen. Verordnung (EG) Nr. 443/2009.*

Eyerer, P. & Busse, G. (1983), 'Photothermische Wärmewellenanalyse von Kunststoffen', *Kunststoffe,* vol. 73, no. 9, pp. 547–549.

Eyerer, P. & Wintergerst, S. (1971), 'Untersuchungen zum Verlauf der Härtung dünner Epoxidharzschichten (Metallverklebungen)', *Adhäsion,* no. 4, pp. 106–113.

Favro, L. D. & Han, X. (1998), 'Thermal Wave Materials Characterization and Thermal Wave Imaging', *Sensing for Materials Characterization, Processing and Manufacuring,* pp. 399–415.

Flemming, M.; Ziegmann, G. & Roth, S. (1999), *Faserverbundbauweisen. Fertigungsverfahren mit duroplastischer Matrix,* Springer Berlin Heidelberg, Berlin, Heidelberg. ISBN: 978-3-642-58371-1.

Förstner, W. & Wrobel, B. (2016), *Photogrammetric computer vision. Statistics, geometry, orientation, and reconstruction,* Springer, Cham. ISBN: 978-3-319-11549-8.

Fraunhofer-Institut für System- und Innovationsforschung ISI; Fraunhofer-Institut für Chemische Technologien ICT; Fraunhofer-Institut für Produktionstechnik und Automatisierung IPA; Fraunhofer-Institut für Arbeitswirtschaft und Organisation IAO & Karlsruhe Institut für Technologie – wbk Institut für Produktionstechnik (2014), *Leichtbau – Trends und Zukunftsmärkte und deren Bedeutung für Baden-Württemberg.* Leichtbau BW GmbH (ed.), Stuttgart.

Fritz, H.-G. & Eisenbach, C. D. (eds.) (2003), *18. Stuttgarter Kunststoff-Kolloquium,* Univ. IKT IAMC, Stuttgart. ISBN: 3-00-010663-4.

Fürtjes, T. (2016), *Echtzeitfähige Machine-Vision-Systeme zur Qualitätssicherung im Faserverbundleichtbau.* Dissertation, RWTH Aachen.

Galovska, M.; Petz, M. & Tutsch, R. (2012), 'Unsicherheit bei der Datenfusion dimensioneller Messungen', *tm – Technisches Messen*, vol. 79, no. 4, pp. 238–245.

Geiss, C. & Hornfeck, C. (2015), 'Comparison of Mobile Nondestructive Testing Methods to Detects Impact Damages in Fiber Reinforced Plastics'.

Gleiter, A. (2011), *Mess- und Auswertemethoden für die dynamische Thermografie*. Dissertation, Universitätsbibliothek der Universität Stuttgart, Stuttgart, Institut für Kunststofftechnik.

Gleiter, A.; Spießberger, C. & Busse, G. (2007), 'Tiefenaufgelöste Defekterkennung mit optisch angeregter Lockin-Thermografie', *Thermografie-Kolloquium 2007*, Stuttgart, Germany.

Gleiter, A.; Spießberger, C. & Busse, G. (2010), 'Lockin-thermography with optical or ultrasound excitation', *Strojniski Vestnik/Journal of Mechanical Engineering*, vol. 56, no. 10.

Grellmann, W.; Seidler, S. & Altstädt, V. (eds.) (2013), *Polymer testing,* Hanser, Munich. ISBN: 978-1-56990-548-7.

Gros, X. E.; Bousigue, J. & Takahashi, K. (1998), 'NDT data fusion at pixel level', *NDT&E International,* pp. 283–292.

Hall, D. L. & Llinas, J. (1997), 'An Introduction to Multisensor Data Fusion', *Prceedings of the IEEE*, vol. 85, no. 1, pp. 6–23.

Hall, D. L. & McMullen, S. A. H. (2004), *Mathematical techniques in multisensor data fusion,* Artech House, Boston. ISBN: 1580533353.

Harich, J. (2008), *Theorie und Numerik unidirektional verstärkter Faserverbundwerkstoffe. 3D-Finite-Element-Untersuchungen der Faser-Matrix-Mikroinstabilitäten*. Dissertation, Inst. für Baustatik, Karlsruhe. ISBN: 3935322151.

Härtig, F.; Hirsch, J.; Jusko, O.; Kniel, K.; Neuschaefer-Rube, U. & Wendt, K. (2009), 'Koordinatenmesstechnik als Schlüsseltechnologie der FertigungsmesstechnikCoordinate Metrology as a Key Technology in Production Measurement', *tm – Technisches Messen*, vol. 76, no. 2, pp. 73–82.

Härtig, F. & Krystek, M. (2009), 'Correct treatment of systematic errors in the evaluation of measurement uncertainty', *Proceedings of the 9th International Symposium on Measurement Technology and Intelligent Instruments* 2009, 1-016 - 1-019.

Hellier, C. (2013), *Handbook of nondestructive evaluation,* McGraw-Hill, New York. ISBN: 978-0071777148.

Henning, F. & Moeller, E. (eds.) (2011), *Handbuch Leichtbau. Methoden, Werkstoffe, Fertigung,* Hanser, München. ISBN: 978-3-446-42267-4.

Hertlin, I. & Herkel, T. (2003), *Riss- und Gefügeprüfung mit akustischer Resonanzanalyse im Schall- und Ultraschallbereich für Kfz-Sicherheitsteile.* DGfZP (ed.), DGZfP-Jahrestagung 2003. http://www.ndt.net/article/dgzfp03/papers/v18/v18.htm [26.06.2018].

Heuer, H.; Schulze, M.; Pooch, M.; Gäbler, S.; Nocke, A.; Bardl, G.; Cherif, C.; Klein, M.; Kupke, R.; Vetter, R.; Lenz, F.; Kliem, M.; Bülow, C.; Goyvaerts, J.; Mayer, T. & Petrenz, S. (2015), 'Review on quality assurance along the CFRP value chain – Nondestructive testing of fabrics, preforms and CFRP by HF radio wave techniques', *Composites Part B: Engineering*, vol. 77, pp. 494–501.

Heuss, R.; Müller, N.; van Sintern, W.; Starke, A. & Tschiesner, A. (2012), 'Lightweight, heavy impact-How carbon fiber and other lightweight materials will develop across industries and specifically in automotive', *Advanced Industries McKinsey & Company*.

Hillger, W. (2000), 'Erfahrung mit luftgekoppelter Ultraschallprüftechnik', *DGZfP-Jahrestagung 2000*, no. 73, pp. 781–786. http://www.dlr.de/fa/Portaldata/17/Resources/dokumente/institut/2000/u2000_2.pdf [26.06.2018].

Hillger, W. & Wachter, F. K. von (1991), 'Ultraschallprüfung an Faserverbundkunststoffen Grundlagen, Methoden der bildhaften Darstellung und Ergebnisse', *Materialwissenschaft und Werkstofftechnik*, vol. 22, no. 6, pp. 217–224.

Hochrein, T. (2013), 'Ich sehe was, was du nicht siehst', *Kunststoffe*, no. 11, pp. 70–74.

Holstein, P.; Effenberger, I.; Bariska, A.; Fulga, S.; Springhoff, A.; Bodi, A.; Steinhausen, R.; Neuenschwander, J. & Plamondon, M. (2015), 'Automatische Fehlererkennung in Kunststoffkompositbauteilen', *DACH-Jahrestagung 2015*, Salzburg, Austria.

Hopmann, C.; Eckstein, L.; Schmitt, R. & Reisgen, U. (2017), 'Industrie-4.0-Techniken für CFK-Reparaturen an Fahrzeugen', *Lightweight Design*, vol. 10, no. 2, pp. 44–49.

Hornfeck, C.; Geiss, C.; Rücker, M. & Grosse, C. U. (2015), 'Comparative Study of State of the Art Nondestructive Testing Methods with the Local Acoustic Resonance Spectroscopy to Detect Damages in GFRP', *Journal of Nondestructive Evaluation*, vol. 34, no. 2, p. 1839.

Ibarra Castanedo, C. (2005), *Quantitative subsurface defect evaluation by pulsed phase thermography: depth retrieval with the phase*. Dissertation, Université Laval, Québec, Faculté des Sciences et de Génie.

Ibarra-Castanedo, C.; Genest, M.; Guibert, S.; Piau, J.-M.; Maldague, X. P. V. & Bendada, A. (2007), 'Inspection of aerospace materials by pulsed thermography, lock-in thermography, and vibrothermography. A comparative study', *Defense and Security Symposium*, Orlando, Florida, United States.

Ibarra-Castanedo, C.; Grinzato, E.; Marinetti, S.; Bison, P.; Avdelidis, N.; Grenier, M.; Piau, J.-M.; Bendada, A. & Maldague, X. (2008), 'Quantitative assessment of aerospace materials by active thermography techniques', *QIRT 2008 9th International Conference on Quantitative InfraRed Thermography*, Krakow, Poland.

Ilinzeer, S. (2018), *Material IRTG*. Submitted via E-Mail.

Ilschner, B. & Singer, R. F. (2010), *Werkstoffwissenschaften und Fertigungstechnik. Eigenschaften, Vorgänge, Technologien,* Springer-Verlag Berlin Heidelberg, Berlin, Heidelberg. ISBN: 978-3-642-01734-6.

Imkamp, D. & Berthold, J. (2009), 'Schneller, sicherer, genauer. Roadmap Fertigungsmesstechnik 2020', *QZ – Qualität und Zuverlässigkeit*, vol. 54, no. 5, pp. 36–39.

Imkamp, D. & Sommer, K.-D. (2009), 'Roadmap Fertigungstechnik 2020 (Teil 4) – Für eine sichere Fertigung', *QZ – Qualität und Zuverlässigkeit* 2009, pp. 31–33.

InfraTec GmbH (2016a), *Angebot. ImageIR® 5385 S / 25 mm*. Submitted via E-Mail.

InfraTec GmbH (2016b), *Broschüre: High-End-Kameraserie ImageIR®. Thermografiesysteme für höchste Ansprüche. Thermografiesysteme für höchste Ansprüche*. Submitted via E-Mail.

InfraTec GmbH (2018), *Bildfeldrechner*. https://www.infratec.de/thermografie/waermebildkameras/bildfeldrechner/?camera=67 [14.11.2018].

Ishikawa, M.; Hatta, H.; Habuka, Y.; Fukui, R. & Utsunomiya, S. (2013), 'Detecting deeper defects using pulse phase thermography', *Infrared Physics & Technology*, vol. 57, pp. 42–49.

Jähne, B. (1997), *Digitale Bildverarbeitung,* Springer Berlin Heidelberg, Berlin, Heidelberg.s.l. ISBN: 978-3-662-06733-8.

JCGM (100), *JCGM 100:2008: Evaluation of Measurement Data - Guide to the Expression of Uncertainty in Measurement,* 2008.

JCGM (101), *JCGM 101:2008: Evaluation of measurement data — Supplement 1 to the "Guide to the expression of uncertainty in Measurement" — Propagation of distributions using a Monte Carlo method,* 2008.

Kaiser, H. & Karbhari, V. M. (2001), *Quality and Monitoring of Structural Rehabilitation Measures. Part 1: Description of potential defects.* https://www.academia.edu/3317362/QUALITY_AND_MONITORING_OF_STRUCTURAL_REHABILITATION_MEASURES [07.01.2019].

Kalender, W. A. (2006), *Computertomographie. Grundlagen, Gerätetechnologie, Bildqualität, Anwendungen,* Publicis Corp. Publ, Erlangen. ISBN: 978-3895782152.

Kärger, L.; Böhlke, T.; Weidenmann; Kay André; Seelig, T. & Henning, F. (2016), *Integrated engineering of continuous-discontinuous long fiber reinforced polymer (CoDiCo-FRP) structures in the framework of the International Research Training Group GRK 2078,* Hamburg.

Keckl, C.; Kuppinger, J. & Henning, F. (2014), 'Noch weniger Gewicht', *Kunststoffe*, no. 2, pp. 30–32.

Keferstein, C. P.; Marxer, M. & Bach, C. (2018), *Fertigungsmesstechnik. Alles zu Messunsicherheit, konventioneller Messtechnik und Multisensorik,* Springer Vieweg, Wiesbaden. ISBN: 978-3-658-17756-0.

Kia, H. G. (ed.) (1993), *Sheet molding compounds. Science and technology,* Hanser, Munich. ISBN: 9783446162136.

Kochan, A. (2012), *Untersuchungen zur zerstörungsfreien Prüfung von CFK-Bauteilen für die fertigungsbegleitende Qualitätssicherung im Automobilbau.* Dissertation, Shaker, Aachen. ISBN: 9783844008203.

Kosse, P.; Soemer, E.; Schmitt, R.; Engel, B. & Deitmerg, J. (2016), 'Optische Erfassung und Analyse der Faserwelligkeit gebogener Faser-Thermoplast-Verbunde', *tm – Technisches Messen*, vol. 83, no. 1.

Krämer, A.; Lin, S.; Brabandt, D.; Böhlke, T. & Lanza, G. (2014), 'Quality Control in the Production Process of SMC Lightweight Material', *Procedia CIRP*, vol. 17, pp. 772–777.

Krüger, M. & Mook, G. (2006), 'Detektion von Defekten in adaptiven CFK-Laminaten mittels bildgebender Laservibrometrie', *ZfP. Zeitung*, vol. 99, pp. 36–41.

Kruth, J. P.; Bartscher, M.; Carmignato, S.; Schmitt, R.; Chiffre, L. de & Weckenmann, A. (2011), 'Computed tomography for dimensional metrology', *CIRP Annals-Manufacturing Technology*, vol. 60, no. 2, pp. 821–842.

Lahiri, B. B.; Bagavathiappan, S.; Reshmi, P. R.; Philip, J.; Jayakumar, T. & Raj, B. (2012), 'Quantification of defects in composites and rubber materials using active thermography', *Infrared Physics & Technology*, vol. 55, 2-3, pp. 191–199.

Lanza, G. & Brabandt, D. (2012), 'A Concept for Inline Quality Assurance in the Automated Production of Carbon-Fiber-Reinforced Plastics (CFRP)', *Quality-Access to Success,* pp. 187–192.

Lasagni, F.; Rodriguez, B.; Santamaria, M. L.; Galleguillos, C.; Hernández, S. & Cuevas, E. (2015), 'On-Line Damage Monitoring and Evaluation in CFRP Aerospace Structures During Mechanical Testing', *7th International Symposium on NDT in Aerospace*, Bremen, Germany.

Lässig, R.; Eisenhut, M.; Mathias, A.; Schulte, R. T.; Peters, F.; Kühmann, T.; Waldmann, T. & Begemann, W. (2012), 'Serienproduktion von hochfesten Faserverbundbauteilen. Perspektiven für den deutschen Maschinen-und Anlagenbau', *Studie Roland Berger*, Munich, Germany.

Lightfoot, J. & Wisnom, M. & Potter, K. (2013), 'Examination of drape-induced defects using computer x-ray tomography', *ICCM 19,* pp. 7108–7116.

Liu, J.; Gong, J.; Qin, L. & Wang, Y. (2015), 'Study on Lock-in Thermography Defect Detectability for Carbon-Fiber-Reinforced Polymer (CFRP) Sheet with Subsurface Defects', *International Journal of Thermophysics*, vol. 36, 5-6, pp. 1259–1265.

Lizaranzu, M.; Lario, A.; Chiminelli, A. & Amenabar, I. (2015), 'Non-destructive testing of composite materials by means of active thermography-based tools', *Infrared Physics & Technology*, vol. 71, pp. 113–120.

Losch, D.; Ekanayake, S.; Nienheysen, P.; Bethlehem-Eichler, K.; Schmitz, R.; Bier, S. & Rossmann, J. (2016), 'An Industry 4.0-based repair concept for structural CFRP components in the automotive sector'. *2016 2nd IEEE International Symposium on Robotics and Manufacturing Automation (ROMA),* IEEE, pp. 1–6. ISBN: 978-1-5090-0928-2.

Luo, R. C. & Kay, M. G. (1989), 'Multisensor integration and fusion in intelligent systems', *IEEE Transactions on Systems, Man, and Cybernetics*, vol. 19, no. 5, pp. 901–931.

Maier, A.; Schmidt, R.; Oswald-Tranta, B. & Schledjewski, R. (2014), 'Non-Destructive Thermography Analysis of Impact Damage on Large-Scale CFRP Automotive Parts', *Materials*, vol. 7, no. 1, pp. 413–429.

Maierhofer, C.; Myrach, P.; Steinfurth, H.; Reischel, M. & Röllig, M. (2014), 'Development of standards for flash thermography and lock-in thermography', *QIRT 2014 12th International Conference on Quantitative Infrared Thermography*, Bordeaux, France.

Maldague, X. P. V. (2001), *Theory and practice of infrared technology for nondestructive testing,* Wiley, New York, NY. ISBN: 0471181900.

Maldague, X. P. V. & Moore, P. O. (eds.) (2001), *Infrared and thermal testing,* American Society for Nondestructive Testing, Columbus, Ohio. ISBN: 1-57117-044-8.

Mathes, V. & Witten, E. (eds.) (2014), *Handbuch Faserverbundkunststoffe/Composites. Grundlagen, Verarbeitung, Anwendungen,* Springer Vieweg, Wiesbaden. ISBN: 9783658027551.

Matthews, F. L. (1999), 'Damage in Fibre-Reinforced Plastics; Its Nature, Consequences and Detection', *Key Engineering Materials*, 167-168, pp. 1–16.

Mayr, G.; Dietermayr, B.; Hendorfer, G. & Sekelja, J. (2008), 'Characterization of Defects in Curved CFRP Samples using Pulsed Thermography and 3D Finite Element Simulation', *QIRT 2008 9th International Conference on Quantitative InfraRed Thermography*, Krakow, Poland.

Mayr, G. & Hendorfer, G. (2010), 'Porosity Determination by Pulsed Thermography in Reflection Mode', *QIRT 10 10th International Conference on Quantitative InfraRed Thermography*, Québec, Canada.

Mayr, G.; Plank, B.; Sekelja, J. & Hendorfer, G. (2011), 'Active thermography as a quantitative method for non-destructive evaluation of porous carbon fiber reinforced polymers', *NDT & E International*, vol. 44, no. 7, pp. 537–543.

Mersmann, C. (2012), *Industrialisierende Machine-Vision-Integration im Faserverbundleichtbau.* Dissertation, Apprimus Wissenschaftsverlag, Aachen. ISBN: 9783863590628.

Michaeli, W. & Begemann, M. (eds.) (1990), *Einführung in die Technologie der Faserverbundwerkstoffe,* Hanser, München. ISBN: 3-446-15786-7.

Michaeli, W. & Kremer, C. (2010), 'Simulativ zur Class-A-Oberfläche von SMC-Bauteilen', *ATZ - Automobiltechnische Zeitschrift*, vol. 112, no. 11, pp. 814–819.

Miene, A. (2009), 'Genau in die Textur geschaut', *Kunststoffe*, no. 5, pp. 62–65.

Miene, A. (2010), 'Bildanalytische Qualitätssicherung in der Preformfertigung', *5. Sitzung der Arbeitsgruppe „Werkstoff- und Bauteilprüfung"*, Augsburg, Germany.

Minkina, W. & Dudzik, S. (2006), 'Simulation analysis of uncertainty of infrared camera measurement and processing path', *Measurement*, vol. 39, no. 8, pp. 758–763.

Minkina, W.; Duzik, S. & Gryś, S. (2010), 'Errors of thermographic measurements – exercises', *QIRT 10 10th International Conference on Quantitative InfraRed Thermography*, Québec, Canada.

Mitchell, H. B. (ed.) (2007), *Multi-Sensor Data Fusion. An Introduction,* Springer-Verlag GmbH, Berlin, Heidelberg. http://site.ebrary.com/lib/alltitles/docDetail.action?docID=10185650. ISBN: 9783540715597.

Mitchell, H. B. (2010), *Multi-sensor data fusion. An introduction,* Springer, Berlin.Heidelberg. ISBN: 3642090672.

Mohammadikaji, M.; Bergmann, S.; Irgenfried, S.; Beyerer, J.; Dachsbacher, C. & Worn, H. (2016), 'A framework for uncertainty propagation in 3D shape measurement using laser triangulation'. *2016 IEEE International Instrumentation and Measurement Technology Conference Proceedings,* IEEE, pp. 1–6. ISBN: 978-1-4673-9220-4.

Mook, G.; Lange, R. & Koeser, O. (2001), 'Non-destructive characterisation of carbon-fibre-reinforced plastics by means of eddy-currents', *Composites Science and Technology*, vol. 61, no. 6, pp. 865–873.

Müllerferli, G. (1993), *Vergleich von radiologischen, zerstörungsfreien Prüfverfahren für Faserverbundkunststoffe*. Dissertation, Verl. der Augustinus-Buchh., Aachen. ISBN: 3860731173.

Muntzinger, W. (2013), 'Optimierung von CFK-Strukturen. Kolloquienreihe Innovation und Nachhaltigkeit 2013', *Schriftenreihe der Universität der Bundeswehr München*, Munich, Germany.

Myrach, P.; Maierhofer, C.; Reischel, M.; Rahammer, M. & Holtmann, N. (2014), 'Untersuchung der Auflösungsgrenzen der Lockin-Thermografie zur Prüfung von Faserverbundwerkstoffen', *DGZfP-Jahrestagung 2014*, Potsdam, Germany.

Neitzel, M.; Mitschang, P. & Breuer, U. (2014), *Handbuch Verbundwerkstoffe. Werkstoffe, Verarbeitung, Anwendung,* Carl Hanser Fachbuchverlag, s.l. http://ebooks.ciando.com/book/index.cfm/bok_id/1551122. ISBN: 978-3-446-43697-8.

Orth, A. (2008), *Entwicklung eines Bildverarbeitungssystems zur automatisierten Herstellung faserverstärkter Kunststoffstrukturen*. Dissertation, Shaker, Aachen. ISBN: 3832269835.

Oster, R. (2012), 'Herausforderungen an die ZfP bei Ihrer Anwendung an Faserverbundbauteilen', *Fachseminar Mikrowellen-und Terahertz-Prftechnik. Graz, Austria: DACH-Jahrestagung,* pp. 1–3.

Perterer, M.; Höchtl, F.; Kiefmann, A.; Baier, H. & Senner, V. (2011), 'Kosteneffiziente phasenmodulierte Thermographie zur Schadensdetektion an flachen und stark gekrümmten Bauteilen aus CFK', *DGZfP-Jahrestagung 2011*, Bremen, Germany.

Pfeifer, T. & Schmitt, R. (2010), *Fertigungsmesstechnik,* Oldenbourg Wissenschaftsverlag, München. ISBN: 978-3-486-59202-3.

Plank, B.; Ellert, F.; Gruber, J.; Gusenbauer, C. & Kastner, J. (2013), 'Detektion von Fehlern in kohlenstofffaserverstärkten Kunststoffen mittels Sichtprüfung, Ultraschallprüfung, Radioskopie, aktiver Thermographie und Röntgen Computertomografie', *DGZfP-Jahrestagung 2013*, Dresden, Germany.

Polynt Composites Germany GmbH (2016), *UDCarbon® 24 CF60-12K.* Submitted via E-Mail, Miehlen.

Potter, K. (1997), *Resin Transfer Moulding,* Springer Netherlands, Dordrecht. ISBN: 978-94-009-0021-9.

RAMPF (2014), *3-Achs-Portal. Produkthandbuch*. V1.2.

Raol, J. R. (2010), *Multi-sensor data fusion with MATLAB,* CRC Press, Boca Raton, FL. ISBN: 1439800057.

Richter, H.-U. (ed.) (1999), *Chronik der zerstörungsfreien Materialprüfung,* Verl. für Schweißen und Verwandte Verfahren DVS-Verl., Berlin. ISBN: 978-3-87155-942-6.

Ricolfe-Viala, C. & Sanchez-Salmeron, A.-J. (2010), 'Lens distortion models evaluation', *Applied optics*, vol. 49, no. 30, pp. 5914–5928.

Rieth-Hoerst, S. (2007), 'Akustische Methoden zur Prüfung von Werkstücken', *etz*, no. 5, pp. 2–4.

Roos, E. & Maile, K. (2015), *Werkstoffkunde für Ingenieure. Grundlagen, Anwendung, Prüfung,* Springer Vieweg, Berlin. ISBN: 978-3-642-54988-5.

RTE Akustik + Prüftechnik GmbH (2018), *Akustische Materialprüftechnik.* https://www.rte.de/pruefbereiche/akustische-materialprueftechnik/ [25.06.2018].

Ruser, H. & Puente León, F. (2007), 'Informationsfusion. Eine Übersicht', *tm Technisches Messen*, vol. 74, no. 3.

Sackewitz, M. (2011), *Leitfaden zur Wärmefluss-Thermographie: zerstörungsfreie Prüfung mit Bildverarbeitung,* Fraunhofer-Verlag. ISBN: 3839602343.

Sauerwein, C.; Burdairon, S.; Knupe, G.; Krumm, M.; Oster, R.; Diewel, B. & Sindel, M. (2012), 'Qualifikationsunterstützung von Faserverbund-Bauteilen für den industriellen Einsatz mit Hilfe von spezialisierten CT-Verfahren', *DACH-Jahrestagung 2012*, Graz, Austria.

Schäferling, M.; Berger, D.; Häfner, B. & Lanza, G. (2018), 'Data Fusion for Quality Assurance of Fibre-Reinforced Plastics', *International Symposium on Structural Health Monitoring and Nondestructive Testing.* https://www.ndt.net/article/shmndt2018/papers/SHM-NDT-2018_paper_9.pdf [05.12.2018].

Schmidt, T. & Dutta, S. (2013), 'CFRP manufacturing process chain observation by means of automated thermography', *5th International Symposium on NDT in Aerospace*, Singapore.

Schmitt, R. (2008), *FALCON - Fiber Automatic Live Control. Aufbau eines Inline-Prüfsystems zur automatisierten Konfektion faserverstärkter Kunststoffstrukturen.* Schmitt, R. (2008), FALCON - Fiber Automatic Live Control. Aufbau eines Inline-Prüfsystems zur.

Schmitt, R. & Damm, B. E. (2008), 'Prüfen und Messen im Takt. Wie Sie mit Inline-Messtechnik Ihre Wertschöpfung maximieren', *QZ – Qualität und Zuverlässigkeit*, vol. 53, no. 9, pp. 57–59.

Schmitt, R.; Ekanayake, S. & Nienheysen, P. (2018), 'Digitale Reise ins kohlenstofffaserverstärkte Innere. Multisensorbasierte Schadenserfassung im CFK-Reparaturprozess', *Kunststoffe*, no. 2, pp. 27–30.

Schmitt, R.; Fürtjes, T.; Abbas, B.; Abel, P.; Kimmelmann, W.; Kosse, P. & Buratti, A. (2015), 'Real-Time Machine Vision System for an Automated Quality Monitoring in Mass Production of Multiaxial Non-Crimp Fabrics', *IFAC-PapersOnLine*, vol. 48, no. 3, pp. 2393–2398.

Schmitt, R.; Kosse, P.; Kimmelmann, W. & Fürtjes, T. (2014), 'Inline-Qualitätssicherung im FVK-Umflechtprozess. Automatisierte Inline-Qualitätssicherung im Faserverbundleichtbau mittels Sensordatenfusion', *wt Werkstattstechnik online*, vol. 104, no. 11, pp. 747–752. https://www.werkstattstechnik.de/wt/get_article.php?data%5barticle_id%5d=81881 [27.06.2018].

Schmitt, R.; Pfeifer, T.; Mersmann, C. & Orth, A. (2008), 'A method for the automated positioning and alignment of fibre-reinforced plastic structures based on machine vision', *CIRP Annals - Manufacturing Technology*, vol. 57, no. 1, pp. 501–504.

Schulze, M.; Goldbach, S.; Heuer, H. & Meyendorf, N. (2011), *Ein Methodenvergleich - ZfP an Kohlefaserverbundwerkstoffen mittels wirbelstrom- und ultraschallbasierender Prüfung*.

Schulze, M. H.; Heuer, H.; Küttner, M. & Meyendorf, N. (2010), 'High-resolution eddy current sensor system for quality assessment of carbon fiber materials', *Microsystem Technologies*, vol. 16, no. 5, pp. 791–797.

Schürmann, H. (2007), *Konstruieren mit Faser-Kunststoff-Verbunden,* Springer-Verlag Berlin Heidelberg, Berlin, Heidelberg. ISBN: 978-3-540-72189-5.

Schwenke, H. & Franke, M. (2007), 'Bestimmung der Unsicherheit von Messungen mit KMG – Status und Ausblick', *PTB-Mitteilungen* 2007, pp. 363–371.

Siemer, U. (2010), *Einsatz der Thermografie als zerstörungsfreies Prüfverfahren in der Automobilindustrie*. Dissertation, Shaker, Herzogenrath. ISBN: 978-3832296742.

Soldan, S. (2014), *Sensordatenfusionsansätze in der Thermografie zur Verbesserung der Messergebnisse*. Dissertation, Kassel Univ. Press, Kassel. ISBN: 9783862195497.

Sommer, K.-D. & Siebert, B. R. L. (2004), 'Praxisgerechtes Bestimmen der Messunsicherheit nach GUM (Practical Determination of the Measurement Uncertainty under GUM)', *tm – Technisches Messen*, vol. 71, 2-2004, pp. 52–66.

Spießberger, C.; Gleiter, A. & Busse, G. (2008), 'Aerospace Applications of Lockin-Thermography with Optical, Ultrasonic, and Inductive Excitation', *International Symposium on NDT in Aerospace*, Fürth, Germany.

Stachel, P. (2012), 'SMC/BMC - bewährtes Material für neue Problemlösungen', *AVK, Industrievereinigung Verstärkte Kunststoffe e.V.*, Frankfurt, Germany.

Stewart, R. (2009), 'Lightweighting the automotive market', *Reinforced plastics*, vol. 53, no. 2, pp. 14–21.

Süße, H. & Rodner, E. (2014), *Bildverarbeitung und Objekterkennung. Computer Vision in Industrie und Medizin,* Springer Vieweg, Wiesbaden. ISBN: 978-3-8348-2605-3.

Suter Kunststoffe AG (2018), *Faserverbund-Werkstoffdaten. Eine Sammlung der wichtigsten Werkstoffdaten für den Anwender von Faserverbund-Materialien sowie allgemeine Daten und Tabellen.* Suter Kunststoffe AG (ed.). https://www.swiss-composite.ch/pdf/i-Werkstoffdaten.pdf [16.11.2018].

Teschner, R. (2013), *Glasfasern,* Springer Berlin Heidelberg, Berlin, Heidelberg. ISBN: 978-3-642-38329-8.

Thiemann, C. (2015), *Methode zur Konfiguration automatisierter thermografischer Prüfsysteme.* Dissertation, Herbert Utz Verlag, München. ISBN: 978-3-8316-4574-9.

Ullmann, T. (2008), *Zerstörungsfreie Prüfung von CMC-Strukturbauteilen,* DLR Stuttgart, Institut für Bauwesen und Konstruktionsforschung, Faserkeramik-Kolloquium.

Vaara, P. & Leinonen, J. (2012), *Technology Survey on NDT of Carbon-fiber Composites,* Uniprint, Oulu. ISBN: 978-952-5897-43-2.

VDA (Band 5), *VDA Band 5:2011: Prüfprozesseignung, Eignung von Messsystemen, Mess- und Prüfprozessen, Erweiterte Messunsicherheit, Konformitätsbewertung,* Henrich Druck + Medien GmbH, Berlin, 2011.

VDI/VDE (2011), *Fertigungsmesstechnik 2020. Technologie-Roadmap für die Messtechnik in der industriellen Produktion,* Düsseldorf, Germany.

VDI/VDE (2617), *VDI/VDE 2617:2011: Genauigkeit von Koordinatenmessgeräten Kenngrößen und deren Prüfung,* Beuth, Berlin, 2001.

VDI/VDE (2617), *VDI/VDE 2617-8:2017: Genauigkeit von Koordinatenmessgeräten Kenngrößen und deren Prüfung,* Verein Deutscher Ingenieure e.V., Düsseldorf, 2017.

VDI/VDE-Gesellschaft Mess- und Automatisierungstechnik (2018), *6. VDI-Fachtagung Optische Messung von Funktionsflächen,* VDI Verlag GmbH, Düsseldorf. ISBN: 978-3-18-092326-0.

Vollmer, M.; Mouml & Ilmann, K.-P. (2011), *Infrared Thermal Imaging. Fundamentals, Research and Applications,* Wiley-VCH, Weinheim. ISBN: 978-3-527-40717-0.

Wald, L. (1999), 'Some terms of reference in data fusion', *IEEE Transactions on Geoscience and Remote Sensing*, vol. 37, no. 3, pp. 1190–1193.

Wallbrink, C.; Wade, S. A. & Jones, R. (2007), 'The effect of size on the quantitative estimation of defect depth in steel structures using lock-in thermography', *Journal of applied physics*, vol. 101, no. 10, p. 104907.

Walton, S. R., *Patent: Method and System for two-dimensional and three-dimensional inspection of a workpiece* (2006a), US US 9,052,294 B2.

Walton, S. R., *Patent: Apparatus and methods for two-dimensional and three-dimensional inspection of workpiece* (2006b), US US 7.495,758 B2.

Walton, S. R., *Patent: System and method for identifying a feature of a workpiece* (2007), US US 8,050,486 B2.

Wandelt, M. (2008), *JetCheck: Systemlösung für Inspektionen an Luftfahrzeugen mit aktiver Thermografie.* https://www.ndt.net/article/v13n06/wandelt.pdf [26.06.2018].

Wang, J.; Shi, F.; Zhang, J. & Liu, Y. (2008), 'A new calibration model of camera lens distortion', *Pattern Recognition*, vol. 41, no. 2, pp. 607–615.

Weckenmann, A. & Gawande, B. (2012), *Koordinatenmesstechnik. Flexible Meßstrategien für Maß, Form und Lage,* Carl Hanser Fachbuchverlag, München, Wien. ISBN: 978 3 446 40739 8.

Weckenmann, A.; Jiang, X.; Sommer, K.-D.; Neuschaefer-Rube, U.; Seewig, J.; Shaw, L. & Estler, T. (2009), 'Multisensor data fusion in dimensional metrology', *CIRP Annals - Manufacturing Technology*, vol. 58, no. 2, pp. 701–721.

Weckenmann, A. & Knauer, M. (1999), 'Causes and consequences of measurement uncertainty in production metrology', *e & i Elektrotechnik und Informationstechnik*, vol. 116, no. 4, pp. 234–239.

Weckenmann, A. & Lorz, J. (2001), 'Bedeutung der Messunsicherheit in der Fertigungs-messtechnik (Importance of Measurement Uncertainty in Manufacturing Metrology)', *tm – Technisches Messen*, vol. 68, 1/2001, p. 326.

Wedekind, M. (2014), *Charakterisierung von Steifigkeit und Festigkeit heterogen ver-stärkter Verbundstrangpressprofile*. Dissertation, Technische Universität München, München.

Wendt, K.; Keck, C. & Schwenke, H. (2007), 'Prüfprozesseignung von Inline-Messtech-nik im Karosseriebau', *PTB-Mitteilungen* 2007, pp. 417–424.

Wiora, G. (2001), *Optische 3D-Messtechnik. Präzise Gestaltvermessung mit einem er-weiterten Streifenprojektionsverfahren*. Dissertation, Ruprechts-Karls-Universität Hei-delberg, Heidelberg.

Witten, E.; Sauer, M. & Kühnel, M. (2017), 'Composites-Marktbericht 2017. Marktent-wicklungen, Trends, Ausblicke und Herausforderungen'. https://www.avk-tv.de/fi-les/20171026_avkccev__marktbericht_2017.pdf [20.06.2018].

Wulfsberg, J.; Herrmann, A.; Ziegmann, G.; Lonsdorfer, G.; Stöß, N. & Fette, M. (2014), 'Combination of carbon fibre sheet moulding compound and prepreg compression moulding in aerospace industry', *Procedia Engineering*, vol. 81, pp. 1601–1607.

Zaiß, M.; Demmerle, J.; Oergele, J.-N. & Lanza, G. (2017a), 'New Concepts for Quality Assurance of Lightweight Material', *Procedia CIRP*, vol. 66, pp. 259–264.

Zaiß, M.; Jank, M.-H.; Netzelmann, U.; Waschkies, T.; Rabe, U.; Herrmann, H.-G.; Thompson, M. & Lanza, G. (2017b), 'Use of Thermography and Ultrasound for the Qual-ity Control of SMC Lightweight Material Reinforced by Carbon Fiber Tapes', *Procedia CIRP*, vol. 62, pp. 33–38.

Zöcke, C.; Langmeier, A.; Stössel, R. & Arnold, W. (2007), 'Quantitative Auswertung von Fehlstellen an Bauteilen aus Faserverbundwerkstoff mit Lock-In Thermographie', *Thermografie-Kolloquium 2007 by DGZfP*, Stuttgart, Germany.

Zöcke, C. M. (2010), *Quantitative analysis of defects in composite material by means of optical lockin thermography*. Dissertation, Shaker, Saarbrücken. ISBN: 3832293019.

List of Figures

List of Tables

Appendix

A 1 Reinforcement Fiber

The reinforcement fiber represents the load-bearing component in FRP. It strongly influences the mechanical properties due to a higher tensile strength, higher modulus of elasticity and lower elongation than the matrix material (Cherif 2011). Further properties of the reinforcing fibers are impact strength, heat resistance and creep behavior (Henning & Moeller 2011). The fibers can be divided into short fibers (l ≈ 0.1-1 mm), long fibers (l ≈ 1-50 mm) and continuous fibers (l > 50 mm) (Schürmann 2007). The critical fiber length is the fiber length at which the surface forces on the fiber transmit sufficiently high forces to cause the fiber to break (Wedekind 2014).

The fibers used can be divided into natural fibers and chemical fibers. The natural fibers are subdivided into vegetable, animal and mineral fibers and are primarily used for components with low mechanical requirements (Neitzel, Mitschang & Breuer 2014; Cherif 2011). Chemical fibers, on the other hand, are based on organic or inorganic materials and are used under high loads. These include glass, carbon and aramid fibers (Neitzel, Mitschang & Breuer 2014). The mechanical properties of these fibers and their production process are described hereafter.

A 1.1 Glass fibers

Glass fiber has a favorable price/performance ratio and other advantages, such as low moisture absorption or thermal and electrical insulation. However, the glass fiber has a too low modulus of elasticity for applications in structural components and therefore is often only used for simple components (Neitzel, Mitschang & Breuer 2014; Schürmann 2007). The strength can however, be attributed to the covalent bonds between silicon and oxygen. These atoms form a three-dimensional network with amorphous structure, whereby the largely isotropic property of glass fibers can be justified (Ehrenstein 2006; Michaeli & Begemann 1990).

The most common production process for glass fibers is the nozzle pulling process, belonging to the direct spinning processes (Cherif 2011). The raw materials used are quartz sand, chalkstone, kaolin, dolomite, boric acid and fluorspar (Ehrenstein 2006). The filaments have a diameter of 3.5 – 24 µm. The properties of glass fibers can be varied depending on the composition of the raw materials. The most common type of fiber is E-glass fiber (E=Electric), which has a low sensitivity to moisture and is therefore

increasingly used in the electrical industry (Henning & Moeller 2011). In addition, there is M-glass (M=module), characterized by an increased modulus of elasticity and therefore high price, C-glass (C=chemical) with improved chemical properties and S-glass (S=strength) with a higher breaking strength than E-glass and particularly resistance to temperature and humidity (Neitzel, Mitschang & Breuer 2014).

A 1.2 Carbon Fibers

Carbon fibers, in approx. 90 % of global output, are produced by pyrolysis and graphitization of polyacrylonitrile (PAN). The remaining 10 % are produced from mesophase pitch. Carbon fibers are brittle and therefore represent a process engineering problem in economical processing at high process speeds. (Neitzel, Mitschang & Breuer 2014)

A differentiation is made between four types of carbon fibers: HT fibers (high tenacity) regarded as high-strength standard fibers, ST fibers (super tenacity) with even higher strength than HT fibers, IM fibers (intermediate modulus) with a higher modulus than HT fibers and HM fibers (high modulus), which are regarded as highly rigid fibers. (Henning & Moeller 2011)

The diameter of the individual filaments is around 5 – 10 µm. The individual rovings differ in number of combined filaments: Commercial units are available in 1 k, 3 k, 6 k, 12 k and 24 k (k = 1000 filaments) rovings. (Schürmann 2007)

The graphite in carbon fibers is built up in layers with strong bonds between the individual graphite crystals. These can be the reason for the high strength and the high modulus of elasticity. Due to the alignment of graphite structure, carbon fibers exhibit a strong anisotropic behavior. Furthermore, the coefficient of thermal expansion in the grain direction is negative and transversely positive. This can be regarded as an advantage if thermal expansion has to be avoided and can be specifically adjusted. The low density of 1.8 g/cm^3, the excellent mechanical properties, the resistance to most acids and alkalis as well as the permeability of X-rays are further advantages. Disadvantages are the brittle fracture behavior, the low compressive strength and the very high fiber price. (Schürmann 2007; Neitzel, Mitschang & Breuer 2014)

A 1.3 Aramid Fiber

Aramid fibers (trade names Kevlar, Twaron, Technora) are plastic fibers made from aromatic polyamides. The polymer is dissolved in sulfuric acid, spun and then stretched

at elevated temperature to a thread of 12 μm diameter. (Neitzel, Mitschang & Breuer 2014; Schürmann 2007)

As aramid fibers are not used in this work, they are not further described but mentioned only for completeness.

A 2 Polymer Matrix

The other essential component of FRP is the polymeric matrix in which the fibers are impregnated. Depending on the processing method, the matrix content is 40-85 vol.-% (Neitzel, Mitschang & Breuer 2014). The matrix transfers the forces to the fibers as well as from fiber to fiber and supports them under pressure load. Furthermore, it offers protection against environmental influences and fixes the fibers in the desired geometric arrangement. Thus the matrix is also responsible for the component design. (Michaeli & Begemann 1990; Ehrenstein 2006)

A basic distinction is made between thermoset and thermoplastic matrices in polymer matrix systems. The thermoplastic matrix used is mainly polypropylene, but also polyamide. Unsaturated polyester resins, vinyl ester resins and polyurethanes are used as thermosets, also called duromer, in their matrix form (Henning & Moeller 2011; Neitzel, Mitschang & Breuer 2014). Both thermoset and thermoplastic matrix systems have to reach a low viscosity state during processing ensuring complete fiber impregnation (Neitzel, Mitschang & Breuer 2014).

Duromer polymers have a low molecular weight in their initial state and are often liquid at room temperature. This supports the complete impregnation of the reinforcing fibers. However, there are also polymers, such as unsaturated polyesters, which are highly viscous to solid in their basic form and become liquid by the addition of solvents. Monostyrene, also a reactive copolymer, is usually used for this purpose and additionally influences the material properties. Through the addition of hardener and accelerator, as well as through energy feeding, the components are hardened and available as three-dimensional interlinked components. By influencing the degree of interlinking it is possible to adjust brittleness and heat resistance. A higher degree of interlinking means more brittle and lower elongation at break. Therefore, a compromise between heat resistance and ductility is targeted. (Ehrenstein 2006; Michaeli & Begemann 1990; Schürmann 2007)

In order to avoid the compromise between brittleness and heat resistance, thermoplastic matrices are used, which can be available in an amorphous or semi-crystalline state. They are characterized by high impact strength, high elongation at break, media resistance, low moisture absorption, short processing cycles, but also recyclability and unlimited storage time at room temperature (Michaeli & Begemann 1990; Neitzel, Mitschang & Breuer 2014). However, the tendency to creep at higher temperatures is disadvantageous, as thermoplastics are composed of linear or branched macromolecules which are not interlinked spatially (Schürmann 2007). Furthermore, the higher viscosity compared to duromers leads to a more difficult impregnation of the fibers although, the impregnation takes place in the molten phase. (Michaeli & Begemann 1990; Ehrenstein 2006)

In this thesis, thermoplastics are not the subject of further consideration, but the duromer Sheet Molding Compound (SMC), which is explained in more detail below.

A 3 Defects in FRP

A 3.1 Pores

Air inclusions or pores are the result of a faulty manufacturing process, for example when the individual components are mixed together. They can occur in a plane or spatially distributed in the matrix. Usually they are in a spherical form. However, there is also the possibility that pores are elongated distorted and run parallel in the direction of the fibers. These pores are responsible for the development of delamination. (Müllerferli 1993; Ilschner & Singer 2010; Potter 1997)

Pore formation is influenced by various factors during production. These include, for example, process parameters, surface tension, degree of wetting and matrix viscosity (Bledzki, Kurek & Gassan 1995).

A 3.2 Delamination

Delamination is a defect that can be attributed to separation. This results in the separation of two adjacent layers within the laminate. This defect is not always visible from the outside, but sometimes it appears through a milky turbidity. Delaminations reduce the strength under pressure load and, due to growing, can lead to total component fail-

ure. Defective formulations, impact loads by ejecting the component or insufficient contact pressure can cause. (Krüger & Mook 2006; Muntzinger 2013; Schürmann 2007; Harich 2008)

A 3.3 Foreign Body

During the production process it is possible that foreign objects (e.g. fibers, foil) may get onto the semi-finished product and be pressed (Mersmann 2012; Miene 2009; Miene 2010). These inclusions of non-natural materials (Müllerferli 1993) disturb the force flow inside the material. Cracks can occur due to sharp-edged inclusions, which can develop into an intermediate fiber breakage. During dynamic loading, such a foreign body can lead to delamination or incomplete adhesion. (Flemming, Ziegmann & Roth 1999; Schürmann 2007)

A 3.4 Fold

Folds are considered to be serious defects in SMC, which cause an accumulation of resin and locally flush out fibers and thus reduce the mechanical properties. Processing of textile products shows that folds lead to shearing of semi-finished products.

Folds are defined as a short vertical projection that can run across the entire width (DIN 65673). However, folds also lead to local deviations of fiber orientation or air inclusions, resulting in local weakening, possibly causing cracks and delaminations due to notch effects (Kaiser & Karbhari 2001).

A 3.5 Incorrect Fiber Orientation

The fiber orientation is decisive for the mechanical properties and can lead to a significant reduction of the characteristic values in case of an incorrect orientation (Ehrenstein 2006; Neitzel, Mitschang & Breuer 2014).

Global as well as local deviations of the fiber orientation are possible (Matthews 1999). Global deviations are caused by incorrect placement of the semi-finished product. Local deviations are mainly known from semi-finished fiber products, where these deviations may occur due to drape-related distortion. The exemplary resulting gaps are a space in the fiber material. (Miene 2010)

A 4 Quality Assurance Methods

A 4.1 Radiographic Procedures

Radiographic procedures are based on the interaction of a test objects material with the X-rays. In non-destructive material testing, various methods can be used, such as X-ray transmission, X-ray computed tomography or X-ray refraction. (Kochan 2012)

In *transmission radiographic testing*, the X-ray radiation is weakened and absorbed by interacting with the test object. In this inspection, the local intensity is evaluated. This attenuation or absorption of radiation describes the exponential attenuation law according to Lambert-Beer:

$$I(x_t) = I_0 e^{-\mu_{CT} x_t}$$

Equation A-1

The measured intensity results from weakening the original intensity I_0 by a volume element of thickness x_t and a material-specific attenuation coefficient μ_{CT}. (Kochan 2012; Fürtjes 2016)

The result of transmission radiographic testing is a projection image of the tested objects volume onto a projection plane. The material-specific radiation attenuation leads to a radiation intensity distribution, whereby inhomogeneities in the form of thickness differences and density changes are detected. The result can be displayed in real time whereby image processing systems increase error detection and enable automatic error detection. (Kochan 2012; Grellmann, Seidler & Altstädt 2013)

X-ray computed tomography is another imaging method. The method provides three-dimensional information about the test object and its internal structures. (Kalender 2006; Christoph & Neumann 2011)

It is a combination of transmission radiographic testing and the subsequent application of a mathematical reconstruction. The radiographic images, also called projections, are taken at different angular positions. This leads to different paths through the test object and thus different radiation attenuation occurring on the detector. Due to the mathematical reconstruction, a 3D model can be created and evaluated by measurement technology. (Kochan 2012; Kalender 2006; Kruth et al. 2011)

Due to many projections followed by reconstruction, X-ray computed tomography is a time-consuming process and therefore not suitable for time-critical uses (Fürtjes 2016).

X-ray refractometry is another method, based on beam deflection at microscopically small interfaces. These interfaces have different electron densities. These can be pores, cracks, delaminations or particles. (Kochan 2012; Fritz & Eisenbach 2003)

In FRP, a fiber acts like a cylindrical lens. Thus the beam is deflected perpendicularly to the fiber and the fiber orientation, averaged over the layer thickness, can be determined (Grellmann, Seidler & Altstädt 2013).

In case of larger test objects, the surface has to be scanned in a grid pattern. The refracted intensities are recorded and the respective counting rate is converted into a location depending grey value depicted in an X-ray refraction topogram. The long measurement time required by this method is a major disadvantage. (Kochan 2012)

A 4.2 Acoustic Procedures

In acoustic NDT the resolution of the reverberation time has to be examined. This method is probably used for 8,500 years, starting with the quality check of fired ceramics. (Richter 1999)

A simple acoustic test method in audible range is the *sound test*, in which a component is mechanically excited and subsequently the derivation of acoustic noises allows conclusions about the component quality based on empirical values (Kochan 2012).

The *acoustic resonance analysis* is based on the fact that components have characteristic eigenmodes and eigenfrequencies after excitation (RTE Akustik + Prüftechnik GmbH 2018; Hertlin & Herkel 2003). These depend, for example, on stiffness, density and hardness of the material as well as structure type and geometry. Excitation can be continuous, pulsed, non-contact or contacting (Kochan 2012). Acoustic resonance analysis assesses the dynamic strength of a component, as defects or cracks cause a change in the resonance spectrum. This method is one of the volume-oriented test methods, since the workpiece as a whole is evaluated. It is a comparative test only allowing qualitative statements, but not providing information about defect size or location. During the test, the resonance aspects of series parts are compared with that one of good parts. Applications for this process include manufacture of cast components in sintered and roof tile industry, but also inspection of glass and steel products. (Kochan 2012; RTE Akustik + Prüftechnik GmbH 2018; Hertlin & Herkel 2003; Rieth-Hoerst 2007)

The most widely used NDT method is *ultrasonic testing*, which is characterized by acoustic waves in the frequency range from 20 kHz to 1 GHz (Erhard 2014). Most ultrasonic methods are based on a transit time measurement of elastic waves, coupled into the material and reflected or weakened at interfaces. Basically, a distinction is made between two arrangements. In the transmission method, transmitter and receiver are separated. In the reflection method, the ultrasonic transducer is both transmitter and receiver. (Kochan 2012)

Reflection techniques include the pulse-echo method, using a short signal pulse emitted from the probe, which is a single oscillator or phased-array probe. The resulting echoes from the boundary surfaces are received. In case of defects, which are considered further boundary surfaces, additional echoes are generated between inlet and back wall echoes. The propagation time of the echo and the known speed of sound can be used to determine the error depth.

Ultrasonic frequency analysis as well as transit time and intensity methods are distinguished in transmission methods. In the intensity method, the test specimen is located between transmitter and receiver, placed directly opposite to each other. This design requires the test object to be available from two sides. The intensity of the coupled sound signal is evaluated over the sample thickness and defects or inhomogeneities weaken the sound value in comparison to a flawless material. For an exact inspection, the adjustment of the opposite probes is crucial. A disadvantage is that the error depth cannot be determined and that a coupling medium, such as water or special gel, is required between probe and test object. With water coupling, the test is usually carried out in an immersion bath locating the entire test setup in a water basin. Therefore, this type of testing is very expensive and time-consuming. Furthermore, large test surfaces have to be scanned mechanically or manually, also taking an enormous amount of time. (Kochan 2012; Grellmann, Seidler & Altstädt 2013; Roos & Maile 2015) (Bargel & Schulze 2018; Deutsch 2000)

With the ultrasonic method it is possible to detect different defects. These include delamination, impact damage, inclusions, porosity or resin accumulations (Hillger & Wachter 1991)

The disadvantage of the necessary coupling agent can be avoided with the use of *air coupled ultrasound* (Ambrozinski et al. 2012). In this case a coupling angle has to be maintained (Döring 2011). Due to the high impedance difference between air and the

test object, an intensity loss of the sound signal occurs, which is why probes with a low frequency (<1 MHz) are required. Up to now, only the transmission technology could be implemented, resulting in the loss of depth information. Air-coupled ultrasound also offers the possibility of automating the inspection and examining complex geometries. (Hillger 2000; Hillger 2000; Grellmann, Seidler & Altstädt 2013)

Acoustic test methods show a great potential for the investigation of FRP. However, the examination can only be carried out on cured components (Fürtjes 2016)

A 4.3 Electrical Procedures

For the electrical processes, dielectric spectroscopy and the eddy current method are used. *Dielectric spectroscopy* is a characterization method investigating the dielectric material properties and their change over time. This process can be used with electrically non-conductive materials, such as glass fiber SMC, but is not suitable for electrically conductive materials such as carbon fiber reinforced plastics (CFRP) and the corresponding semi-finished material. (Kochan 2012)

In contrast, *eddy current testing* is performed exclusively on electrically conductive materials and is based on the effect of magnetic induction. In this method, the test object is either brought locally into the sphere of influence of an inductive sensor or it passes through a comprehensive test coil. (Dobmann 2005) A constant current generates a magnetic field interacting with the test object and, depending on the conductivity of the material, a modulated current flow, known as eddy current, is induced. The eddy current generates a modulated magnetic field interacting with the coil again. The voltage tapped at the coil is proportional to its impedance. The impedance can be influenced by several factors, whereby changing distance between test object and coil has the greatest influence. By keeping the distance constant, the impedance is determined by local properties of the test object. Thus it is possible to detect disturbances of the electrical conductivity by the contactless power consumption at the coil. (Dobmann 2005; Grellmann, Seidler & Altstädt 2013; Kochan 2012; DIN EN ISO 15549)

With this method it is possible to detect delaminations, fiber breaks, wrinkles, impact damages and missing fiber bundles, but also to determine and check fiber orientations in CFRP semi-finished products (Grellmann, Seidler & Altstädt 2013; Schulze et al. 2010; Mook, Lange & Koeser 2001).

In general, the eddy current process is a non-contact and point-shaped process. For the inspection of flat components, the probe is guided over the sample surface at a constant distance. (Kochan 2012; Fürtjes 2016)

A major advantage of the eddy current process in comparison to optical systems is the possibility to determine fiber orientation of CFRP semi-finished products in the inner layers and not only at the top layer. The method is also suitable for real-time measurement. However, the scanning speed is low and limited to a small measuring range, making it impossible to inspect large areas in a short time. (Fürtjes 2016)

A 4.4 Optical Procedures

Optical methods are a widely used method for quality assurance, therefore a selection of optical systems is presented below.

Visual inspection is one of the optical methods. The aim is to identify and evaluate surface characteristics of components. It is allowed to use tools such as a magnifying glass or microscope. (DIN EN 13018) distinguishes between direct and indirect visual inspection. The visual inspection allows a quick and easy execution for a wide range of applications. However, this type of inspection is time-consuming, error-prone and cost-intensive. (Kochan 2012; Fürtjes 2016)

In principle, optical methods work according to five methods (Pfeifer & Schmitt 2010):

- Running time: How long does a light beam take to be registered by a sensor after reflection at the component surface?
- Intensity: Distribution of light intensity on the detector
- Geometry of the sensor arrangement: Geometrically determination of a points location (e.g. triangulation)
- Phase: Measuring and reference light have a phase shift
- Polarization: Determination of polarization for shape determination

Another optical method is the *strip projection*, providing complete 3D information on free-form surfaces. Projected strips are placed on the test object, simultaneously or several light sections shortly after each other, and recorded with a camera from another direction. Greater height resolution can be achieved with narrower strips as the line patterns distortion depends on the test objects shape. This distorted line pattern is then captured by the camera, transformed into a high-density cloud of points and calculated

to geometrical information. Requires are knowledge of position and orientation of projector, camera and other imaging parameters. This process is particularly suitable for diffusely reflective materials but not for transparent and reflective surfaces. (Keferstein, Marxer & Bach 2018; Bauer 2008)

Stripe projection systems with two cameras are increasingly used today. The projector is only a light source and triangulation is performed by the cameras. Inaccuracies of the projection are not relevant here, since the measurement is carried out by the cameras. Other advantages are that shiny spots and shadows are more likely to be avoided, as there is a higher probability that one of the cameras will detect these areas. (Keferstein, Marxer & Bach 2018)

Today, this method is used in geometric quality inspection of three-dimensional workpieces. Quality statements about the geometry can be made directly by a target/actual comparison. (Bauer 2008) Stripe projection is also used for FRP, whereby the optical properties of CFRP and GFRP must be taken into account (Effenberger et al. 2013).

An optical method for distance measurement is *laser triangulation*, which is also performed without contact. It is based on the determination of a triangle side by determining two triangle angles and knowing the length of the distances enclosed by these angles. Triangulation can be divided into active and passive triangulation. Passive systems do not require a specific lighting unit. A specific point on the test objects surface is detected from at least two different perspectives. The active processes requires special lighting, usually a laser, which also represents the marking to be detected on the surface. (Bauer 2008; Wiora 2001)

In this process, a radiation source for parallel light beams of visible or infrared light is imaged onto the test object with the assistance of an optic. The structure is shown in Figure A-1. This light is reflected from the test objects surface. The diffuse light is then imaged onto a sensor at the triangulation angle by the receiver optics. This sensor consists of a position-sensitive photo element or Charge-Coupled Device/ Complementary Metal Oxide Semiconductor (CCD/COMS) lines to determine the position of the center of gravity of the imaged light spot. Depending on the distance of the workpiece, the position of the center of gravity shifts. The illustrated position makes it possible to obtain distance information. (Keferstein, Marxer & Bach 2018)
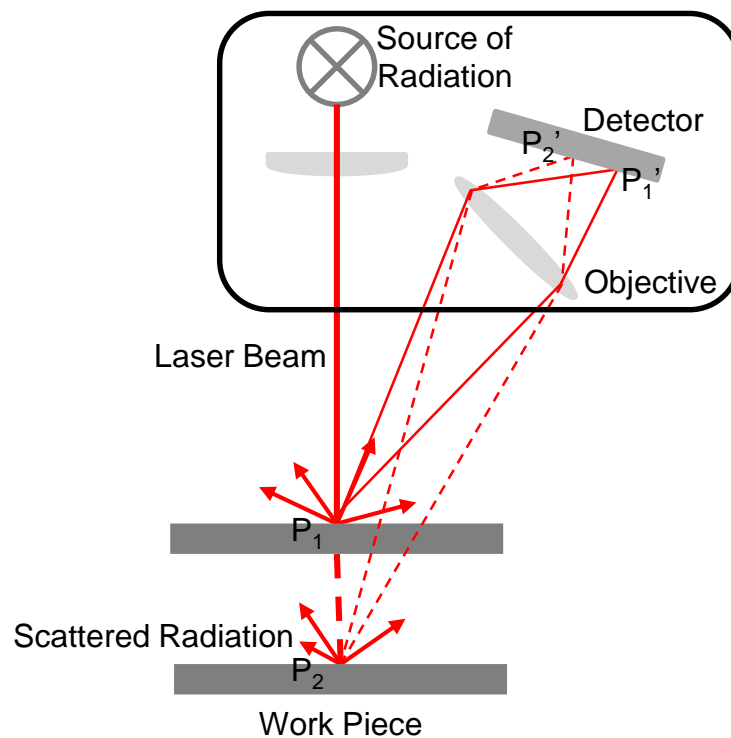
Figure A-1: Principle of laser triangulation according to (Keferstein, Marxer & Bach 2018; Donges & Noll 2015)

The investigation result can be influenced for example by surface roughness causing speckle effects. The test objects color can also be important as different penetration depths of different materials can cause a systematic deviation of the measurement result. (Keferstein, Marxer & Bach 2018)

The laser triangulation process is characterized by a high dynamic impossible with touching probes. Furthermore, no measuring force is applied to the test object. (Keferstein, Marxer & Bach 2018; Bauer 2008)

In laser triangulation, the measurement quality also significantly depends on the test objects material, since diffuse reflection is required. Transmission properties can play an important role, especially with plastics, since different penetration depths can lead to a systematic measurement error of the measurement result. In addition absorption and transmission properties have to be taken into account, because a contrast between material and laser beam is necessary for an exact differentiation and thus also the accuracy of the measuring system. (Keferstein, Marxer & Bach 2018)

The described method can be extended to the so-called *light section method*, in which the workpiece is scanned by a one-dimensional section (Beyerer, Puente León & Frese 2016) as shown in Figure A-2. A laser line passes over the test object. Furthermore,

the line sensor is replaced by an area sensor (CCD or CMOS camera). The camera records a line instead of a point. Triangulation can be performed for each point of the line if the angle of incidence is known and the distance of the surface point is therefore calculated. (Keferstein, Marxer & Bach 2018; Orth 2008)
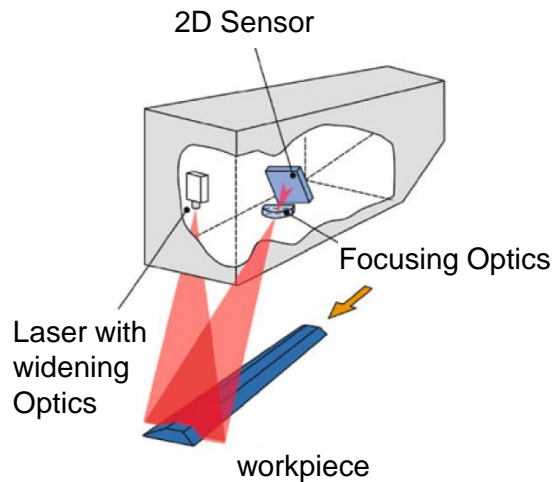
Figure A-2: Principle of the light section method according to (Keferstein, Marxer & Bach 2018)

In order to enable digitization at all, sensor arrangement consisting of laser and camera or test object have to be moved relatively, resulting in high demands on the motion axes with regard to positioning accuracy. All errors are directly included in the measurement result. (Berndt & Bauer 2003)

Laser and sensor can be arranged in four different versions. The variants are shown in Figure A-3 (AT - Automation Technology GmbH 2014).
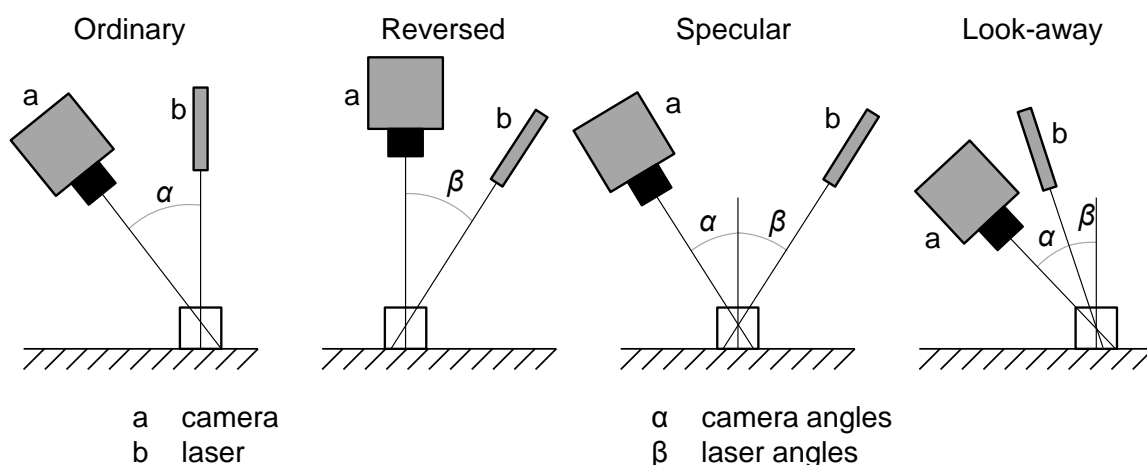
Figure A-3: Camera and laser arrangements according to (AT - Automation Technology GmbH 2014)

A disadvantage of the light section method is the occurrence of shadowing at sharp edges and corners (Bauer 2008). This happens when the laser axis and the optical axis of the camera do not intersect at the observation point. To counteract this disadvantage (Brabandt & Lanza 2015) has developed a process consisting of two laser triangulation systems in the look-away arrangement. The results of the two systems are combined to produce a complete image of the geometry. The schematic representation of the procedure is shown in Figure A-4.
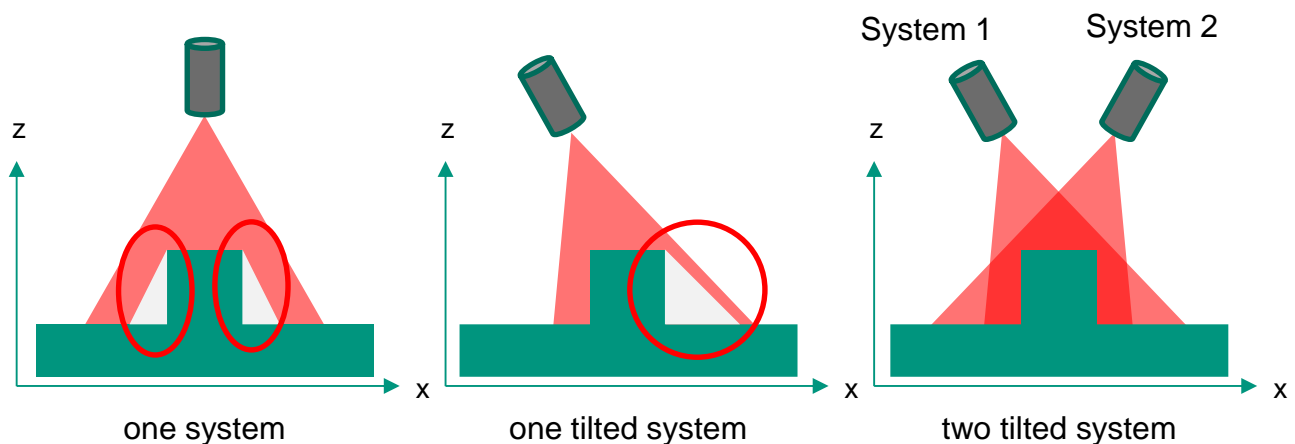
Figure A-4: Laser stripe sensors and shadowing effects (Brabandt & Lanza 2015)

A 4.5 Thermographic Procedures

Thermography is the measurement and visualization of surface temperatures. With the help of a thermal imaging camera, the test objects electromagnetic radiation frequency is recorded on basis of their intensity in the infrared spectrum. A distinction is made between *active* and *passive* thermography.

Passive thermography does not use an external heat source, but only the heat flow generated by the test object itself. *Active thermography* is characterized by using an artificial or natural energy source to produce a transient heat flow for testing purposes. (Vollmer, Mouml & Ilmann 2011) (DIN EN 16714-3)

The fields of application for thermography in production technology are wide. For example, this method is used to evaluate surfaces, joints, material integrity and fiber composites, but also for process monitoring, function control and surface inspection (Thiemann 2015). In contrast to other NDT methods, thermography has the advantage of inspecting large areas without contact within a short testing time (Fürtjes 2016).

Active thermography is used to detect defects and other irregularities (cracks, delamination and inclusions), to determine geometries and shapes parallel to the measuring surface, to determine the layer thickness and to compare thermal material properties. (DIN 54192) In CFRP components, defects such as delaminations, porosities and air inclusions can reliably be detected in areas close to the surface (Mayr & Hendorfer 2010).

The process of thermographic testing can be divided into four steps. The first step is signal generation with excitation of the test object taking place. The next step is heat propagation in the component. This is followed by signal acquisition, i.e. recording with an infrared camera. In the last step signal analysis and thus evaluation of the recordings is carried out (Siemer 2010). If there are no defects or inhomogeneities, the heat penetrates evenly into the test object (Thiemann 2015). Defective or other thermal structures show a locally higher or lower thermal conductivity and promote or hinder the dissipation of heat into the objects interior (Maldague & Moore 2001; Maldague 2001).

Thermal excitation can take place with different energy sources and be based on different effects. These include the absorption of optical radiation and/or microwaves, electromagnetic induction, the conversion of elastic waves (e.g. ultrasound) or convection (hot/cold air) (DIN 54192). Furthermore, the temporal modes of excitation are varied, for example by a pulse or periodic modulation (Thiemann 2015).

In active thermography with pulse excitation, an intensive energy source is used for short time, e.g. a flash of light from a flash lamp or laser. The necessary diffusion processes leads to an image contrast at the end of excitation. The recorded image sequence is evaluated in time or frequency domain. This process is called pulse-phase thermography (PPT). (DIN 54192; Sackewitz 2011)

In contrast to the short time in PPT, in step excitation the diffusion processes takes place during excitation, provided by a halogen spotlight for example. The analysis takes place as described above. (DIN 54192; Sackewitz 2011)

The periodic excitation uses an intensity modulated source. Amplitude-modulated halogen spotlights are suitable for this purpose. This so called lock-in thermography uses excitation in sinusoidal or rectangular form. For this process a sufficient observation period is necessary, including several modulation periods. The recorded image sequence is evaluated in frequency domain. (DIN 54192; Sackewitz 2011)

Other excitation modes are based on high power ultrasound, induction, laser or microwave (Kochan 2012). These forms are not relevant for this work and therefore not explained in detail.

Several factors have an influence on the raw data quality. Uneven heating, aberrations in optics, noise and local differences in emissivity are among these factors, limiting the potential sensitivity of thermography. (Maldague & Moore 2001; Maldague 2001)

As already described, the recorded image sequences can be analyzed in different ways, with methods available in time domain and frequency domain. The analysis in time domain is mainly used for pulsed excitation. Figure A-5 shows the temporal behavior of surface temperature T_{Sa} over an error-free reference range and surface temperature T_d over a defect area after pulse-shaped excitation.
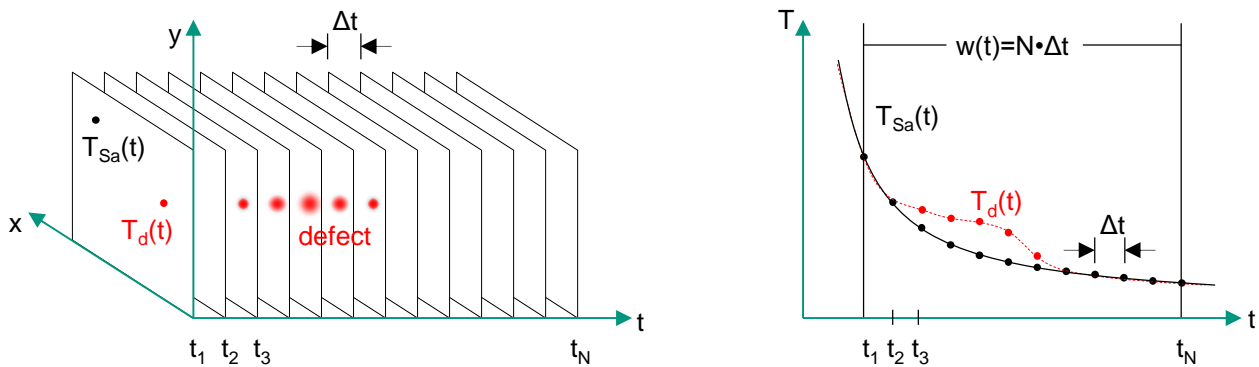
Figure A-5: Temperature evolution: (left) data 3D matrix, and (rigth) temperature profile for a defective (dotted line) and nondefective (Ibarra-Castanedo et al. 2007)

The error depth determines, when a measurable temperature difference appears after thermal excitation. The deeper the error, the later it can be detected. (Thiemann 2015)

The achievable defect contrast can be low, due to interference and noise effects, meaning that only errors at a low depth can be detected. An empirical rule states that the diameter of detectable errors has approximately to be equivalent to its depth, in order to be just detected (Maldague & Moore 2001).

For a flat test object and the use of a uniform periodic heat source with the angular frequency ω, a mathematical formulation with the temperature T being a function of depth z_d and time t can be used (Maldague 2001):

$$T(x,t) = T_0 e^{-\frac{z_d}{\mu}} cos\left(\frac{2\pi z_d}{\lambda} - \omega t\right) = T_0 e^{-\frac{z_d}{\mu}} cos\left(\omega t - \frac{2\pi z_d}{\lambda}\right) \qquad \text{Equation A-2}$$

The thermal diffusion length μ is described by the following equation:

$$\mu = \sqrt{\frac{2k_{th}}{\omega\rho C}} = \sqrt{\frac{2\,\vartheta}{\omega}} = \sqrt{\frac{\vartheta}{\pi \cdot f}}$$
Equation A-3

where k_{th} is the thermal conductivity, ρ the density, C the specific heat capacity, ϑ the thermal diffusivity and λ the thermal wavelength ($\lambda = 2\pi\mu$). (Favro & Han 1998)

Frequency domain analysis is used for both lock-in thermography and PPT. Since PPT is important for this thesis, only the evaluation in frequency domain with a pulse-shaped excitation is explained in more detail here.

Thermal waves of different frequencies are generated under the test objects surface by a thermal, rectangular excitation pulse. The recorded images are analyzed with the Fast Fourier Transform (FFT). (Maldague & Moore 2001)

The frequency components are determined according to the following equation:

$$F(n) = \sum_{m=0}^{N-1} T(m)e^{\frac{2n\pi im}{N}} = \text{Re}(n) + i\text{Im}(n)$$
Equation A-4

where Re is the real part of transform, Im the imaginary part of transform, n the frequency increment, N the number of measuring points, m the thermogram number in the sequence and i the imaginary number.

Therefrom amplitude and phase can be calculated:

$$A(f) = \sqrt{\text{Re}(n)^2 + \text{Im}(n)^2}$$
Equation A-5

$$\Phi(n) = \arctan\frac{Im(n)}{Re(n)}$$
Equation A-6

With N thermograms in the sequence, $N/2$ frequency values are available, which can be determined using the following equation:

$$f_n = \frac{n}{N\Delta t}; n = 1, \dots, N/2$$
Equation A-7

with Δt as time resolution and n for the frequency increment. (DIN 54192; Zöcke et al. 2007)

The procedure is shown in Figure A-6.
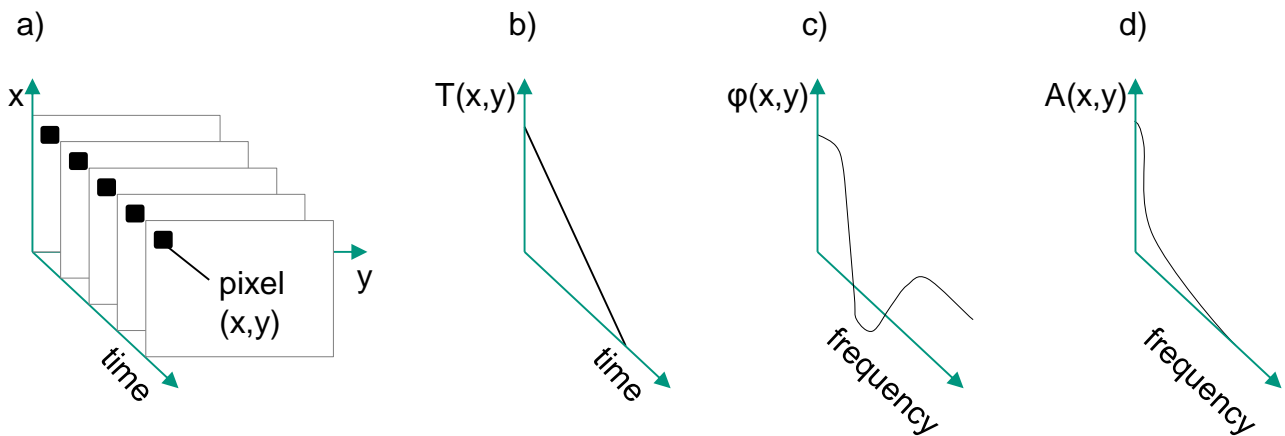
Figure A-6: Thermal image sequence (a); temperature profile of a pixel (x,y) in time domain (b); phase profile of the pixel (x,y) after FFT (c); amplitude profile of the pixel (x,y) after FFT (d) (Maldague & Moore 2001; Zöcke et al. 2007)

With this method, each pixel of the thermal image sequence is converted into the frequency domain and thus has a phase and amplitude component. The amplitude and phase images are characterized by the following properties:

- The amplitude represents the amount of temperature change at a certain frequency f_n
- The phase image shows the time delay of the heat wave, which is caused by irregularities, compared to the excitation at a certain frequency f_n

The phase value is generally independent of slight unevenness in the excitation of the test object. (DIN 54192))

A 5 Used Material
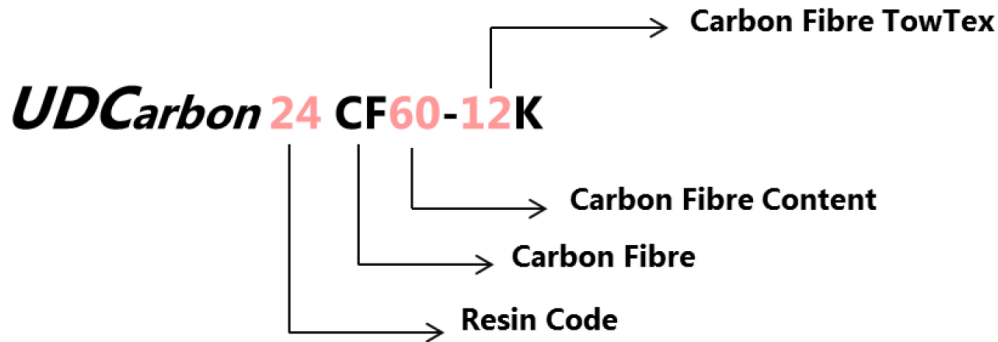
Packaging: roll
Material width: 500 mm
Shelf life at -18°C: 6 months
Shelf life at RT 23°C: 8 weeks

Fibre length: continuous
Fibre: 12K
Nominal fibre content $^w/_w$: 60 %
Areal weight: 800 g/m^2
Typical cure temperature: 125-140 °C
Typical moulding pressure: 80-120 bar
Typical cure time: 35 sec/mm

Figure A-7: Technical datasheet CF-SMC – UDCarbon 24 CF60-12K (Polynt Composites Germany GmbH 2016)

A 6 IRTG Demonstrator
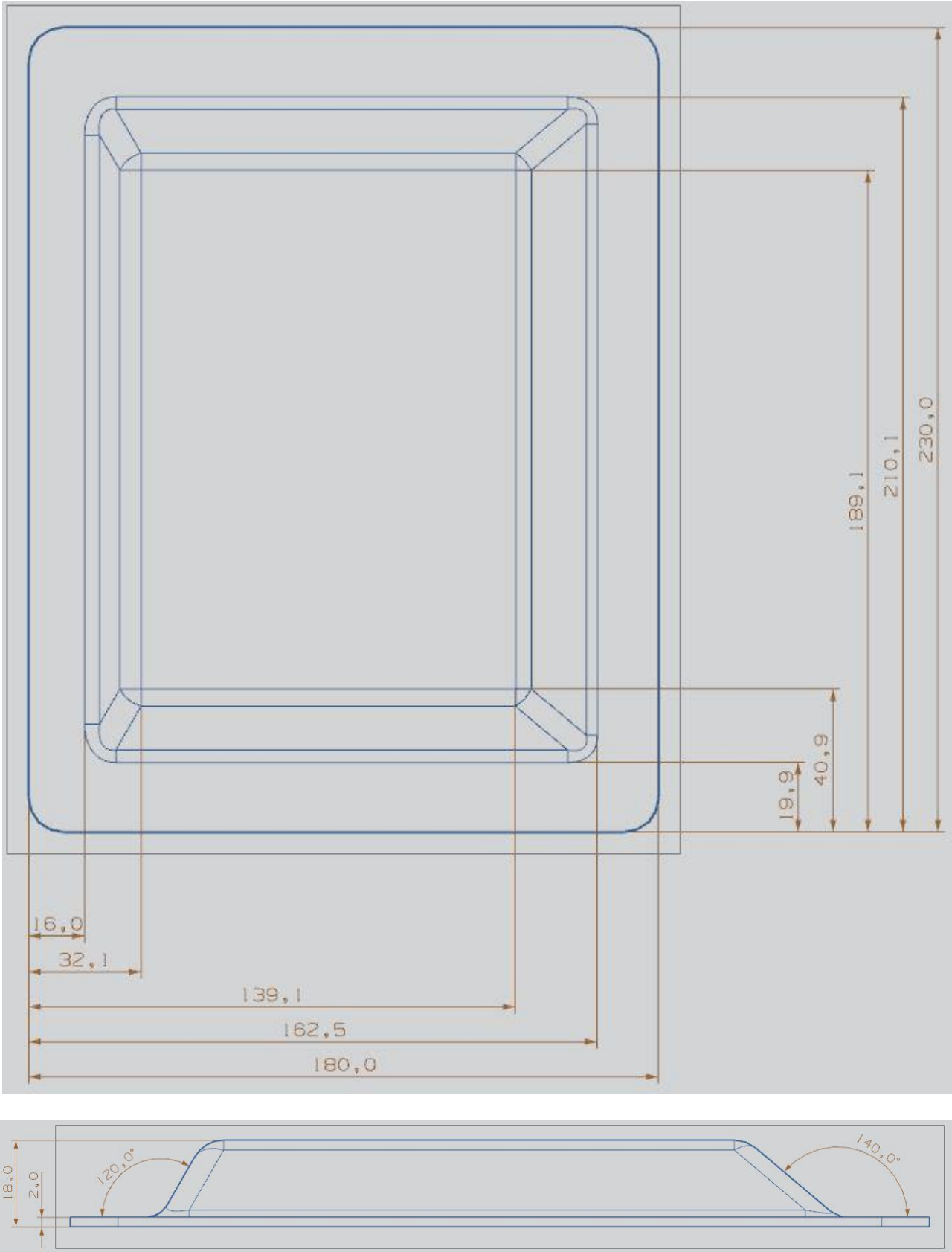
Figure A-8: Technical drawings of IRTG demonstrator

A 7 IRTG Demonstrator small
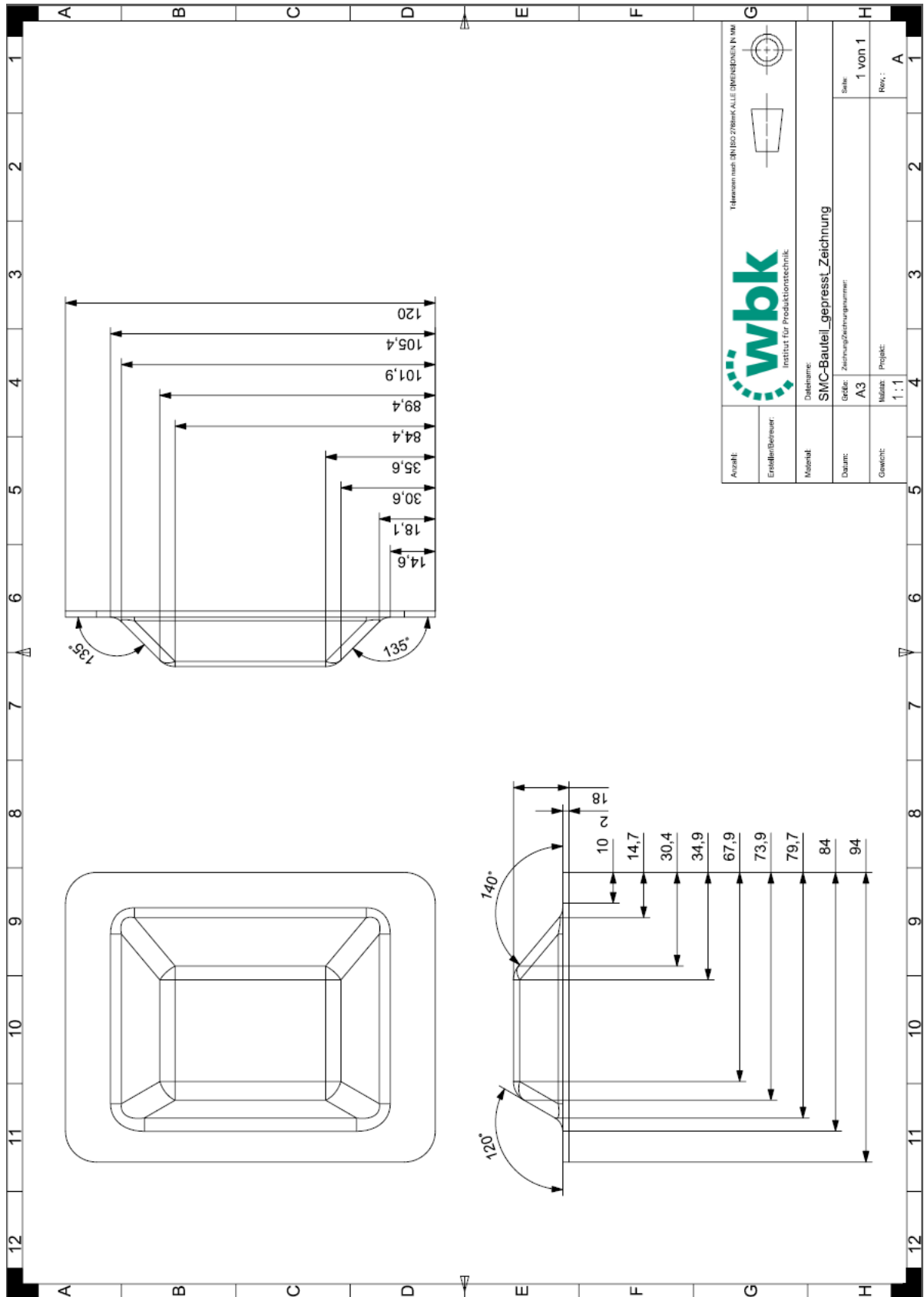
Figure A-9: Technical drawings of small IRTG demonstrator (A_Schwende 2017)

A 8 Components of the Laser Light Section System

In the following, all components of the LLSS are explained in more detail.

A 8.1 Portal with Tool Center Point

The portal with the TCP ensures the motion kinematics for the LLSS, but is separated from the operating principle of the LLSS. The TCP is movable in the three spatial directions (x, y and z) and turnable around the height axis (c). Furthermore, it is the interface for all attached measuring systems.

In x- and y-direction a travel length of 1,300 mm are possible plus 400 mm in z-direction, all at a travel speed of 400 mm/min. Due to cabling, the maximum rotation is ± 90 degrees. To ensure the highest possible positioning and repeating accuracy, the axes are equipped with high-precision glass scales. These ensure a positioning accuracy of ≤ 50 μm and a repeatability of ≤ 25 μm with a permissible payload of 40 kg (RAMPF 2014). The LLSS is attached to the TCP flange via an adapter plate. (A_Demmerle 2016; Brabandt 2018)

A 8.2 Laser Light Section System

The structure of the LLSS is depicted in Figure A-10 in detail. It consists of two sets, each with a laser and a camera, which can be placed at different angles to each other to avoid shading effects. Laser and camera are positioned in the "look-away" geometry, as illustrated in Figure A-3. Furthermore, different side panel angles can be set (0°, 5°, 10°, 15°). Various tilt angles of the LLSS can be realized with the side panel angles.
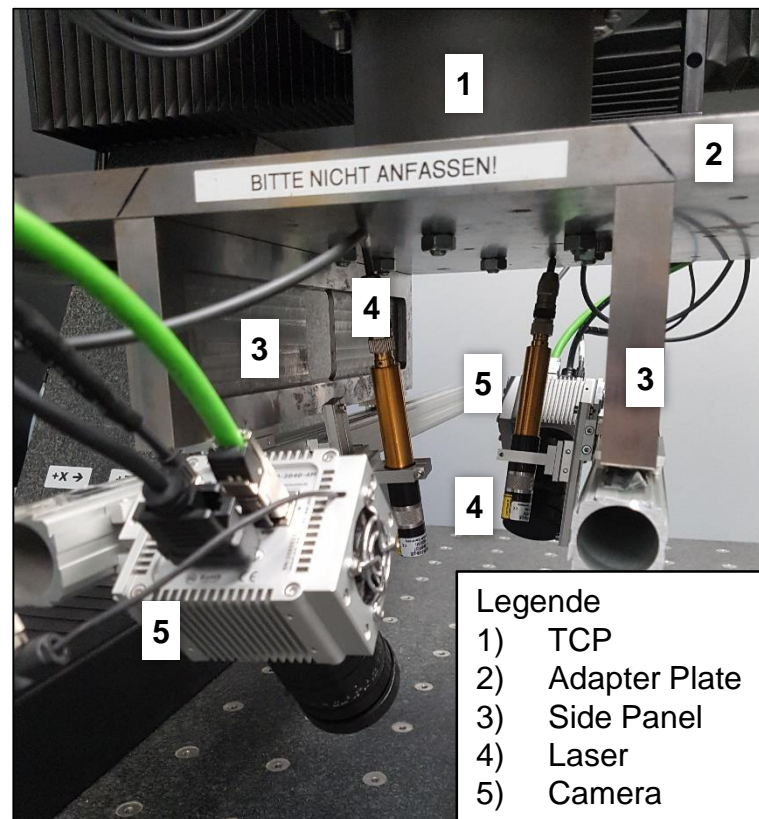
Figure A-10: Laser light section system in detail according to (A_Pohlmann 2017)

The lasers are of type "Z120M18H-660-lp30" from Z-Laser Optoelektronik GmbH, with a laser protection class 3B and a wavelength of 660 nm (Stemmer Imaging GmbH 2015c). The maximum power of the laser is 120 mW and the focus adjusted manually. The laser line has an opening angle of 30° and thus, at a working distance of approx. 25 mm, a laser line width of 130 mm. (Brabandt 2018)

The camera is the model C4-2040-4M-GigE from Automation Technology GmbH, able to convert the image of the projected laser line directly into a height profile. The resolution of the camera is 2048 x 2048 pixels with a 16 bit gray scale. The FUJINON HF25SA-1/1.4 from Fujifilm Europe GmbH is used as lens and it is additionally equipped with a bandpass filter of the wavelength 660 nm. (Brabandt 2018)

The two sets of the LLSS are positioned in a way that a common measuring range is covered, whereby the edge area is not taken into account. Thus an average lateral acquisition of the camera system of 100 mm can be assumed. With a lateral sensor resolution of 2048 pixels, a calculated resolution of 49 µm is achieved. (Brabandt 2018)

The limited depth of field of the LLSS requires that the system is always in the focus area. This is achieved by continuous equidistant height tracking in z-direction of the LLSS depending on test object geometry. (Brabandt & Lanza 2015)

Data transfer happens via one GigE interface per camera. A laser control output is used for coupling to the respective laser, as well as for transmitting the recording settings and triggering. (A_Demmerle 2016)

A 8.3 Beckhoff Operating Panel

The Beckhoff operating panel is the user interface for controlling the portal. The Beckhoff TwinCAT 3 CNC control with machine tool module is used for this purpose, enabling manual and automatic operation using a numerical control (NC) program. Furthermore, the zero offset and trigger intervals necessary for a measurement are set. In addition, the operating panel is connected to the evaluation computer, transmitting position information at any time. Thus, individual frames can be assigned to the respective positions. (A_Demmerle 2016)

A 8.4 Evaluation Computer

The evaluation computer is used for camera and laser settings and to start a scan. Furthermore, the image information for the creation of a three-dimensional cloud of points (CoP) is processed on this computer. Different programs are necessary for this. A detailed process flow is depicted in Figure A-11 in Appendix A 9. A detailed procedure of data acquisition and data evaluation is described in (Brabandt 2018).

A 8.5 Switch Cabinet

The switch cabinet is used to supply the individual components with energy. The Industrial PC for the Beckhoff control system is also located in the switch cabinet.

A 9 LLSS Data Processing
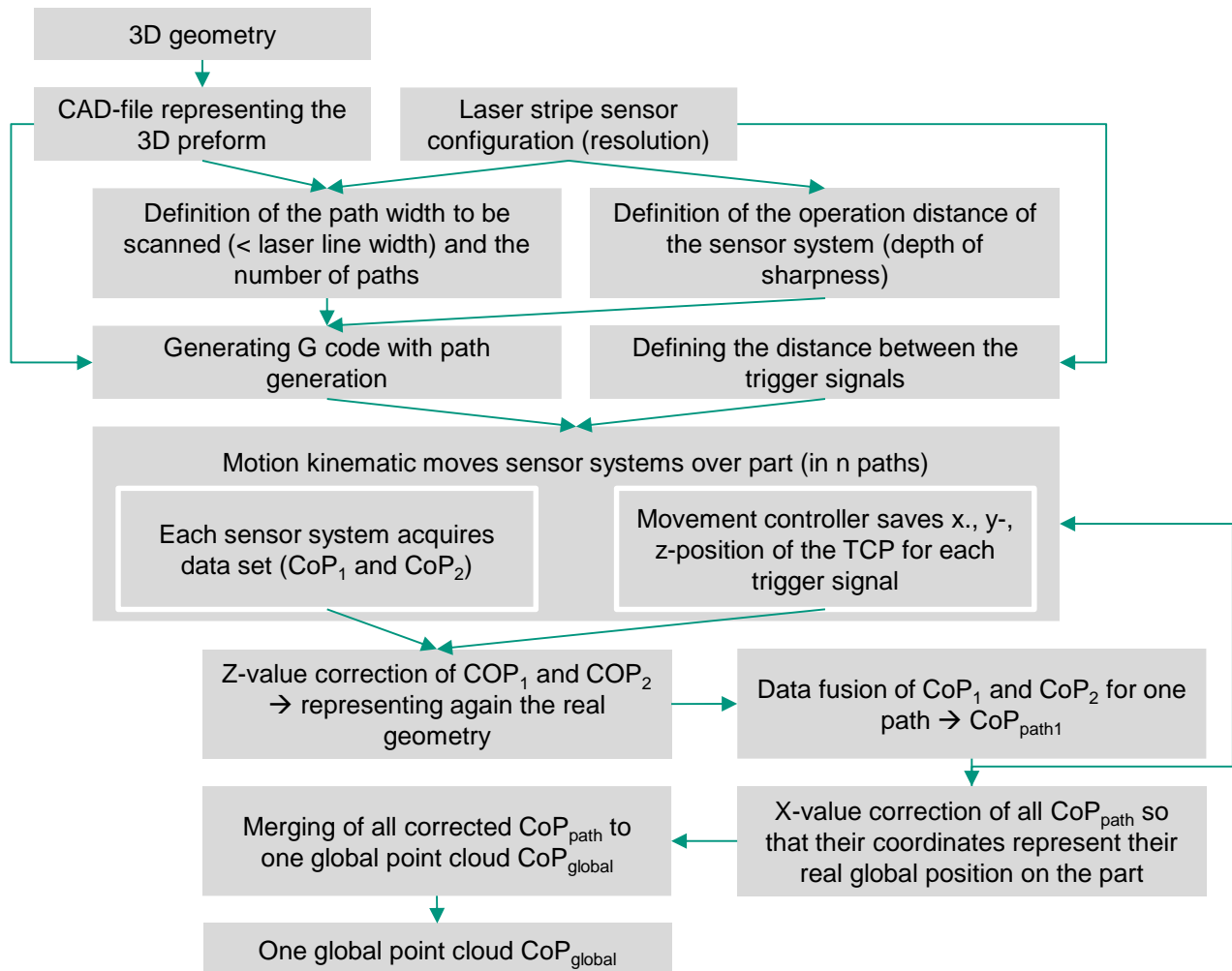
Figure A-11: Overview of the LLSS data processing according to (Brabandt & Lanza 2015)

A 10 Test Plan for Parameter Analysis of LLSS

All tests carried out are highlighted in grey. Initial tests were carried out, followed by additional measurements. The best parameter combination is marked in green. (A_Pohlmann 2017)

Table A-1: Test Plan of semi-finished test object according to (A_Pohlmann 2017)

Parameters		First tests		Additional tests	
Threshold		600	800	600	
Exposure time [µs]		900		600	1200
laser intensity [V]	2.5	sf1	sf2		
	3.5	sf3	sf4	sf5	sf6

Table A-2: Test Plan of cured test object according to (A_Pohlmann 2017)

Parameters		First tests				Additional tests	
Threshold		600		800		600	800
Exposure time [µs]		300	600	300	600	900	
Laser intensity [V]	2.5	cu1	cu2	cu5	cu6		
	3.5	cu3	cu4	cu7	cu8	cu9	cu10

A 11 Results of the Experiments to determine the LLSS Variable Parameters for Semi-Finished Test Object
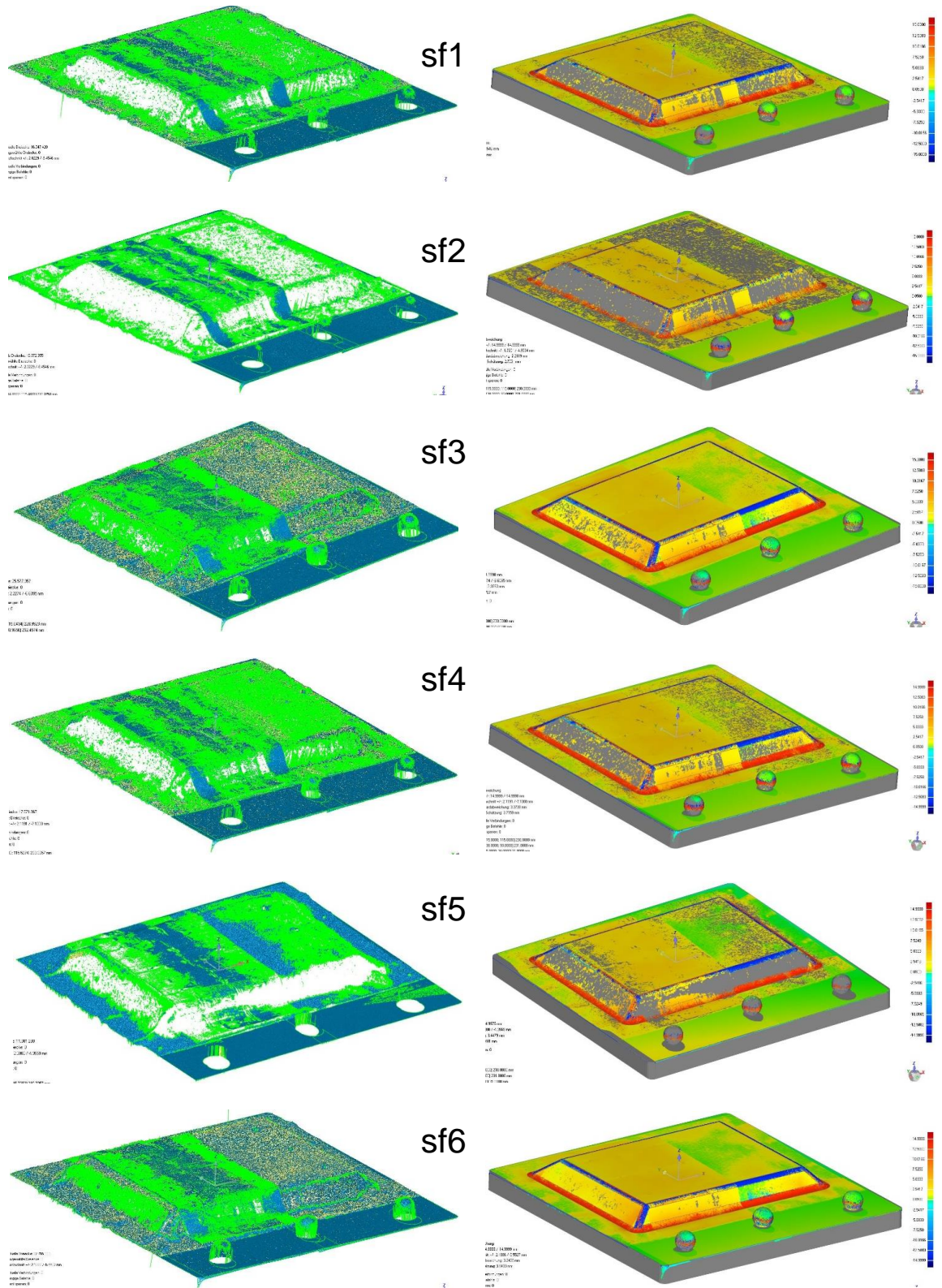
Figure A-12: CoP (left) and CAD comparison (right) for the semi-finished test object (A_Pohlmann 2017)

A 12 Results of the Experiments to determine the LLSS Variable Parameters for Cured Test Object

cu1

cu2

cu3

cu4

cu5
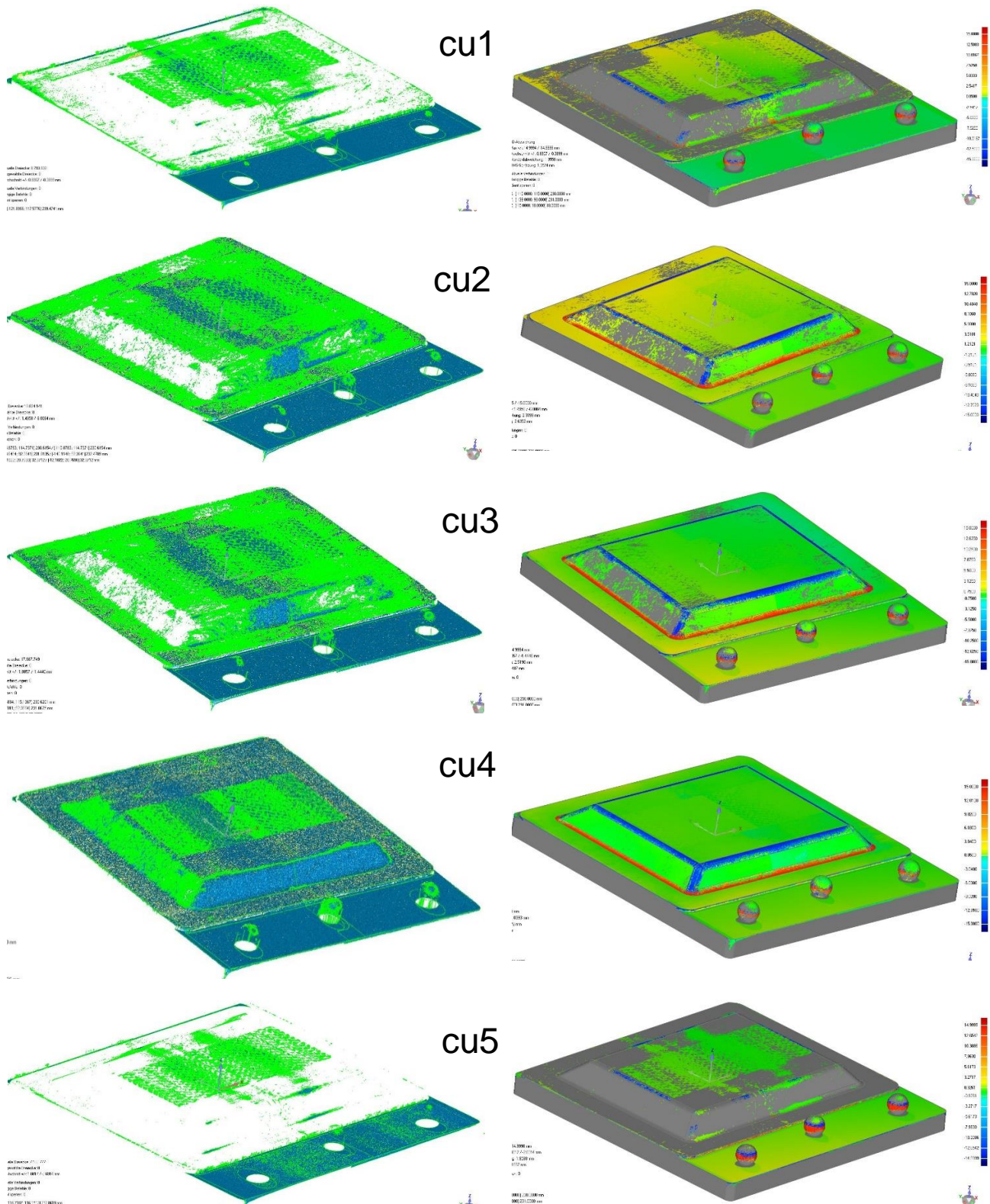
Figure A-13: CoP (left) and CAD comparison (right) for the cured test object part 1 (A_Pohlmann 2017)

cu6

cu7

cu8

cu9

cu10
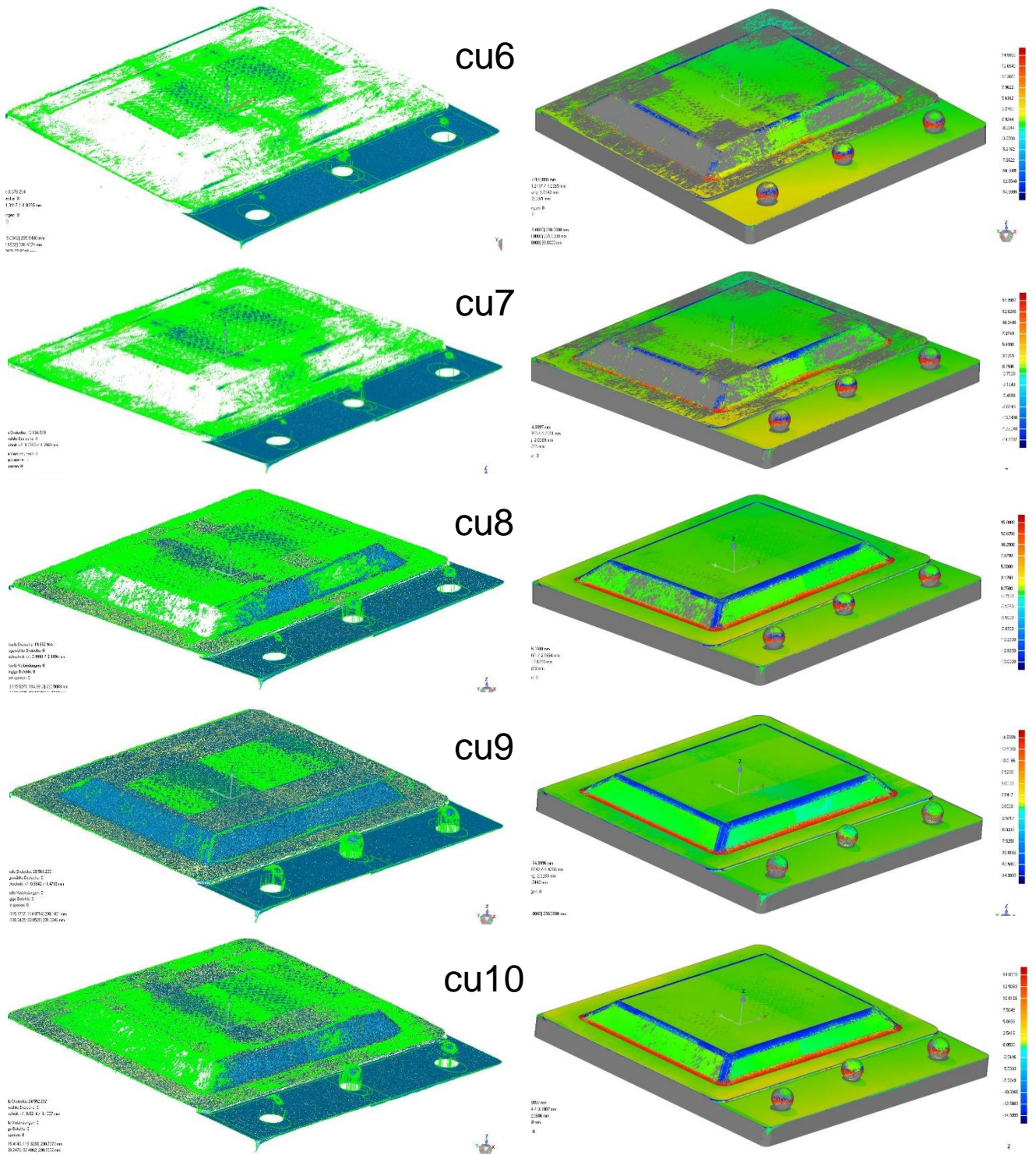
Figure A-14: CoP (left) and CAD comparison (right) for the cured test object part 2 (A_Pohlmann 2017)

A 13 Setting Parameters of the CT Measurement for LLSS Measurement Uncertainty

Table A-3: Setting Parameters of the CT measurement for measurement uncertainty of LLSS

Setting parameters	Semi-finished test object	Cured test object
Tube voltage [kV]	85	116
Tube current [µA]	300	200
Integration time [ms]	1000	1000
Gain	2.5	2.5
Image averaging	off	off
Binning	1x1	1x1
Voxel size [µm]	40	40
Focal spot [µm]	83	84
Magnification factor	1.54	1.52
Number of projections	1550	1550
Prefilter	1 mm Aluminum	1 mm A
Image filter	Sheep Logan Filter	Sheep Logan Filter

A 14 Measurement with tactile CMM on the Cured Test Object

Table A-4: Measurement with tactile CMM on the cured test object

Trail	Distance between planes [mm]	Angle 120° [°]	Angle 140° [°]
1	15.8771	118.8694	139.4042
2	15.8773	118.8692	139.4033
3	15.8775	118.8692	139.4033
4	15.8774	118.8694	139.4033
5	15.8776	118.8692	139.4028
6	15.8776	118.8689	139.4031
7	15.8775	118.8694	139.4033
8	15.8776	118.8692	139.4033
9	15.8777	118.8694	139.4031
10	15.8777	118.8694	139.4031
11	15.8775	118.8692	139.4031
12	15.8775	118.8692	139.4031
13	15.8777	118.8694	139.4028
14	15.8777	118.8692	139.4031
15	15.8776	118.8694	139.4031
16	15.8776	118.8694	139.4033
17	15.8777	118.8697	139.4031
18	15.8776	118.8694	139.4033
19	15.8776	118.8694	139.4031
20	15.8776	118.8697	139.4031
Arithmetic average $\bar{y}$	15.8776	118.8693	139.4032
Standard deviation equaling standard uncertainty of CMM $u_{p\_CMM\_cu}$	0.0002	0.0002	0.0003

A 15 Measurement with CT on the Cured Test Object for LLSS Measurement Uncertainty

Table A-5: Measurement with CT on the Cured Test Object for LLSS measurement uncertainty

Trail	Distance between planes [mm]	Angle 120° [°]	Angle 140° [°]
1	15.9167	119.3404	139.3482
2	15.9333	119.4452	139.3376
3	15.8877	119.4939	139.3410
4	15.9221	119.3960	139.3095
5	15.9232	119.3799	139.3164
6	15.8956	119.3708	139.3498
7	15.9289	119.3370	139.3606
8	15.8991	119.3398	139.4030
9	15.9052	119.3581	139.3603
10	15.8993	119.4727	139.4211
11	15.9043	119.3518	139.3858
12	15.9132	119.3547	139.3280
13	15.8944	119.3341	139.3135
14	15.8947	119.4349	139.4335
15	15.9115	119.4384	139.3621
16	15.9133	119.4951	139.3688
17	15.8843	119.4086	139.3278
18	15.9285	119.3988	139.3227
19	15.9313	119.3220	139.3232
20	15.8968	119.3312	139.3524
21	15.9054	119.4630	139.3454
22	15.9321	119.3140	139.3278
23	15.9032	119.3742	139.3461
24	15.9161	119.4034	139.3173
25	15.9133	119.3977	139.3188
Arithmetic average $\bar{y}$	15.9101	119.3902	139.3488
Standard deviation equaling standard uncertainty of CT $u_{p\_CT\_cu}$	0.0144	0.0545	0.0330

A 16 Measurement with CT on the Semi-Finished Test Object for LLSS Measurement Uncertainty

Table A-6: Measurement with CT on the semi-finished test object for LLSS measurement uncertainty

Trail	Distance between planes [mm]	Angle 120° [°]	Angle 140° [°]
1	16.0886	121.3813	139.2052
2	16.0699	121.3910	139.3735
3	16.0347	121.1097	138.5825
4	16.0270	121.3996	139.6523
5	16.0911	121.6414	140.0847
6	16.0044	122.1111	140.1177
7	16.0361	121.2564	140.2402
8	16.0761	121.9118	139.0542
9	16.0536	121.8832	139.1624
10	16.0454	121.8946	139.6029
11	16.0396	122.7900	139.7237
12	16.0700	122.1370	139.2305
13	16.1107	122.4218	139.4797
14	16.0281	122.8894	139.4930
15	16.0422	121.5967	139.6797
16	16.0849	122.5211	139.5235
17	16.0366	122.4395	139.3763
18	16.0922	121.7961	139.7729
19	16.0625	121.5314	139.1334
20	16.0432	121.3526	139.1110
21	16.1236	121.9680	139.5307
22	16.1057	121.3979	139.5110
23	16.0900	121.4311	139.7249
24	16.0921	121.7428	139.1685
25	16.0350	121.3904	139.3541
Arithmetic average $\bar{y}$	16.0633	121.8154	139.4755
Standard deviation equaling standard uncertainty of CT $u_{p\_CT\_sf}$	0.0310	0.4927	0.3687

A 17 Measurement with LLSS on the Cured Test Object for LLSS Measurement Uncertainty

Table A-7: Measurement with LLSS on the cured test object for LLSS measurement uncertainty

	Y-Distance from co-ordinate origin [mm]	76	81	86	91	96
1	Distance between planes [mm]	16.1158	15.9533	15.9518	15.8451	15.9304
	Angle 120° [°]	118.6801	119.2915	119.1442	119.2478	119.2701
	Angle 140° [°]	139.7274	139.6478	139.4427	139.2229	139.5172
2	Distance between planes [mm]	16.1353	15.9900	15.9678	15.8737	15.9156
	Angle 120° [°]	118.3696	119.7385	119.2048	119.3962	119.3708
	Angle 140° [°]	139.3195	139.5260	139.4389	139.1358	139.5750
3	Distance between planes [mm]	16.1305	15.9713	15.9903	15.8610	15.9210
	Angle 120° [°]	118.3954	119.7630	119.2046	119.3645	119.2719
	Angle 140° [°]	139.3735	139.3825	139.6658	139.1972	139.5832
4	Distance between planes [mm]	16.1403	15.9862	15.9739	15.8912	15.9158
	Angle 120° [°]	118.3844	119.6521	119.2970	119.3126	119.3417
	Angle 140° [°]	139.2526	139.3756	139.4250	139.2053	139.5314
5	Distance between planes [mm]	16.1375	15.9806	15.9473	15.8765	15.9273
	Angle 120° [°]	118.4701	119.5816	119.1658	119.1878	119.3648
	Angle 140° [°]	139.3711	139.3506	139.5619	139.1336	139.5831
6	Distance between planes [mm]	16.1358	15.9975	15.9653	15.8942	15.9213
	Angle 120° [°]	118.4174	119.6923	119.3071	119.1571	119.1745
	Angle 140° [°]	139.3892	139.5324	139.4634	139.1827	139.5855
7	Distance between planes [mm]	16.1302	15.9983	15.9596	15.8840	15.9051
	Angle 120° [°]	118.4093	119.9420	119.3324	119.2960	119.6578
	Angle 140° [°]	139.3058	139.4711	139.4397	139.2688	139.4390
8	Distance between planes [mm]	16.1341	15.9939	15.9616	15.8511	15.9189
	Angle 120° [°]	118.4762	119.7089	119.0518	119.2414	119.3290
	Angle 140° [°]	139.3678	139.4915	139.4377	139.2226	139.5045

9	Distance between planes [mm]	16.1394	15.9752	15.9596	15.8771	15.9100
	Angle 120° [°]	118.4240	119.8304	119.4642	119.2460	119.4504
	Angle 140° [°]	139.4296	139.5716	139.4418	139.2199	139.4790
10	Distance between planes [mm]	16.1373	15.9679	15.9712	15.8683	15.9066
	Angle 120° [°]	118.6895	119.8483	119.2767	119.1225	119.2820
	Angle 140° [°]	139.2646	139.4556	139.5107	139.2108	139.5158
11	Distance between planes [mm]	16.1413	15.9819	15.9553	15.8668	15.9202
	Angle 120° [°]	118.5447	119.6441	119.1416	119.1964	119.2976
	Angle 140° [°]	139.3570	139.2769	139.4422	139.2881	139.5512
12	Distance between planes [mm]	16.1413	15.9961	15.9676	15.8871	15.9078
	Angle 120° [°]	118.6283	119.7008	119.1011	119.1298	119.5558
	Angle 140° [°]	139.3185	139.3775	139.3933	139.3011	139.4762
13	Distance between planes [mm]	16.1049	15.9997	15.9773	15.8862	15.9091
	Angle 120° [°]	118.6676	119.6959	119.1282	119.2466	119.1753
	Angle 140° [°]	139.5689	139.5177	139.4145	139.1212	139.5653
14	Distance between planes [mm]	16.1363	15.9935	15.9779	15.8567	15.9183
	Angle 120° [°]	118.5424	119.6766	119.2258	119.3288	119.3566
	Angle 140° [°]	139.3753	139.4187	139.4519	139.4154	139.5147
15	Distance between planes [mm]	16.1401	15.9801	15.9750	15.8747	15.9151
	Angle 120° [°]	118.5208	119.7456	119.2166	119.2799	119.7421
	Angle 140° [°]	139.3593	139.5143	139.3246	139.2573	139.5518
16	Distance between planes [mm]	16.1369	15.9797	15.9598	15.8605	15.9216
	Angle 120° [°]	118.7745	119.8196	119.1155	119.0333	119.2131
	Angle 140° [°]	139.4148	139.5051	139.5048	139.2165	139.4810
17	Distance between planes [mm]	16.1403	15.9618	15.9810	15.8896	15.9200
	Angle 120° [°]	118.6587	119.8137	119.4244	119.1988	119.8388
	Angle 140° [°]	139.3700	139.6172	139.4822	139.3088	139.6163
18	Distance between planes [mm]	16.1319	15.9879	15.9831	15.8590	15.9073
	Angle 120° [°]	118.5679	119.9571	119.1043	119.4585	119.5304
	Angle 140° [°]	139.4668	139.5773	139.4080	139.2090	139.5609

19	Distance between planes [mm]	16.1432	15.9980	15.9669	15.8748	15.9275
	Angle 120° [°]	118.3850	119.7376	118.9783	119.1288	119.4367
	Angle 140° [°]	139.3855	139.6522	139.5139	139.2127	139.4798
20	Distance between planes [mm]	16.1371	15.9918	15.9680	15.8795	15.9216
	Angle 120° [°]	118.7399	119.8043	119.3546	119.1918	119.2089
	Angle 140° [°]	139.3462	139.5805	139.5561	139.2134	139.5613
21	Distance between planes [mm]	16.1386	15.9835	15.9675	15.8794	15.9166
	Angle 120° [°]	118.3594	119.7816	119.6012	119.0568	119.2818
	Angle 140° [°]	139.4311	139.5929	139.4383	139.3541	139.5733
22	Distance between planes [mm]	16.1393	15.9964	15.9659	15.8800	15.9142
	Angle 120° [°]	118.6854	119.5110	119.3345	119.2134	119.3397
	Angle 140° [°]	139.4650	139.6220	139.6553	139.3592	139.5538
23	Distance between planes [mm]	16.1371	15.9788	15.9778	15.8790	15.9079
	Angle 120° [°]	118.5387	119.2937	119.1502	119.7565	119.3332
	Angle 140° [°]	139.4235	139.3494	139.4057	139.2630	139.4702
24	Distance between planes [mm]	16.1372	15.9958	15.9709	15.8778	15.9191
	Angle 120° [°]	118.5907	119.6199	119.4605	119.1495	119.3662
	Angle 140° [°]	139.4711	139.7102	139.4593	139.3075	139.4553
25	Distance between planes [mm]	16.1348	15.9662	15.9515	15.8854	15.9152
	Angle 120° [°]	118.4668	119.7985	119.2007	118.9376	119.8572
	Angle 140° [°]	139.4425	139.5052	139.2861	139.2070	139.5102

Arithmetic average planes [mm] $\bar{y}$	15.9756
Arithmetic average angle 120° $\bar{y}$	119.2236
Arithmetic average angle 140° $\bar{y}$	139.4276
Standard deviation planes [mm] equaling standard uncertainty of LLSS $u_{p\_LLSS\_cu}$	0.0896
Standard deviation angle 120° equaling standard uncertainty of LLSS $u_{p\_LLSS\_cu}$	0.4162
Standard deviation angle 140° equaling standard uncertainty of LLSS $u_{p\_LLSS\_cu}$	0.1331

A 18 Measurement with LLSS on the Semi-Finished Test Object for LLSS Measurement Uncertainty

Table A-8: Measurement with LLSS on the semi-finished test object for LLSS measurement uncertainty

	Y-Distance from co-ordinate origin [mm]	73	78	83	88	93
1	Distance between planes [mm]	15.9217	16.0105	15.9384	16.0200	16.0077
	Angle 120° [°]	121.4310	122.5027	120.9788	122.3357	124.8259
	Angle 140° [°]	138.4862	138.4385	138.5535	140.6693	140.8026
2	Distance between planes [mm]	15.9141	16.0441	15.9257	16.0195	16.0396
	Angle 120° [°]	122.6555	122.1379	120.9027	121.7909	120.4850
	Angle 140° [°]	137.9980	138.3289	139.6145	141.5017	140.6687
3	Distance between planes [mm]	15.8988	16.0304	15.9196	16.0149	16.0351
	Angle 120° [°]	124.4450	121.8667	118.4084	124.4645	120.0336
	Angle 140° [°]	136.9570	138.1989	138.2670	140.9093	140.4957
4	Distance between planes [mm]	15.9121	16.0169	15.9254	16.0354	16.0278
	Angle 120° [°]	121.7190	123.3495	120.5842	121.6857	119.7852
	Angle 140° [°]	137.4472	138.4699	136.7531	141.4149	142.0776
5	Distance between planes [mm]	15.9265	16.0179	15.9271	16.0364	16.0164
	Angle 120° [°]	122.3812	123.9247	121.1395	120.8184	119.8035
	Angle 140° [°]	136.9595	138.1080	138.1153	140.4065	140.4718
6	Distance between planes [mm]	15.9380	16.0114	15.9198	16.0105	16.0308
	Angle 120° [°]	121.1277	122.7865	120.5376	122.3789	120.0219
	Angle 140° [°]	137.1134	137.9820	137.8595	141.5503	141.1659
7	Distance between planes [mm]	15.9330	16.0218	15.9313	16.0010	16.0324
	Angle 120° [°]	122.6628	123.5299	120.0613	120.0574	120.6488
	Angle 140° [°]	137.2618	137.8896	138.6269	141.8844	141.6931
8	Distance between planes [mm]	15.9320	16.0153	15.9328	16.0213	16.0370
	Angle 120° [°]	120.1706	122.8863	120.8425	123.1907	122.5469
	Angle 140° [°]	137.2265	137.8760	138.2841	141.5540	141.5921

9	Distance between planes [mm]	15.9360	16.0224	15.9262	16.0358	16.0017
	Angle 120° [°]	120.3371	121.4320	122.7806	122.6579	119.9780
	Angle 140° [°]	136.7636	137.5901	138.6203	141.8258	141.2207
10	Distance between planes [mm]	16.0135	16.0205	15.9331	16.0389	16.0509
	Angle 120° [°]	123.1808	121.7431	122.1020	120.5413	120.9585
	Angle 140° [°]	137.3471	137.3648	138.1339	141.5851	141.3724
11	Distance between planes [mm]	15.9115	16.0115	15.9354	16.0339	16.0292
	Angle 120° [°]	122.7803	122.4338	120.0690	121.0007	123.3481
	Angle 140° [°]	137.3253	137.4572	138.6773	141.9912	140.5903
12	Distance between planes [mm]	15.9325	16.0125	15.9118	16.0194	16.0305
	Angle 120° [°]	122.5444	123.5173	118.8817	124.3368	120.6293
	Angle 140° [°]	136.8711	138.1221	138.7959	141.1900	140.7914
13	Distance between planes [mm]	15.9234	16.0138	15.9477	16.0106	16.0096
	Angle 120° [°]	121.8061	122.8442	120.1311	122.5971	123.5348
	Angle 140° [°]	136.8041	137.6552	138.1251	142.0972	140.9746
14	Distance between planes [mm]	15.9203	16.0139	15.9330	16.0357	16.0025
	Angle 120° [°]	119.9664	123.7230	119.5589	120.9939	120.5165
	Angle 140° [°]	139.5100	138.4541	138.6385	141.5879	141.6553
15	Distance between planes [mm]	15.9218	16.0235	15.9351	16.0291	15.9312
	Angle 120° [°]	121.7517	122.6249	119.9464	123.6798	122.6677
	Angle 140° [°]	136.8278	138.2236	139.3681	141.8141	138.2535
16	Distance between planes [mm]	15.9278	16.0187	15.9352	16.0252	16.0105
	Angle 120° [°]	121.2797	122.2438	121.7734	122.3806	122.1398
	Angle 140° [°]	137.1736	137.2949	139.2346	140.6580	141.9028
17	Distance between planes [mm]	15.9261	16.0358	15.9544	16.0187	16.0319
	Angle 120° [°]	121.4120	123.2548	121.9352	119.2851	120.6694
	Angle 140° [°]	136.8094	138.1520	138.8653	140.4718	141.1705
18	Distance between planes [mm]	15.9182	16.0159	15.9362	16.0366	16.0105
	Angle 120° [°]	123.4008	122.8237	120.6532	122.5535	120.7834
	Angle 140° [°]	137.4241	138.3073	138.0743	142.5286	140.7469

19	Distance between planes [mm]	15.9116	16.0196	15.9332	16.0164	16.0252
	Angle 120° [°]	123.1179	122.4892	119.8119	120.8967	121.7589
	Angle 140° [°]	136.7070	137.9302	138.6025	140.0585	140.6293
20	Distance between planes [mm]	15.9226	16.0164	15.9446	16.0270	16.0147
	Angle 120° [°]	122.8601	122.4045	122.9596	122.1679	121.4809
	Angle 140° [°]	136.8229	138.0881	138.4973	141.2288	140.8562
21	Distance between planes [mm]	15.9303	16.0234	15.9260	15.9970	16.0402
	Angle 120° [°]	121.9723	122.1586	120.9181	119.2471	122.7157
	Angle 140° [°]	136.8828	137.8285	138.9076	141.5668	140.5897
22	Distance between planes [mm]	15.9052	16.0161	15.8837	16.0336	16.0398
	Angle 120° [°]	122.1459	122.8109	120.5386	121.0607	120.8081
	Angle 140° [°]	136.8077	137.3282	138.6483	140.8533	140.5032
23	Distance between planes [mm]	15.8995	16.0271	15.9268	16.0534	16.0319
	Angle 120° [°]	121.1943	123.1373	118.7610	122.3014	120.7126
	Angle 140° [°]	136.7708	138.3756	138.4800	140.7364	141.1070
24	Distance between planes [mm]	15.9084	16.0149	15.9321	16.0233	16.0324
	Angle 120° [°]	122.9494	122.3941	120.6952	120.4944	119.9813
	Angle 140° [°]	137.2758	138.2626	138.7666	141.1100	141.3481
25	Distance between planes [mm]	15.9003	16.0137	15.9303	16.0171	16.0262
	Angle 120° [°]	122.4920	122.4498	119.8221	120.7297	120.2889
	Angle 140° [°]	136.6760	137.6568	138.1736	141.4871	141.0736

Arithmetic average planes [mm] $\bar{y}$	15.9838
Arithmetic average angle 120° $\bar{y}$	121.6705
Arithmetic average angle 140° $\bar{y}$	139.1900
Standard deviation planes [mm] equaling standard uncertainty of LLSS $u_{p\_LLSS\_sf}$	0.0498
Standard deviation angle 120° equaling standard uncertainty of LLSS $u_{p\_LLSS\_sf}$	1.3376
Standard deviation angle 140° equaling standard uncertainty of LLSS $u_{p\_LLSS\_sf}$	1.7451

A 19 Components of PPT System

In the following, all components of the PPT system are explained in more detail.

A 19.1 Infrared Camera

The used camera from the company InfraTec GmbH is of type ImageIR 5385S. The detector type is a cooled mercury-cadmium-telluride-focal plane array with a size of 320 x 256 pixels, designed for the medium infrared range of 3.7-4.8 µm. In full-screen mode it is possible to capture 450 frames per second. The temperature resolution at 30°C is 0.015 K. The camera has a lens with a focal length of 25 mm and a f-number of 2.0. The camera is connected to the control and evaluation software via a Gigabit Ethernet interface. (A_Weinhardt 2017; InfraTec GmbH 2016b; InfraTec GmbH 2016a)

A 19.2 Mainframe

The mainframe consists of three components for active thermography, described in the chapters below. These are housed in a 19" rack.

EWS 7 – Edevis Workstation Core i7

The workstation is the central computer for the thermography system. It contains the software for control and evaluation of a thermographic measurement. A powerful computer is required for fast data evaluation, therefore Core i7 4771 (4x 3.6 - 4.0 GHz) is used as the central processing unit and 16GB DDR3 RAM as random access memory. (A_Weinhardt 2017; edevis GmbH 2016)

Edevis Signal Generator

The signal generator is the central interface for the edevis system. Via a uniform user interface, represented by the DisplayIMG software, it controls all used system components. This includes excitation module and triggering of the infrared camera. (A_Weinhardt 2017; edevis GmbH 2016)

Software DisplayIMG Professional

The software is responsible for data acquisition and evaluation. The modular design ensures extensibility for several infrared cameras and excitation modes, as well as a strong robustness. Automatization components control measuring process plus transfer of results and are compatible with numerous common Programmable Logic Controllers (PLC). The use of Open Platform Communications (OPC) standard also guarantees

support for PLC controllers. Data can be loaded directly into other programs such as MATLAB® through existing plug-ins. (A_Weinhardt 2017; edevis GmbH 2016)

A 19.3   Excitation System

The excitation system is responsible for unbalancing the test objects thermal equilibrium. A generator with flash lamp is used for active excitation.

Flash Generator PTvis 6000

The used flash generator has been developed for industrial applications in pulse thermography. It is installed in the 19" rack. The stored flash energy amounts to 6 kJ. (A_Weinhardt 2017; edevis GmbH 2016)

Flash Lamp PTvis 6000

The flash lamp provides the optical excitation for pulse thermography. The used one is characterized by a short flash duration with a maximum energy of 6 kJ. An additional glass filter in front of the flash lamp ensures spectral separation between excitation light and detection area of the infrared camera. (A_Weinhardt 2017; edevis GmbH 2016)

A 20 Test Procedure for PPT

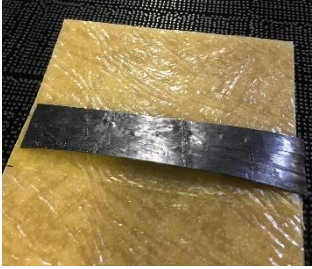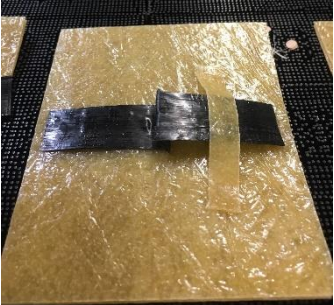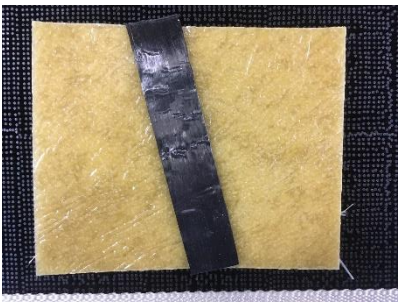The most important points of the test procedure are briefly described below.

Initially, the camera, the signal generator and the DisplayIMG Professional software from edevis have to be started. As soon as the camera has been booted, it can be connected to the software and a live image is received. A calibration data set is then selected from a so-called NUC table (Non-Uniformity-Correction). The selection is based on the used lens and the expected temperatures. The parameters selected in this thesis are described in Chapter 7.3.1. Subsequently, each new start of the software program requires a non-uniformity correction (NUC comparison) of the captured image area. This comparison minimizes inhomogeneities between individual infrared pixels of focal plane array detector. The necessity for a NUC adjustment is made clear by faulty pixels in the live image. (A_Griener 2018)

Afterwards, only the frame rate, the recording time and the pulse delay have to be set. In the last step the flash generator and the flash lamp are switched on and the measurement can be carried out.

A 21 Component for PPT Defect Characterization

Table A-9: Component for PPT defect characterization

Cured Test Objects	Semi-Finished Test Objects
Reference Test Object Surface	

Foreign Body Test Object Surface	

Fold Test Object Surface	

Angular Devistion 15° Test Object Surface	

Reference Test Object Depth
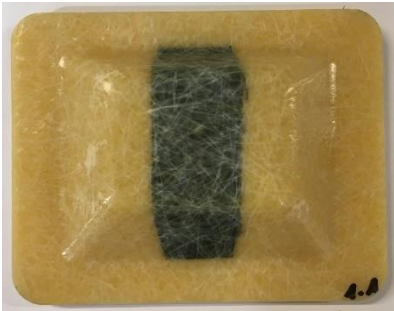
Foreign Body Test Object 1 Depth
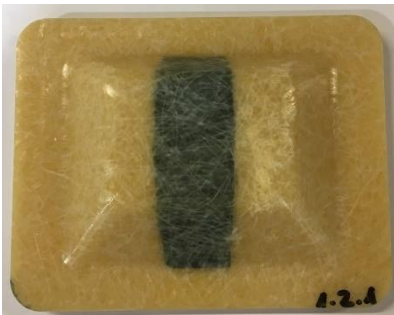
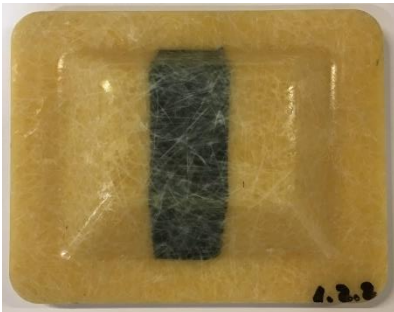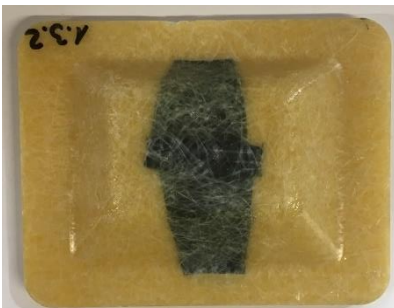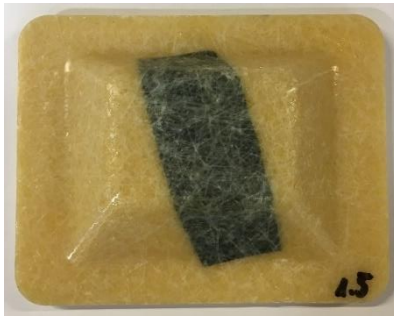## Foreign Body Test Object 2 Depth

Fold Test Object Depth

Angular Devistion 15° Test Object Depth

A 22 Summary of Evaluation Process for Defect Characterization

Table A-10: Summary of the two-stage evaluation process optimum combination in frequency spectrum and location-related value progression for clear defect characterisation in cured state according to (A_Griener 2018)

Surface Defect		
	Evaluation in the frequency spectrum	**Evaluation of location-related values**
	1st stage of the evaluation process	*2nd stage of the evaluation process*
Foreign Body 1	**Phase Spectrum**	**Amplitude Curve**
Defect characteristics description	A stronger decrease of the phase values from a frequency of 0.5 Hz.	Amplitude at all considered frequencies indicate increased values compared to reference curves.
Example		
Fold	**Phase Spectrum**	**Phase Curve**
Defect characteristics description	Increased phase values up to 1.7 Hz. Intersection with the reference course. From 0.5 Hz continuously decreasing phase values.	Phase values increased at low frequencies in the defect area. Frequency increase leads to phase value decrease in defect area → Global minimum.
Example		

Depth Defect		
	Evaluation in the frequency spectrum	**Evaluation of location-related values**
	1st stage of the evaluation process	*2nd stage of the evaluation process*
Foreign Body 1 & 2	**Phase Spectrum**	**Amplitude Curve**
Defect characteristics description	Phase jump between 0.2 – 1 Hz is significantly attenuated. Increased phase values in high-frequency range (>2.5 Hz).	Amplitude at all frequencies considered increased values compared to reference curves.
Example		
Fold	**Phase Spectrum**	**Amplitude Curve**
Defect characteristics description	Strongly attenuated curve (phase angle difference to reference object up to 90°), no phase jump detected.	Clear amplitude increase in defect area. Increased layer structure of the fold indicates up to five times higher amplitude values in the course of the defect.
Example		
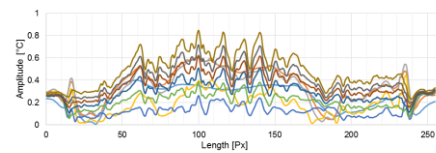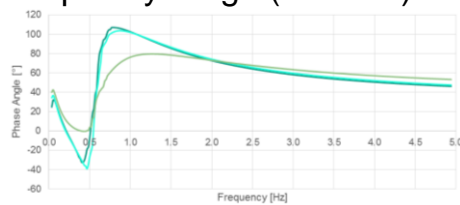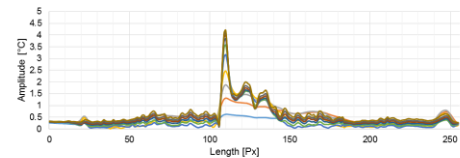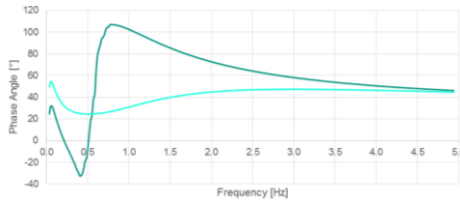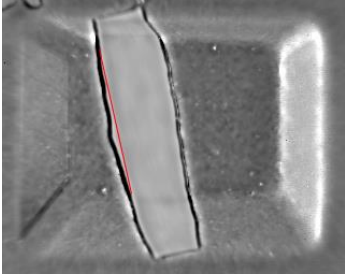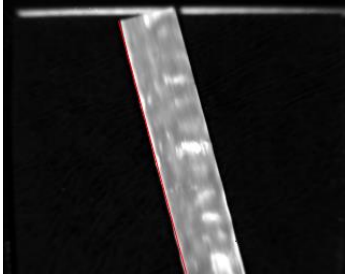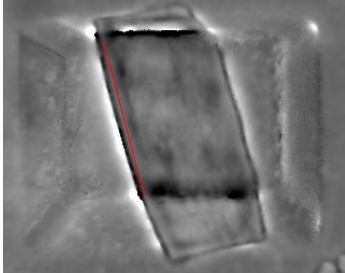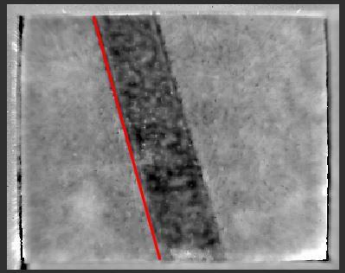
Table A-11: Defect characterization for angle deviation in the cured and semi-finished test objects

	Surface Defect	
	Evaluation in frequency spectrum	
Angle 15°	**Cured test object**	**Semi-finished test object**
Defect character- istics description	Co-SMC strip is located on the surface. Clear demarcation to the surrounding area in the phase image	Co-SMC strip is located on the surface. Clear demarcation to the surrounding area in the amplitude image
Example		
	Depth Defect	
	Evaluation in frequency spectrum	
Angle 15°	**Cured test object**	**Semi-finished test object**
Defect characteris- tics description	Co-SMC strip is attached in depth. Clear demarcation to the surrounding is visible in phase image.	Co-SMC strip is attached in depth. Clear demarcation to the surrounding is visible in phase image.
Example		

A 23 Setting Parameters of the CT Measurement for PPT Measurement Uncertainty

Table A-12: Setting parameters of the CT measurement for PPT measurement uncertainty

Setting parameters	Cured test object	Thin semi-finished test object	Thick semi-finished test object
Tube voltage [kV]	118	130	95
Tube current [µA]	200	130	300
Integration time [ms]	1000	1000	1000
Gain	2.5	2.5	2.5
Image averaging	off	off	off
Binning	1x1	1x1	1x1
Voxel size [µm]	70	70	70
Focal spot [µm]	40	40	40
Magnification Factor	1.81	1.81	1.81
Number of projections	1550	1550	1550
Prefilter	1mm Aluminum	-	1mm Aluminum

A 24 Measurement with CT on the Cured Test Object for PPT Measurement Uncertainty

Table A-13: Measurement with CT on the cured test object for PPT measurement uncertainty

Trail	Area of blind hole 1 [mm^2]	Area of blind hole 2 [mm^2]	Area of blind hole 3 [mm^2]	Area of blind hole 4 [mm^2]	Area of blind hole 5 [mm^2]
1	311.65	111.22	110.47	311.03	110.47
2	311.03	111.22	109.73	310.40	111.22
3	311.03	111.22	109.36	310.40	110.10
4	310.40	110.47	110.47	310.40	110.47
5	310.40	110.47	110.10	311.03	110.47
Arithmetic average $\bar{y}_{CT\_cu}$	310.90	110.92	110.03	310.65	110.55
Standard deviation equaling calibration uncertainty of PPT $u_{cal\_PPT\_cu}$	0.47	0.37	0.43	0.31	0.37

A 25 Measurement with PPT on the Cured Test Object for PPT Measurement Uncertainty

Table A-14: Measurement with PPT on the cured test object for PPT measurement uncertainty

Trail	Area of blind hole 1 [mm^2]	Area of blind hole 2 [mm^2]	Area of blind hole 3 [mm^2]	Area of blind hole 4 [mm^2]	Area of blind hole 5 [mm^2]
1	319.82	112.56	107.83	309.27	127.19
2	326.27	108.47	110.62	316.16	115.14
3	333.59	118.80	112.99	315.73	115.36
4	332.30	110.41	109.98	329.72	112.56
5	331.01	111.48	111.27	317.45	117.73
6	335.74	112.56	108.69	316.37	113.21
7	319.39	105.03	107.61	317.88	111.48
8	317.66	113.21	119.02	315.51	117.94
9	318.09	113.21	118.59	314.87	114.93
10	338.33	124.61	107.83	318.52	112.56
11	331.87	136.66	136.66	322.61	114.28
12	330.58	129.56	111.70	312.50	113.85
13	326.70	109.98	111.05	314.65	112.78
14	318.52	118.80	122.24	314.65	108.90
15	319.39	120.09	114.71	314.87	110.19
16	320.68	111.48	114.07	310.99	117.51
17	324.77	109.76	117.73	310.99	114.28
18	316.16	111.05	113.42	316.16	113.21
19	316.16	121.38	102.23	317.45	111.91
20	317.66	115.57	117.29	310.56	112.99
21	313.79	109.76	111.05	315.30	110.41
22	315.73	123.54	108.69	315.30	112.34
23	312.71	116.86	112.99	318.31	117.08
24	314.87	108.47	106.32	317.02	113.85
25	319.17	108.90	119.45	312.50	117.51
Arithmetic average $\bar{y}$	322.84	115.29	113.36	315.81	114.37
Standard deviation equaling standard uncertainty of PPT $u_{p\_PPT\_cu}$	7.44	7.28	6.64	4.04	3.54

A 26 Measurement with CT on the Semi-Finished Test Objects for PPT Measurement Uncertainty

Table A-15: Measurement with CT on the semi-finished test objects for PPT measurement uncertainty

	Thin test object		Thick test object	
Trail	Angle 8°	Angle 12°	Angle 8°	Angle 12°
1	7.97	12.04	8.07	13.97
2	7.82	12.09	8.19	14.07
3	8.25	11.9	8.08	14.02
4	8.37	12	7.78	13.91
5	8.1	12.24	7.89	13.78
Arithmetic average $\bar{y}_{CT\_sf}$	8.10	12.05	8.00	13.95
Standard deviation equaling calibration uncertainty of PPT $u_{cal\_PPT\_sf}$	0.20	0.11	0.15	0.10

A 27 Measurement with PPT on the Semi-Finished Test Objects for PPT Measurement Uncertainty

Table A-16: Measurement with PPT on the semi-finished test objects for PPT measurement uncertainty

Trail	Thin test object		Thick test object	
	Angle 8°	Angle 12°	Angle 8°	Angle 12°
1	8.6	12.1	9.2	13.8
2	8.1	12.0	8.2	13.3
3	8.2	12.0	8.4	13.1
4	8.1	12.0	7.6	13.5
5	8.1	12.1	8.2	13.7
6	8.1	11.7	8.3	13.4
7	8.8	12.1	8.3	13.4
8	8.0	11.9	8.0	13.2
9	8.4	12.0	7.8	13.9
10	8.4	12.0	8.0	13.6
11	8.7	11.9	8.3	13.7
12	8.6	12.2	8.1	13.7
13	8.1	12.3	8.3	13.6
14	8.0	12.1	8.0	13.6
15	8.1	12.1	8.4	13.4
16	8.4	11.9	8.2	13.5
17	8.2	12.3	7.9	13.3
18	8.6	11.9	8.1	13.3
19	8.0	12.3	8.1	13.2
20	8.3	12.2	8.0	13.5
21	8.5	12.2	8.3	13.6
22	8.3	11.8	8.1	13.2
23	8.4	12.6	8.3	13.3
24	8.2	12.1	7.4	13.2
25	8.2	12.3	8.2	13.4
Arithmetic Average $\bar{y}$	8.30	12.08	8.15	13.46
Standard deviation equaling standard uncertainty of PPT $u_{p\_PPT\_sf}$	0.23	0.19	0.32	0.21

A 28 Pinhole Camera Model

The aim of data fusion is to project PPT images onto the LLSS CoP. For this purpose, the relationship between the CoP and the pixels of a thermographic image has to be determined. The pinhole camera model is considered suitable and therefore briefly explained below.

Initially, the camera coordinate system (COS) is equated with the world COS, as illustrated in Figure A-15.

Initially, the camera coordinates X_C, Y_C and Z_C are equated with the world coordinates X, Y and Z, as illustrated in Figure A-15.
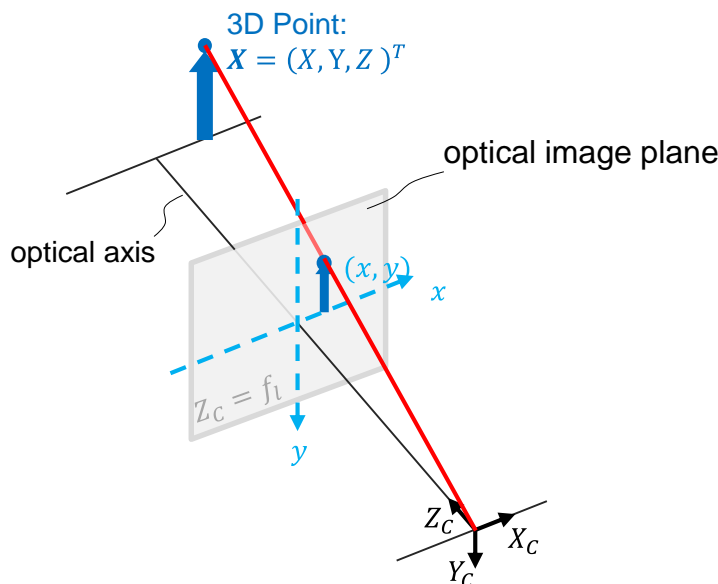
Figure A-15: Pinhole camera model for world COS = camera COS according to (A_Pohland 2017)

Thus, the 3D coordinates of both systems are identical and the following applies

$$\boldsymbol{X} = (X, Y, Z)^T = (X_C, Y_C, Z_C)^T = \boldsymbol{X}_C \qquad \text{Equation A-8}$$

The Z_C axis is defined to be the optical axis. Thus, the image distance from the camera COS origin equals the f_l and is perpendicular to the optical axis. Due to the relationship for similar triangles, the following applies

$$\frac{X}{Z} = \frac{x}{f_l} \; ; \frac{Y}{Z} = \frac{y}{f_l} \qquad \text{Equation A-9}$$

The 3D point projection on the optical image plane is specified in vector notation as

$$x = \begin{pmatrix} x \\ y \end{pmatrix} = \frac{f}{Z} \begin{pmatrix} X \\ Y \end{pmatrix}.$$ Equation A-10

Applying homogeneous coordinates, results in a matrix equation for the perspective transformation

$$\begin{pmatrix} x \\ y \end{pmatrix} = \frac{f}{Z} \begin{pmatrix} X \\ Y \end{pmatrix} \overset{hom}{\Longrightarrow} \begin{pmatrix} f\dfrac{X}{Z} \\ f\dfrac{Y}{Z} \\ 1 \end{pmatrix} = \begin{pmatrix} fX \\ fY \\ Z \end{pmatrix} = \begin{pmatrix} f & 0 & 0 & 0 \\ 0 & f & 0 & 0 \\ 0 & 0 & 1 & 0 \end{pmatrix} \begin{pmatrix} X \\ Y \\ Z \\ 1 \end{pmatrix}$$ Equation A-11

with the projection matrix M_p. (Süße & Rodner 2014)

$$M_p = \begin{pmatrix} f & 0 & 0 & 0 \\ 0 & f & 0 & 0 \\ 0 & 0 & 1 & 0 \end{pmatrix}$$ Equation A-12

This projection matrix can be divided into the matrices M_f and M_0, whereby M_f is used to model the interior of a pinhole camera.

$$M_p = \begin{pmatrix} f & 0 & 0 & 0 \\ 0 & f & 0 & 0 \\ 0 & 0 & 1 & 0 \end{pmatrix} = \begin{pmatrix} f & 0 & 0 \\ 0 & f & 0 \\ 0 & 0 & 1 \end{pmatrix} \begin{pmatrix} 1 & 0 & 0 & 0 \\ 0 & 1 & 0 & 0 \\ 0 & 0 & 1 & 0 \end{pmatrix} = M_f M_0$$ Equation A-13

In the next step, it is assumed that the camera has its own COS. If the 3D points in world coordinates are known, the transformation in Cartesian coordinates can be described by rotation and translation. (Förstner & Wrobel 2016).

$$\begin{pmatrix} X_C \\ Y_C \\ Z_C \end{pmatrix} = \begin{pmatrix} r_{11} & r_{12} & r_{13} \\ r_{21} & r_{22} & r_{23} \\ r_{31} & r_{32} & r_{33} \end{pmatrix} \begin{pmatrix} X \\ Y \\ Z \end{pmatrix} + \begin{pmatrix} t_x \\ t_y \\ t_z \end{pmatrix}$$ Equation A-14

A compact description is possible by using homogeneous coordinates:

$$\begin{pmatrix} X_C \\ Y_C \\ Z_C \\ 1 \end{pmatrix} = \begin{pmatrix} r_{11} & r_{12} & r_{13} & t_x \\ r_{21} & r_{22} & r_{23} & t_y \\ r_{31} & r_{32} & r_{33} & t_z \\ 0 & 0 & 0 & 1 \end{pmatrix} \begin{pmatrix} X \\ Y \\ Z \\ 1 \end{pmatrix}$$ Equation A-15

With Equation A-11, the projection of 3D world points on the optical plane is described by the following equation:

$$\binom{x}{y} = hom^{-1}\left(\begin{pmatrix} f & 0 & 0 \\ 0 & f & 0 \\ 0 & 0 & 1 \end{pmatrix}\begin{pmatrix} r_{11} & r_{12} & r_{13} & t_x \\ r_{21} & r_{22} & r_{23} & t_y \\ r_{31} & r_{32} & r_{33} & t_z \end{pmatrix}\begin{pmatrix} X \\ Y \\ Z \\ 1 \end{pmatrix}\right) \qquad \text{Equation A-16}$$

As these assumptions refer to an ideal camera, necessary adjustments for a real camera include influences of the used sensor. To perform the last modeling step, transferring the continuous x, y coordinates of the optical image plane into the pixel coordinates u, v of the digital image, the following has to be considered:

- Position of the main image point u_c, v_c (in pixel coordinates), representing the perpendicular projection center point on the image plane
- Possible, different sensor scaling s_x, s_y in x and y direction
- The axial misalignment s_θ, also called diagonal distortion

With these influences, the digital image coordinates $\boldsymbol{u} = (u, v)^T$ are determined from the optical image coordinates $\boldsymbol{x} = (x, y)^T$ according to the following equation:

$$\binom{u}{v} = hom^{-1}\left(\begin{pmatrix} s_x & s_\theta & u_c \\ 0 & s_y & v_c \\ 0 & 0 & 1 \end{pmatrix}\begin{pmatrix} x \\ y \\ 1 \end{pmatrix}\right). \qquad \text{Equation A-17}$$

The model for the real camera is created by integrating Equation A-17 into the model equation of the ideal pinhole camera:

$$\binom{u}{v} = hom^{-1}\left(\begin{pmatrix} s_x & s_\theta & u_c \\ 0 & s_y & v_c \\ 0 & 0 & 1 \end{pmatrix}\begin{pmatrix} f & 0 & 0 \\ 0 & f & 0 \\ 0 & 0 & 1 \end{pmatrix}\begin{pmatrix} r_{11} & r_{12} & r_{13} & t_x \\ r_{21} & r_{22} & r_{23} & t_y \\ r_{31} & r_{32} & r_{33} & t_z \end{pmatrix}\begin{pmatrix} X \\ Y \\ Z \\ 1 \end{pmatrix}\right)$$

$$= hom^{-1}\left(\begin{pmatrix} f_x & f_\theta & u_c \\ 0 & f_y & v_c \\ 0 & 0 & 1 \end{pmatrix}\begin{pmatrix} r_{11} & r_{12} & r_{13} & t_x \\ r_{21} & r_{22} & r_{23} & t_y \\ r_{31} & r_{32} & r_{33} & t_z \end{pmatrix}\begin{pmatrix} X \\ Y \\ Z \\ 1 \end{pmatrix}\right) \qquad \text{Equation A-18}$$

$$\boldsymbol{u} = hom^{-1}(\boldsymbol{M}_i(\boldsymbol{Rt}) \cdot hom(\boldsymbol{X}))$$

The matrix $\boldsymbol{M}_i$ contains the intrinsic parameters representing the camera's 'interior'. It describes the projection of 3D world points in the camera COS onto the digital pixel coordinates. Matrix $\boldsymbol{Rt}$ describes the extrinsic parameters, representing the camera's 'exterior' and providing information about the camera position and orientation in the

world COS as well as the transformation from the world COS to the camera COS. Figure A-16 illustrates the entire camera model.
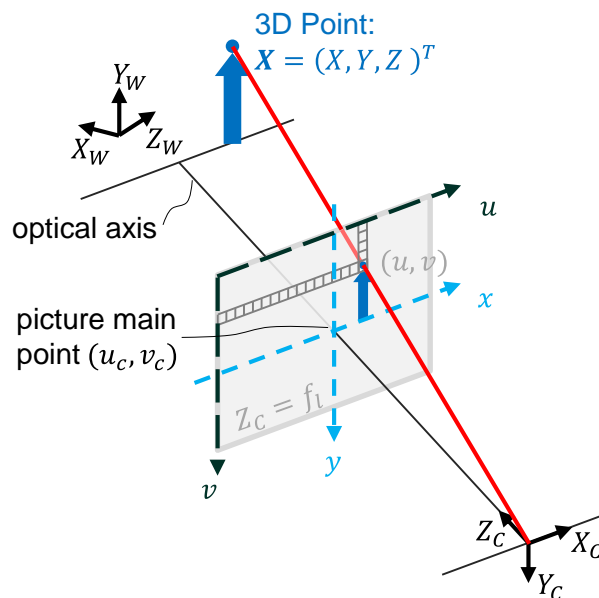

Figure A-16: Complete pinhole camera model according to (A_Pohland 2017)

During calibration, the intrinsic and extrinsic parameters are determined. If the camera setting is not changed, the intrinsic parameters remain constant. The extrinsic parameters have to be redefined as soon as camera orientation to test object is changed. The use of lenses in a real camera results in radial and tangential distortions, descried in (Beyerer, Puente León & Frese 2016; Ricolfe-Viala & Sanchez-Salmeron 2010; Wang et al. 2008).

A 29 Setting Parameters of the CT Measurement for Data Fusion Measurement Uncertainty

Table A-17: Setting parameters of the CT measurement for data fusion measurement uncertainty

Setting parameters	Cured test object
Tube voltage [kV]	118
Tube current [µA]	200
Integration time [ms]	1000
Gain	2.5
Image averaging	Aus
Binning	1x1
Voxel size [µm]	78
Focal spot [µm]	40
Magnification factor	1.63
Number of projections	1550
Prefilter	1 mm Al

A 30 Measurement with CT on the Data Fusion Test Object for Data Fusion Measurement Uncertainty

Table A-18: Measurement with CT on the data fusion test object for data fusion measurement uncertainty

Trail	Distance between Co-SMC and edge [mm]
1	65.56
2	65.59
3	65.63
4	65.62
5	65.59
6	65.55
7	65.47
8	65.55
9	65.54
10	65.58
11	65.54
12	65.53
13	65.55
14	65.6
15	65.59
16	65.59
17	65.63
18	65.65
19	65.5
20	65.54
21	65.6
22	65.53
23	65.57
24	65.58
25	65.5
Arithmetic average $\bar{y}_{CT}$	65.57
Standard deviation equaling calibration uncertainty of DF u_{cal_DF}	0.04

A 31 Measurement with Data Fusion for Data Fusion Measurement Uncertainty

Table A-19: Measurement with data fusion for data fusion measurement uncertainty

Trail	Distance between Co-SMC and edge [mm]
1	65.72
2	65.66
3	64.74
4	66.09
5	65.65
6	65.20
7	65.77
8	65.63
9	65.96
10	64.79
11	64.65
12	65.53
13	64.61
14	65.04
15	65.90
16	64.48
17	65.37
18	65.28
19	64.76
20	65.74
21	64.63
22	64.78
23	65.61
24	65.02
25	64.97
Arithmetic average $\bar{y}$	65.26
Standard deviation equaling standard uncertainty of DF u_{p_DF}	0.49